Investigation and design of SERS active nanoparticle assemblies *via* biological interactions

Derek Craig

July 2013

This thesis is the result of the author's original research. It has been composed by the author and has not been previously submitted for examination which has led to the award of a degree.

Signed: Date:

Acknowledgements

Initial thanks are reserved for both of my supervisors, Dr. Karen Faulds and Professor Duncan Graham for this opportunity and for their continuing support throughout my PhD and beyond. I would also like to thank both the former and present members at the centre for molecular nanometrology for making my time in the group enjoyable during the good times and bearable during the bad.

Special thanks are reserved for Kristy, Stacey, Rooney, Alan, Lee, Elley and Jen for all of the banter. Specific thanks to Sarah for the inappropriate banter and for being cultured like our cells. Mhairi for not only being 'my rock' but for showing me how to baseline correct with more than two points and for the many laughs I have shared sitting next to her. For Jane who in the good and the bad times has provided support even in the absence of being in the office and for her dazzling collection of Pat Butcher earrings. Finally, to Jonathan for reinvigorating my PhD and for his many terrible stories and jokes.

The support of my family and friends has been incredible throughout my studies. In particular I would like to thank Kevin, my brothers (and sisters), my gran and Ann for their unwavering support and constant encouragement which helped drag me over the finishing line.

Finally, this thesis is dedicated to both my parents for all of their encouragement and belief for which I will always be grateful.

Abstract

The overarching theme of this research was to further the understanding of the interactions of both the proteome and the glycome. An initial soft focus was placed upon increasing the stability of nanoparticles *via* the design of novel linker chemistries for nanoparticle functionalisation. From these initial studies, the synergic theme of studying different types of biological interactions using SERS has come to the forefront of this research.

Novel nanotag synthesis has been detailed using a one-step functionalisation methodology. The stability of these nanotags has been investigated and found to be on par with the stability achieved using the current leading methods of nanotag functionalisation. Reproducible SERS spectra have been obtained in the presence of high electrolyte concentrations as well as in highly acidic conditions. These novel nanotags have been employed to differing degrees of success in a number of immunoassay formats. Successful detection has been achieved in a TMB ELISA format indicating that the biological integrity of the biomolecules attached to these nanotags remains intact following their functionalisation.

Following the success of the linkers devised for nanotags synthesis several novel short chain carbohydrate linker groups were devised. These carbohydrate linkers were then attached to both gold and silver nanoparticle for deployment in the formation of nanoparticle assemblies mediated by the interaction with carbohydrate specific proteins known as lectins. The formation of these nanoparticle assemblies has shown to be dependent on the concentration of lectin present and as such, linear ranges of detection have been achieved using both extinction spectroscopy and SERS, which are unrivalled when using current detection methods.

The converse of this approach, lectin functionalised nanoparticles, were employed as molecular imaging agents for the elucidation of the surface carbohydrate composition of multiple cell lines. These studies have been extended to detecting disease directed cellular modifications *via* binding to over expressed sialic acid residues present on prostate cancerous cells. This has elicited a method by which it may be possible to discriminate between both cancerous and non-cancerous cells in a clinical environment.

Abbreviations

3-MPA- 3-mercaptopropionic acid

P8 – PEG8 linker

P41- PEG 41 linker

ARMS-Amplification refractory mutation system

Asn - Asparganine

Asp – Aspartic acid

BRCA1 – Breast cancer susceptibility gene 1

CA - ConA

CCD – Charge coupled device

CDI - 1,1'-Carbonyldiimidazole

CFTCR – Cystic fibrosis trans membrane conductance regulator

CHO – Chinese hamster ovarian

ConA – Concanavalin A

DAB - *p*-(dimethylamino)azobenzene

DCC - N,N'-dicyclohexylcarbodiimide

DCLS – Discreet component least squares

DCM - Dichloromethane

DIC - N,N'-diisopropylcarbodimide

DLS – Dynamic light scattering

DMF - Dimethylformamide

DMSO - Dimethylsulfoxide

DNA – Deoxyribose nucleic acid

DNBT – Dinitrobenzene thiol

DTT - Dithiothrietol

EDC.HCl – N'ethylcarbodiimide hydrochloride

ELISA - Enzyme linked immunosorbent assay

FIA – Fluorescent immunoassay

FRET – Fluorescence resonance energy transfer

GAGs – Glycosamino glycans

GBPs – Glycan binding proteins

HeLa – Henrietta Lacks

HRP – Horse radish peroxidase

LC – Lens Culinaris

LSPR – Localised Surface Plasmon Resonance

LOD – Limit of detection

LWD – Long working distance

MALDI – Matrix Assisted Laser desorption ionisation

MG2 – Meracapto galactose

MGITC – Malachite Green Isothiocyanate

ML3 – Meracapto lactose

MM1 – Meracapto mannose

mRNA – Messenger RNA

MRI – Magnetic Resonance Imaging

MS – Mass Spectrometry

NMR – Nuclear Magnetic Resonance

NPs - Nanoparticles

PBS – Phosphate buffer saline

PC3 – Prostate cancer cells

PCR – Polymerase Chain Reaction

PEG – Polyethylene glycol

PNT2A – Human cells

PNA – Peanut Agglutinin

PPIs – Protein-Protein Interactions

PTMs – Post-translational modifications

RIA - Radioactive Immunoassay

rpm – Revolutions per minute

ROX – 6-Carboxyl-X-Rhodamine

SEM – Scanning Electron Microscopy

SERS – Surface Enhanced Raman Scattering

SERRS – Surface Enhanced Resonance Raman Scattering

SPR – Surface Plasmon Resonance

sNHS – N-hydroxysulfosuccinimide

TEM – Transmission Electron Microscopy

TFA – Trifluoroacetic acid

TLC – Thin Layer Chromatography

TMB - Tetramethylbenzidine

TSH – Thyroid stimulating hormone

tRNA – Transfer RNA

WGA – Wheat Germ Agglutinin

1. Introduction

In 2003, the Human Genome Project (HGP) was completed after a 13-year study involving the collaboration of over 200 laboratories. The HGP was a collaborative project, which set out to define the entire gene complement of human DNA and to determine the sequences of its 3 billion chemical base pairs. The HGP has provided a wealth of knowledge about the sequences of many individual genes. From the successful mapping of the human genome a new industry was spawned known as genomics. Genomics is the study of gene expression and has provided a blue-print for specific gene products.[1] However, studying of the genome alone has been found to have its limitations as it does not describe dynamic cellular processes and it is unable to describe the many post translation modifications proteins undergo which are critical to both their function and activity. The field of genomics is based upon a tight correlation existing between the level of mRNA expressed within a cell and the amount of active protein present.[2-4] However, this has been found to be inaccurate, a study by Anderson and Seilhamer provided evidence that there is no such direct relationship between levels of mRNA and protein expressed.[3] From this conclusion, a new avenue was then explored as the role of proteins within the cellular environment became increasingly important.

Proteomics is the study of the full protein complement of a cell i.e. the proteome of a cell. The main aim of proteomics is to profile the entire protein complement from a cell including the many post-translational modifications, which may occur. However, proteomics is not without its own limitations.[5] Reproducibility is the biggest disadvantage of proteomics with results showing a wide disparity in the number of proteins identified in two identical studies.[6,7] This is because proteomics is much more diverse than genomics due to the proteome being varied from cell to cell and whilst genomics can be performed on a large scale due to the ability to replicate nucleic acids by the polymerase chain reaction, there is no such equivalent in the field of proteomics.

Using proteomics with genomics comparatively has enabled the discovery of many therapeutic targets. Based upon the need for complementary studies of both the genome and proteome the central dogma of molecular biology is believed to be as shown in figure 1.1:

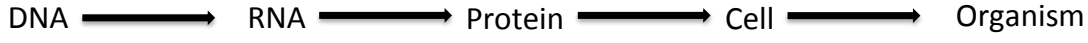

Figure 1.1 Central dogma of molecular biology

However, the creation of a cell requires two other key components in the form of lipids and carbohydrates, which play key roles as signal inducing molecules and as structural components. The central dogma of molecular biology should then be extended as follows in figure 1.2:

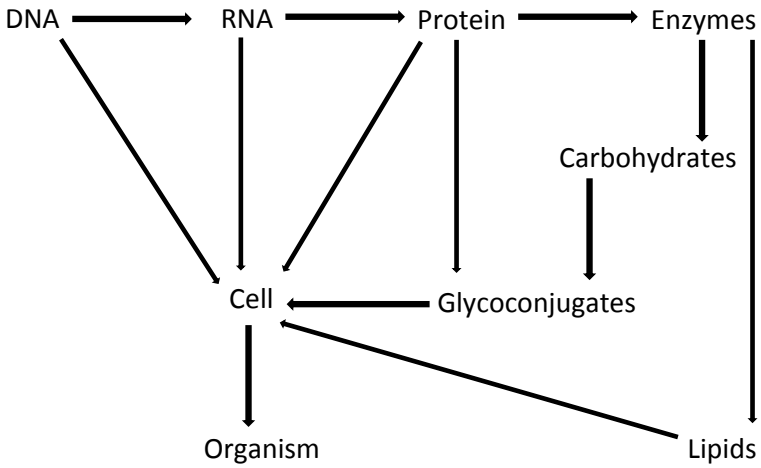

Figure 1.2 Central dogma of molecular biology extended

Carbohydrates are the third largest class of biopolymer, the least understood and the most complex. Glycomics (otherwise known as glycobiology) is the study of the structure, biosynthesis and biology of saccharides, which are widely distributed in nature.[8] The complexity of carbohydrates originates from the variety of saccharides and the 32 types of sugar linkages found in oligosaccharides.[9] Oligosaccharides and polysaccharides are also known as glycans. Glycans are found to be attached to many cell surfaces and extracellular proteins and lipids.[10] The strategic arrangement of these glycans throughout cells highlight the critical roles carbohydrates play in cell-to-cell communication, recognition and transduction events.[11] Glycobiology had been labeled the *Cinderella of Biology* i.e. an area that remains highly complex and requires a tremendous amount of work but remains in the shadow of its *ugly sisters* genomics and proteomics. However, as it has become abundantly clear the functions of cells and organisms remain unexplained when only investigating proteins and nucleic acids alone, therefore, a multidisciplinary approach inclusive of glycobiology is required.

As the field of nucleic acids has garnered a vast amount of interest, the research documented within this thesis focuses only in the areas of proteomics, glycomics and the interactions between both these classes of biopolymer. Therefore, an understanding of the basic concepts of both protein and carbohydrate chemistry is required.

1.1 Proteins

Proteins are complex organic macromolecules, which exhibit an array of unique functions, which are essential to moderate cellular function. They are essential to many processes such as the storage and transportation of particles ranging from macromolecules to electrons. Present in hair, tendons, bones and the filamentous architecture of cells many proteins are vital structural components. As enzymes they regulate the chemical processes, which provide a continual supply of energy to sustain life and as hormones they transmit information between specific cells and organs.

Studying their structures and interactions within various signalling pathways is critical to further the understanding of disease pathogenesis. Knowledge of such interactions should lead to the elucidation of specific targets for future drug development.

1.1.1 Protein synthesis

Archibald Garrod was the first to propose a direct relationship between DNA and proteins in 1902.[12] Garrod's observations led to the seminal experiments in which the discoveries of protein synthesis were made. Initially many scientists believed that due to the correlation between genes and protein abundance that protein synthesis must occur within the nucleus. This was disproved by Hammerling in 1953 as when studying acetabularia cells with removed nuclei, protein synthesis continued to occur.[13] As no DNA exists outwith the nucleus, scientists remained confused about the missing link between DNA and protein synthesis until pioneering work by Brachet and coworkers who discovered a second type of nucleic acid known as ribonucleic acid (RNA) which was found to act as an intermediary between DNA and protein production.[14]

1.1.1.1 Transcription[15]

Two key processes, transcription and translation, moderate the synthesis of all proteins within a cell. Transcription is the synthesis of ribonucleic acid as directed by deoxyribose nucleic acid (DNA). RNA is a single strand sequence of nucleotide bases and has a very similar structure to that of DNA. The structural differences between RNA and DNA are that DNA has a double helical structure with two complementary strands consisting of a sequence of deoxyribose sugar, a nucleotide base and a phosphate sugar. The integrity of the double helical structure of DNA is maintained due to the formation of hydrogen bonds between complementary base pairs on each strand. RNA consists of a ribose sugar, a nucleotide base and a phosphate group.

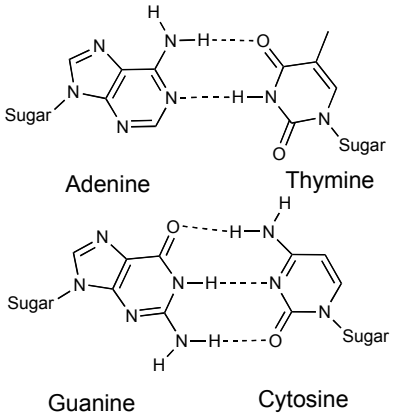

Figure 1.3 Complementary recognition *via* nucleic acids

A key difference between DNA and RNA is the replacement of the base thymine with uracil.

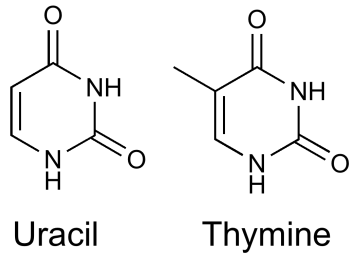

Figure 1.4 Structures of nucleotides Uracil and Thymine

Uracil has the ability to act as both a hydrogen donor and acceptor and as a result, the complementary base pairing rules are relaxed allowing uracil to pair with both adenine and guanine. This is key to protein translation as it allows a wider variety of amino acids to be coded for in the same peptide sequence.

As in DNA synthesis, a DNA strand acts as a template for assembling a sequence of RNA nucleotides. To synthesise a specific amino acid a triplet of nucleotide bases are required to transcribe the information from the gene to the required amino acid. These triplets of nucleotide bases are known as codons. This form of RNA is known as messenger RNA (mRNA) as it carries the genetic information from DNA in the nucleus to the site of protein synthesis at the ribosome of the rough endoplasmic reticulum in the cell cytosol.

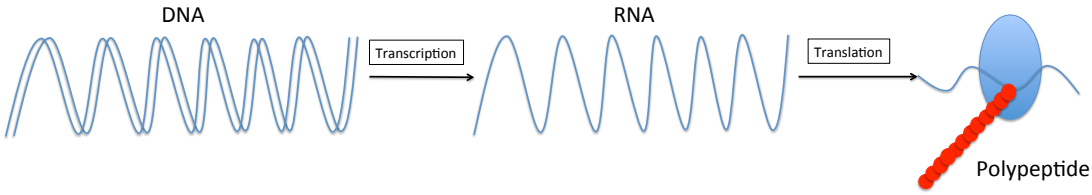

Figure 1.5: Process exhibiting the role of DNA in protein synthesis

1.1.1.2 Translation[15]

Translation is the RNA-directed synthesis of a polypeptide. During protein synthesis, transcription RNA (tRNA) interprets the codons of the mRNA resulting in the correct amino acid being inserted into the polypeptide sequence. tRNA consists of a single strand of RNA and is typically 80 nucleotides in length. The single RNA strand becomes folded back upon itself to form a three dimensional structure which is stabilized by hydrogen bonding between the complementary nucleotide bases within the strand. The resulting 3D structure consists of four based pair regions and three loops. At the 3' end of this structure is an attachment site for an amino acid. The amino acid becomes attached to the molecule of tRNA *via* covalent attachment catalyzed by the enzyme aminoacyl-tRNA synthetase. On one of the tRNA loops, there exists a triplet nucleotide base sequence known as an anticodon. These anticodons are complementary to specific mRNA codons and as mRNA passes across the ribosome tRNA translate each of the codons into a specific amino acid sequence as depicted by figure 1.6.

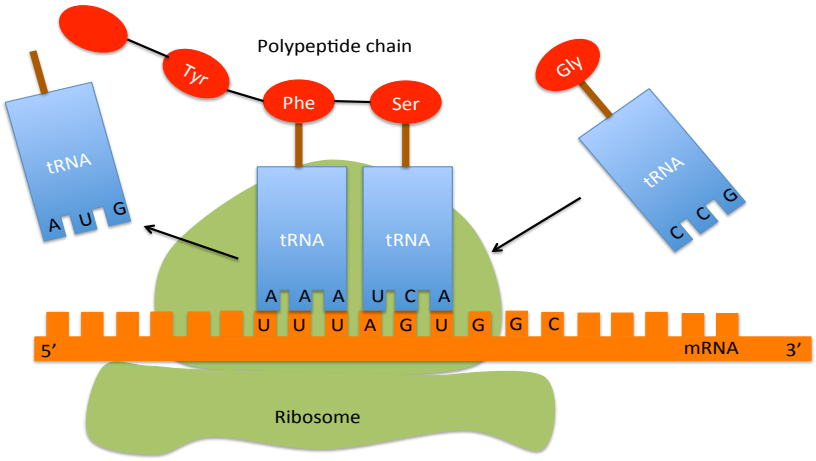

Figure 1.6 Protein translation occurring at a ribosome of the rough endoplasmic reticulum

1.2 Protein structure[15,16]

1.2.1 Primary structure

The primary structure of a macromolecule is defined as a sequence of monomeric units within a chain. For proteins the primary structure is known as a polypeptide chain, which is constructed from a source of 20 fundamental building blocks known as amino acids. The unique sequencing of these amino acids within each unique polypeptide chain creates a great diversity in function of each specific protein.

1.2.1.1 Amino Acids

For all of their diverse biological functions, all proteins stem from a homogeneous class of molecules, the amino acids. Twenty amino acids exist from which each unique polypeptide chain can be formed. Individual proteins differ by the order in which these amino acids are assembled into the polymer chain.

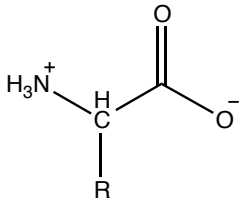

Figure 1.7 General structure of an amino acid

Amino acids are important organic molecules, which consist of a central carbon centre, which is bonded to both a free amino group at one end and a free carboxylic acid at the other. Typically amino acids contain a chiral carbon centre with the exception to this being the achiral amino acid glycine. Amino acids can be classified by their chemical properties depending on the configuration of their side chain group, denoted as R in figure 1.7. These classifications include: hydrophobic, hydrophilic, acidic and basic.

Synthesis of polypeptide chains occurs *via* the formation of peptide bonds between two adjacent amino acids, as shown in figure 1.8. The peptide bond forms as a result of a condensation reaction between the terminal amino group (N-terminus) of one amino acid and the terminal carboxyl group (C- terminus) of another.

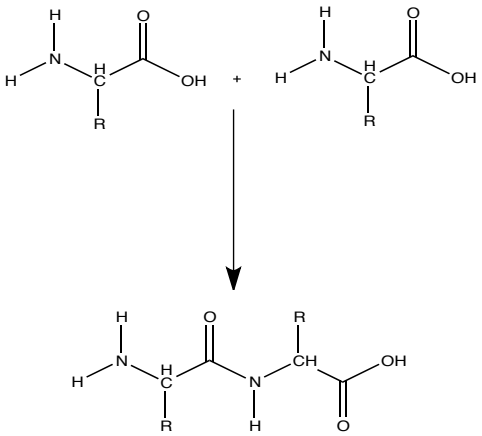

Figure 1.8 Amide bond formation between adjacent amino acids

1.2.2 Secondary Structure

The conformation of the secondary structure of a macromolecule arises from the interactions between sections of the primary structure. These interactions range from ionic interactions, to the formation of salt bridges. However, the primary interaction considered when discussing the secondary structure of a protein is the formation of hydrogen bonds. Within the primary protein structure intramolecular hydrogen bonding occurs between amide and carbonyl groups present in the polypeptide chain. Hydrogen bonds are inherently weak, in comparison to other types of bonding, but when numerous hydrogen bonds are present then secondary structures can form. There are two defined types of secondary protein structure; α-helix and β-pleated sheets. The majority of proteins consist of both types of secondary structure, which become linked to one another *via* loops and turns.

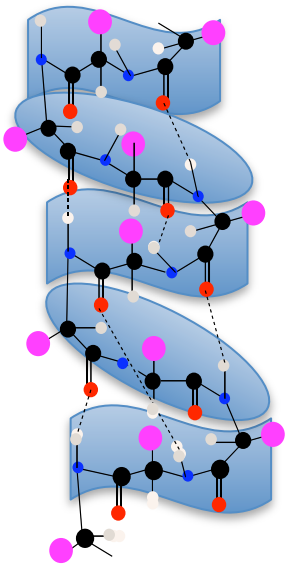

Figure 1.9 Protein secondary structure : α-helix

The most widely recognised polypeptide structures are α-helical structures, as shown in figure 1.9. After every 3.6 residues there is a turn in the α-helix, which is stabilised by the formation of hydrogen bonds between amide groups and carbonyl groups four residues away in the polypeptide backbone. Atoms in the backbone of these structures are able to pack together more closely thus maximising van der Waals interactions.

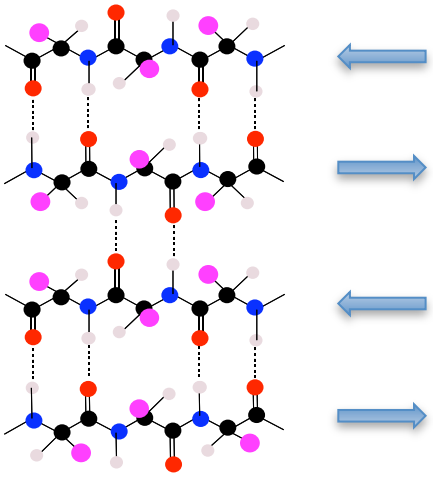

Figure 1.10 Protein Structure: β-pleated sheet

β-pleated sheets are the second most regular form of protein secondary structure. The main structural components of these sheets are known as β-strands. On their own these single strands are not stable as there is no internal bonding occurring between atoms. To overcome this instability these strands are incorporated into β-sheets. In the β-sheet structure hydrogen bonds are formed between peptide groups on adjacent strands. The orientation of these sheets can be either parallel or antiparallel to adjacent strands. Antiparallel sheets are energetically favoured as hydrogen bonds are more regularly formed between adjacent amino and carboxyl groups. Side chains of antiparallel strands face outward which in turn reduces steric hindrance. In areas of steric crowding β-turns occur which are typically attributed to the presence of proline and glycine amino acid residues.

When the hydrogen bonding of a protein becomes disrupted the conformation of the secondary structure of the protein is lost and as a result the protein becomes denatured.

1.2.3 Tertiary Structure

Tertiary protein structure forms due to the folding of protein secondary structure. The main driving force behind the formation of this structure is the aqueous environment of the cell. Hydrophobic pockets form at the centre of the protein due to the clustering of hydrophobic amino acid residues. These pockets become stabilised by weak van der Waals interactions. Other interactions taking place, which play a role in the stabilising of tertiary protein structure, include the formation of hydrogen bonds between polar side groups and the ionic interactions between opposing charged groups. Figure 1.11 depicts a crystallographic image of the lectin concanavalin A (ConA) consisting mainly of β sheet secondary structures linked *via* loops and bends of α helices.

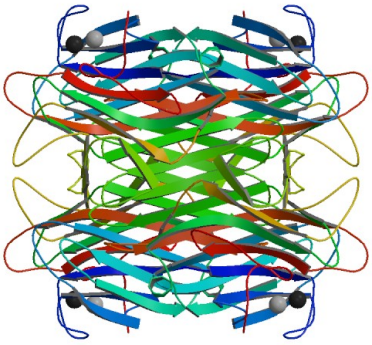

Figure 1.11 Tertiary structure of Concanavalin A (ConA) which contains mainly β-sheet secondary structures. PDB ID: 2CNA.

1.2.4 Quaternary Structure

Quaternary protein structure arises from the association of two or more polypeptide chains, which become aggregated into one macromolecule with multiple subunits. The chains, which become aggregated, may be identical or different and each is known as a subunit. Each subunit becomes folded into an independent globular conformation, which is then able to interact with other subunit monomers. Interactions between subunits stabilise the protein arrangement as indicated in figure 1.12.

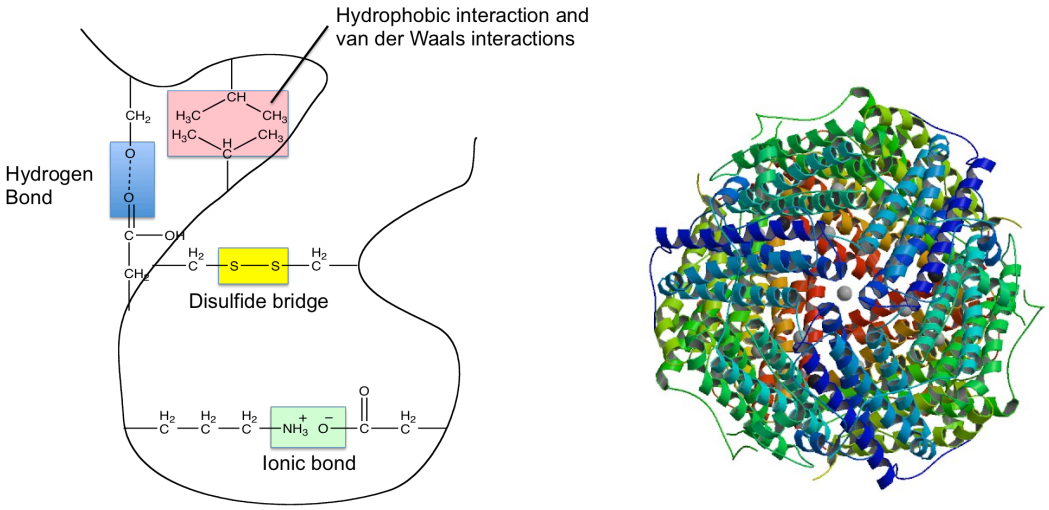

Figure 1.12 Quarternary protein structure and the stabilising interactions which exist between subunits.Quartnary protein structure of Mycobacterium Smegmatis PDB ID:2Z90

Proteins comprised of identical subunits are known as homo-oligomers and those with non-identical subunits are known as hetero-oligomers respectively.

1.2.4.1 Post translational modifications

There are two routes by which the proteome can be diversified, route one occurs during the transcription process and involves the splicing of mRNA whilst route two occurs due to covalent posttranslational modifications (PTMs) of a protein at either a single or multiple positions.[17-19] PTMs can be broadly classified as occurring by two different routes:

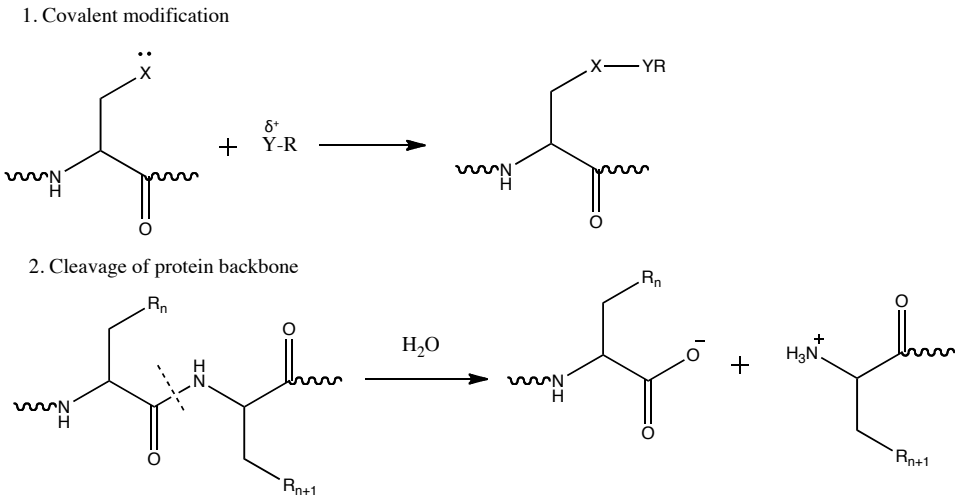

Scheme 1.1 Routes by which PTMs can proceed 1) covalent modification of a nucleophilic amino acid by an electrophilic substrate 2) cleavage of a protein backbone at a specific peptide bond

Covalent modification of the amino acid side chain occurs *via* a catalysed process, which involves the addition of an electrophilic chemical group. Backbone cleavage occurs mainly by proteases.[19] The five most common types of covalent PTMs are phosphorylation, acylation, alkylation, glycosylation and oxidation.[19,20] For each of these modifications there exists a dedicated family of enzymes, which catalyse each reaction. As a result of these PTMs five subsets of the proteome are created and within each new subset there exists further substantial diversity.[19]

1.3 Protein-Protein Interactions (PPIs)

Understanding the interface of protein-protein interactions is essential in deciphering biochemical pathways and understanding disease progression. Some proteins are highly involved with others, whilst others have very few interactions. The dysfunctions of protein interactions are the main cause of many diseases including cancer. When new therapeutic treatments are devised, it is essential to extensively study protein interactions to identify any disruption in disease pathways. Protein-protein interactions can be classified based on their composition, affinity and lifetime. Four main sets of classification exist, (i) homo and hetero-

oligomeric complexes, (ii) non-obligate and obligate complexes, (iii) transient and permanent complexes (iv) domain-domain and domain-peptide complexes.[21-23]

1.3.1 Homo-oligomeric and hetero-oligomeric complexes

When protein interactions occur between identical chains they are said to form a homo-oligomer and the converse when interactions occur between non-identical chains hetero-oligomer complexes are formed. Due to the identical nature of homo-oligomers, they tend to form symmetrical structures, which can be utilised as scaffolds for stable macromolecules.

1.3.2 Obligate and non-obligate protein complexes

Obligate interactions originate from the instability of the constituents of protein complexes when *in vivo*. This compared to the constituents of a protein complex, which is stable *in vivo*, such complexes establish non-obligate interactions, as they are stable independently. An example of an obligate interaction is the role of Ku proteins, which bind to DNA to form obligate homodimers, which are key to DNA repair.[24] Non-obligate interactions include the majority of signaling protein complexes which fulfill their role in propagating a signal before dissociating into stable constituent proteins such as the G-Protein H-Ras.[25]

1.3.3 Transient and permanent complexes

Permanent interactions are defined as those, which are stable through the lifetime of a complex. Transient interactions occur between components, which dissociate and associate temporarily when *in vivo* whereas permanent interactions are stable and irreversible. The majority of non-obligate interactions are predominantly transient whereas obligate interactions tend to be permanent in nature. Examples of transient complexes include G-proteins and membrane bound proteins, which are responsible for the targeting of components in the plasma membrane resulting in a cascade of signaling events.

1.3.4 Domain-domain and domain-peptide complexes

PPIs can be considered by their folding which gives rise to two types of classification known as domain-domain and domain-peptide interactions. Domains are defined as modular domains present in a protein or small peptide motifs, which bind to target proteins. Domain-domain complexes occur in binding events such as that of cytoskeletal proteins that bind to actin *via* modular gelsolin repeat domains. Domain-peptide complexes are typically transient due to their formation occurring *via* the recognition of a globular domain, a short linear motif and the small interface on which the interaction takes place. Src homology

domain is the most abundant in the human proteome and it recognises and binds to proline rich peptides with a core motif.[26]

Although only a brief explanation of each of these interaction classifications has been provided it provides perspective in regards to the multiple considerations, which must be made when analyzing protein-protein interactions.

1.4 Carbohydrates[8,27]

Emil Fischer pioneered the discovery of carbohydrates between 1884 and 1894. Fischer's greatest success is widely regarded to be the synthesis of glucose, mannose and fructose in 1891.[27] The synthesis of these compounds confirmed his previous observations about the relationship, which exists between all three and was key to another of his landmark achievements; the elucidation of the stereochemical configuration of all known sugars and their isomeric forms.[27]

1.4.1 Carbohydrate structure

Carbohydrates are polyhydroxyaldehydes and polyhydroxyketone compounds. They consist of three main structural classes monosaccharides, oligosaccharides and polysaccharides.[28] The definition of a monosaccharide is a carbohydrate, which cannot be hydrolysed to a simpler unit. Monosaccharides are the simplest form of carbohydrates and exist as aldehydes or ketones with two or more hydroxyl groups. Monosaccharides obey the empirical formula $(CH_2O)_n$ where n = 3 to 7. Figure 1.13 shows one of the simplest monosaccharides known as glyceraldehyde (n=3), which consists of two enantiomeric forms, *D*-glyceraldehyde and *L*-glyceraldehyde.

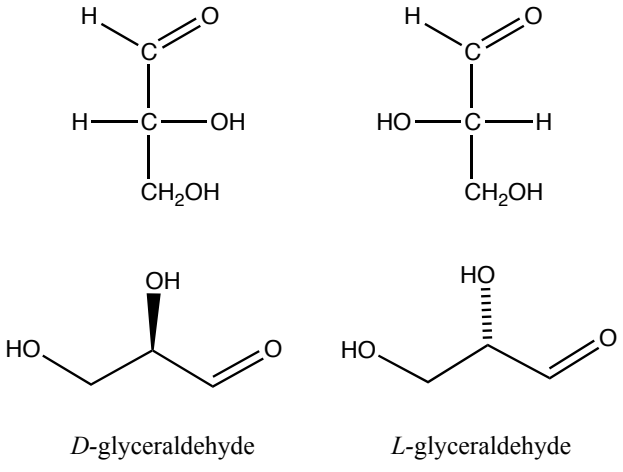

Figure 1.13 Enantiomeric forms of glyceraldehyde

For stability, when in solution the open chain formations of monosaccharides tend to cyclize to the more stable ring form. Upon cyclisation an additional asymmetric center is created giving rise to the formation of two ring structures known as anomers. For example, upon cyclisation, *D*-glucose exists in two anomeric forms as α-*D*-glucose and β-*D*-glucose as shown in figure 1.14. The anomeric notation of these ring structures indicates the equatorial or axial position of the hydroxyl group at the anomeric carbon atom (C-1 for aldo sugars and C-2 for keto sugars). The conversion of one anomer to another is termed mutarotation[29].

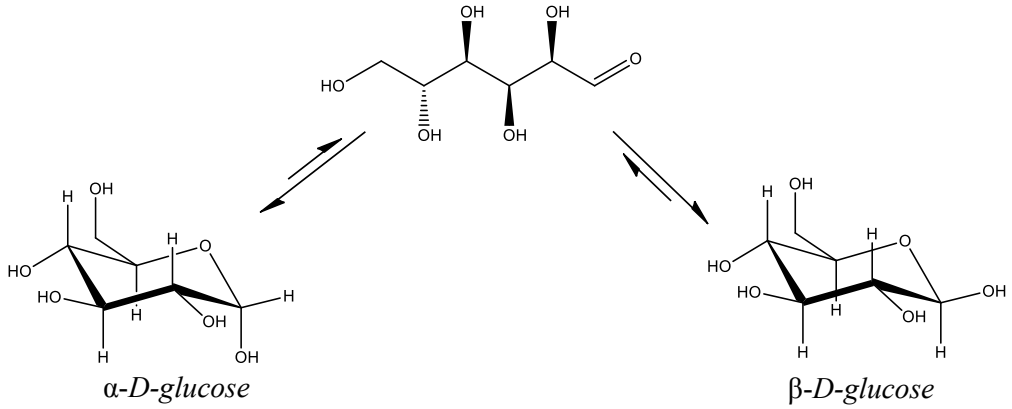

Figure 1.14. Chain and chair equilibria of α- and β- anomers of *D*-glucose

Ring-form monosaccharides can bind other sugar rings, giving rise to disaccharides, which include sucrose (composed of glucose and fructose) and lactose (composed of glucose and galactose).[28]

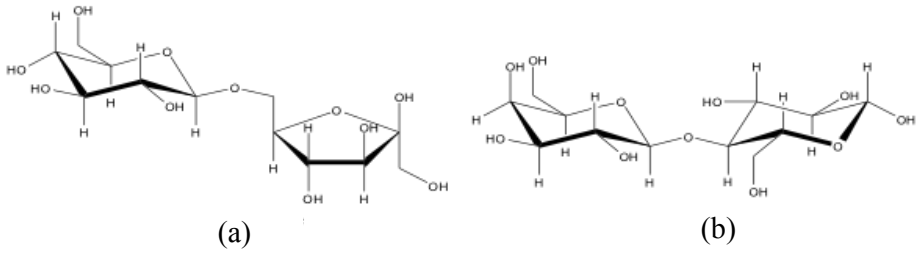

Figure 1.15. Structures of (a) β-*D*-sucrose and (b) β-*D*-lactose

Disaccharides exist from the formation of a covalent linkage from the hydroxyl group on the anomeric carbon of one monosaccharide to any hydroxyl group present on another monosaccharide. This type of covalent bond is termed a glycosidic linkage. Theoretically due to the ability of monosaccharides to generate either an α or β linkage with any of a number of hydroxyl groups present on another monosaccharide the linkage variation can be extremely complex in comparison to the linear linkage of nucleotides and peptides. However,

in reality the combination of monosaccharides occurs in a relatively small number of variations. For example, two glucose saccharides may be linked by a few possible linkages, such as a α(1-4) or a β(1-6) linkage.

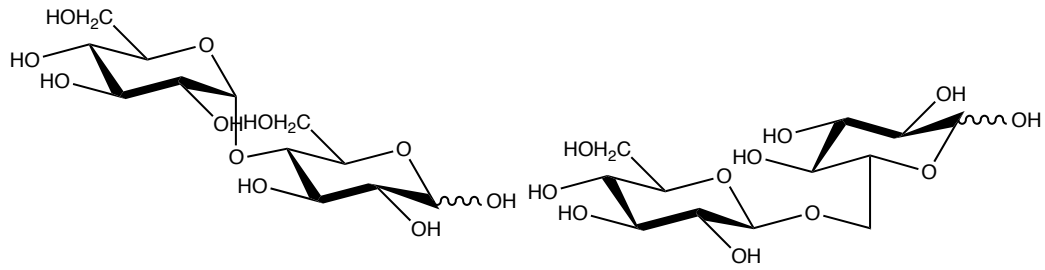

D-glucose-α(1-4)-*D*-glucose
(maltose)

D-glucose-β(1-6)-*D*-glucose
(gentiobiose)

Figure 1.16 The two most common types of glycosidic linkages which exist between monosaccharide units as shown in the examples of disaccharides maltose and gentiobiose

The linkages between C1-4 and C1-6 are two of the most common linkages, although others are possible. By forming glycosidic linkages in a variety of positions, different physical properties are imparted and can result in multiple conformations being adopted in solution. The combination of monosaccharides in this manner results in the formation of oligosaccharides. Combinations of up to 10 monosaccharides are known as oligosaccharides and these include the aforementioned disaccharides, trisaccharides etc. Once 10 monosaccharides have been linked large polymeric sugar structures form known as polysaccharides. Polysaccharides have two distinct classes, homopolysaccharides and heteropolysaccharides.

Glycogen is the most common homopolymer found in animal cells and is essentially a storage form of glucose. As glycogen can be easily metabolized, it is an essential energy store for animals. Glycogen is a large branched polymer consisting of α-1,4-glycosidic bonds with branches being formed by α-1,6- glycosidic bonds after every 10 residues.

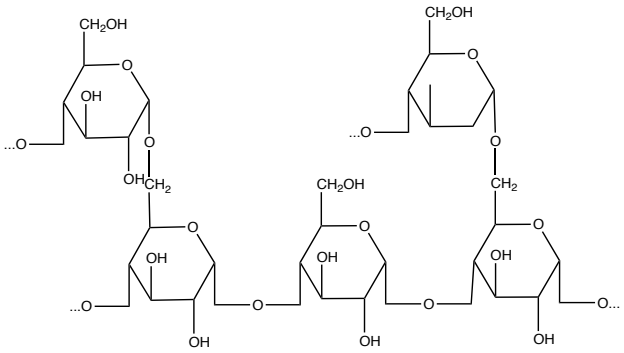

Figure 1.17 1,4 and 1,6 glycosidic branching present in glycogen

Cellulose and starch are the main two homopolymers found in plants. Each is a polysaccharide of glucose, however, they serve different roles. Starch, akin to glycogen, is the main form of energy storage in plants for nutrition. Starch is formed of two subsets of polysaccharide known as amylose and amylopectin. Amylose is unbranched and consists of α 1-4 linkage of glucose units. Amylopectin is the branched form of amylose and has α 1-6 linkages per every thirty α 1-4 linkage. Whilst starch is key to food storage, cellulose is a critical structural component. Heteropolysacchairdes are composed of two or more different monosaccharide units and are closely associated with both lipids and proteins. Due to the complex nature of their structures, detailed structural studies have proved difficult to achieve. Heteropolysaccharides are located in the connective tissues of all animals and as well as being key structural components, they have a variety of functions such as acting as lubricants and shock absorbers. Although less structurally understood in comparison with homopolysaccharides, heteropolysaccharides are essential molecules to human survival.

1.4.2 Carbohydrates at work

At the cell surface, carbohydrates are present in the form of complex carbohydrates. These act as cell recognition molecules and are thought to contribute to crucial cellular processes including cell growth, motility and morphology.[30] The carbohydrates present on mammalian cells are a combination of 9 different monosaccharides as shown in figure 1.18.

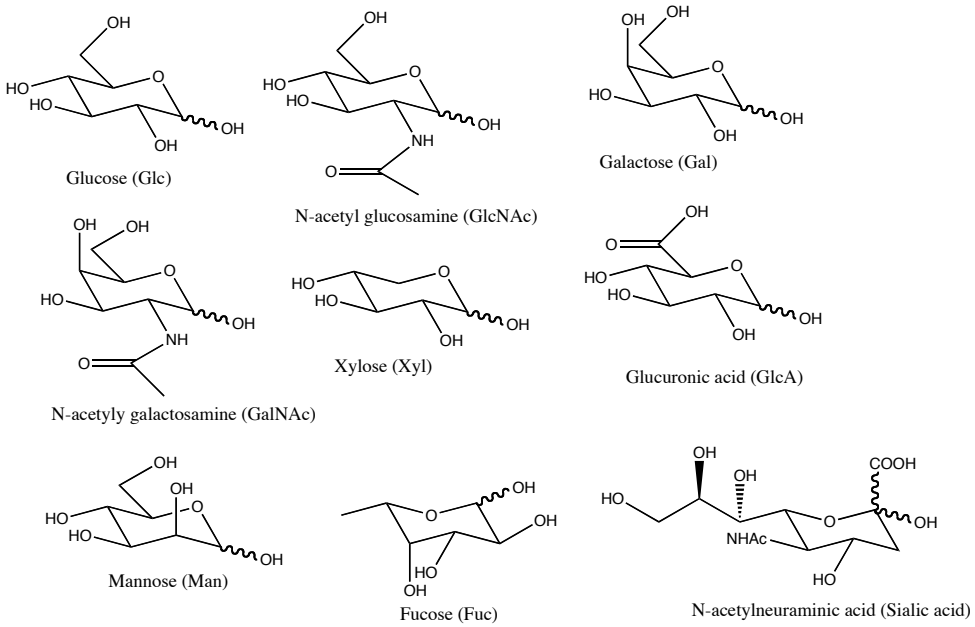

Figure 1.18 Nine common monosaccharides of mammalian cells

A carbohydrate layer exists on the cell surface termed the glycocalyx and is composed of glycoproteins and glycolipids; polysaccharides and smaller sugar chains covalently linked to proteins or lipids respectively.[31] Various combinations of these sugar analogues can be found on a variety of cell types and are responsible for a variety of interactions.[32] Cell trafficking, development of the nervous system and processes key to fertility, for example embryogenesis and spermatogenesis, are all thought to occur as a result of complex carbohydrate interactions[32]. Figure 1.19 highlights the most widely studied types of such interactions.

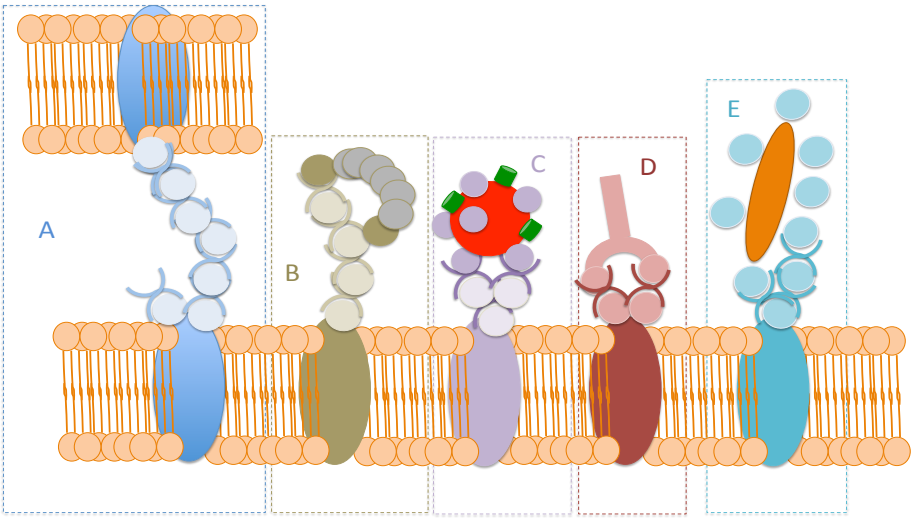

Figure 1.19 Interaction of cell surface carbohydrates in recognition events with (A) another cell (B) toxins (C) viruses (D) antibodies and (E) bacteria

In a similar manner to proteins, carbohydrates can undergo a variety of post-translational modifications. These include glycosylation, phosphorylation, sulfation, methylation, O-acetylation or fatty acetylation. Glycosylations are the key PTM of proteins. Glycosylation is an enzymatic process, which attaches glycans to proteins, lipids or other organic molecules. The majority of proteins that are synthesized in the rough endoplasmic reticulum undergo enzyme directed site-specific glycosylation. Glycosylation also takes place in the cell cytosol and nucleus as an O-GlcNAc modification. There are five distinct classes of glycosylation, which include N, O and C- linked, phospho-serine glycosylation's and glipations.

1.5 Carbohydrate-Protein interactions

The specific biological roles played by glycans are mediated by interactions with glycan-binding proteins (GBPs).[8] Due to the diverse nature of glycans found in a variety of organisms, an array of proteins have evolved which recognise discrete glycans and are able to mediate certain physiological and pathological processes. Thus, the interactions of GBPs and glycans are key components in a myriad of diverse and critical interactions taking place within all organisms. GBPs can be sub classified into glycosaminoglycans (GAGs), proteoglycans or lectins.

1.5.1 GAGS and proteoglycans

GAGs, also known as mucopolysaccharides, are polysaccharide side chains consisting of free complex carbohydrates, which are composed of linear disaccharide repeating units and typically a uronic acid residue of either *D*-glucuronic acid or iduronic acid.[33] Proteoglycans

consist of a central protein, which is covalently attached to either a singular or multiple GAG chains.[8,34] Proteoglycans are synthesised by almost every mammalian cell and are exchanged into the cell surroundings in a number of ways such as; secretion into the extra cellular matrix (ECM), insertion into the cell plasma membrane or storage in secretory granules for future use.[10] Cell surface proteoglycans play key roles in cell adhesion and migration. Due to the unique structural diversity possible, with the numerous GAG chains that can be attached to the core protein in a proteoglycan, proteoglycans and GAGs play key roles in a number of cellular processes. These proteins are critical to the pathophysiology of diseases such as diabetes, metastasis and atherosclerosis.[35] They also play regulatory roles in some tissues by binding transcription factors which regulate protein secretion and gene expression.[36] Additionally, GAGs bind cell growth factors and factors at the cell surface for localization in order to protect their function and to prevent proteolytic denaturing to occur.[33]

1.5.2 Lectins

Lectins are a ubiquitous family of proteins throughout nature and they display a high level of specificity towards certain carbohydrate structures. Lectins are classified into sub groups of lectin families, which are evolutionarily related to each other.

Ricin was the first lectin discovered by Stillmark in 1888 when he found that extracts of ricin from castor bean seeds had an agglutinating effect on red blood cells.[37] Prompted from this discovery, Paul Ehrlich employed ricin and the lectin abrin as model antigens in immunological studies.[38] Using both of these toxic haemagglutinins, Ehrlich was able to prove the fundamental principles of immunology by providing clear evidence of a specific immune response to both of these lectins when they were injected into mice.

The carbohydrate specificity of lectins was first established by Howell *et al.* who demonstrated that the agglutinating activity of the lectin Concanavalin A (ConA) was inhibited in the presence of the complex carbohydrate sucrose. From these findings, Howell and co workers hypothesised that the agglutinating activity of ConA on red blood cells was due to interactions with surface carbohydrates on the cells.[39]

Another landmark application of lectins was their use in blood group typing. In the late 1940s two independent studies published findings of human blood group specificity of lectins.[40] Morgan and Watkins found that the agglutination of both type A and O red blood cells could be inhibited by specific sugar residues which further substantiated the association of the agglutinating activity of lectins to sugars on the cell surface.[41] By 1970, the presence of lectins had been detected in numerous organisms but primarily in plants. This was due to

the difficulties in isolating lectins by conventional techniques at that point in time. The advent of affinity chromatography was a key factor in the dramatic increase in the number of purified lectins being made available. These lectins can be broadly classified as shown in table 1.1.

Current interest in lectins has arisen from their activity as potent allergens and the discovery of their role in establishing disease states. The over consumption of lectins by sensitive individuals has been associated with detrimental physiological effects with cases such as severe intestinal damage, disrupted digestion and growth retardation having been documented.[42] Other consequences of over consumption of lectin are derived from the blocking of glucose and insulin receptors which have been shown to contribute to Celiacs disease.[43,44] Lectins are also known to provoke immune responses including IgG and IgM as well as lymphocyte mitogenisis. [44] The danger of certain lectin types has spawned new avenues of research and in order to fully understand the role these lectins play in the establishment of new disease states it is of importance to understand the fundamentals of carbohydrate and protein chemistry.

Table 1.1 Description of lectin classes and their functions

Lectin Family	Type of saccharide ligand	Subcellular location	Examples of functions
Calnexin	Glc_1Man_9	ER	Protein sorting in the E.R.
M-type lectins	Man_8	ER	ER associated degradation of glycoproteins
L-type Lectins	Various	ER, Golgi	Protein sorting
P-type Lectins	Man 6-phopsphate	Secretory Pathway	Protein sorting, glycoprotein trafficking, enzyme targeting
C-type lectins	Various	Cell membrane extracellular	Cell adhesion, innate immunity
Galectins	β-Galactosides	Cytoplasm, extracellular	Glycan crosslinking in extracellular matrix
I-type lectins	Sialic acid	Cell membrane	Cell adhesion
R-type lectins	Various	Golgi, cell membrane	Enzyme targeting, glycoprotein hormone turnover
F-box lectins	$GlcNAc_2$	Cytoplasm	Degradation of misfolded glycoproteins
Ficolins	GlcNAc, GalNAc	Cell membrane	Innate immunity
Chitinase-like lectins	Chito-oligosaccharides	Extracellular	Collagen Metabolism
F-type lectins	Fucose terminating oligosaccharides	Extracellular	Innate immunity
Intelectins	Gal, pentose, galactofuranose	Extracellular/Cell membrane	Innate immunity, fertilization and embryogenesis

1.6 Monitoring Biological Interactions

For the creation of new therapeutics for disease treatment it is essential to be able to study a variety of biological interactions, which are occurring simultaneously. To study such interactions a vast array of spectroscopic techniques have been implemented which enable the detection of molecular binding events.

1.6.1 Fluorescence spectroscopy

Fluorescence occurs following the absorption of a photon by a molecule that becomes promoted to an electronic excited state from the ground electronic state. This excited state is unstable; as a result, relaxation of the molecules occurs to the lowest excited state. The molecule does not exist in this excited state for long and relaxes to the ground state accompanied with the emission of excess energy as light, known as fluorescence.[45]

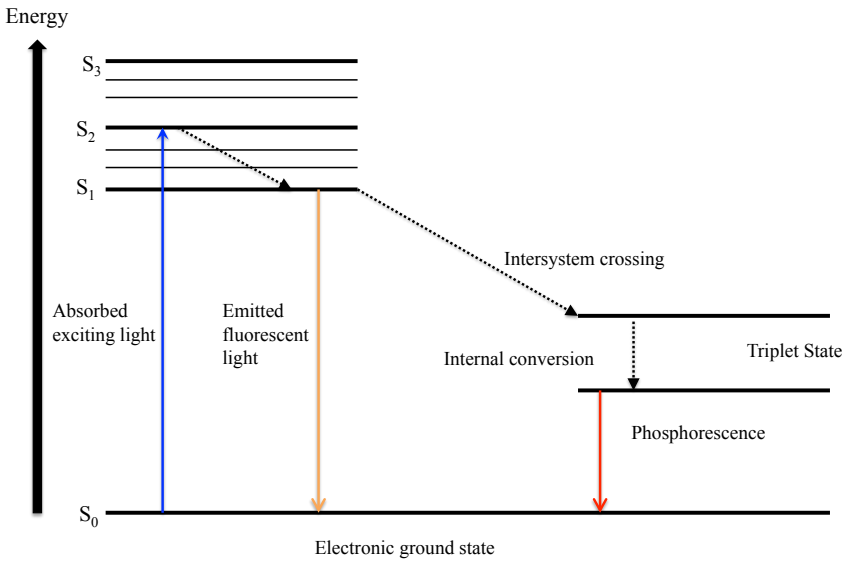

Figure 1.20 Jablonski diagram to illustrate the electronic states of a molecule and the transitions, which occur between them

Fluorescence spectroscopy is a sensitive technique, which is utilised in bioanalysis due to its non-invasive nature and its ability to characterise many biological interactions.[46,47] Fluorescence spectra detail the emission profile of the fluorophores being analysed, the emission profile obtained is independent of the excitation wavelength used. Therefore, it is possible to discriminate between multiple analytes at a variety of excitation wavelengths.[45]

Fluorescence resonance energy transfer (FRET) can provide a wealth of information in relation to various biological studies. FRET occurs when there is a resonance between singlet-singlet electronic transitions of two fluorophores that is generated from the coupling

of the emission transition dipole moment of the donor and the corresponding absorption dipole moment of the acceptor. A transfer of excitation energy between the donor and acceptor occurs which can be observed in a number of ways, such as a reduction in the fluorescent quantum yield of the donor or an increased fluorescent emission of the acceptor.[48,49] FRET has been used in a wide variety of studies such as the elucidation of DNA double helix geometry, the dissection of the folding of RNA and the interactions of protein-DNA complexes such as the unwinding of DNA by helicases.[50-52]

1.6.2 Surface plasmon resonance

Surface plasmon resonance (SPR) is a label free detection technique, which has been used to monitor biomolecular interactions.[53] SPR instruments typically measure the interactions of an immobilised ligand and free analyte at the surface of a metal layer *via* changes in the resonance angle of light due to an increase in the concentration of analyte in the surface vicinity. Measurements based upon the change in resonance angle correspond to the coupling of incoming light with the surface plasmon of the metal particles and are dependent on the refractive index of the metal surface layer. At a particular angle of incidence the irradiating photons of light become in resonance with the surface plasmon electrons of the metal layer resulting in a collective resonate oscillation of the surface plasmon. Detection is also possible using other properties such as wavelength, intensity or phase sensors.[54]

SPR has been widely used for the monitoring of biological interactions in areas such as carbohydrate-lectin interactions, protein-protein interactions and protein-DNA interactions.[55-57] However, there are significant disadvantages of SPR such as low sensitivity, reproducibility, multiplexing and most importantly non-specific binding. To overcome these drawbacks further enhancement was gained in these systems *via* the introduction of nanoparticles. Colloidal metal nanoparticles exhibit localized surface plasmon resonances (LSPR) in the visible region. Upon aggregation of these nanoparticles, their absorbance band undergoes a red shift upon the coupling of the LSPRs of neighbouring particles. Induced aggregation of metal particles due to a biomolecular interaction has been utilised to increase the sensitivity of SPR measurements. This approach has been applied successfully for a variety of DNA interaction studies which have induced the aggregation of gold nanoparticles upon the hybridization of complementary DNA sequences.[58,59] Control of this aggregation process has been shown *via* the increase or reduction in length of the inter-nanoparticle junction by variation of the complementary DNA sequences chosen.[60] Research using this approach has not been restricted to the area of DNA studies, research has been published in

the area of proteins for streptavidin and anti-protein A and in the area of carbohydrate lectin interactions.

1.6.2.1 Nanoparticles

Nanoparticles, and in particular noble metal nanoparticles, are of great interest due to their unique physical properties. The light scattering qualities of nanoparticles has enabled them to be implemented as tracer labels in a wide range of clinical and biological applications.

A nanoparticle can defined as 'clusters of atoms in the size range of 1 – 100 nm'.[61] Along with their small size, nanoparticles are appealing biological labels due to their greater surface area to volume ratio, easily tailored physical and chemical properties and as they are thought to be structurally robust materials.[62] The unique physical and chemical properties displayed by nanomaterials differ from those properties of the bulk material. Typically nanoparticles are synthesised *via* the reduction of a metal salt in the presence of surface capping ligands, which prevent aggregation occurring by physical or electrostatic repulsion.

Nanomaterials have been used in bioanalysis for many years; however, the development of new synthesis and fabrication techniques has provided the opportunity for a greater level of control of the properties of these structures. Specifically from a labelling perspective the ability to tailor the physical properties of these materials has enabled the manipulation of the light scattering properties of nanomaterials.

The phenomenon of surface plasmon resonance arises from the collective oscillation of the free conductive electrons on the surface of a metal due to irradiation by an electromagnetic field. The electron cloud becomes displaced relative to the nuclei and a restoring force arises due to coulombic attraction between electrons and nuclei that results in the oscillation of the electron cloud relative to the nuclei of the particle.[63] This collective oscillation is known as localized surface plasmon resonance (LSPR).[64]

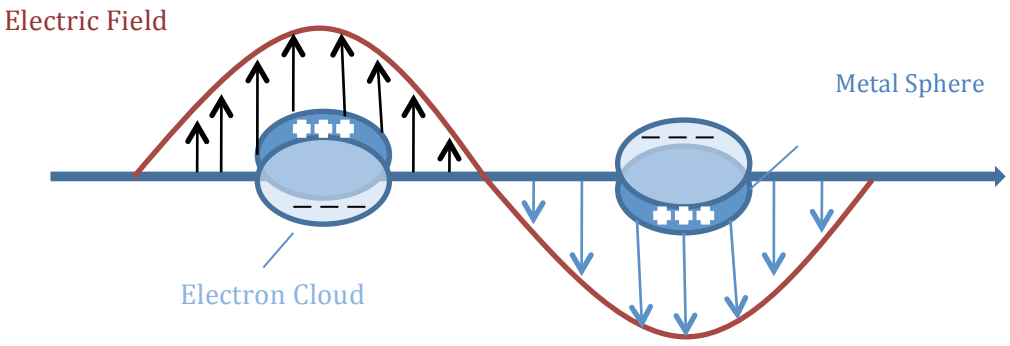

Figure 1.21 Illustration of a localized surface plasmon of a metal sphere.

According to electromagnetic theory, an oscillating electron radiates electromagnetic radiation of the same frequency as the oscillating electron. This type of secondary radiation is what is known as scattered light.[65] The light scattering properties of nanoparticles depend not only on their size and shape but their homogeneity and the refractive index of the medium in which they are present.

Mie proposed a widely accepted theory in 1908 to explain the scattering of light from particles.[66] Mie attributes the plasmon band of spherical particles to dipole oscillations of the free electrons in the conduction band occupying energy states immediately above the Fermi energy level. Independent experimental analyses have found particles which are of the appropriate size range (5-100 nm) and which are spherical in shape to be in agreement with Mie's solutions; as the size of particles increase there is a shifting of the absorption and scattering profiles to longer wavelengths.[67-69]

In recent years, the use of metallic nanoparticles and their unique optical properties has underpinned the techniques most traditionally used to observe biological interactions such as fluorescence spectroscopy and SPR. Fluorescence spectroscopy has actively been used in the field of bioanalysis for DNA detection and the detection of protein-protein interactions however; fluorescence spectroscopy suffers from broad, overlapping spectra from molecular fluorophores as well as photobleaching and the requirement for multiple excitation sources. Additionally when interrogating biological samples the autofluoresence from background components can make it difficult to achieve an accurate analysis. Significant advances have been made in this area to circumvent these issues *via* the development of quantum dots which are specifically designed nanocrystals which produce a narrow fluorescence emission profile with a broad excitation profile. Another commonly used technique is extinction spectroscopy, which plays a key role in defining any changes in localised surface plasmon resonance of the nanoparticles. However, low sensitivity in comparison to other techniques and the inability to analyse more than one component within a sample simultaneously limit the use of this technique for the detection of biological interactions.

1.6.3 Raman Scattering

Raman spectroscopy can be used as an alternative to the optical spectroscopies already discussed. The advantages of using a Raman based technique are that both electronic and vibrational information can be obtained for the analyte of interest and analysis can be undertaken in a wide variety of solvents including water.

Smekal first proposed the theory of Raman scattering in 1923.[70] However, it took until 1928 before Raman and Krishnan first observed this phenomenon experimentally.[71]

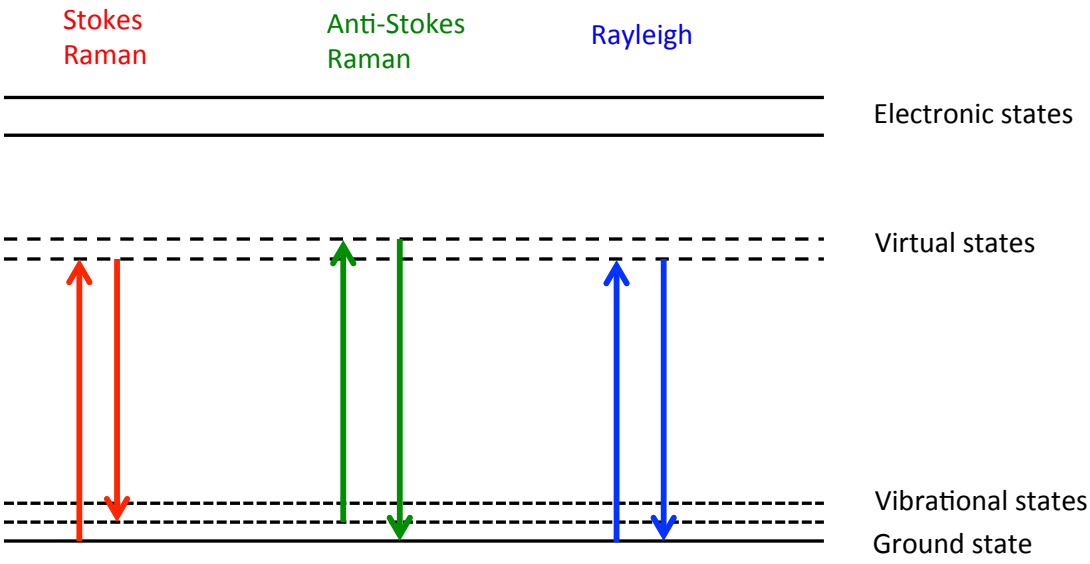

Figure 1.22 Jablonski diagram illustrating the transition between energy levels involved in the scattering of light

When an analyte of interest is interrogated by a light source such as a laser, the photons interact with the electrons of the analyte and can either be absorbed, scattered or there may be no interaction at all. If the energy of the incident photon matches the energy of the gap between the ground state of the molecule and an excited state then absorption of the incident photon results in the molecule being promoted to an excited state. During the scattering process the electron clouds of the analyte become distorted upon interaction with the photons of laser light. This causes a polarisation of the electron cloud and causes a photon to be scattered.[72,73] If the wavelength of scattered light is equal to the wavelength of the incident light then the scattering is termed as elastic scattering and is known as Rayleigh scattering. However, if energy is transferred to or from the nuclei, the scattering is shifted in energy by one vibrational unit. This type of scattering is known as Raman scattering. During Raman scattering the polarisation of the electron cloud results in the formation of a short-lived state known as virtual states. The Raman spectrum is constructed from the transitions between the vibrational states and the short-lived virtual states. There are two types of Raman Scattering, Stokes and anti- Stokes scattering.[74] Stokes scattering is the strongest form of Raman scattering. It occurs when energy is transferred from the incident photon to the molecule. Anti-stokes is a weak form of Raman scattering. It occurs when, due to thermal energy, some

molecules already exist in an excited state. Therefore, it becomes possible for the energy of the excited state to transfer to the scattered photon.

In comparison to Rayleigh scattering, Raman scattering is a weak process as only one of 10^6-10^8 scattered photons are Raman scattered.[72-74] This is the main disadvantage of the Raman scattering technique and the reason why it remained in the background as an analytical technique. However, due to significant advances in instrumentation the inefficiencies of this technique have been overcome.

1.6.4 Resonance Raman scattering

When Raman scattering was in its infancy the analysis of coloured analytes was avoided. This was due to the intense fluorescence signals produced due to the re-absorption of the scattered light by the molecule.

It has been shown that when a wavelength of light is chosen which coincides with an electronic transition of a chromophore contained within the analyte of interest that enhancements of Raman scattering to the order of 10^3 to 10^4 and even 10^6 have been observed.[73] During this process electrons are promoted to an excited electronic state, however, the time the electrons exist in this excited state is significantly shorter for resonant scattering in comparison to the absorption process. This is due to the scattering process preventing the nuclei from reaching equilibrium positions in the excited state whereas during the absorption process equilibrium is reached. This is known as resonance Raman scattering.[73,74]

Due to the enhancement obtained in resonance Raman scattering sensitivity is increased when compared to Raman scattering and certain bands in the Raman spectra can be selectively enhanced.[73] The main disadvantage of this technique is that fluorescence remains a significant problem.

1.6.5 Surface Enhanced Raman Scattering (SERS)

One of the main limitations of Raman and resonance Raman spectroscopy are that they are relatively insensitive techniques in comparison to other commonly used analytical techniques. A marked enhancement of the Raman signal occurs when the analyte has been adsorbed onto a roughened metal surface. This effect is known as SERS.

Fleischman *et al*. unknowingly discovered SERS in 1974 when they reported increased Raman scattering from pyridine molecules that were absorbed onto a roughened silver

electrode.[75] During this study, the effect was attributed to an increased number of pyridine molecules being present on the roughened electrode surface. In 1977, subsequent publications by Jeanmaire and Van Duyne and Creighton and Albrecht furthered our understanding of this effect with the discovery that an intrinsic surface enhancement was in fact the key to the phenomena observed.[76,77]

On a smooth metal surface, there exist free conductive electrons known as the local surface plasmon. These plasmons oscillate in a parallel motion with respect to the smooth surface. Upon roughening, these plasmons are able to further oscillate in a perpendicular direction to the roughened surface resulting in an increased scattering efficiency.[78] Publications by both Van Duyne and Otto proposed two mechanisms by which, this enhancement was occurring with electromagnetic and chemical enhancement effects being proposed respectively.[79]

1.6.5.1 Chemical Enhancement

Chemical enhancement (or charge transfer) involves the formation of a bond between the analyte and the metal surface.[80] The bonding of the analyte species to the surface results in an increase in the polarisability of the analyte due to interactions with the surface plasmons of the metal. In principle, it is believed that enhancement occurs due to the generation of new electronic states formed from the bonding of the analyte to the surface. During the Raman process instead of the radiation, being absorbed or scattered by the metal surface the analyte absorbs it. After the Raman process occurs this photon becomes re-radiated.

1.6.5.2 Electromagnetic Enhancement

The electromagnetic enhancement is widely accepted as being the dominant contribution to SERS signal enhancement. The collective oscillation of the surface plasmon results in an increased local electric field being experienced by the molecule absorbed onto the metal surface.[81] As a result, due to the increase in this local electric field, the polarizations of the surface electrons become intensified. When the electrons of the absorbed molecule interact with the intensified cloud of surface electrons a greater polarization of the electrons around the absorbed molecule occurs. This results in a significant enhancement of the Raman scattered field.

As discussed previously, significant enhancements are gained in surface enhanced spectroscopies when aggregated nanoparticles are used as a surface platform. The increased enhancement in these instances arises from an increase in the localization of the electromagnetic field at the inter-particle junction. This field exceeds that experienced by an

isolated nanoparticle by orders of magnitude between 10^3 – 10^4 and provides sufficient enhancement for single molecule SERS detection.[82]

1.6.6 Surface Enhanced Resonance Raman Scattering (SERRS)

SERRS combines the surface enhancement of SERS with an analyte containing a resonant chromophore so that molecular resonanct enhancement as well as surface enhancement is obtained, this allows for greater sensitivity to be achieved.[83]

SERRS was first reported in 1983 by Stacey and Van Duyne.[84] Often the analyte in these experiments is a dye molecule containing a resonance chromophore. For the enhancement to occur the wavelength of light chosen must coincide with the absorption maxima of the resonant chromophore. As well as being far more sensitive than Raman or resonance Raman the main disadvantage of those techniques, fluorescence is overcome due to the presence of the metal surface. Quenching of fluorescence is due to columbic binding of the fluorophores to the roughened surface. Thus, promoting the quenching mechanisms of electron and energy transfer processes from the fluorescent analyte to the surface.[85]

1.7 SERS for biosensing

The reputation of SERS as a key analytical detection method has exponentially grown over the last few decades due to the many advantages it affords over other commonly used techniques.[86] The SERS spectra obtained can be considered as the fingerprint spectra of the analyte irradiated by the laser light. Sharp narrow bandwidths are key to SERS as this prevents the spectral overlap of key bands and as a result, the simultaneous detection of more than one analyte becomes achievable. Common fluorophores exhibit photobleaching and the majority are either toxic or phototoxic. SERS active labels do not undergo photobleaching and fluorescence is quenched when they are held in close proximity to the SERS active surface. Analysis in media such as water is possible as water has a small Raman scattering cross section.

Perhaps the most significant limitation of SERS is that common SERS substrates do not have reproducible enhancement factors. In addition to this, when using metallic materials for the analysis of biological molecules it is possible for high levels of non-specific binding of biological materials to occur, although there are methods by which this issue can be circumvented.

1.7.1 Use of SERS for the monitoring of protein interactions

In contrast to the studies of DNA, there currently exists no technique for the amplification of protein concentrations prior to analysis. Therefore, highly sensitive and discriminatory spectroscopic techniques are desirable when detecting such low concentrations of biological material. As previously discussed, protein interactions are key to understanding the fundamental principles of molecular biology and the existence of sensitive techniques able to detect such interactions are essential to improving our knowledge within this area. Protein detection typically involves the isolation and purification of single proteins, this is due to their presence in such small quantities and subsequently direct protein detection is extremely difficult.

Raman scattering has been used for the elucidation of protein structure previously with the vibrational structure of 20 essential amino acids being elucidated.[87] The progression of these studies allowing SERS to be implemented in direct protein detection has seen the first reports of single molecule detection for both heme and green fluorescent proteins.[88,89] However, typically direct protein detection is severely hampered because of irreversible damage to its native structure as a result of binding the molecule to an enhancing substrate.[90,91] Citrate reduced nanoparticles have been shown to be biocompatible surfaces as enhancing materials in such studies.[92,93] Although, in some cases the high charge density of the citrate surface layer can denature the protein and as a result other surface binding strategies are required.[94] The implementation of these protein-binding strategies has produced two broad classes of protein analysis; immunoassays and enzymatic analysis.

1.7.1.1 Immunoassays

Immunoassays are routinely used in clinical testing and diagnostic treatments for the measurements of proteins. Immunoassays are based on specific recognitions events and tend to fall under three categories, the enzyme-linked immunosorbent assay (ELISA), the fluorescent immunoassay (FIA) and the radioactive immunoassay (RIA).[95-97] A typical sandwich immunoassay involves a monoclonal capture antibody, which is directed towards an antigen, which has been pre-adsorbed onto a biocompatible surface. When the sample containing the target antigen is added to the assay the capture antibody becomes bound to the solid support. A detection antibody in then added which binds to the target antigen *via* a different binding site and the resultant bio-specific recognition can be detected using common spectroscopic techniques. However, common readout methods such as fluorescence spectroscopy have been shown to be time consuming, have relatively low detection limits and exist in environments which do not mirror biological conditions.[98]

Cotton *et al.* reported the first use of SERRS as a readout platform for immunoassay analysis.[99] A resonant dye, *p*-(dimethylamino)azobenzene (DAB), was covalently attached to an antibody directed against human thyroid stimulating hormone (TSH) to be used as the conjugate reporter molecule in a sandwich immunoassay for TSH antigen. An excellent correlation was obtained between the concentration of TSH antigen present and the intensity of the SERS signals observed. As a result, SERS was shown to be a suitable readout platform for immunoassay analysis. A study by Chen *et al.* used a bound enzyme in an immunoassay to reduce silver ions to nanoparticles *via* the production of ascorbic acid. The silver nanoparticles were then used to quantify enzyme activity and approximate antigen concentration was obtained.[100] Although these studies used a straightforward approach with great success, the introduction of SERS active substrates from the outset has been proven to enhance the sensitivity of immunoassay formats. Porter *et al* adopted a different approach by attaching capture antibodies to a gold surface for the capture of free antigen in solution. Indirect Raman detection occurred because of the introduction of gold nanoparticles labelled with detection antibodies and Raman active reporter molecules. A variety of these gold nanoparticle species were introduced containing different active reporter molecules thus enabling the presence of different antigens to be detected due to discrimination of the characteristic vibrational Raman bands of each of the labels. Proof of the success of this approach was shown with two differing analytes detected with limits of detection in the nanomolar region this system.[101] Porter and co workers have since implemented this approach in a number of immunoassay formats for the detection of bacterium, immunoglobin and prostate specific antigen.[102-105] The detection of multiple analyte species has proven the concept of using this type of immunoassay format for multiplexed detection. Using this approach a triplex has been explicitly demonstrated with higher order multiplexing achievable but currently limited by cross-reactivity between antibodies.[106]

1.7.1.2 Enzyme analysis

Enzymatic SERS analysis is based upon the conversion of an inactive precursor to an active product *via* enzymatic action. Ingram *et al* synthesised a number of masked dye species which only produced a SERS active response upon enzymatic cleavage of a masking group allowing the surface attachment moiety to be exposed.[107,108] The success of this approach was extended for multiple masked dye species mixed together with each dye being unmasked by different enzymes.[109] This format allowed for the quantitative detection of alkaline phosphatase and β-galactoside. Moore and co workers have showed further application of these masked dyes in a study using silver nanoparticles to detect the activity of hydrolases at ultra low concentrations. This was facilitated *via* the use of masked enzyme

substrates, which became SERRS active following the turnover of a substrate by the enzyme leading to the release of the SERRS active dye. The correlation between SERRS intensity was proportional to the enzyme activity generated. Using this method the relative activities and enantioselectivities of fourteen different enzymes including lipases, esterases and proteases were detected. This system has the potential of detecting multiple enzyme activities simultaneously at concentrations relative to those found *in vivo*.[110]

Typically, diagnostic studies of biological materials have been performed *in vitro* or on *ex-vivo* tissue samples. Currently there is a move towards the imaging of biological targets *in vivo* and in order for this to progress molecular imaging agents are required which provide discernable SERS signals.

1.7.2 Molecular imaging using SERS active agents

Cells are delicate and complex, which make them ideal structures for interrogation by SERS. Raman spectroscopy has been used previously to monitor small chemical changes within a cell, however, due to the inefficiencies of this technique and high levels of autofluorescence from the cell it is difficult to obtain an unmasked signal. Applying SERS in this manner has led to the shortening of analysis times to a more realistic timescale and has enabled a further understanding of molecular biology and the early diagnosis of a variety of disease states.

Nanoparticles have been extensively used as molecular imaging agents as well as therapeutics and delivery vehicles.[111] The ability to fine-tune both their physical and chemical properties allows them to be engineered for cellular applications. Extensive use of nanomaterials has typically been focused on colloidal nanoparticles such as Au and Ag. Au is an inert metal and as such is deemed a safe material for use in cellular applications.[112,113] However, concerns surrounding the increased use of Ag nanoparticles have gathered in spite of these particles exhibiting novel bactericidal properties.[114] Studies continue with contrasting results in relation to the cytotoxicity of both these types of particle with no consensus having been reached on their use.[114] Parallel studies continue to be performed in an effort to fully understand the effects of nanoparticle size, shape and functionalisation on cell cytotoxicity and damage. As these studies persist, nanoparticles have also continued to show they are valuable constructs for molecular imaging studies.

To understand the complexities of cells nanoparticles have been utilised for a variety of applications from the elucidation of the localization of intracellular components to the targeting of cell organelles. Use of AuNPs in cellular applications has identified specific biomolecule signatures, which are key to obtaining information of the intracellular matrix.

Phenylalanine, an essential amino acid, and adenosine monophosphate have been identified in this manner. Through monitoring the change in intensity of the spectral bands of these cellular components, the chemical composition of the intracellular matrix can be elucidated and the localization of each of these molecules identified throughout the cell *via* the construction of SERS intensity maps.[115]

For the specific targeting of subcellular structures, functionalised nanoparticles have been fabricated, with success being achieved in a number of instances. Kneipp *et al.* used pH sensitive reporter molecules such as mercaptobenzoic acid as intracellular pH probes. The protonated and deprotonated configurations of this molecule elicit different spectral band intensities at 1430 and 1590 cm^{-1} and the ratio of both these peaks intensities can be used to measure cellular pH. Knowledge of cellular pH is essential to discover the mode of cellular uptake, which in turn is essential for the functionalisation of future nanomaterials to appropriately use specific targeting ligands, which can by pass endosome compartments to reach their targets more efficiently.[116,117] A very different approach to identifying cellular pH was taken by Vo-Dinh and colleagues who manufactured SERS active fibre optic nanoprobes. These nanoprobes were used to measure intracellular pH of both epithelial and human prostate cancer cells. The results obtained showed no significant difference in pH existed between both sets of cells. This method of intracellular pH measurement also did not cause cell apoptosis or an aggressive lysosomal response as suffered by other methods of intracellular pH measurement.[118] Specific cellular processes such as cell apoptosis have also been studied successfully. Using a multiplexed approach, silica encapsulated nanomaterials functionalised with specific target antibodies BAX and BAD were used to monitor apoptosis in lung tissue. The SERS results obtained for this study were also corroborated using fluorescence microscopy and flow cytometry due to the use of a fluorophore reporter molecule within these nanoprobes.[119]

Specific biomarkers in relation to various disease states have also been targeted using intracellular nanoprobes. Qian *et al.* constructed gold nanoparticles functionalised with a mixed monolayer of Raman reporter molecules and thiolated polyethylene glycol for the *in vivo* detection of cancerous biomarkers. The thiolated polyethylene glycol molecules terminated in a carboxylic acid, which was exploited for the attachment of single chain variable fragment antibodies to target tumour biomarkers such as epidermal growth factor receptors on human cancer cells.[120]

These studies show the increase in the use of SERS as a detection technique in cellular applications has significantly increased our knowledge of molecular biology and produced new avenues for therapeutic applications using SERS active molecular agents.

The development of functionalised nanomaterials for use in biological applications has been significant for furthering the understanding of bioanalytical chemistry. These materials have been confined mainly to studies of DNA and protein interactions and as such, a significant gap exists to study the area of protein and carbohydrate interactions. This thesis serves to explore these interactions through the creation of novel SERS active functionalised nanomaterials as platforms for biological assays and biological studies in the cellular environment.

2. Aims

This thesis details the preparation and application of biomolecule functionalised nanomaterials for the analysis and detection of biomolecular interactions primarily by surface enhanced Raman scattering (SERS) and by extinction spectroscopy. The aims of this research were to:

- Design and synthesise novel organic linker molecules to improve nanoparticle stability and to facilitate the attachment of biomolecules. Proteins, in the form of antibodies, were employed as the biomolecules of interest to develop immunoassay formats by which the biological activity of these conjugates could be determined. Different assay formats were employed and interactions detected using SERS whilst fluorescence spectroscopy was used to quantify the number of biomolecules attached to each set of nanoparticle conjugates.
- Investigate carbohydrate-protein interactions for the first time using SERS. Carbohydrate linker molecules were devised to establish stable glyconanoparticles. The interaction of these glyconanoparticles with carbohydrate specific proteins known as lectins was initially to be assessed *via* the development of nanoparticle aggregates mediated by these specific biological interactions. These interactions were then to be detected using extinction spectroscopy before using SERS detection to compare the sensitivity achieved.
- Design further carbohydrate linker molecules to produce a series of individual glyconanoparticles. To pair each glyconanoparticle species with a SERS active reporter molecule, which produces a unique signature, which can be, discriminated from a triplex of SERS spectra. Following the development of a unique SERS triplex the interaction of specific carbohydrate and protein interactions was to be induced in the presence of multiple carbohydrate species for detection using SERS.
- Prepare lectin functionalised nanoparticles as cellular imaging agents using SERS detection. The functionalised nanoparticles were to target carbohydrates on the cell surface to achieve a carbohydrate composition profile of the surface of various cell lines. Confocal Raman microscopy was to be utilised for depth profiling of individual cells to determine the localization of the lectin functionalised nanoparticles.

3. Design of novel nanotags for use in the detection of protein-protein interactions by SERS

The identification of biological interactions is typically enabled *via* molecular labeling strategies, which facilitate their detection using spectroscopic studies. The most common labeling methods include the use of molecular fluorophores, however, this type of labeling suffers due to photobleaching and broad emission spectra being obtained which are a distinct disadvantage if multiple analytes are to be analysed simultaneously.[121] The use of quantum dots is an alternative strategy and has garnered great interest in recent times yet their use is not widespread due to cellular toxicity issues.[122] As SERS offers the advantage of simultaneous detection of multiple analytes due to the information rich vibrational spectra obtained and provides sensitivity comparable to that of both quantum dots and molecular fluorophores it has become a leading technique in this area. The specific enhancement of the molecular chromophores of SERS active species in comparison to other materials present within the biological matrix allows for easy identification. This coupled with the ability to tune the wavelength of excitation to be in resonance with the chromophore of the active species allows for the detection of analytes by wavelength selectivity and exploits the resonance enhancement of SERRS.

SERRS labels can be attached to biomolecules *via* three distinct techniques. The direct attachment of a SERS active reporter molecule to the biological molecule of interest followed by addition of colloidal nanoparticles and spectroscopic analysis.[123] The generation of a SERRS active species *via* enzymatic degradation of an inactive substrate followed by colloidal addition and spectroscopic analysis.[124] While the third, and most common approach, is the generation of SERS active nanotags, which are formed *via* the pre-functionalisation of colloidal nanoparticles with a reporter species, which incorporates a reactive group for the subsequent coupling of a biological analyte.

Porter and co-workers first established the nanotags approach *via* the creation of gold nanotags for antibody conjugation. These nanotags consisted of a non-resonant thiolated molecule used for surface complexation and the co-adsorption of antibodies *via* ionic and hydrophobic interactions. Further to this approach, Porter *et al.* have also created gold nanotags modified with a bissuccinimide nitrobenzoic acid derivative for the covalent attachment of antibodies.[103] The nanotags produced by the covalent approach were utilised in a PSA immunoassay format and detection was achieved at femto molar levels. The only inherent disadvantage of these nanotags were that they remained reliant on colloidal stability

which can be influenced due to non-specific surface complexation or change in ionic strength of the colloidal medium causing agglomeration of the particles. To overcome these issues several successful strategies have been employed. Natan and co-workers chose to encapsulate their nanotags in glass, which allowed for their suspension in a broad range of solvents for analysis due to agglomeration being prevented.[125] An alternative strategy employed by Nie and Doering utilised silica encapsulation of their nanotags with enhancement factors reported which indicated the possibility of single nanoparticle detection.[126] Further work by Nie and coworkers circumvented the need for a multiple step functionalisation and encapsulation strategy of the nanotags by functionalising nanoparticles simultaneously with a mixed monolayer containing a reporter molecule and polyethylene glycol (PEG).[120] The PEG molecules stabilized the nanoparticles and prevented aggregation in the presence of high concentrations of electrolytes such as sodium chloride (NaCl) and acids such as hydrochloric acid (HCl). PEG is a block copolymer, which consists of hydrophilic chains, which aid the solubility of any compound to which PEG is tethered. PEG chains, which are adhered to the nanoparticles surface, produce rapid chain motion in an aqueous medium and have a large excluded volume. As a result, steric repulsion is generated, from the loss of conformation entropy of the bound PEG chains, upon neighbouring foreign substances.[127-132]

Here, a more elegant approach is reported for the creation of nanotags, which utilises the strengths of the previous approaches and attempts to reduce the synthesis of these tags to a one step process.

3.1 Design of SERS active nanotags

The idea was conceived to create a ligand that could complex the nanoparticle surface whilst possessing both a SERS active reporter species and a site for the attachment of a biological analyte. As previous research had mainly focused on gold nanotags and their use in biological analysis a different tact was opted for and silver nanoparticles were used. A significant factor in this choice was the increased scattering cross section of silver nanoparticles in comparison to gold. Although believed to be less stable, silver nanoparticles have a molar extinction coefficient, which is ten times greater greater than that of gold nanoparticles of a similar size.

SERS active species need not be fluorophores or dyes but any molecule, which provides a unique SERS signature. Examples of these are the use of haem compounds which give very effective SERS signals as do small molecules such as dinitrobenzene thiol (DNBT) and

mercaptobenzoic acid which cause aggregation of the nanoparticles causing a significant increase in SERS intensity of their molecular signature.[133-135] The main criteria for a SERS active reporter molecule are they can be absorbed to the nanoparticle surface and that they have a molecular chromophore, which has an electronic transition at the extinction frequency of the laser being used. Due to the soft acidic nature of the silver nanoparticle surface, interactions are favourable towards soft base centres such as nitrogen and sulfur.

Benzotriazole has long been used as an anti-tarnishing agent on silver metal due to the formation of a polymeric surface species by complexing more than one surface silver ion.[136-138] Binding occurs covalently at the triazole moiety *via* the formation of covalent dative bonds with the silver ions. Graham *et al.* developed a series of benzotriazole dyes for spectroscopic analysis as the covalent bonding of these species resulted in binding occurring in a fixed orientation, thus, reproducible analysis was possible due to the lack of any significant shifting of the spectral bands.[139] The unmodified silver nanoparticles are stable due to a high negative surface charge, which is derived from the complexing citrate ions on the metal surface. When benzotriazole is added the surface bound citrate species are displaced and irreversible covalent bonding occurs. Once attached the benzotriazole dyes have been shown to remain bound over a variety of experimental conditions and reproducible analysis is continuously obtained.

The benzotriazole molecule opted for use in these studies was 4-(5'-azobenzotriazolyl)naphthalen-1-ylamine which had been synthesised in house previously and been denoted as GM19. This amino derivatised aromatic was chosen as the amine group provides a point of functionalisation to occur post dye synthesis which was critical for the coupling of a PEG spacer unit.

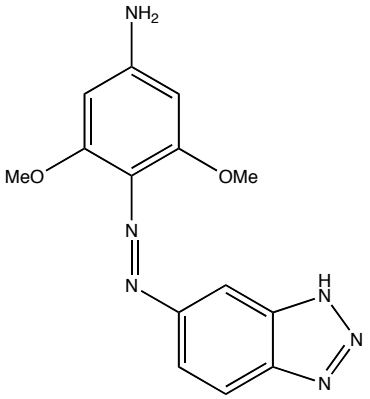

GM19

Figure 23.1 Benzotriazole dye which has been synthesised in house previously and is denoted as GM19

Due to the commercial availability of PEG and its relatively low cost, it was decided that two molecules of differing lengths of PEG chain were to be synthesised. Jeffamine ED-2001, P41, contains 41 repeating units of polyethylene glycol whilst Jeffamine ED-2003, P8, contains 8 repeating units of polyethylene glycol. To test the dependence of nanoparticle stability based upon the length of PEG molecule used each of these molecules were coupled to GM19 to form two linker molecules, denoted as the P41 and P8 linkers respectively. The following synthetic protocol was carried out successfully for the production of both PEG linker molecules and the reaction yields have been denoted for each. The compound notation used in each step correlates to that found in the experimental section chapter **9**.

3.1.1 Synthesis of PEG_{41} and PEG_8 linker

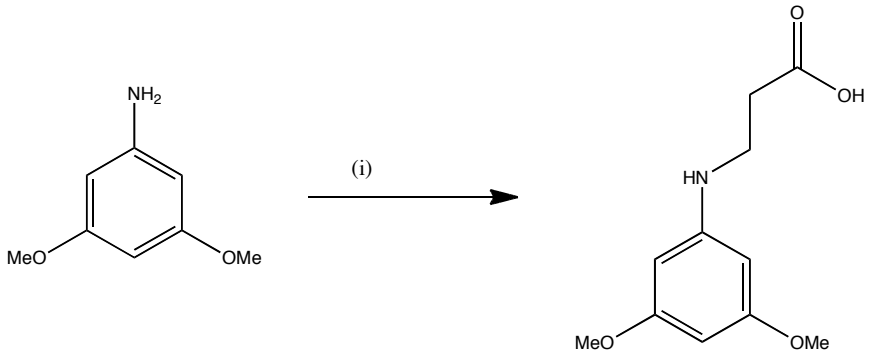

Scheme 1.2 Synthesis of D1 using the following conditions (i) Acrylic Acid, Toluene, 110°C 48 hours. Yield 45%.

The benzotriazole dye precursor compound **D1** was formed by the Michael addition of 3,5-dimethoxyanaline to the α, β unsaturated compound acrylic acid. After purification by flash chromatography a white compound was afforded in a 45 % yield.

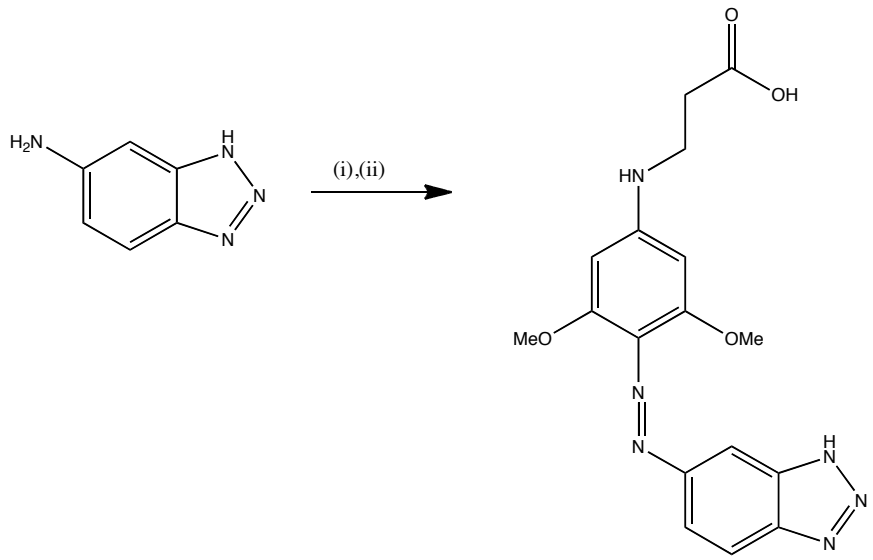

Scheme 1.3 Synthesis of D2 using the following conditions (i) $NaNO_2$, HCl, 0°C, 30 mins (ii) D1, NaOAc (pH 6), r.t., 14 hours. Yield 68%.

The benzotriazole dye **D2** was formed in two synthetic steps. First, the diazotization of 5-aminobenzotriazole was completed and this resulted in the production of a highly reactive diazonium salt which in the second step of the reaction was coupled to **D1** *via* an electrophilic aromatic substitution to form the title compound, as a dark red solid in a 68% yield.

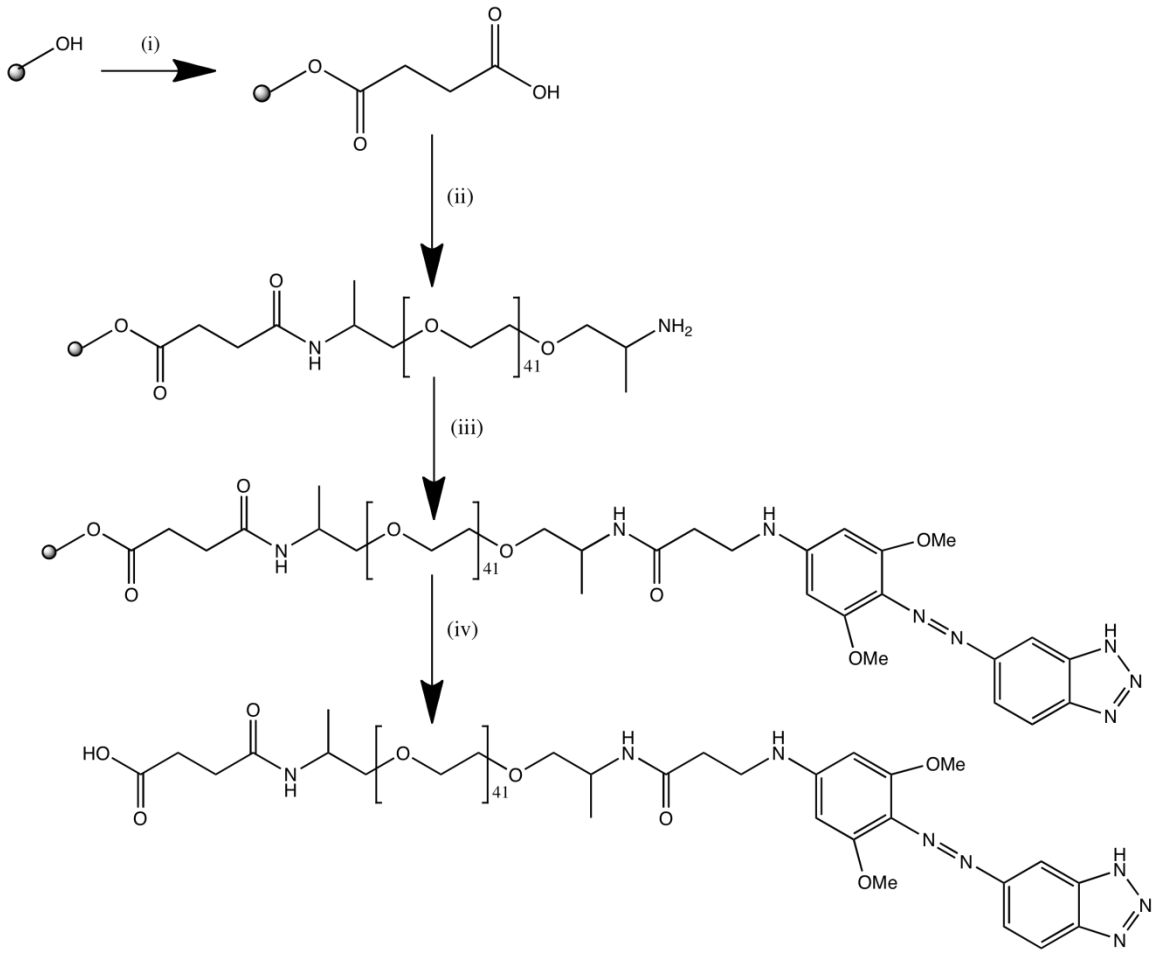

Scheme 1.4 Synthesis of linker D3 using the following conditions (i) Succinic Anhydride, DMAP, DCM, 90°C, 6 hours; (ii) PEG-41, DIC, DCM, r.t., 14 hours; (iii) D2, CDI, DCM, r.t., 14hours; (iv) 10% TFA in DCM, r.t., 3 hours. Yield 42%.

To produce the final linker compound synthesis was performed upon a Wang resin solid support for ease of product recovery and to maximise yield. Succinic anhydride was coupled to the resin *via* surface bound hydroxyl groups using the nucleophillic catalyst DMAP. The resulting resin was therefore, carboxylic acid functionalised. This resin surface was then activated towards amide bond formation *via* the formation of a carboxylic acid ester using *N*'*N*'-diisopropylcarbodimide (DIC). DIC was chosen due to ease of removal of the urea by product from the reaction. Once activated Jeffamine ED-2001 (PEG_{41}) was added and the coupling reaction occurred. After the coupling reaction was complete a small sample of the resin was retrieved and mixed with a few drops of ninhydrin which is a useful colorimetric testing agent for the presence of free amine groups. The resulting colour change from white to blue/purple indicated a positive result. The resin was then dissolved in DMF and D**2** was added alongside the carbodiimide coupling agent 1,1'-carbonyldiimidazole (CDI). The final

product was then cleaved from the resin using a 10% trifluoroacetic acid (TFA) in dichloromethane (DCM) solution, it was elucidated by MALDI-MS and ^{1}H-NMR analysis that the correct final product had been obtained as an orange oil in a yield of 42%.

Therefore, novel linkers were produced with an intrinsic benzotriazole dye for SERS detection and a long polyethylene glycol spacer, which imparts solubility and stability by ensuring the nanoparticles formed are monodisperse, and singly formed. Each linker also contained a terminal carboxylic acid moiety, which permits the conjugation of a variety of biomolecules including DNA and proteins.

The stability of these linkers was compared with other commonly available ligands used for nanoparticle functionalisation including cysteamine and 3-mercaptopropionic acid (3-MPA). Both thiol-containing ligands have the ability to complex the nanoparticle surface by displacement of the citrate capping ligands.

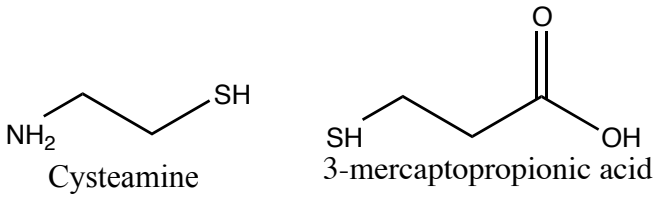

Figure 3.2 Structures of the thiol containing ligands cysteamine and 3-mercaptopropionic acid

3.2 Linker optimisation studies

Following the successful synthesis of each linker species studies were performed to ascertain the optimum linker concentration to be used to complex the silver nanoparticles being used in this study. First, silver nanoparticles were prepared using a modified version of the Lee and Meisel method.[140] Analyses by extinction spectroscopy showed that stable, monodispere nanoparticles had been obtained with a λ_{max} of 408 nm and with no apparent signs of aggregation as shown in figure 3.3.

The protocol for attachment of these ligands to the nanoparticle surface can be found in experimental section 9.9. To test the stability of these nanoparticles when functionalised with the chosen ligands the concentration of each ligand was varied and analyses were performed using extinction spectroscopy and dynamic light scattering (DLS). The data obtained for the extinction spectroscopy measurements is shown in table 3.1 and in figures 3.4-3.7 respectively.

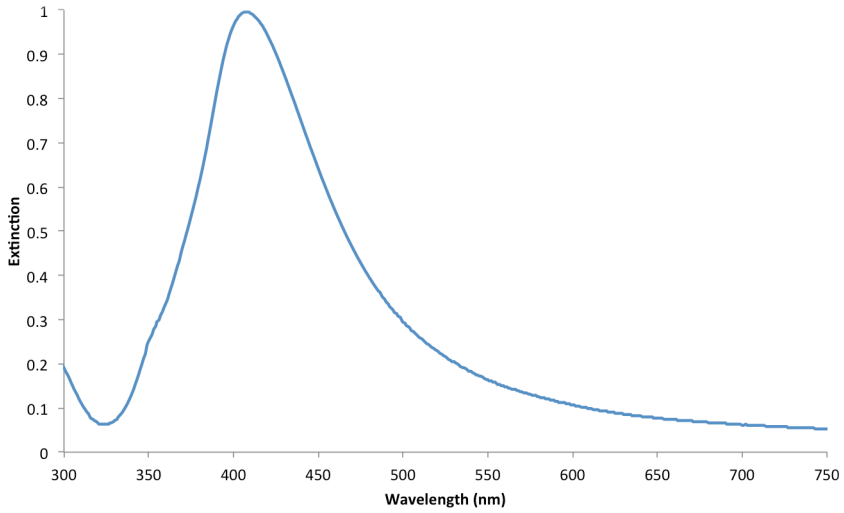

Figure 3.3 Extinction spectra of silver citrate nanoparticles produced by a modified Lee and Meisel method.

Table 3.1 Extinction spectroscopy measurements for the varied linker concentrations. P41 – polyethylene glycol linker of 41 repeating units, P8- polyethylene glycol linker of 8 repeating units, Cys – Cysteamine and 3-MPA – 3-mercaptopropionic acid.

Sample	λ_{max} (nm)	Extinction (au)
Ag Citrate Alone	408	0.996
P41 (1 µM)	406	0.79
P41 (3 µM)	406	0.906
P41 (5 µM)	405	0.712
P8 (1 µM)	406	0.861
P8 (3 µM)	407	0.559
P8 (5 µM)	407	0.96
Cys (1 µM)	405	0.575
Cys (3 µM)	430	0.021
Cys (5 µM)	349	0
3MPA (1 µM)	409	0.904
3MPA (3 µM)	410	0.849
3MPA (5 µM)	410	0.548

Extinction spectroscopy results indicate that stabilisation of the nanoparticles was seemingly achieved for concentrations of 1 μM and 3 μM of 3-MPA. Slight red shifting of the plasmon band occurs indicating a change in the surface dielectric environment of the nanoparticles, which can be assigned to the displacement of the citrate ions and functionalisation by the 3-MPA ligand. At a concentration of 5 μM 3-MPA, there existed a significant broadening and dampening of the plasmon resonance band indicating that aggregation had occurred. The occurrence of aggregation at this concentration was believed to be due to a large excess of the surface capping 3-MPA ligands present competing for the same surface sites resulting in insufficient surface coverage of the nanoparticles, thus leading to aggregation upon centrifugation.

When cysteamine was added at a concentration of 3 μM to the nanoparticles a significant red shifting and dampening of the plasmon band indicated aggregation of the nanoparticles had occurred. When the concentration of cysteamine was increased to 5 μM, no measurement could be obtained due to precipitation of the nanoparticles from solution prior to analysis. Analysis was achieved for a 1 μM concentration of cysteamine however, at this concentration a significant dampening of the plasmon band occurred which was attributed to nanoparticle aggregation. Due to the heterobifunctional nature of the cysteamine ligand, it is possible the binding could occur *via* either the amine or thiol moiety present. It is therefore hypothesised that the aggregation which had occurred was a result of the molecules of cysteamine which are bound less strongly by the thiol moiety to the silver nanoparticle surface becoming displaced by competing ions within solution.

In contrast to these results, the addition of the P41 and P8 linker molecules produced stable modified nanoparticle solutions. Slight plasmon shifting of 1-2 nm was detected as expected and this shifting was indicative of changes in the dielectric environment at the surface of the nanoparticles due to functionalisation by the benzotriazole moiety of both linkers. Reproducible analysis was obtained at each concentration of linker added which was to be expected due to the stabilising nature of the PEG spacer molecule.

All of these results are summarised in figure 3.8, which displays the change in extinction ratio for each set of nanoparticle conjugates with varying linker concentration. The extinction ratio was calculated by using the values measured for extinction at the λ_{max} of the plasmon resonance and the extinction measurement at 500 nm which indicates aggregation of the nanoparticles. As shown, when the linker concentration was increased for 3-MPA aggregation of the nanoparticles occurred as indicated by the extinction ratio becoming significantly increased. This trend was mirrored for the various concentrations of cysteamine

linker whilst the measurements for both of the polyethylene glycol linkers showed no significant changes in extinction ratio following the increase in linker concentration present at the nanoparticle surface.

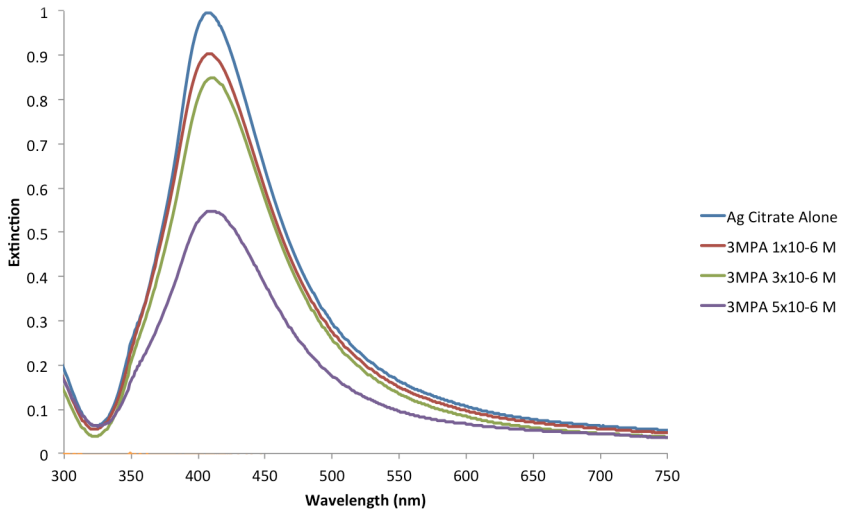

Figure 3.4 Extinction spectra of 3-MPA functionalised Ag citrate nanoparticles

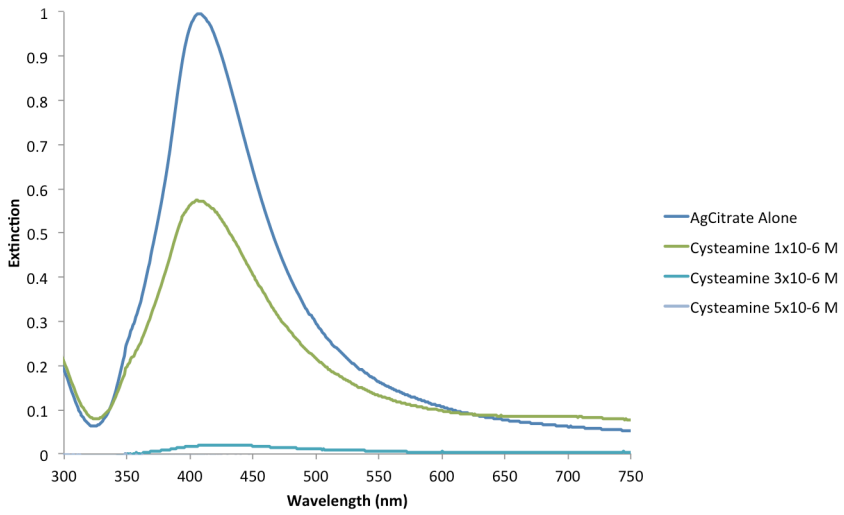

Figure 3.5 Extinction spectra of cysteamine functionalised Ag citrate nanoparticles

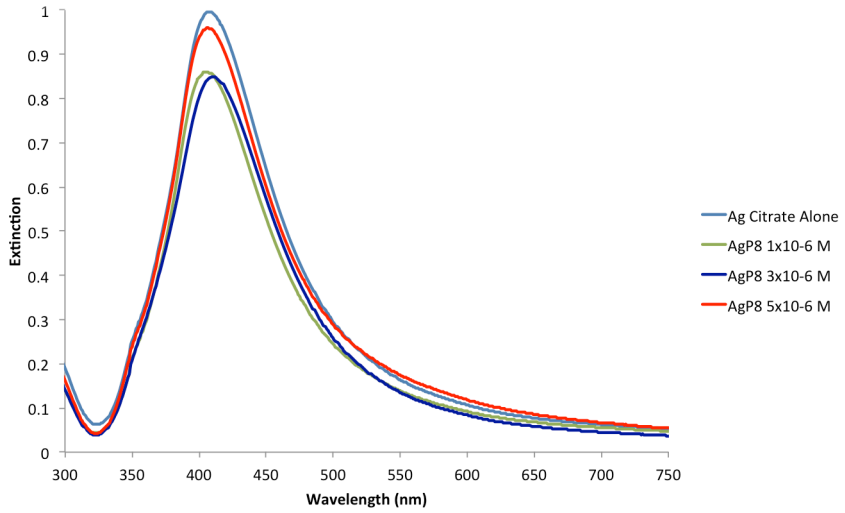

Figure 3.6 Extinction spectra of P8 linker functionalised Ag citrate nanoparticles

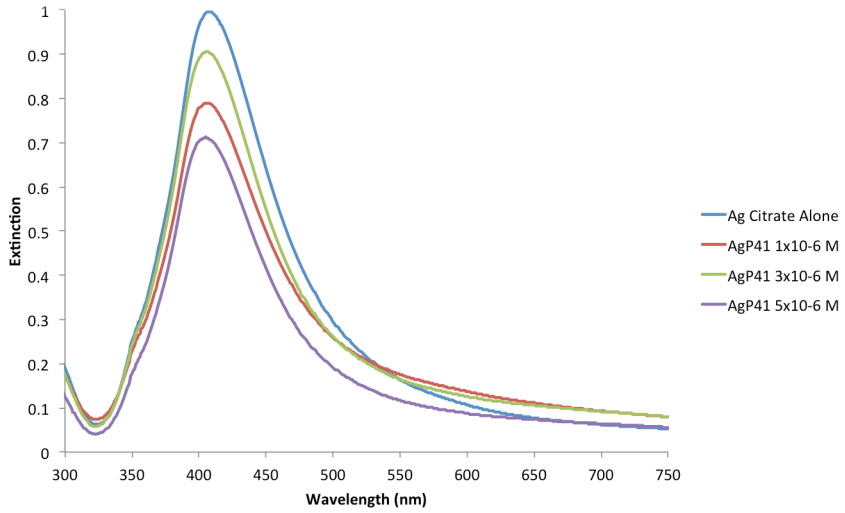

Figure 3.7 Extinction spectra of P41 linker functionalised Ag citrate nanoparticles

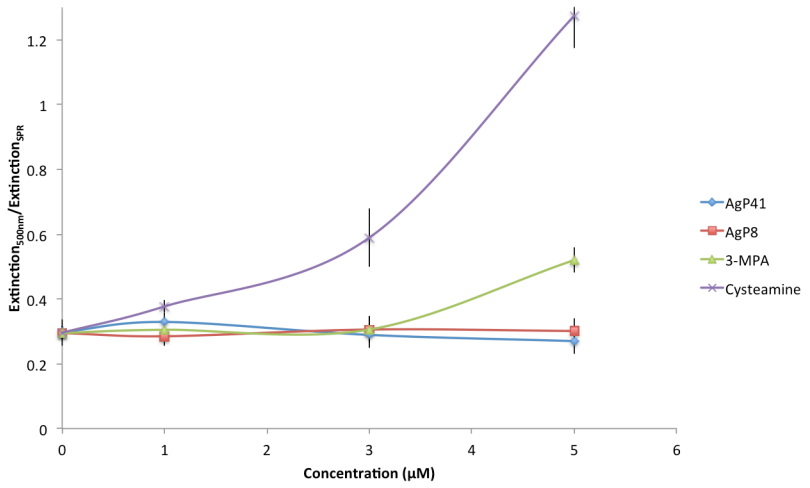

Figure 3.8 Ratio of extinction measured at 500 nm and at λ_{max} of SPR band vs. varying linker concentration

The DLS instrumentation used provided the facility to obtain DLS and Zeta potential analysis of each sample concurrently. The principles of DLS measurements are as follows. Each particle creates an interference pattern due to its orientation within a solution. As the particles move within solution fluctuations in this pattern occur causing flickering of the interference pattern. Assuming Brownian motion of the particles, the time scale at which these fluctuations occur can be correlated to the size of particle in solution.

Zeta potential is a measurement of the electric potential difference between the media in which the particles are dispersed and that of a stationary layer of fluid attached to the dispersed particles. A high zeta potential (negative or positive) confers stabilisation of the colloidal material whilst low zeta potentials are a measurement of low stability i.e. the nanoparticles are prone to aggregation.

The stabilisation of the silver nanoparticles due to the presence of the citrate capping ligands was apparent with a zeta potential measurement of -46.5 mv obtained. Each of the ligands added caused an increase in the zeta potential indicating a lesser degree of stability of each of these solutions in comparison to the citrate capped silver nanoparticles. However, the zeta potential of each set of nanoparticle conjugates remains above -30 mv indicating a good level of stability was obtained from each conjugated nanoparticle set following multiple analyses. These results are shown in figure 3.9 and table 3.2.

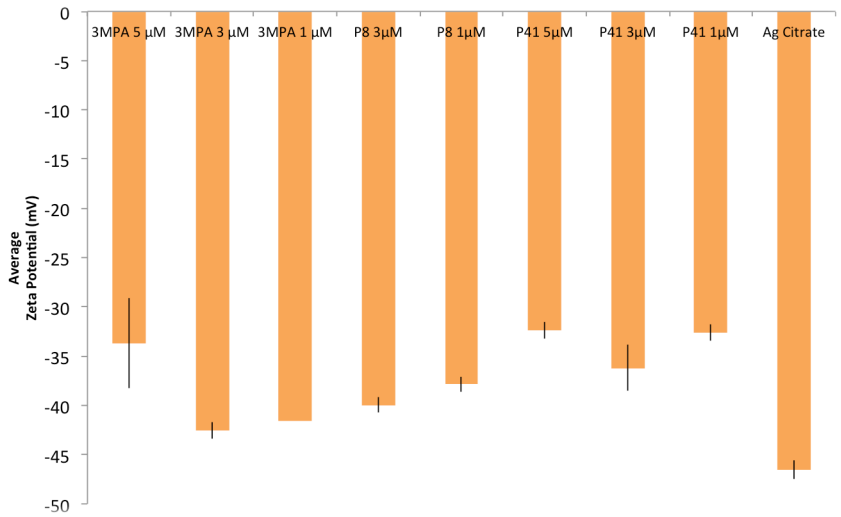

Figure 3.9 Measurements of the average zeta potential of the nanoparticle conjugates. Each measurement was performed in triplicate with the average of each measurement presented. Error bars shown are the standard deviations of each triplicate set of measurements.

Table 3.2 Measurements of the average zeta potential of the nanoparticle conjugates. Each measurement was performed in triplicate with the average of each measurement presented

Sample	Zeta Potential (mV)	Std Dev (mV)
3MPA 5 µM	-33.7	4.55
3MPA 3 µM	-42.53	0.85
3MPA 1 µM	-41.63	0.005
P8 3µM	-39.96	0.757
P8 1µM	-37.86	0.757
P41 5µM	-32.4	0.818
P41 3µM	-36.2	2.31
P41 1µM	-32.63	0.802
Ag Citrate	-46.5	0.971

The measurements for cysteamine functionalised nanoparticles were not recorded as following the analysis of the extinction spectroscopy measurements it was impossible to

obtain any further batches of cysteamine stabilized nanoparticles with each set aggregating during the purification step of their synthesis.

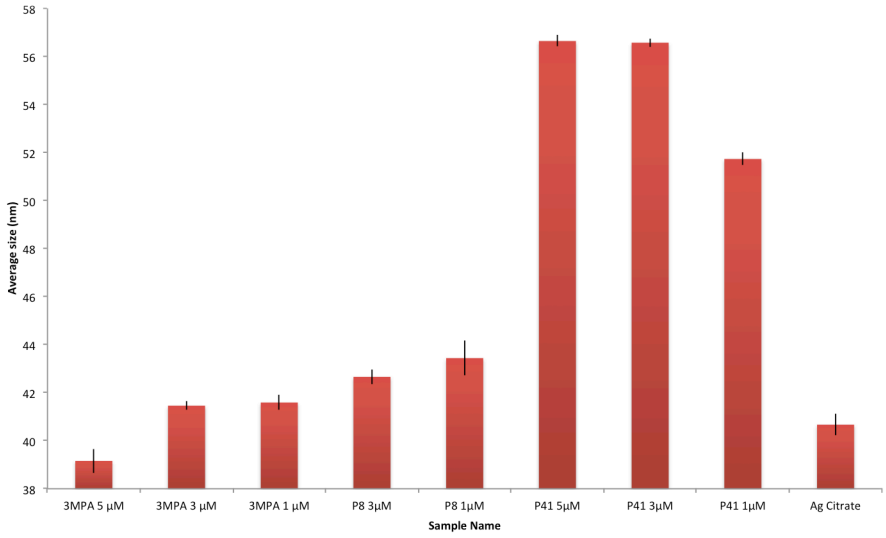

Figure 3.10 Average diameter of each modified nanoparticle solution at various linker concentrations as measured by DLS. Error bars represent the standard deviations of each set of triplicate measurements.

Table 3.3 DLS sizing data for Ag citrate nanoparticles modified with various linker concentrations.

Sample	Size (nm)	Std Dev (nm)
3MPA 5 µM	39.16	0.5
3MPA 3 µM	41.46	0.168
3MPA 1 µM	41.59	0.3
P8 3µM	42.66	0.303
P8 1µM	43.44	0.715
P41 5µM	56.64	0.235
P41 3µM	56.57	0.175
P41 1µM	51.73	0.262
Ag Citrate	40.67	0.46

Figure 3.10 and table 3.3 document the DLS measurements obtained for each sample. These results indicated that functionalisation with each ligand was successful by comparing the

results achieved to those of the unmodified citrate functionalised silver nanoparticles. Only slight size differences were obtained for 3-MPA modified nanoparticles due to the small length of the ligand. The result obtained for the 5 µM concentration of MPA is anomalous as these results indicate that these particles are smaller than the Ag citrate particles. A high standard deviation is obtained for both the Ag citrate and 3-MPA samples indicating a variety of sizes are present for each. The greatest increase in diameter was achieved for the nanoparticles functionalised with the P41 linker. This was expected due to the large number of ethylene glycol repeating units present in this spacer molecule and the brush conformation the spacer molecule is known to adopt when adsorbed onto the nanoparticle surface.

Further conclusive proof of the functionalisation of the nanoparticles by both the PEG_8 and PEG_{41} linkers are the ability to obtain reproducible SERS analysis at various concentrations of each linker. This confirms that the linker has been bound to the nanoparticle surface as expected *via* covalent bonding of the triazole moiety to the silver nanoparticle surface. The spectra observed are shown in figures 3.11 and 3.12.

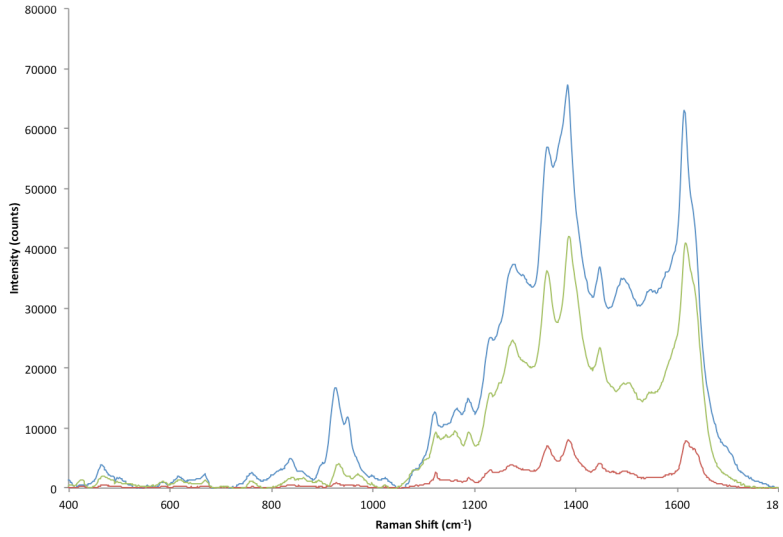

Figure 3.11 SERS analysis of P8 linker functionalised silver nanoparticles obtained at 514.4 nm. Each spectra was obtained using a 1s exposure time with 10 accumulations. Concentrations are depicted as follows 1 µM (blue) 3 µM (red) 5 µM (green).

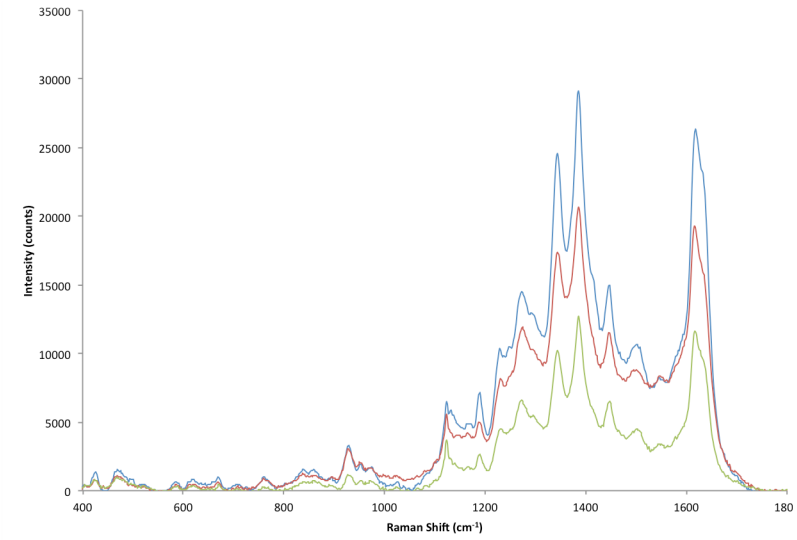

Figure 3.12 SERS analysis of P41 linker functionalised silver nanoparticles obtained at 514.4 nm. Each spectra was obtained using a 1s exposure time with 10 accumulations. Concentrations depicted as follows 1 µM (blue), 3 µM (red), 5 µM (green)

On comparison of the intensities obtained for measurements using the P8 and P41 linkers it was clear that the particles functionalised with P8 produced a more intense SERS spectra regardless of the concentration of linker added to the nanoparticles. This indicates that a greater number of dye molecules are present on the nanoparticle surface. This is as expected due to the greater steric hindrance produced when using the P41 linker because of the increased number of ethylene glycol repeating units. This prevents a similar number of molecules being present on the nanoparticle surface in comparison to when the P8 linker was used.

3.3 Mixed monolayer approach

To enable the nanoparticles functionalised with 3-MPA to be SERS active a mixed monolayer approach was adopted to functionalise the nanoparticle surface with both the ligand and a SERS active reporter molecule. 3-MPA and a second benzotriazole (BT) dye known as RB1 were added to the nanoparticles in tandem to create a SERS active species. RB1 is very similar in structure to the GM19 dye complexed to the PEG linkers. RB1 has a hydroxyl group present at the apex position instead of the amine present for GM19. The use of RB1 conferred no detrimental effect on the nanoparticle stability due to the hydroxyl group present becoming ionized at physiological pH. This results in the reporter molecule having a net negative charge, which repulses interfering ions.

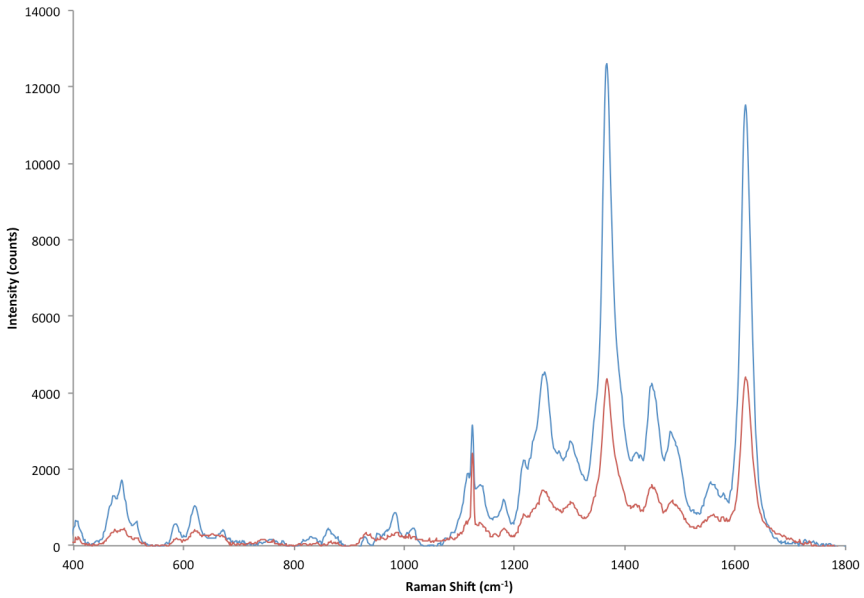

Figure 3.13 SERS spectra for mixed monolayer functionalised silver nanoparticles. Concentrations of RB1 present are identical to the final 3-MPA concentrations shown. Spectra obtained at 514.4 using a 1 second exposure time with 10 accumulations. 3-MPA 1μM (blue line) 3-MPA 5 μM (red line)

As shown in figure 3.13, the SERS intensities obtained for these nanotags were significantly less than those obtained for the P8 and P41 linkers. Thus, the mixed monolayer approach had proven successful, however, as the SERS intensities were lower than those obtained by the respective PEG linkers these nanotags were pursued no further. However, due to the success of the 3-MPA and RB1 mixed monolayer approach this protocol was extended to the use of both the P8 and P41 linkers in a similar manner. Optimisation studies were again performed using extinction spectroscopy and DLS/Zeta potential measurements.

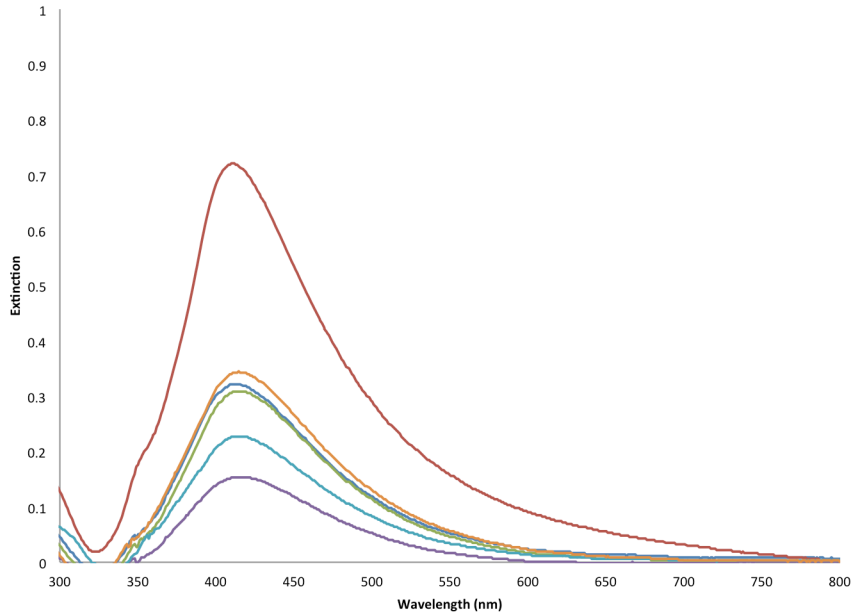

Figure 3.14 Extinction spectra of Ag nanoparticles functionalised with both P41 and P8 linkers in a mixed monolayer format. Each linker was added simultaneously in tandem. Ag Citrate (red) P41P8 ratio 50:50 (dark blue) P41P8 ratio 60:40 (green) P41P8 ratio 80:20 (purple) P41P8 ratio 40:60 (light blue) P41P8 ratio 20:80 (orange)

Initially studies were performed following the simultaneous addition of individual solutions of both linkers to a stirring nanoparticle solution. Using a stock solution of each linker at a concentration of 1 mM the linkers were added in tandem to achieve a final concentration of 1 μM linker on the nanoparticle surface. To identify the most suitable ratio of the linker molecules that confers nanoparticle stability, the volume of each ligand added was varied as shown in the extinction study results detailed in figure 3.14. From these results, it can be inferred that by simultaneously adding each linker individually to the nanoparticle solution aggregation of the silver citrate nanoparticles was occurring. This may be a result of the linkers competing for surface sites on the nanoparticles and as a result of this total monolayer coverage was not achieved which resulted in the aggregation of the nanoparticles upon centrifugation. Studies in the literature have shown that for mixed monolayer studies the most important consideration is the total concentration of analyte added to nanoparticle solution.[141] It has been shown that addition of the analyte molecules in a premixed solution of known concentration is favoured over the addition of each individual analyte in tandem. This could explain the apparent aggregation of the nanoparticle linker conjugates and as a result, the premixed method was tested.

A stock solution was prepared at $1x10^{-4}$ M concentration containing both linkers in an equal ratio. The volume of the combined linker solution added to the nanoparticle was altered accordingly to achieve the various final linker concentrations shown in table 3.4.

Table 3.4 Extinction spectroscopy measured for PEG mixed monolayer functionalised nanoparticles

Sample	$\lambda_{max.}$ (nm)	Extinction (au)
Ag Citrate Alone	407	0.798
P8P41 (10 μM)	404	0.305
P8P41 (5 μM)	405	0.571
P8P41 (3 μM)	404	0.142
P8P41 (1 μM)	403	0.09

At concentrations above and below 5 μM of the P8P41 mixture extensive aggregation occurred as indicated by the significant dampening of the extinction band and broadening of the plasmon peak which is indicative of nanoparticle clusters forming. Thus, to obtain stable nanoparticles an optimal final concentration of 5 μM P8P41 linker solution was used. When the mixed monolayer nanotags were analysed using SERS, reproducible analysis was obtained at the concentration of 5 μM shown previously to be the most stable. The corresponding average SERS spectrum of 5 replicate measurements is shown in figure 3.15.

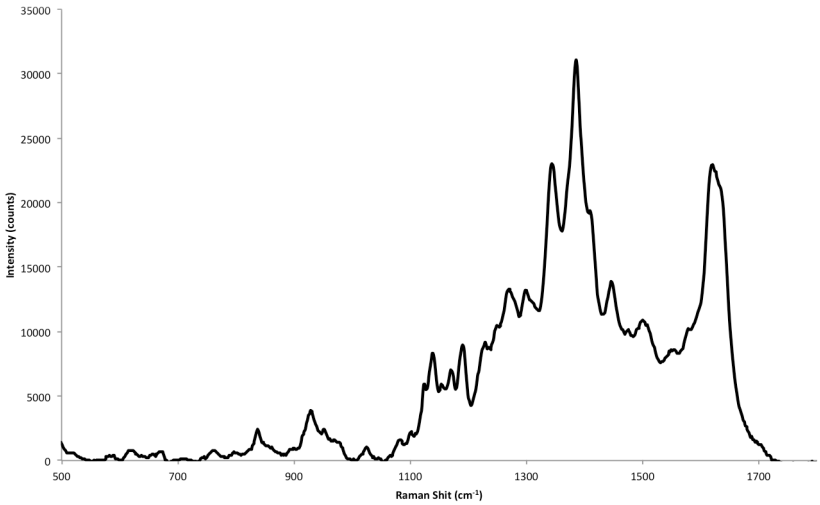

Figure 3.15 Average SERS spectra obtained at 514.4 nm of silver nanoparticle conjugated with premixed P8P41 solution to form a mixed monolayer of concentration 5 μM. Analyses obtained using a 1 second exposure using 10 accumulations.

SERS spectra with intensities comparable to the individual PEG linkers were obtained for nanotags formed from the mixed monolayer approach. Limit of detection (LOD) studies were then performed for each nanoparticle conjugate configuration in both the single linker and mixed monolayer linker formats to calculate the lowest detectable limit at which the dye present on the nanoparticle surface could be detected. These studies were performed to assess the suitability of each linker format to be used in sensitive detection assays. Due to the varying nature in size, length and functionalisation approach, it was interesting to detect if the limit of detection of each conjugate format was significantly different. To facilitate the calculation of the LOD for each conjugate set SERS spectra were measured at varying linker concentrations with the quadrant ring stretch of the benzotriazole reporter molecule (1613 cm^{-1}) being used to quantify the effect altering the concentration of linker present had on the SERS intensity obtained. Analyses were performed using a 514.5 nm laser excitation wavelength and the results for each respective linker are shown in figures 3.16 – 3.18.

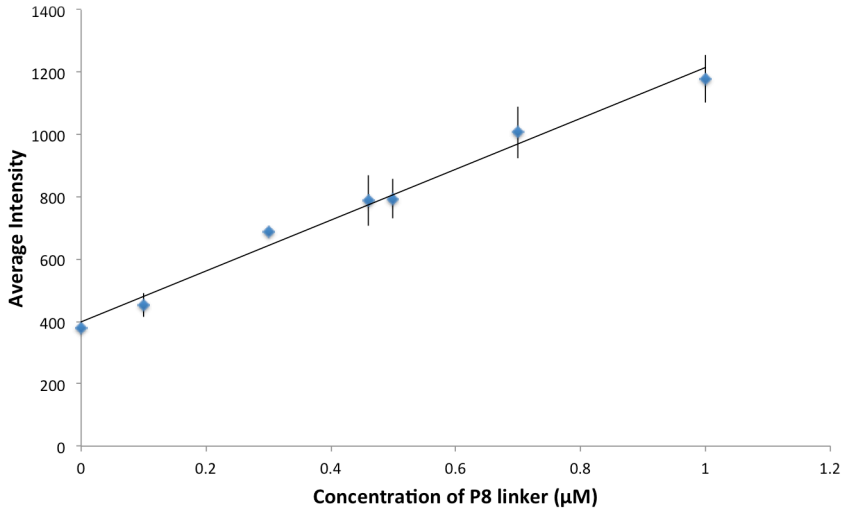

Figure 3.16 LOD study for P8 linker using 514.5 nm excitation. Spectra were analysed 5 times at each concentration using a 1 second exposure with 10 accumulations. Each point plotted is the average of these replicates

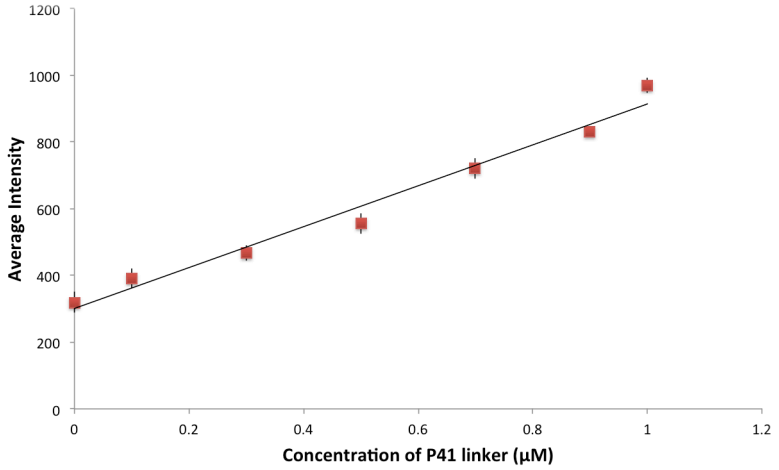

Figure 3.17 LOD study for P41 linker using 514.5 nm excitation. Spectra were analysed 5 times at each concentration using a 1 second exposure with 10 accumulations. Each point plotted is the average of these replicates

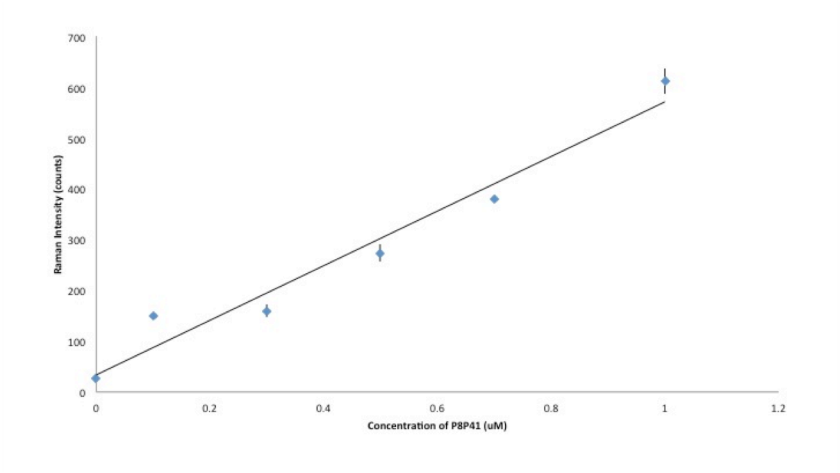

Figure 3.18 LOD study for P8P41 linker mixed monolayer using 514.5 nm excitation. Spectra were analysed 5 times at each concentration using a 1 second exposure with 10 accumulations. Each point plotted is the average of these replicates

Table 3.5 Calculated LOD for each linker set

Sample	Calculated LOD
P8	74.5 nM
P41	100 nM
P8P41	17.9 nM

Following the achievement of a linear range of detection for each linker, the LOD value was calculated for each conjugate set using the equation shown in experimental section 9.15. The results of these calculations are shown in table 3.5. The LOD results measured for each linker set were unanticipated. As expected the LOD for the single P8 linker functionalised nanoparticles was lower than that of the LOD obtained when the nanoparticles were functionalised with the P41 linker as P8 is less sterically hindered therefore a higher ratio of linker molecules should theoretically be able to bind to the nanoparticle surface. Therefore, as the linker concentration was decreased a higher number of P8 linker molecules remained attached to the surface of the nanoparticles in comparison to the number of P41 molecules present at the nanoparticle surface when the concentration of P41 was altered. Contrary to this the LOD obtained for the mixed monolayer approach is significantly lower than that of the individual linker functionalised nanotags. The presence of the P41 linker in the premixed solution would be expected to cause steric hindrance and prevent a number of P8 molecules being able to attach to the nanoparticle surface. However, the binding of the mixed monolayer approach must therefore be more efficient than that of the individual linkers and result in an increase in the number of dye molecules bound at the nanoparticle surface. It is possible to rationalize this by assuming that the P8 linker molecules are able to complex the nanoparticle surface at almost full monolayer coverage of the nanoparticle surface. The more sterically hindered P41 linker molecules are then able to attach to the nanoparticle surface at the free surface sites to complete coverage of the nanoparticle surface.

3.4 Assessment of the SERS stability of the nanotags

Previous work performed by Nie and co-workers established that the PEGlayted nanoparticles they constructed presented an inherent stability at high salt concentrations and in the presence of both hydrochloric acid (HCl) and sodium hydroxide (NaOH).[119] To compare the stability of these nanotags to those of Nie, the unique SERS signature of these nanotags were monitored for any significant changes when they were redespered in solutions of the aforementioned materials. The results of the SERS analysis obtained when the particles were dispersed in each of these solutions have been shown in figures 3.19 and 3.20 respectively.

These results show the nanotags created using the modified PEG spacer units have stability comparable to that of the nanotags produced by Nie *et al*. The only significant difference being the instability of these nanotags when redispered in a solution of 1M sodium hydroxide. A possible cause of this aggregation could be that the increase in ionic strength of the solution has resulted in the displacement of the linker molecules from the nanoparticle

surface. The trace signal, which was obtained, could have emanated from the free linker molecules within solution which are close to but not bound upon the nanoparticle surface.

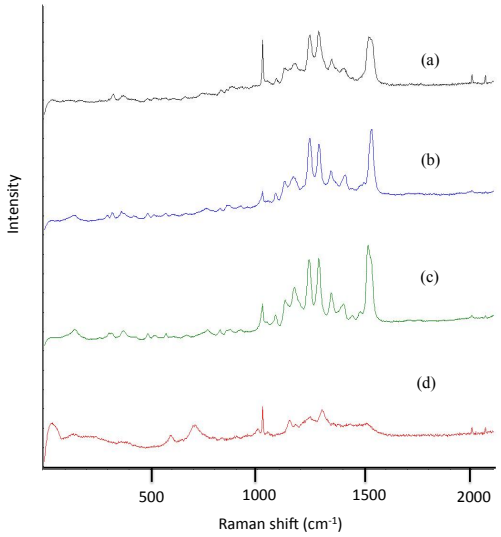

Figure 3.19 SERS stability studies for mixed monolayer functionalised Ag citrate nanoparticles performed at 514.5 nm using a 20x lens with 1s exposure with 10 accumulations. The functionalised nanoparticles were analysed in the following solutions : (a) distilled water (b) 1M hydrochloric acid (c) 1 x PBS (d) 1M sodium hydroxide

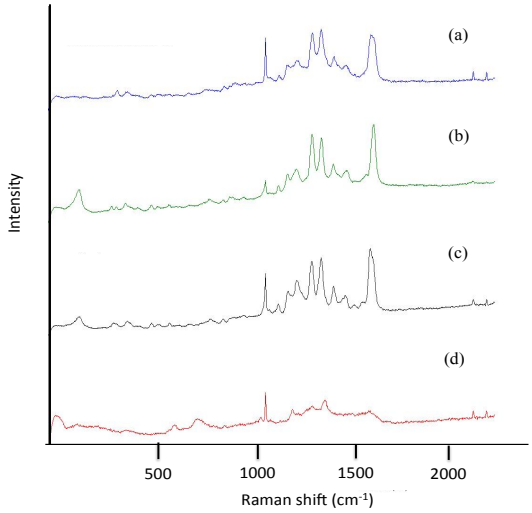

Figure 3.20 SERS stability studies for P41 linker functionalised Ag citrate nanoparticles performed at 514.5 nm using a 20x lens with 1s exposure with 10 accumulations. The functionalised nanoparticles were analysed in the following solutions : (a) distilled water (b) 1M hydrochloric acid (c) 1 x PBS (d) 1M sodium hydroxide

As similar results were achieved in accordance with using both the mixed monolayer and single monolayer methods either approach would be deemed satisfactory based on stability.

3.5 Characterisation of analyte attachment per nanoparticle

The previous characterisation and stability studies of the PEGlayted nanoparticle conjugates were working towards the end goal of achieving biologically active nanoparticles to monitor protein-protein interactions (PPIs). The next step in this process was to attempt the functionalisation of the PEG modified nanoparticles using a biologically relevant molecule, in this case an IgG antibody. Antibodies are commonly used in nanoparticle studies due to their cost and their specific interactions with certain proteins and antigens.[142] Using a protocol established previously by McKenzie *et al*. the nanoparticles were functionalised with a fluorescent antibody before the surface species were displaced and the free fluorescent antibodies in solution detected using fluorescence spectroscopy.[143] Briefly, a polyclonal IgG antibody was functionalised with the fluorophore ROX-isothiocyanate *via* EDC.HCl and sNHS coupling. Once purified, using a molecular weight spin column, the functionalised antibody solution was then conjugated to the PEGlayted nanoparticles using EDC sulfo NHS coupling chemistry. These nanoparticles were purified by centrifugation and redispered in 10 mM phosphate buffer pH 7.4 to preserve the biological integrity of the nanoparticle conjugates. Dithiothreitol (DTT) was then added to these solutions overnight at a final concentration of 2.5 M to displace any surface bound species from the Ag nanoparticles. Following centrifugation the free fluorescently tagged antibodies were retrieved by retaining the supernatant of each corresponding nanoparticle solution. Prior to analysis of these supernatant solutions calibration of the spectrometer was performed for a range of ROX-ITC solutions at various concentrations the resultant calibration graph has been shown in figure 3.21. From linear regression analysis, the number of ROX molecules per antibody was calculated to be 1.19.

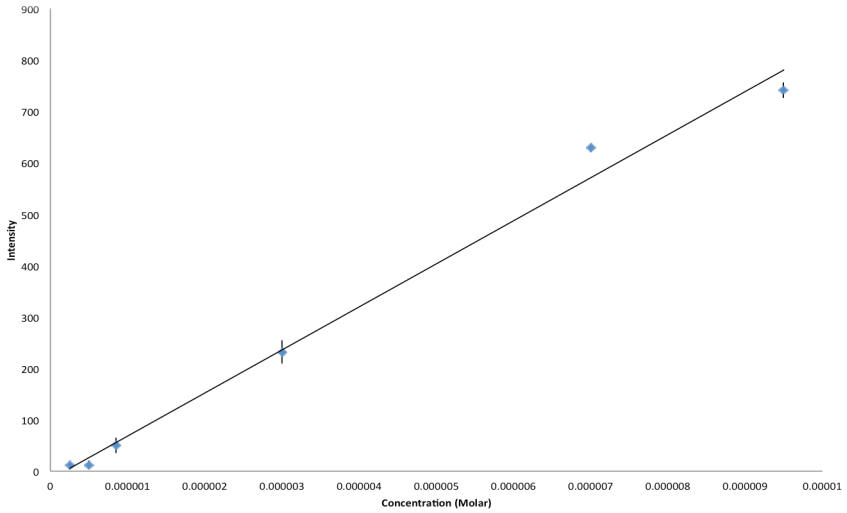

Figure 3.21 Calibration of fluorescence intensity for ROX-ITC solutions at various concentrations. Measurements performed using a 570 nm excitation over the range 575 – 625 nm. Average intensity of the profile at 585 nm was obtained for 5 samples of each solution and averaged. The error bars shown are the standard deviation for each set of five measurements performed.

Analysis of the retrieved supernatant solutions was then performed and the results are shown in table 3.6. From table 3.6 it can be calculated that for P41 functionalised nanoparticles there was an average of 56.9±11.7 antibodies per nanoparticle and for P8 functionalised nanoparticles an average of 21.2±5.6 antibodies per nanoparticle. From previous data it was concluded that more P8 linker molecules had become attached to the nanoparticle surface in comparison with the P41 linker molecules due to the higher SERS intensities obtained. At first glance, this appears contrary to this conclusion as the assumption would be that as more linker molecules were thought to be attached to the nanoparticle surface that therefore, more antibodies would also be attached. However, steric hindrance must therefore play a key role in the number of antibodies attached to each particle. Although there are thought to be less P41 molecules present the conformation of their binding to the nanoparticle surface shall result in a greater spacing between each molecule. As a result, the free carboxylic acid of these linker molecules would be more accessible to the antibody than the more sterically hindered P8 molecules, which are more crowded together on the nanoparticle surface. Also, it should be stated that although this analysis was repeated with a standard 5 replicates the standard deviations obtained would suggest that there is significant variance in the number of antibodies attached between each functionalised nanoparticle.

Table 3.6 Fluorescence spectroscopy data obtained for each sample and the number of antibodies calculated to be present on each.

Sample	Fluorescence Intensity (a.u.)	Calibration Curve Concentration (nM)	Concentration prior to addition to nanoparticles (M)	Nanoparticle concentration (nM)	Number of antibodies per nanoparticle
P41 No. 1	46.95	2.37	9.49×10^{-8}	1.3	72.97
P41 No. 2	74.28	3.5	1.38×10^{-7}	2.4	56.98
P41 No. 3	56.03	2.75	1.25×10^{-7}	0.21	51.77
P41 No. 4	56.84	2.79	1.1×10^{-8}	0.24	45.82
P41 No. 5	14.51	1.16×10^{-7}	4.48×10^{-9}	0.79	5.67
P8 No. 1	44.59	2.3	9.11×10^{-9}	0.73	12.48
P8 No. 2	53.89	2.67	1.05x10-8	0.42	25.08
P8 No. 3	40.18	2.14	8.43×10^{-9}	0.32	26.37
P8 No. 4	32.13	1.83	7.22×10^{-9}	0.38	19.01
P8 No. 5	51.85	2.59	1.02×10^{-8}	0.44	23.28

This protocol was also followed to characterise the number of antibodies attached to the mixed monolayer functionalised nanoparticles, however, when fluorescence measurements were performed on the supernatant of these solutions no fluorescence intensity was obtained. This was believed to be due to unsuccessful displacement of the fluorescently labelled antibodies from the nanoparticle surface following addition of DTT due to the increased stability of the PEGlayted nanoparticles. Upon repeated analysis similar results were again achieved and as a result, no value could be measured for the P841 modified nanoparticles.

3.6 TMB ELISA

Following the successful conjugation of antibodies to the nanotags it was important to prove that the biomolecule attached to the tags remained biologically active. As discussed previously in section **1.7** immunoassays are a common method used to monitor protein-protein interactions. One of the most common types of immunoassay is the ELISA. TMB is the most common and popular substrate for HRP detection in ELISA. Due to the successful conjugation of antibodies to these nanotags previously and the commercial availability of

HRP conjugated antibodies this platform was chosen to demonstrate the bioactivity of these conjugates. Figure 3.22 describes the ELISA format used for this study.

SERS analysis at 514.5 nm of each well was undertaken to determine the successful attachment of the nanoparticles to the well and to establish that a biological interaction had successfully occurred between the TMB and HRP-Ab functionalised nanoparticles. Figure 3.23 displays the spectra obtained from analysis of the polystyrene wells prior and post to the final wash step of the ELISA. Analysis of the polystyrene wells prior to the final wash step indicated that nanoparticles were indeed present due to the appearance of characteristic peaks of the benzotriazole dye attached to the PEG linker molecules. However, following the final wash step the only signals achieved from the polystyrene wells were that of polystyrene. An explanation for this could be that the nanoparticle conjugates were not bound strongly enough to the polystyrene wells, and during the final washing phase, were displaced from the well surface and removed during aspiration. There may have also been an excess of free HRP conjugated antibody present within the well, which had filled the active sites available to the incoming nanoparticle, conjugates and prevented their binding. This would explain why the oxidation of TMB continues to occur due to the presence of HRP within each of the wells.

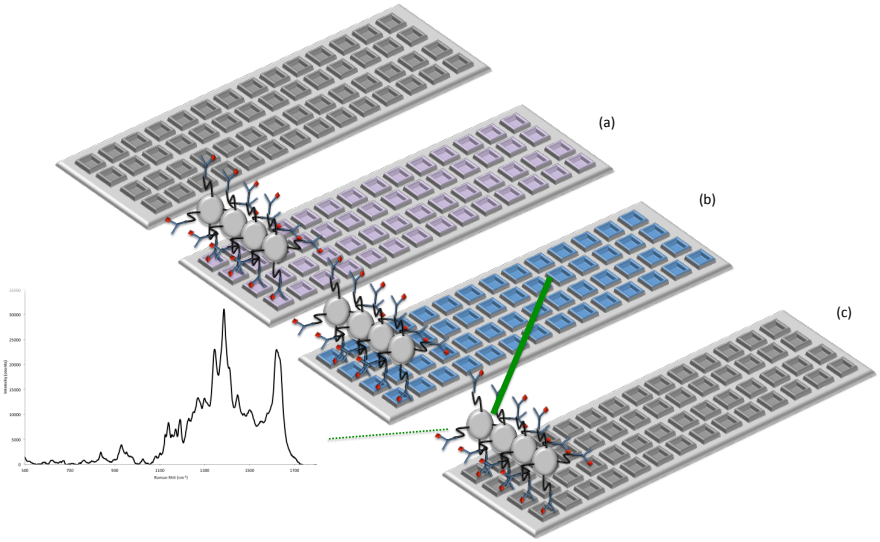

Figure 3.22 (a) To maleic anhydride activated polystyrene wells 100 µL of nanoparticles functionalised with horse radish peroxidase (HRP) conjugated antibodies were added and the plate agitated for 1 hour (b) Following washing and blocking of the wells 100 µL of 3,3',5,5'-tetramethylbenzidine (TMB) was added to each well resulting in the appearance of the blue colour indicating the binding of antibody conjugated nanoparticles to the well (c) Further washing with 1xPBS followed by analysis at 514.5 nm using a 1 second exposure and 10 accumulations.

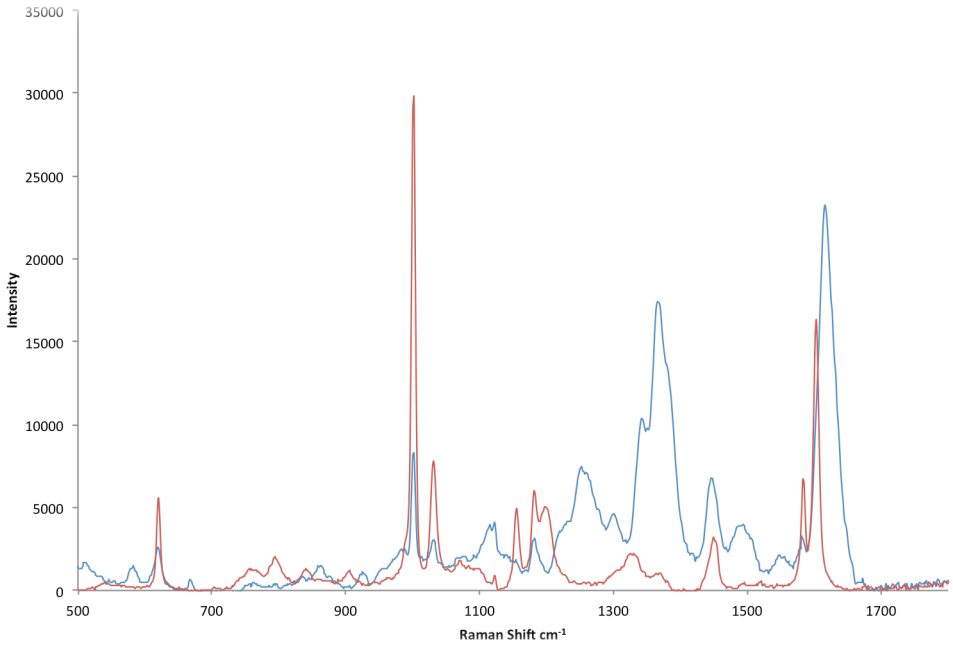

Figure 3.23 Analysis of polystyrene wells pre (blue line) and post (red) final wash step. Signals of PEG molecule were not obtained after the final wash step.

3.7 Bulk Protein A IgG Assay

As the ELISA assay provided unexpected results a second assay format was investigated to establish the biological integrity of a protein attached to these nanoparticle conjugates could be preserved following the conjugation procedure. A second assay was devised in the form of a bulk protein assay, which could be performed on an epoxy resin coated glass slide.

Protein A is present in the cell wall of gram-positive bacterium *Staphylococcus aureus* and plays a major role in the virulence of this bacterium.[144] Protein A is recognised as being a versatile tool for studying protein interactions due to its high affinity towards IgGs. The structure of protein A consists of a single polypeptide chain folded into five homologous domains.[145] This structural configuration gives rise to many of its interesting properties including the ability to remain stable over a broad range of pH, ability to reversibly bind a variety of IgGs *via* their Fc fragment and that it remains active after IgG-Protein A complexes have been dissociated under highly acidic conditions. [146-148]

For this assay, Ag citrate nanoparticles were functionalised using a mixed monolayer of P41P8 linker molecules followed by Protein A (1mg/mL, 10 µL) conjugation using EDC.HCl and sulfo NHS coupling chemistry as detailed previously. An epoxy resin glass slide was then functionalised overnight with a monoclonal IgG antibody prior to addition of

the nanoparticle conjugates. The protocol for this assay has been provided in section 9.11 and a representative image of the assay performed has been shown in figure 3.24.

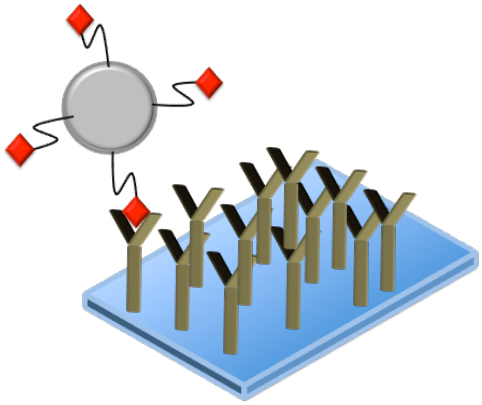

Figure 3.24 Epoxy glass slide immunoassay **(Note not to scale)**

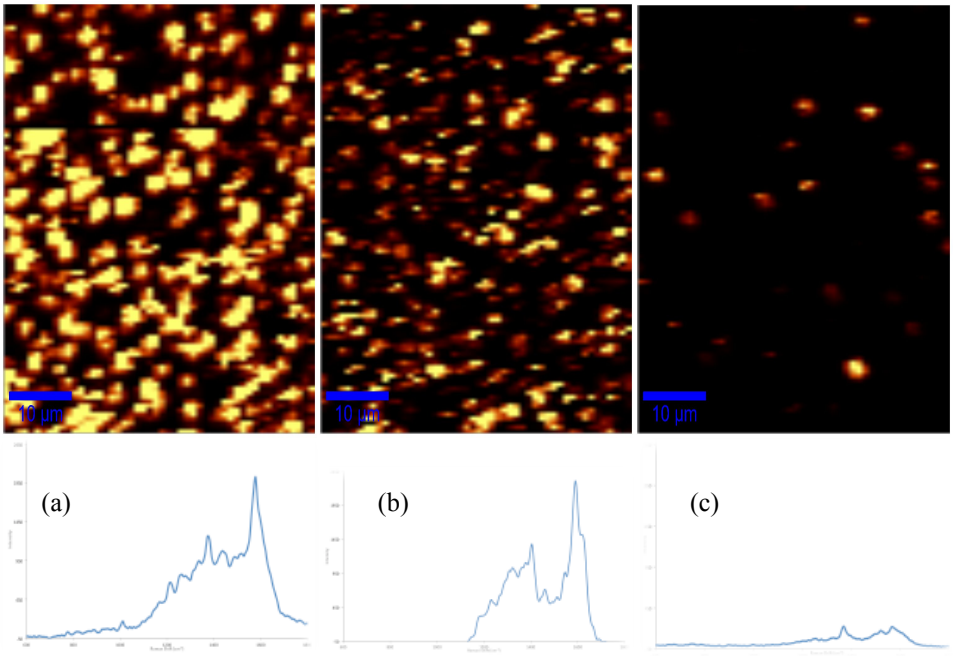

Figure 3.25 Bulk protein A assay results using 532 nm laser excitation wavelength: (a) False colour image of bulk area and average spectra of area when 100 µL of nanoparticle conjugates have been added for 5 minutes to the region (b) false colour image of bulk area and average spectra of area when 50 µL of nanoparticle conjugates have been added (c) false colour image and average spectra of control area where no IgG had been spotted and 100 µL of nanoparticle conjugates had been added. All false colour intensity maps have been set to the same intensity thresholds and the SERS spectra have been adjusted to the same scale for comparison.

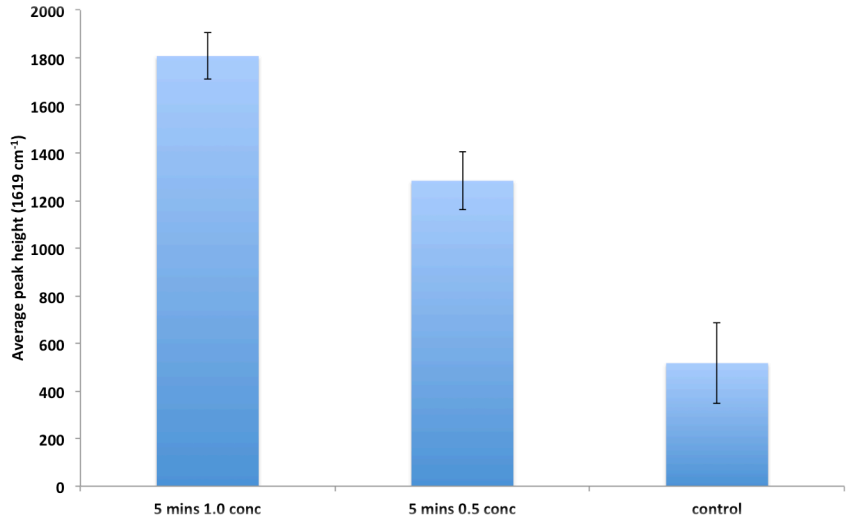

Figure 3.26 Measurement of peak height at 1619 cm^{-1}. Error bars are the standard deviation for the average of 15 spectra from each false colour map

The bulk assay was performed at two different concentrations to identify any binding differences of the protein A functionalised nanoparticles to the antibody functionalised glass slide. To evade any ambiguity with the results obtained control experiments were also performed using the same conditions with the exception of using PEG conjugated nanoparticles that had no protein attached and were therefore unable to bind to the IgG antibody present on the slide.

Following the performance of the bulk protein assay, analysis of the glass slide was performed using a confocal Raman microscope at an excitation wavelength of 532 nm. Figure 3.25 shows the spectra and corresponding false colour images from a selected bulk assay region. The false colour images were generated following the construction of an intensity profile map corresponding to the peak intensity of the spectral peak at 1613 cm^{-1}. This peak has been previously used for concentration dependent analysis and appears to be the most intense peak observed when the assay slide was analysed. For data analysis purposes, the spectra obtained from each bulk spot were baseline corrected using a polynomial of degree 3 followed by averaging of the spectra using the WITec software package. For each set of conditions used the average peak height of the 1613 cm^{-1} peak was monitored and the results obtained are shown in figure 3.26. This peak was chosen as it has been identified as the aromatic quadrant ring stretch and has been found to be a very intense peak in each of the spectra recorded.

As expected the most intense spectra obtained corresponded to the nanoparticle conjugates being present at the highest concentration. When the concentration was reduced by 50%, binding of the nanoparticle conjugates to the slide still occurred, however, both the false colour intensity maps and the spectral measurements indicated the binding was decreased in comparison to the more concentrated samples. Although signal was obtained in the control area this can be considered as non-specific absorption of the nanoparticle conjugates to the glass surface and has been considerably restricted due to the functionalisation of the nanoparticle surface with PEG.

3.8 Conclusions

In conclusion, novel polymeric linkers have been successfully synthesised and utilised for the attachment of biomolecules to the surface of silver nanoparticles. This was the first report of the preparation of modified silver nanoparticles in this manner. The inclusion of an intrinsic benzotriazole dye proved advantageous, as it was possible to obtain reproducible SERS in both a qualitative and quantitative manner due to the covalent bonding of the benzotriazole dye to the nanoparticle surface. Extinction spectroscopy studies showed these modified nanoparticles to be stable with no significant changes in the surface plasmon when the optimised linker conditions were used. The SERS signal achieved was shown to be both reproducible and stable in the presence of various agents, which have proven destructive to a range of materials in other studies. These results are comparable to the current standard PEG functionalisation protocol for gold nanoparticles previously published in Nature by Nie and co-workers. Displacement studies have provided a means by which the number of biomolecules attached to the modified nanoparticles could be quantified and it has been shown *via* the use of a bulk protein immunoassay that these nanoparticle conjugates retain their biological activity and integrity following conjugation. These properties make these linker-modified nanoparticles highly attractive for future biodiagnostic applications.

3.9 Future Work

The design of novel linker chemistries utilizing this synthetic approach should be attempted for other similar polymeric spacer groups to exploit the benefits of solid phase synthesis and the design of ligands which include an intrinsic reporter molecule.

The ligands established should also be used in further biological assays for the detection of other biomolecules.

Quantification of the biomolecules attached to the ligands should also be attempted once more for the mixed monolayer ligand approach. One possible means by which this could be achieved could be to use trypsin to free the fluorescent antibodies attached to the purified nanoparticles prior to employing the approach used previously.

4. Formation of SERS active nanoparticle assemblies *via* carbohydrate-protein interactions

Carbohydrate and protein interactions are key to cellular process and disease pathogenesis. These interactions are known to play key roles in biological binding events such as the interaction of viruses and bacteria at the cellular interface, cell-to-cell adhesion, cell differentiation and cell development to name but only a few examples. Research in this field has primarily focused upon a group of carbohydrate binding proteins known as lectins. Lectins are a family of proteins ubiquitous in nature and are primarily associated with the agglutination of cells, which enables them to play a key role in blood typing. Of the family of lectins, the most widely studied and researched is Concanavalin A.

4.1 Concanavalin A

In 1936 the discovery of Con A by Sumner and Howell, and their subsequent discovery of both its agglutinating and precipitating properties towards erythrocytes and glycoproteins were the first observations of lectins possessing carbohydrate specificity.[149] Con A has since been used for analysis of cell surface saccharides in phenomena such as cell proliferation and cell-to-cell interactions.[149-151]

4.1.1 Con A structure

Con A exists as dimeric, tetrameric and higher order structures, depending on the physiological environment, which consist of identical protomers of 237 amino acids.[152,153] At physiological pH, Con A exists as a tetrahedral molecule comprised of four ellipsoidal domes. As a pseudo tetrahedral molecule Con A has four carbohydrate binding sites, one per each protomer subunit.[154-156] Carbohydrate specificity of Con A has been established towards both mannose and glucose, however, carbohydrate interactions with oligosaccharide sequences in the absence of both mannose and glucose residues have been shown to occur. Structurally Con A exists almost exclusively in a β-sheet conformation with almost no α-helical regions. The activity of Con A is dependent on the pH of its environment with maximum activity being achieved within the pH range of 6 – 7 when Con A exists in the tetrameric form. However, activity is still achieved at pH as low as 2.4 where Con A exists only as a dimer, in this form Con A retains the ability to bind derivatives of both glucose and mannose. At pH higher than the range of maximum activity, ConA is inactive due to undergoing an irreversible change in conformation, which results in the adoption of a random coil structure.

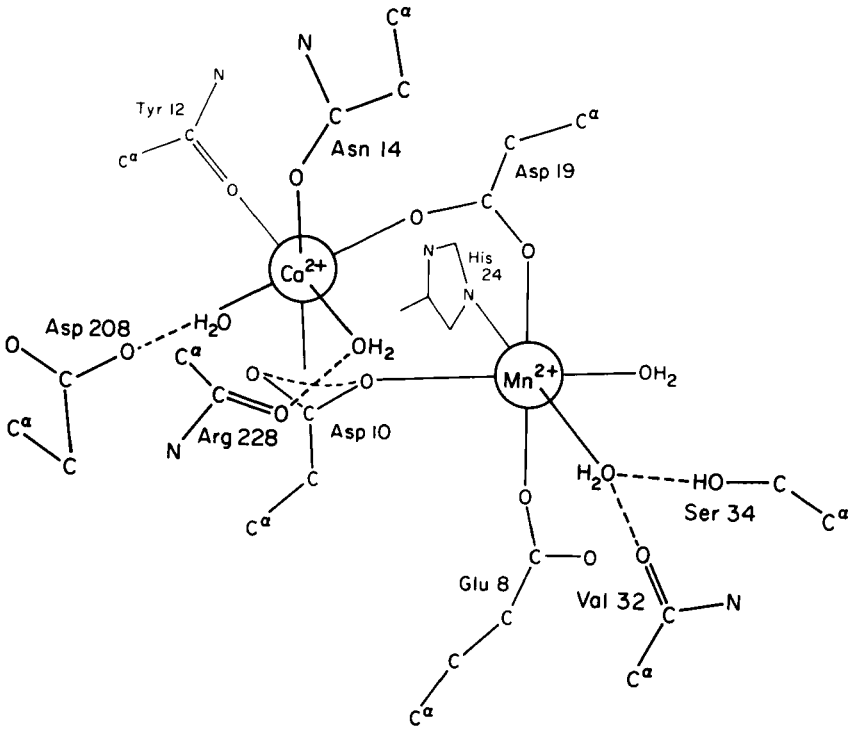

Figure 4.1 Schematic of the metal-binding region of Con A. Mn^{2+} and Ca^{2+} ions are octahedrally coordinated by four protein ligands and two water molecules[157]

Each protomer of Con A contains two metal ions, Ca^{2+} and Mn^{2+}, which are positioned 5 Å apart and found at the apex of the molecule. The presence of these ions is significant, as research has shown that the saccharide-binding site of Con A undergoes a conformational change, which facilitates saccharide binding. When these ions are not present, in acid labile conditions, Con A is unable to bind to any saccharides.[156] It has been shown that different transition metals are also capable of occupying the Mn^{2+} and Ca^{2+} binding sites with differing effects. The Mn^{2+} binding site is capable of binding a range of other divalent transition metal ions including Co^{2+}, Ni^{2+} and Cd^{2+}. While studies have shown, that Cd^{2+} can replace Ca^{2+}, although no other transition metal has been found to substitute for Ca^{2+} at this site. This indicates a considerable metal ion specificity at this site towards Ca.[158] Studies have also shown that in order for Ca^{2+} ions to bind to Con A Mn^{2+} must already be in place in each protomer. Once bound the Ca^{2+} ion has a direct influence on the rate of Mn^{2+} uptake indicating a relationship exists between the conformations of both of these binding sites.[159]

The saccharide-binding site of Con A was elucidated by Derewenda *et al.* who discovered that mannose was bound in the C-1 chair conformation.[160] The hydroxyl groups of carbons 3, 4 and 6 are equatorial and the hydroxyl of carbon 2 is axial. The anomeric carbon also has an axial hydroxyl group, which plays no part in the binding site of the protein and only interacts

with the surrounding solvent. Con A binds the saccharide by forming hydrogen bonds with nearly all of the donors and acceptors of the saccharide hydroxyl groups. Of the seven hydrogen bonds formed four are to backbone NH groups of proteins and two are to amino acid residues which are bound to the calcium ion. Further stabilizing interactions include van der Waals forces, which also contribute to saccharide binding. [160]

4.1.2 Detection of Con A

As Con A is readily available and inexpensive, it has been used as a model lectin for many carbohydrate-lectin studies. Due to its specificity towards the monosaccharide glucose, Con A has been employed in a number of in vitro glucose sensor studies including research by Tang *et al.* in which whole blood serum samples were analysed using Con A functionalised quantum dots to create a biosensor using fluorescence resonance energy transfer (FRET) as the method of detection. This study emphasised the efficiency of using Con A in this manner and achieved low detection limits of 50 nM glucose present in whole blood serum.[161] Similar studies of glucose detection using Con A include the electrochemical detection of Con A functionalised gold nanoparticles in a capacitive glucose biosensor with detection levels achievable at micromolar concentrations. The specificity of Con A to mannose has also been exploited by Russell *et al.* whom functionalised gold nanoparticles with mannose derivatives for the colorimetric detection of Con A using extinction spectroscopy. This rapid assay format yielded a limit of detection in the range of 0.1 micromolar, although, this study reiterates a lower limit of detection is possible but only at the compromise of time taken to detect the carbohydrate- protein interaction in this study. [162]

Various techniques have been used to explore carbohydrate lectin interactions including extinction spectroscopy, transmission electron microscopy (TEM), surface plasmon resonance (SPR) and fluorescence spectroscopy.[162-166] Herein, the first use of SERS to detect the formation of carbohydrate lectin interactions is described.

4.2 Nanoparticle assemblies overcome issues of multivalency

Carbohydrate lectin interactions are known to have weak binding affinities with binding constants in the region of millimolar levels. To increase the binding affinity and the number of interactions occurring a multivalent platform is required. To circumvent this issue in nature clusters of sugar molecules are created which enhance binding affinities exponentially resulting in these interactions remaining physiologically relevant. To replicate this phenomena in a controlled environment sugar clusters have been formed in a number of ways including the conjugation of multiple sugar derivatives to nanoparticles, the

conjugation of sugar clusters to surfaces for exploitation in array formats and the conjugation to other biologically relevant molecules in the form of carrier proteins, dendrimers and micelles.[167-170]

The functionalisation of nanoparticles with sugar molecules by Hone *et al.* for use in the detection of Con A by extinction spectroscopy achieved detection limits in the nanomolar region. These detection limits were only possible due to the ConA, like many other lectins, containing more than one saccharide-binding site. As a result Con A was able to interact with more than one sugar functionalised nanoparticle at a time resulting in the formation of nanoparticle aggregates. These nanoparticle assemblies caused significant broadening and dampening of the extinction band due to the coupling of adjacent surface plasmons. As a result of the plasmon coupling a secondary peak arose in the extinction spectra which was shown to have a direct dependence on the concentration of Con A present in the solution.

Similar studies have been successfully achieved using SERS for the interactions of other types of biomolecule such as DNA-DNA interactions. Graham *et al.*, functionalised the surface of the metallic nanoparticles using a mixed monolayer approach by tethering both DNA and a Raman active dye to the surface. Nanoparticles were functionalised with complementary strands of DNA and as they arrived in close proximity, they became bound together resulting in the formation of nanoparticle aggregates. As a result the Raman signal measured for the dye increased due to the formation of hot spots between the nanoparticles (areas of dense plasmon).[73,171,172]

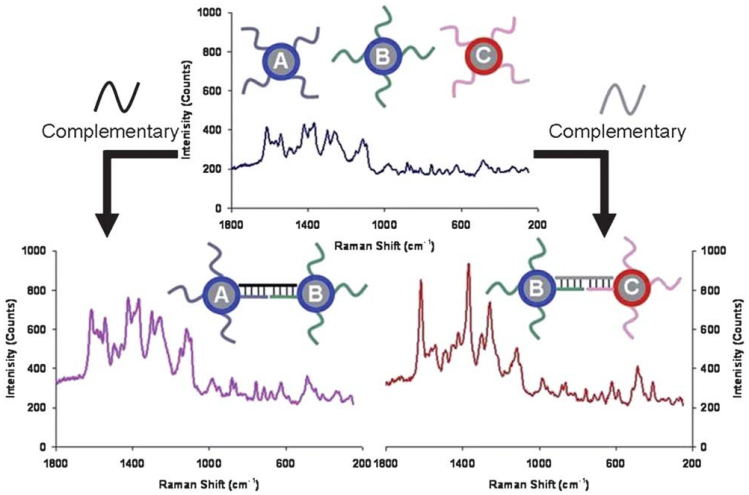

Figure 4.2 Multiplexed detection of DNA-DNA interactions *via* the formation of nanoparticle assemblies.[159]

Exploiting the success of this study Graham *et al.* carried out research into the sensitive and selective detection of a series of different DNA–functionalised silver nanoparticles[173]. This was achieved by assigning a different dye to each type of conjugate. The DNA sequences used included those corresponding to the VT2 gene of E. coli and the human papillomavirus (HPV). Across two different wavelengths (the difference as a result of attempting to match the excitation of the dye chromophores) the multiplexed SERRS spectra clearly displayed the peaks characteristic of each dye molecule and hence, DNA strands to which they were assigned, as shown in figure 4.2.[173] The limits of detection in the multiplex when compared with individual SERRS measurement were comparable, emphasising that the sensitivity of detection was not lost through multi-analyte detection (multiplexing).[173] Prior to undertaking the following work, no studies had previously been published of the study of carbohydrate-lectin interactions by SERS.

4.3 Carbohydrate linker synthesis

In order to construct the glyconanoparticles (sugar coated nanoparticles) many options were considered in terms of carbohydrate functionalisation, however, due to previous research (Chapter 3) into linker synthesis it was decided to attach the carbohydrate to a spacer ligand, which would tether the carbohydrates to the nanoparticle surface. As thiol functionalised molecules are known to attach to both silver and gold nanoparticles a series of thiol-terminated linkers were synthesised to enable choice between nanoparticle systems.

For an uncomplicated synthetic process, conjugation of the chosen carbohydrate to the spacer molecule was performed *via* an esterification reaction. Research to link different carbohydrates, for example dextran and sucrose, to thiol containing carboxylic acids *via* ester formation, has been reported.[174-176] This work was therefore consulted and partly used in the attempted syntheses, with adjustments made accordingly.

Lactose is a disaccharide made up of galactose and glucose, possessing two primary alcohol groups. Rationalisation of the preferred hydroxyl group for ester formation was necessary to aid in subsequent determination of the likely product.

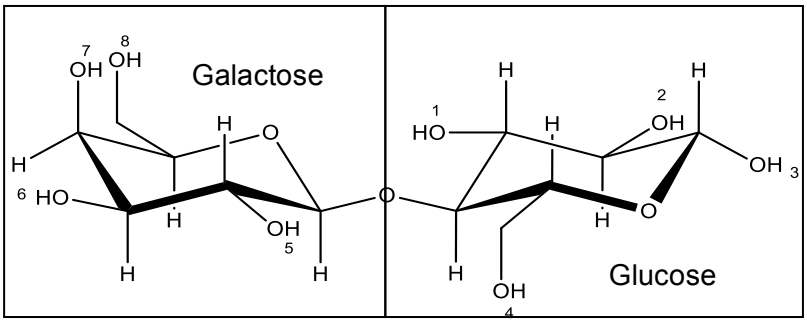

Figure 4.3 Thelwall numbering of lactose

According to research by Thelwall, ester formation occurs preferentially at hydroxyl groups 8 > 6 > 4 > 2.[177] Though the second primary alcohol is on the glucose ring, ester formation is preferred (after 8-OH) at the secondary alcohol, 6-OH, of the galactose ring. The rationale for this is that the cis-orientated 7-OH activates 6-OH towards ester formation. The positioning of 4-OH, close to the interglycosidic linkage, makes this group more hindered, discouraging ester formation. Additionally, the secondary alcohol groups close to ring linkage point (5-OH and 1-OH) are also hindered, further encouraging reaction at 8-OH. Subsequent esterification at 8-OH of the disaccharide would leave the glucose moiety available for subsequent interaction with glucose specific proteins.

4.3.1 Synthesis of ML-3

Due to the availability of the compounds in our laboratory, the first linker molecules to be investigated were 3-mercaptopropionic acid, 16- mercaptohexadecanoic acid and 11-mercaptoundecanoic acid. However, only 3-mercaptopropionic acid (3-MPA) was pursued further due to the cost per unit mass of the other two compounds making them unfeasible to use in repeated attempts to synthesise the correct product.

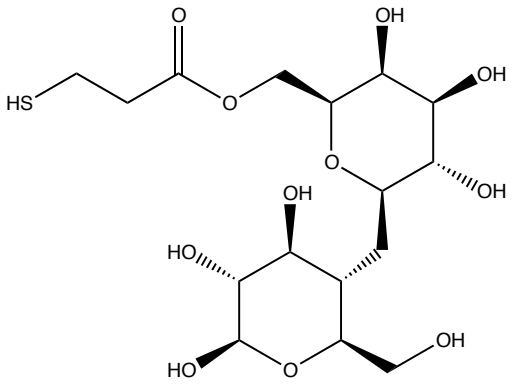

Figure 4.4 Structure of the proposed 3-mercaptopropyl β-*D*-lactoside (ML3) product

3-Mercaptopropyl β-*D*-lactoside (ML3) was prepared following the esterification methods by Neises and Steglich and partly that of Choi *et al*.[175,176] In the research by Choi *et al.,* the esterification reaction proceeded *via* a carbodimiide coupling intermediary. Choi *et al* chose to use N,N'-dicyclohexylcarbodiimide (DCC) and 4-dimethyalaminopyridine (DMAP) in equal proportions and used dimethylsulfoxide (DMSO) as the reaction solvent. DMAP behaves both as a nucleophile and acyl transfer agent, thus preventing the formation of the inactive N-acyl urea by-product arising from the rearrangement of the O-acyl intermediate formed in the esterification reaction. However, after the esterification reaction was complete the solvent was due to be removed by lyphollisation followed by washing with water to remove the insoluble urea by-product giving rise to the desired product. This was impossible to achieve due to analyses repeatedly showing that DMSO remained present following repeated lyphollisation and washing attempts. The method was therefore modified using the Steglich and Neses protocol, which used dimethylformaide (DMF) as the reaction solvent as it was easier to remove upon completion of the esterification reaction. DMF was removed *in vacuo* before the insoluble dicyclohexylurea by-product was removed *via* washing with deionized water and filtration. This allowed the separation of the water-soluble ester product which was then reduced *in vacuo* before being dried. As 3-MPA is stable at temperatures below 140°C, it was possible to use this with the sugar dissolved in DMF or DMSO, as heating was required at 60°C to remove the solvent upon completion of the reaction. By using this temperature, charring and burning of the sugar was also prevented.[178] The final product obtained was a yellow, crystalline solid and was analysed by TLC and submitted for ^{1}H NMR and ESI-MS analysis.

4.3.2 Benedicts reagent testing

Once the linker had been prepared and confirmed *via* NMR and MS analysis, a simple indicative test was performed to confirm the presence of the sugar within the linker molecule. Benedicts reagent is used to test for the presence of reducing sugars including glucose, fructose, lactose and mannose. Present in the reagent are copper (II) ions, which become reduced to copper (I) ions by the present sugar. To perform this test, the sugar and reagent where mixed in a 4:1 ratio (sugar linker: benedicts reagent) and heated to enable the reduction reaction to occur. A positive test shall provide a colour change from blue to green or red.[179]

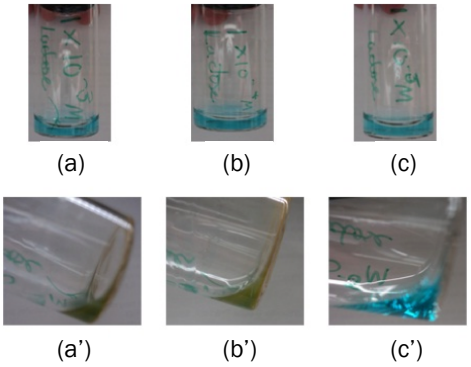

Figure 4.5 Solutions of lactose mixed with benedicts reagent before heating (a) and after heating (a'). (a) $1x10^{-3}$M lactose (b) $1x10^{-4}$M lactose (c) $1x10^{-5}$M lactose

To illustrate the effectiveness of this test three differing concentrations of lactose where tested with Benedicts reagent as shown in figure 4.5. Two of those solutions at a concentration of $1x10^{-3}$ and $1x10^{-4}$ M of lactose showed a distinct colour change when heated with Benedicts indicating the presence of sugar as expected. The solution containing $1x10^{-5}$M of lactose showed no colour change upon heating and this was thought to be due to an insufficient mass of lactose being present in order for the reduction reaction to occur sufficiently. Following this, the solutions of linker prepared as detailed earlier were tested with Benedicts reagent to confirm the presence of sugar within the linker. All of the solutions showed a positive result for the Benedicts reagent test at a concentration of 1×10^{-3}M. However, below this concentration negative test results occurred for each linker indicating that there was insufficient sugar present at these concentrations to facilitate the copper reduction reaction.

4.4 Nanoparticle stabilisation

To produce stable glyconanoparticles both gold and silver nanoparticles were initially tested with varied concentrations of each linker to establish at which concentration the glycoconjugates were most stable.

4.4.1 Gold-ML3 stability

Gold (Au) conjugates were prepared with varying ML3 concentrations and analysed by extinction spectroscopy. Table 4.1 details the extinction properties of each set of conjugates.

Table 4.1 Exctinction spectroscopy analysis: λ_{max} and extinction of gold-ML3 samples

Sample	λ_{max} (nm)	Extinction (au)
Au Colloid	528	1.445
Au-ML3 (100 µM)	679	0.182
Au-ML3 (50 µM)	523	0.065
Au-ML3 (25 µM)	524	0.077
Au-ML3 (10 µM)	522	0.124
Au-ML3 (5 µM)	523	0.176
Au-ML3 (2.5 µM)	525	0.239
Au-ML3 (1 µM)	528	0.880
Au-ML3 (0.5 µM)	526	0.782
Au-ML3 (0.25 µM)	529	0.108
Au-ML3 (0.1 µM)	525	0.509
Au-ML3 (0.05 µM)	526	0.701
Au-ML3 (0.025 µM)	525	0.493

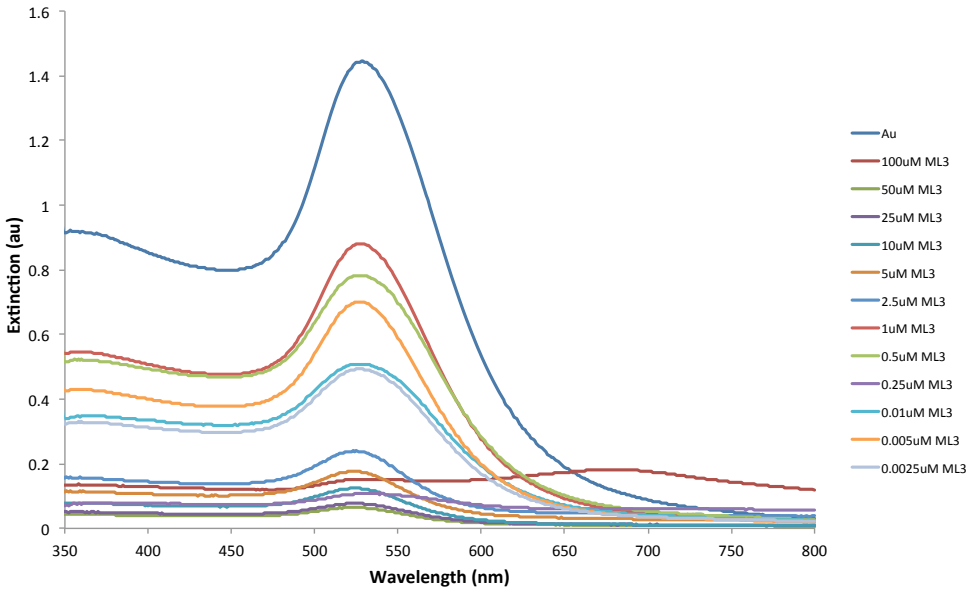

Figure 4.6 Extinction spectra of Au nanoparticles mixed with differing ML3 linker concentrations.

As indicated by the extinction spectra, figure 4.6, Au nanoparticles functionalised with ML3 at concentrations between 1 and 0.05 µM were the most stable conjugates. ML3 concentrations above and below this range appeared to cause aggregation of the Au particles resulting in severe dampening and broadening of the extinction band as well as significant

red shifting of the λ_{max} of these solutions. At a concentration of 100 µM a second extinction band is present at 679 nm which is indicative of the formation of small nanoparticle clusters.

To confirm this data the solutions within the stable range were analysed further by dynamic light scattering (DLS).

Table 4.2 DLS data of AuML3 conjugates

Sample	Size (nm)	Standard Deviation (nm)
Au Colloid (Batch 4)	53.1	0.02
Au-ML3 (1 µM)	58.4	0.87
Au-ML3 (0.5 µM)	53.3	0.61
Au-ML3 (0.25 µM)	54.2	0.95
Au-ML3 (0.1 µM)	53.2	0.44
Au-ML3 (0.05 µM)	54.4	0.48
Au-ML3 (0.025 µM)	56.8	0.76

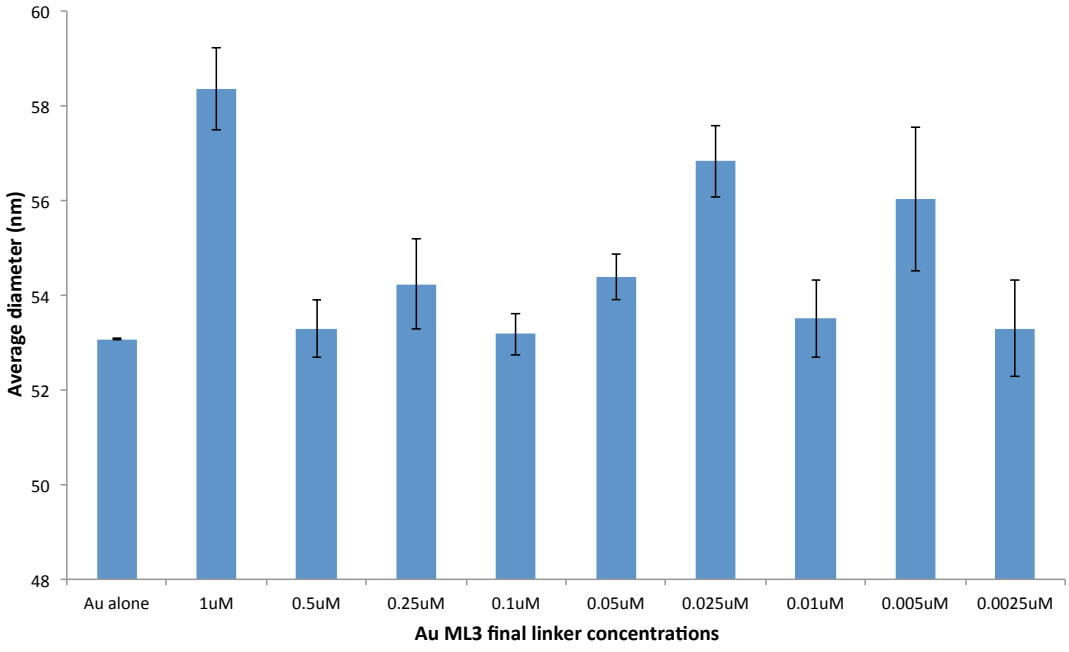

Figure 4.7 DLS data of the average size of AuML3 conjugates at different ML3 concentrations.

As illustrated by table 4.2 and figure 4.7, the DLS data for AuML3 conjugates displays a general trend of decreasing average diameter as the concentration of ML3 is decreased.

However, there are a few anomalies to this trend with ML3 concentrations 0.025 μM and 0.005 μM. As shown by the error bars for these measurements there was significant variance in the average measurements obtained and as a result these concentrations are not relevant as the use of ML3 at both of these concentrations is non-reproducible.

From both the extinction spectra and sizing data, it was concluded that a concentration of 1 μM ML3 should be used to obtain reproducible Au-ML3 conjugates. The sizing data showed that there is a significant increase in size of the nanoparticles when ML3 is added at a 1 μM concentration, therefore, it can be concluded that there has been an increase in the average diameter of the nanoparticles due to the functionalisation with the ML3 linker molecules as expected.

4.4.2 Silver ML3 stability

Using the same protocol as for AuML3 conjugates, the stability of silver (Ag) nanoparticles was tested using varied ML3 linker concentrations. These colloidal solutions were then analysed by both extinction spectroscopy and DLS as previous.

Extinction spectroscopy results, as shown in table 4.3 and figure 4.8, concluded that at a final concentration of 1 μM ML3 the conjugates were most stable. At concentrations of 100 and 10 μM there is significant broadening and dampening of the extinction band. This indicates the presence of larger aggregates of particles.

Table 4.3 Extinction spectroscopy results for varying the concentration of ML3 attached to Ag nanoparticles

Sample	λmax. (nm)	Absorbance (au)
Ag Colloid (Batch 2)	411	0.696
Ag-ML3 (100 μM)	408	0.040
Ag-ML3 (10 μM)	409	0.180
Ag-ML3 (1 μM)	410	0.546

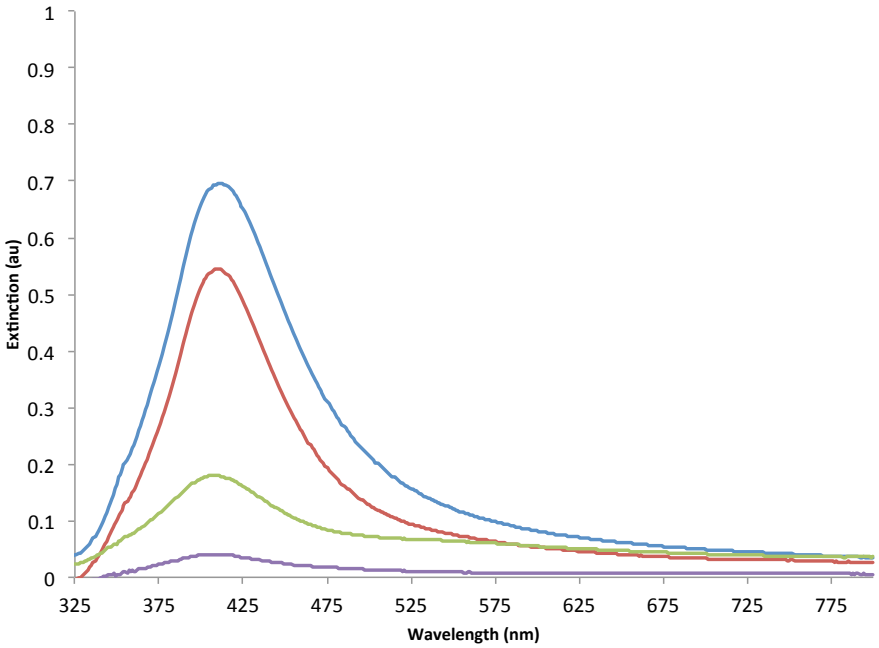

Figure 4.8 Extinction spectroscopy measurements for Ag functionalised nanoparticles with differing concentrations of ML3. AgCitrate (blue) AgML3 1 µM (red) AgML3 10 µM (green) AgML3 100 µM (purple)

As shown by table 4.4 and figure 4.9, this data was confirmed by DLS measurements, which established that at a concentration of 1 µM ML3 the conjugates remained stable and there was no apparent aggregation of the particles occurring. An increase in size was established for all three concentrations measured. The most significant size increase occurring for the 100 µM ML3 with the smallest increase of 2.1 nm occurring for 1 µM. This trend of increasing nanoparticle size with increasing ML3 concentration mirrors the trend of increasing aggregation with increasing ML3 concentration as established by extinction spectroscopy.

Table 4.4 DLS data measured for AgML3 conjugates at varied linker conjugations

Sample	Size (nm)	Standard Deviation (nm)
Ag Colloid (Batch 2)	54.4	0.095
Ag-ML3 (100 µM)	70.4	1.702
Ag-ML3 (10 µM)	60.7	0.395
Ag-ML3 (1 µM)	56.5	0.444

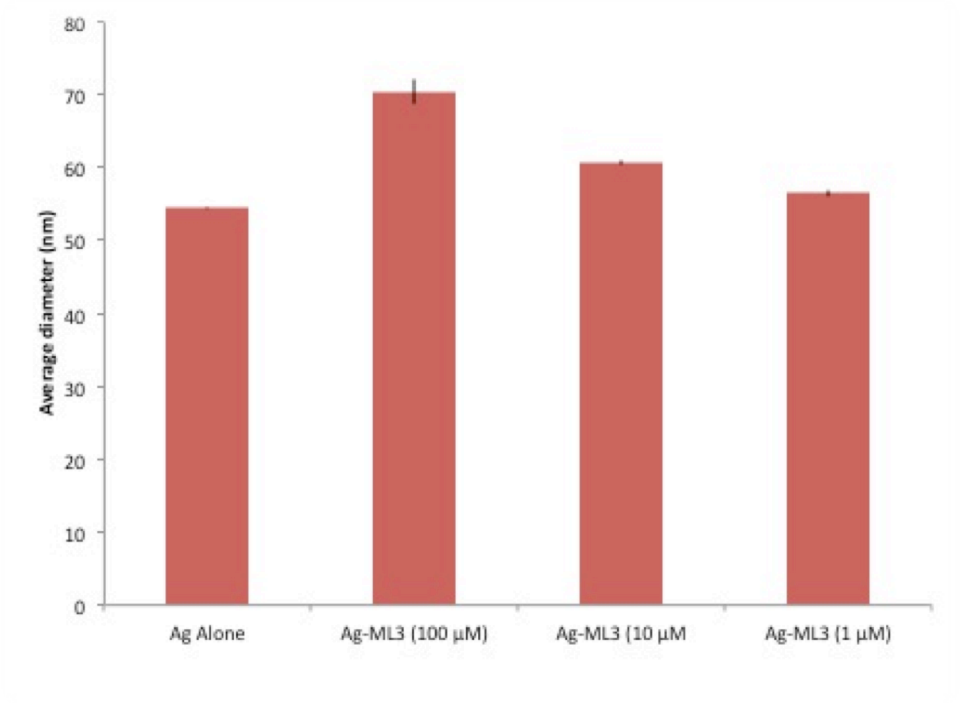

Figure 4.9 DLS data measured for AgML3 conjugates at varied linker conjugations

In comparison to the results obtained for Au-ML3 conjugates, Ag-ML3 conjugation was also optimised at a 1µM concentration. The DLS data for Au-ML3 conjugates at this concentration shows a greater increase in size, 5.3 nm, in comparison to the size increase shown by Ag-ML3 conjugates. This is believed to be due to a higher degree of surface coverage of ML3 linker molecules being present on the Au nanoparticle surface due to the favourable interaction between the thiol of ML3 and the Au surface. Although the surface coverage appears to be less for Ag nanoparticles, this was not of concern as the nanoparticles are also to be functionalised with a Raman reporter molecule, which would fill any vacant spaces on the nanoparticle surface.

4.4.3 Mixed monolayer stability of ML3 conjugates

To decrease any non-specific binding and to ensure the nanoparticle has monolayer surface coverage it was necessary to select a Raman reporter molecule which would bind irreversibly to the nanoparticle surface. For Au nanoparticles malachite green isothiocyanate (MGITC) was chosen as it binds to the nanoparticle surface *via* the isothiocyanate group present and is bound in a specific orientation which allows for reproducible SERS measurements to be obtained.[126,180] Figure 4.10 shows the structure of MGITC and the corresponding peaks obtained when analysed at a 633 nm excitation wavelength.

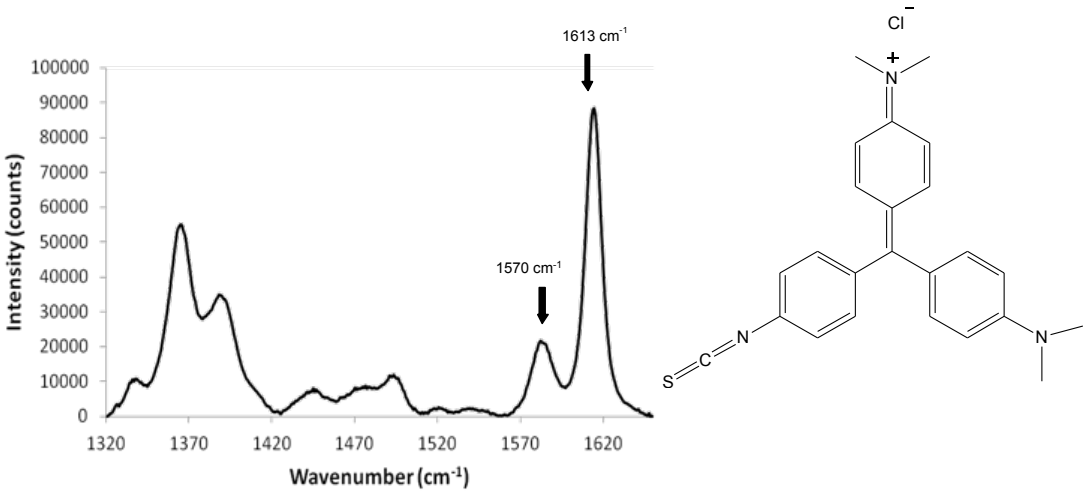

Figure 4.10 SERS spectra of AuML3 conjugates with a MGITC reporter molecule attached. SERS spectra obtained using a 1 second exposure with 10 accumulations using a 633 nm excitation wavelength.

The peaks of interest of MGITC are at 1570 cm^{-1} which is attributed to the aromatic ring stretches and 1613 cm^{-1} which is attributed to ring breathing and C=N vibrations.[73] To ensure the glyconanoparticles remained stable upon addition of the dye two different concentrations of dye were tested. These results are shown in table 4.5 and figure 4.11.

Table 4.5 Extinction results for AuML3 conjugates with MGITC attached at varied concentrations.

Sample	λ_{max} (nm)	Extinction (au)
Au Colloid (Batch 7)	530	0.860
Au-ML3 Conjugate (MGITC 1 μM)	530	0.623
Au-ML3 Conjugate (MGITC 0.02 μM)	528	0.729

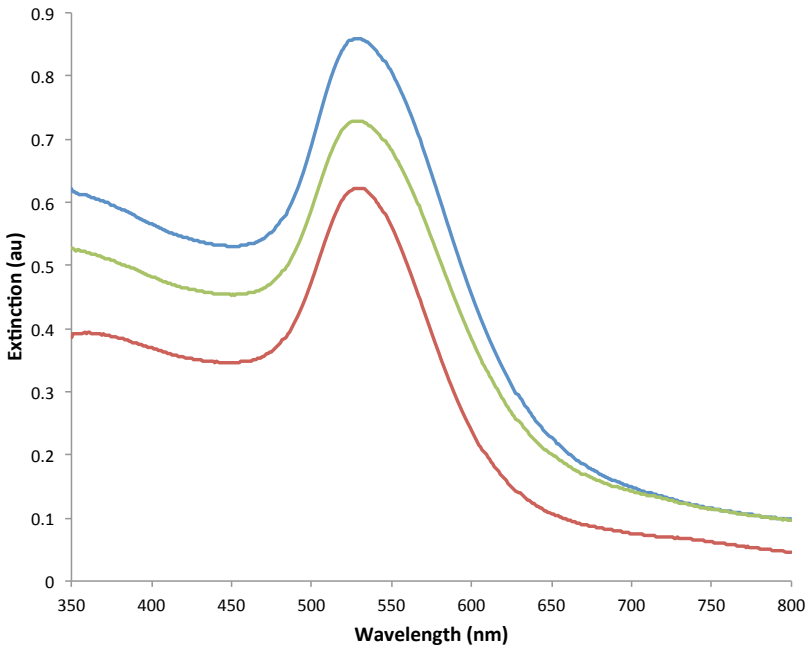

Figure 4.11 Extinction measurements of AuML3 conjugates following the addition of malachite green isothiocyanate (MGITC). AuCitrate (blue), AuML3 with 1 μM MGITC (red) AuML3 with 0.02 μM MGITC (green)

Analysis by extinction spectroscopy shows that both concentrations appear stable, however, addition of dye at a concentration of 0.02 μM produces an extinction band with a higher extinction, which indicates this to be the most stable of the two concentrations. Subsequent Au ML3 conjugates were prepared using this concentration of MGITC.

For Ag ML3 conjugates the Raman reporter molecule chosen was an in house synthesised benzotriazole dye known as RB1. Figure 4.12 shows the structure of the RB1 molecule and the characteristic SERS spectra obtained following analysis using a 514.5 nm excitation wavelength.

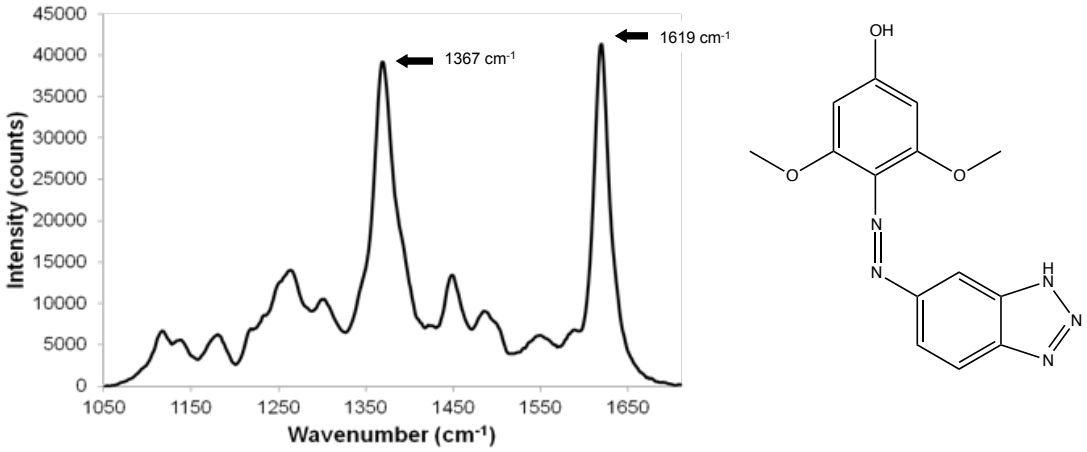

Figure 4.12 SERS spectra of AgML3 conjugates with RB1 attached. SERS spectra obtained using a 1 second exposure and 10 accumulations using a 514.4 excitation wavelength.

From previous studies, it has been established that at a concentration of 1 μM RB1 has established full monolayer coverage on the surface of Ag nanoparticles.[136] To confirm the stability of AgML3 conjugates using this concentration of RB1 samples were prepared and analysed by extinction spectroscopy. Table 4.6 and figure 4.13, show that as expected the nanoparticles do not aggregate upon addition of RB1 at this concentration.

Table 4.6 Extinction spectroscopy results for Ag citrate nanoparticles when functionalised with a final concentration of 1 μM RB1.

Sample	**λ_{max}**	**Extinction (au)**
Ag colloid Batch 1	413	0.88
Ag ML3 conjugate (RB1 1 μM)	414	0.68

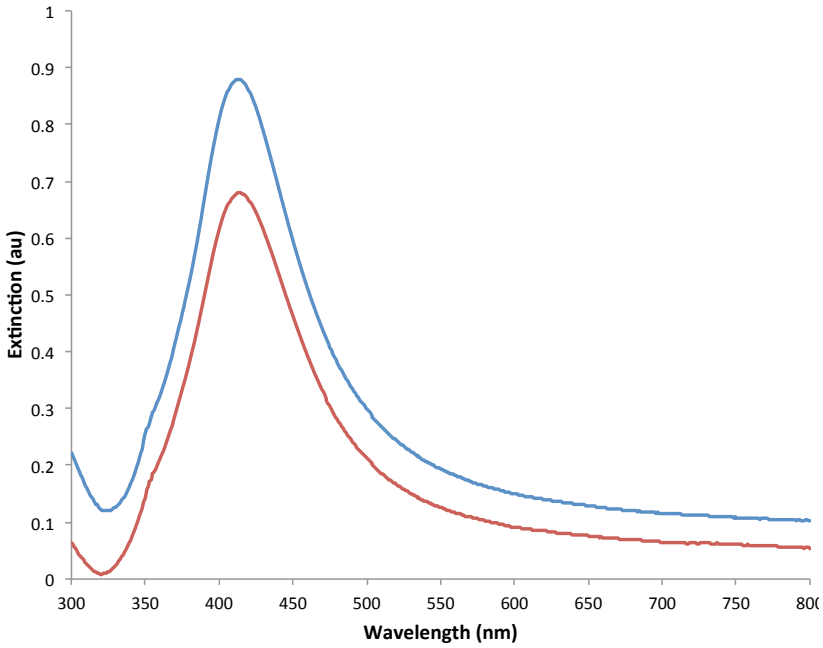

Figure 4.13 Extiction spectra of AgCitrate colloid (blue) and AgML3 following the addition of 1 μM RB1 (red).

Subsequent AgML3 conjugate samples were prepared with 1 μM RB1 for SERS analysis.

4.5 Lectin preparation

Due to affordability and prior knowledge, Con A was the lectin chosen for interaction with the glyconanoparticle conjugates prepared. As Con A has specificity towards glucose, it was expected to interact with the glucose moiety of the lactose linker. To confirm any possible interaction was occurring a negative control was required which had no established affinity to glucose. Peanut agglutinin, (PNA) is a galactose specific lectin and was expected to have little or no interaction with the prepared glyconanoparticles. As both of these lectins are tetrameric at physiological pH then it was expected that extensive aggregation would occur when present with glyconanoparticles functionalised with the respective sugars to which they are aligned.

4.5.1 Glyconanoparticle buffer testing

The stability of nanoparticle conjugates is typically dependent upon the media in which they are stored. In the presence of common aggregating agents such as spermine, poly-L-Lysine and high concentrations of salts such as sodium chloride and magnesium sulfate, nanoparticles undergo spontaneous and uncontrollable aggregation. To preserve the stability of the glyconanoparticles for as long as possible it was key to discover the correct buffering

media which allows the particles to remain stable but also allows the lectin Con A or PNA to remain at pH > 7 in their tetrameric form. There are many common buffers used in the study of biological interactions, therefore, using the most commonly reported the glyconanoparticle stability was tested in each buffer for any signs of aggregation commencing.

Table 4.7 Extinction spectroscopy results for AuML3 MGITC conjugates resuspended in various buffer conditions.

Sample	λ_{max} (nm)	Extinction (au)
Au Colloid (Batch 8)	529	0.760
Au-ML3 Conjugate (Borate 100 mM, pH 7.5)	529	0.603
Au-ML3 Conjugate (Phosphate 10 mM, pH 7.6)	529	0.542
Au-ML3 Conjugate (HEPES 10 mM, pH 7.5)	529	0.593
Au-ML3 Conjugate (HEPES 20 mM, pH 7.5)	528	0.413
Au-ML3 Conjugate (Tris 10 mM, pH 7.5)	528	0.576
Au-ML3 Conjugate (Tris 20 mM, pH 7.5)	524	0.318

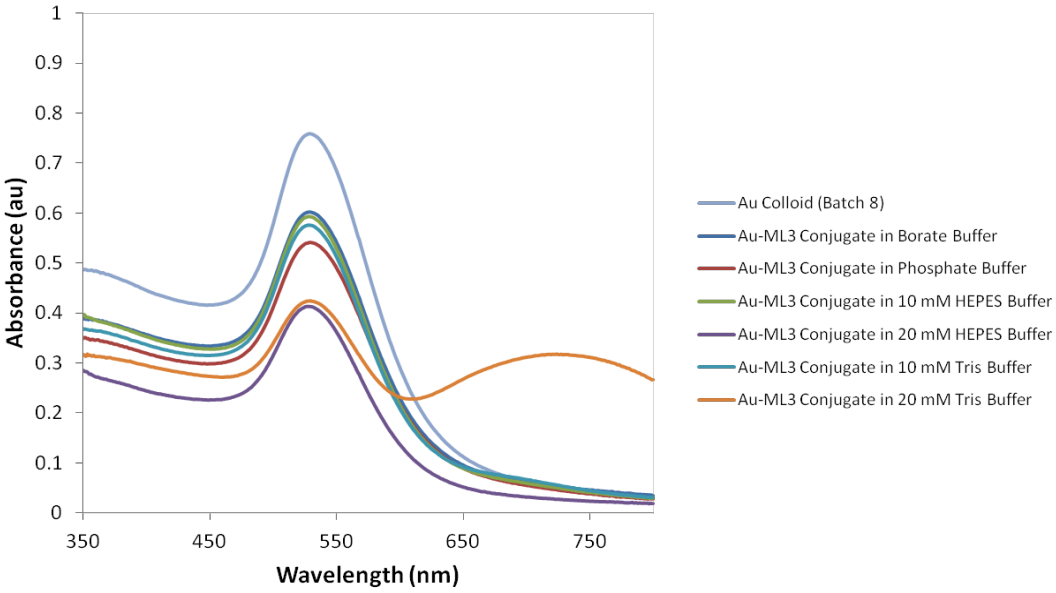

Figure 4.14 Extinxtion spectra of AuML3 conjugates resuspended in various buffer conditions

Table 4.7 and Figure 4.14, show that in all of the buffer solutions apart from 20 mM Tris and 20 mM HEPES buffer the glyconanoparticle solutions remained stable. In 20 mM Tris and 20 mM HEPES buffer it is concluded the salt concentration is too high in order for monodisperse nanoparticles to exist and as a result the nanoparticles have began to aggregate as indicated by the formation of a secondary peak at 675 nm and a significant dampening and broadening of the extinction band.

As previous studies of lectin carbohydrate interactions have used 10 mM Tris buffer it was decided that this buffer would continue to be used throughout these studies.[162]

4.6 Lectin aggregation studies monitored using extinction spectroscopy

Previous studies of glyconanoparticle interactions with lectins have utilised extinction spectroscopy to monitor the formation of nanoparticle aggregates when specific lectins are present. As a result, quantitative lectin measurements have been obtained in the nanomolar concentration region. Therefore, it was critical to establish a comparison between the Au and Ag ML3 nanoparticles synthesised previously and the studies currently in the public domain.

4.6.1 ConA and PNA AuML3 aggregation studies by extinction spectroscopy

Over a period of 16 hours, solutions of AuML3 were mixed with both 10 μM ConA and PNA. A control sample was prepared with no lectin present and these samples were analysed by extinction spectroscopy for 16 hours to detect the formation of nanoparticle aggregates.

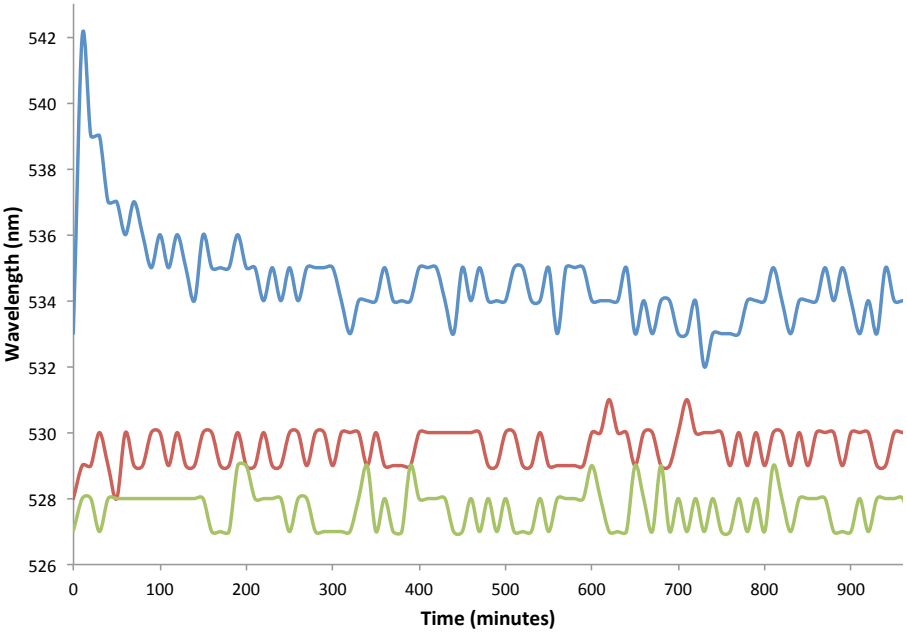

Figure 4.15 Extinction spectroscopy measurements of the change in maximum wavelength of AuML3 nanoparticles following the addition of ConA and PNA over time. AuML3 only (green) AuML3 and ConA (blue) AuML3 and PNA (red)

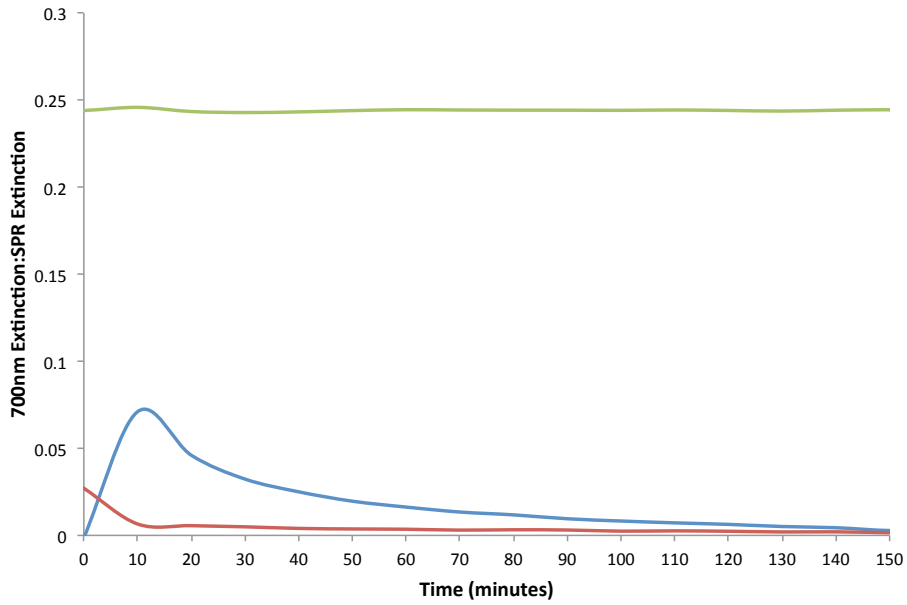

Figure 4.16 Ratio of the extinction spectroscopy measurements taken at 700 nm and at the λ_{max} wavelength of the AuML3 conjugates (λ_{max} = 528 nm) (green) and when in the presence of ConA (blue) and PNA (red) over time.

As shown by Figure 4.15, there was an initial red shifting of the AuML3 conjugates in the presence of 10 μM ConA from 528 nm to 542 nm before decreasing over time. This signifies an initial aggregation caused by the interaction of AuML3 with ConA before the sedimentation of these particles from solution resulting in only a small number of aggregated particles being present, which show a λ_{max} of 538 nm. This conclusion was confirmed by ratioing the extinction achieved at the λ_{max} of the surface plasmon resonance peak to the extinction measured throughout the study at 700 nm. It was decided that the ratio would be to 700 nm as in this area the formation of nanoparticle aggregates and small clusters results in the appearance of a secondary SPR band. It can be clearly identified from figure 4.16, that when ConA is added there was a sharp increase of this ratio over an initial 20 minute time period due to aggregation of the nanoparticles with ConA before a sustained period of decline due to the sedimentation of these particles from solution. In contrast, and as expected, the AuML3 particles mixed with 10 μM PNA exhibit no signs of aggregation when either data set was analysed.

4.6.2 ConA and PNA AgML3 aggregation studies by extinction spectroscopy

Subsequently a similar study was performed for the AgML3 glyconanoparticle conjugates using identical conditions as previously used.

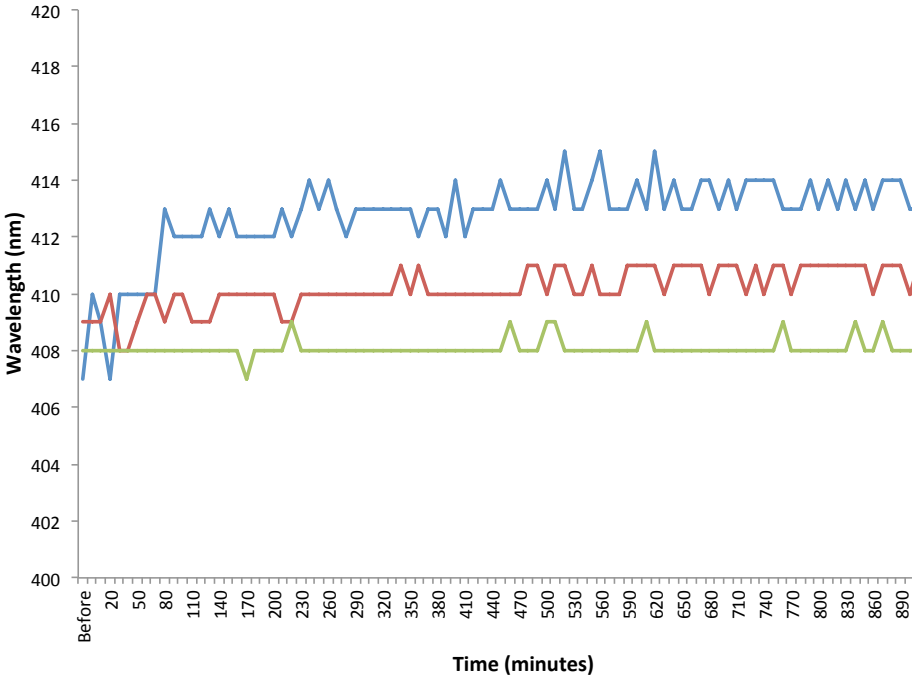

Figure 4.17 Extinction spectroscopy measurements of the change in maximum wavelength of AgML3 nanoparticles following the addition of ConA and PNA over time. AgML3 only (green) AgML3 and ConA (blue) AgML3 and PNA (red)

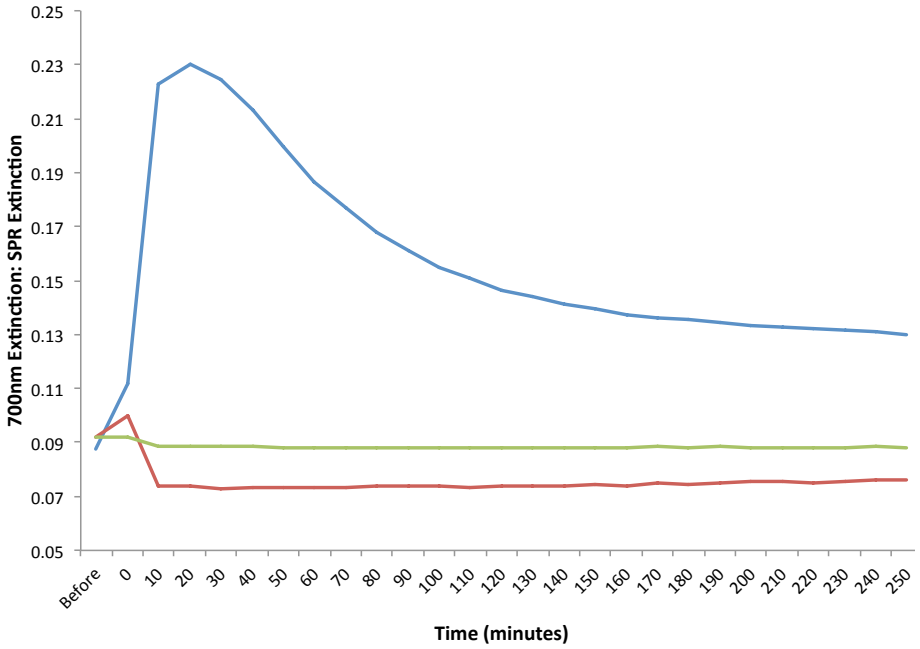

Figure 4.18 Ratio of the extinction spectroscopy measurements taken at 700 nm and at the λ_{max} wavelength of the AgML3 conjugates (λ_{max} = 407 nm) (green) and when in the presence of ConA (blue) and PNA (red) over time.

Similar results were obtained as for the AuML3 studies and the data is shown in figure 4.17 and 4.18. When analysing the maximum wavelength for the SPR band of the AgML3 conjugates mixed with 10 μM ConA a significant red shifting occurs from 407 nm to 414 nm indicating aggregation of the particles had occurred. This is in contrast to the samples mixed with PNA and those with no lectin present which remain constant over time with slight changes due to instrumental error. To validate these conclusions the change in extinction ratio was also calculated over time and once again, a significant increase in extinction ratio from 0.09 to 0.23 over the first 30 minute period indicates the nanoparticles mixed with Con A are aggregating during this time frame. The subsequent decrease in absorbance ratio was again thought to be due to sedimentation of the nanoparticles from solution. AgML3 particles mixed with PNA show an initial decrease to 0.07 before remaining constant over the rest of the time period indicating aggregation had once again failed to occur.

It can be concluded that the system created using the linker ML3 attached to Au and Ag nanoparticles can be used in a similar manner to quantitatively detect the concentration of Con A present within a solution.

4.6.3 Quantitative detection of Con A using extinction spectroscopy

Previous studies have shown that a linear relationship between the concentration of Con A and the detectable range of aggregation of glyconanoparticles can be studied using extinction spectroscopy.

To test the hypothesis a concentration study was performed to enable the calculation of a limit of detection for the glyconanoparticle system created using the AgML3 conjugates.

4.6.3.1 AgML3 and ConA LOD study using extinction spectroscopy

As shown *via* previous studies the most accurate indicator of aggregation occurring when using extinction spectroscopy is the ratio of the extinction of the SPR band and the extinction at 700 nm, as at 700 nm a formation of a secondary SPR band occurs due to the clustering of nanoparticles to form aggregates. AgML3 samples were prepared and mixed with varied concentrations of Con A and the extinction measurements recorded. In order to ensure the measurements were as accurate as possible this process was repeated 5 times for each concentration of Con A. Figure 4.19 shows that a linear range of detection was achieved from which the limit of detection (LOD) for Con A was calculated, as by calculation in section 9.15, to be 78 nM. In comparison to previous studies the LOD value is similar to those previously obtained in comparable studies using extinction spectroscopy.[162,181]

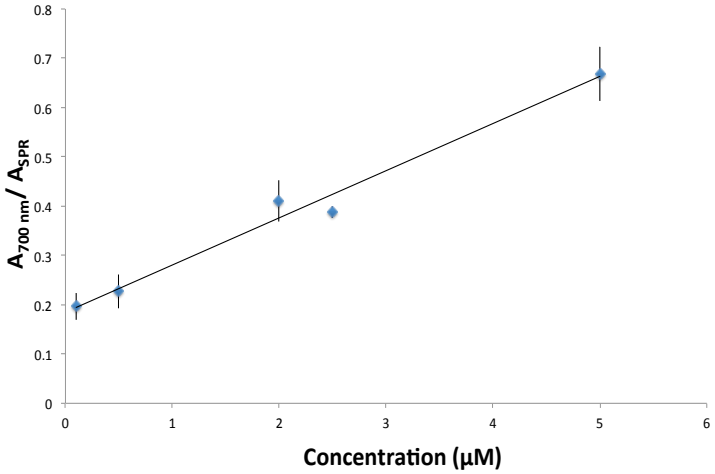

Figure 4.19 Linear range of detection obtained by plotting the ratio of the extinction spectroscopy measurements taken at 700 nm and at the λ_{max} wavelength of the AgML3 (λ_{max} = 410 nm) conjugates plotted against the concentration of Con A present.

4.7 DLS glyconanoparticle aggregation studies

To corroborate the extinction spectroscopy results analysis was performed using DLS to monitor the change in size of the nanoparticles due to their coupling and formation of aggregate structures when interacting with Con A. Various concentrations of Con A were tested to establish a relationship between lectin concentration and the size of nanoparticle clusters formed.

Table 4.8 DLS data obtained for AgML3RB1 conjugates in the presence of varying concentrations of ConA to monitor the formation of aggregates over a 1 hour time period.

Time (min)	No ConA (nm)	5 µM ConA (nm)	2.5 µM ConA (nm)	1 µM ConA (nm)	0.1 µM ConA (nm)	0.01 µM ConA (nm)	1 nM ConA (nm)	0.1 nM ConA (nm)
Before	***55.9***	56.5	58.8	56.0	55.9	55.9	60.7	***55.9***
0	55.7	***173.5***	***370.3***	810.6	940.6	218.8	63.0	55.8
9	54.6	166.3	352.5	***940.0***	1528.3	250.5	63.4	55.5
18	53.4	158.6	322.0	660.4	***1786.7***	284.1	64.3	55.5
27	53.6	154.6	290.5	445.3	1572.0	***294.1***	64.2	55.7
36	52.7	152.8	273.8	335.8	1587.7	282.8	64.6	55.4
45	51.8	191.7	262.1	265.4	1296.7	259.8	64.4	55.4
54	55.5	156.4	245.9	230.3	1284.0	243.6	***64.6***	55.3
63	55.5	156.7	247.7	219.5	1096.7	NA	64.5	55.8

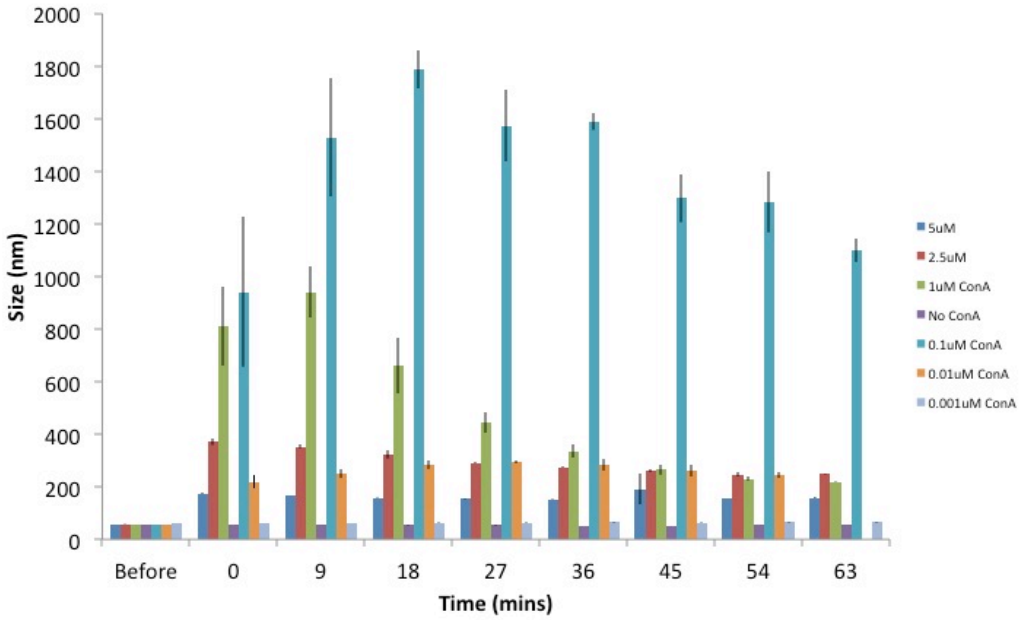

Figure 4.20 DLS data obtained for AgML3RB1 conjugates in the presence of varying concentrations of ConA to monitor the formation of aggregates over a 1 hour time period.

In accordance with the DLS data obtained, shown in table 4.8 and figure 4.20, when ConA is added within the concentration range of 5 μM to 1 nM an immediate increase in nanoparticle size occurs followed by a subsequent period of stabilization of the size of the particles in which the general trend in size does not change. Previous studies of nanoparticle aggregate formation have documented similar trends.[82,182] Upon interaction with the Con A in solution, a number of dimers and trimers will have formed to the detriment of individual nanoparticles. These small clusters continued to form until a number of them began to aggregate together to form larger nanoparticle assemblies. At high concentrations of Con A the formation of these small nanoparticle clusters occurred at an increased rate, in comparison to low ConA concentrations, which resulted in the formation of larger nanoparticle assemblies. The size of these larger nanoparticle assemblies continued to increase over time until they began to sediment from solution. This explains the trend of increasing concentration followed by a period of stability before the cluster size began to decrease because of the larger assemblies sedimenting from solution. These results can be correlated to those obtained for extinction spectroscopy measurements which show broader and weaker plasmon excitations due to the formation of these larger aggregate clusters at high lectin concentrations. Therefore, at high concentrations of ConA aggregation of the nanoparticles mediated by the interaction of lactose and ConA was difficult to control. At low ConA concentrations nanoparticle aggregate formation appeared to be limited over time. The formation of small nanoparticle

clusters in form of dimers and trimers will have occurred at a slower rate when a smaller number of ConA molecules were present. Due to limiting of dimer and trimer formation, larger aggregate clusters are prevented from forming at the same rate as for higher ConA concentrations. This explains why in the presence of lower concentrations of ConA the extinction profiles of these solutions have a more intense and narrower plasmon band.

At a concentration of 0.1 nM ConA there is no distinguishable change in the average nanoparticle size, which infers that the aggregation process is not detectable at this concentration using DLS as it may be outwith the detection range of this apparatus. In comparison to the extinction spectroscopy data obtained it is apparent that aggregation is still occurring at concentrations below those used for this study.

To validate these findings the same analysis was performed for AgML3 samples in the presence of the negative lectin control PNA. Again, varied concentrations of PNA were added to the nanoparticle solutions and their size was monitored over time.

Table 4.9 DLS data obtained for AgML3RB1 conjugates in the presence of varied PNA concentrations over a period of 40 mins

Time (min)	No PNA (nm)	100 nM PNA (nm)	10 nM PNA (nm)	1 nM PNA (nm)
Before	55.9	55.9	57.7	47.6
0	55.7	55.0	57.2	47.4
9	54.6	54.9	56.5	47.5
18	53.4	54.9	57.7	47.3
27	53.6	54.5	56.5	46.9
36	52.7	54.6	53.4	47.3

The sizing data for this study, as shown in table 4.9, as expected shows no dependence on concentration of PNA in terms of the average size of the nanoparticles. Thus, PNA has no detectable interaction with the AgML3 conjugates.

4.8 SERS Studies of AuML3 and AgML3 conjugates

SERS measurements were performed in the presence of both lectins for both AuML3 and AgML3 conjugates. The results obtained were normalized using the cyclohexane standard intensity to allow for comparison between results obtained on different days.

4.8.1 SERS analysis of AuML3 conjugates with ConA and PNA

For AuML3 studies, the intensity of MGITC peak at 1613 cm^{-1} was monitored at 633 nm to establish any trend in aggregation occurring. A concentration of 5 µM ConA and PNA was chosen as from the extinction spectroscopy and DLS studies aggregation was detectable at this concentration.

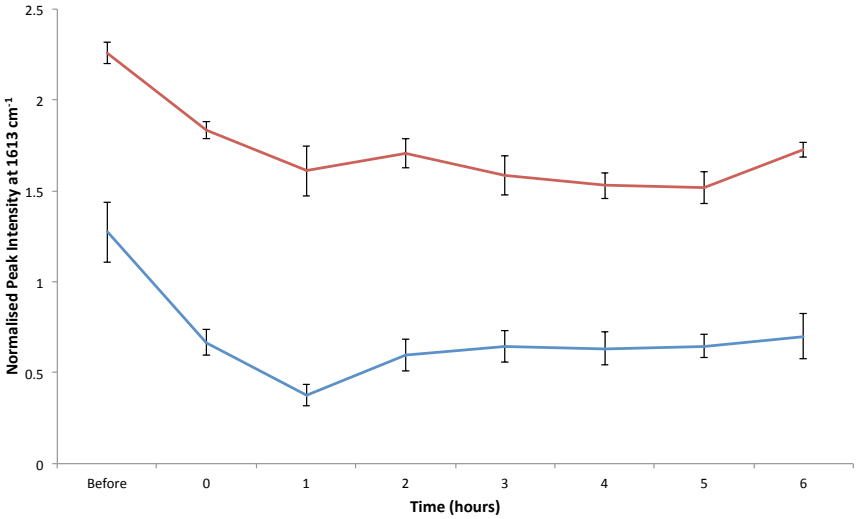

Figure 4.21 Average change in normalised intensity at 1613 cm^{-1} over time for 5 replicates AuML3MGITC conjugates when in the presence of 5 µM PNA (red) and 5 µM ConA (blue). Error bars shown are the the standard deviations obtained from 5 replicate measurements.

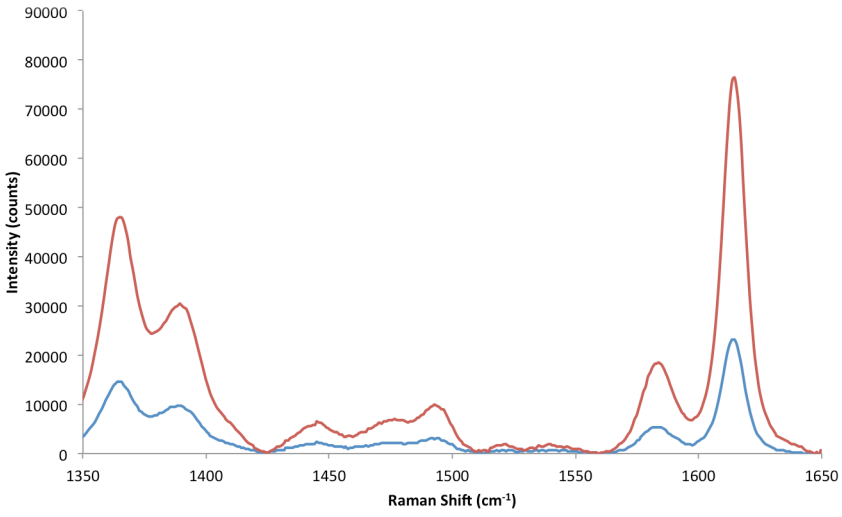

Figure 4.22 Average SERS intensity measured for 5 replicate samples of AuML3MGITC prior to ConA addition (red line) and after 1 hour in the presence of 5 µM ConA (blue line)

As shown in figures 4.21 and 4.22 unpredictably the signal intensity does not appear to increase upon aggregation occurring when ConA is added to solutions of AuML3. In fact, there is a decrease in signal intensity following the addition of both lectins but more significantly for ConA rather than PNA. After the first hour the signal intensity stabilises and begins to slightly increase by hour 6 for the ConA samples, however, this increase was not significant, as the initial intensity was still greater than the intensity achieved at this time point. To overcome this problem the concentration of MGITC on the nanoparticle surface was increased from 0.02 μM to 1 μM, the results obtained are shown in figures 4.23-4.25 respectively.

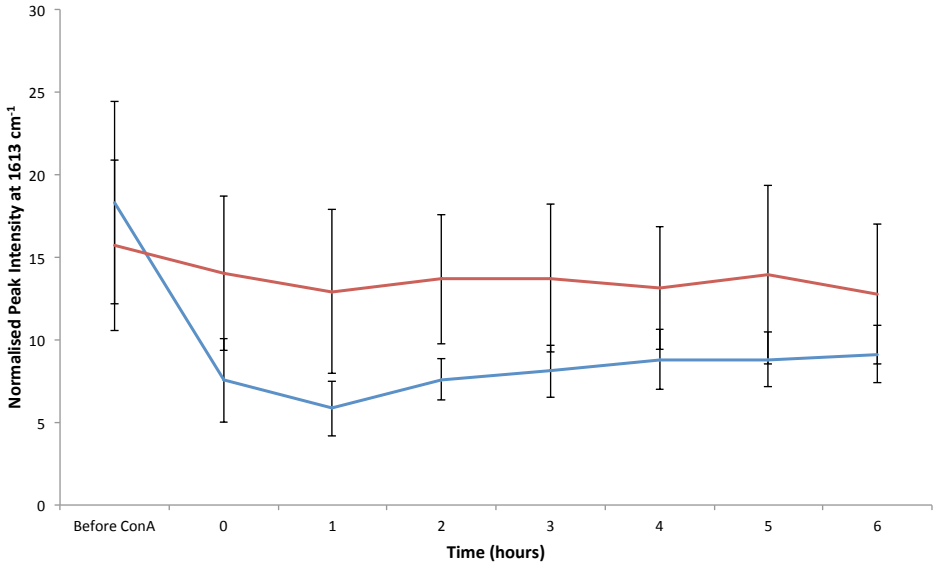

Figure 4.23 Average change in normalised intensity at 1613 cm^{-1} over time for 5 replicates AuML3MG conjugates when in the presence of 5 μM PNA (red) and 5 μM ConA (blue). Error bars shown are the the standard deviations obtained from 5 replicate measurements.

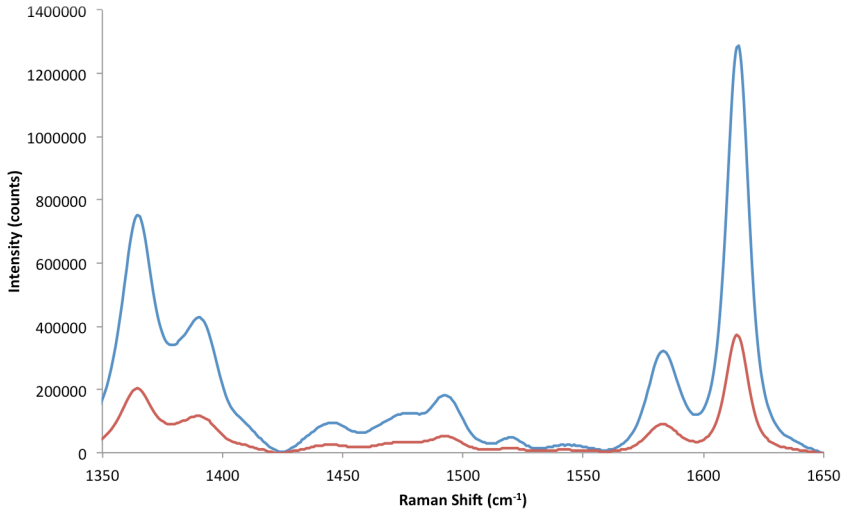

Figure 4.24 Average SERS intensity measured for 5 replicate samples of AuML3MGITC prior to ConA addition (blue line) and after 1 hour in the presence of 5 µM ConA (red line)

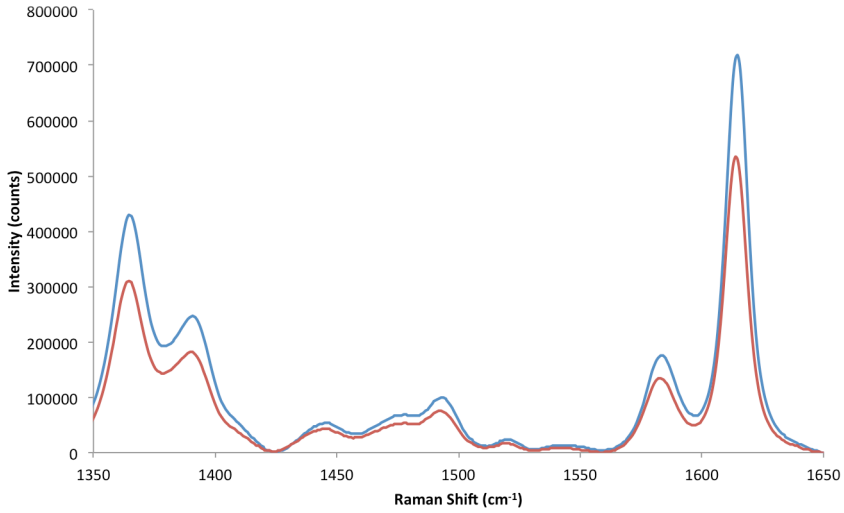

Figure 4.25 Average SERS intensity measured for 5 replicate samples of AuML3MGITC prior to PNA addition (blue line) and after 1 hour in the presence of 5 µM PNA (red line)

After the increase in concentration of MGITC the experiment was repeated, however, significant statistical errors occurred for each measurement. This could be caused by a decrease in nanoparticle stability upon the increase in dye concentration. As a result, it was concluded that analysis at this concentration of MGITC was not possible and no further analyses were made of AuML3 particles using SERS.

A similar experiment was conducted at 514.5 nm for AgML3 nanoparticles with 5 µM ConA and PNA added and the SERS intensity of the RB1 peak 1619 cm^{-1} was monitored over a period of 3 hours.

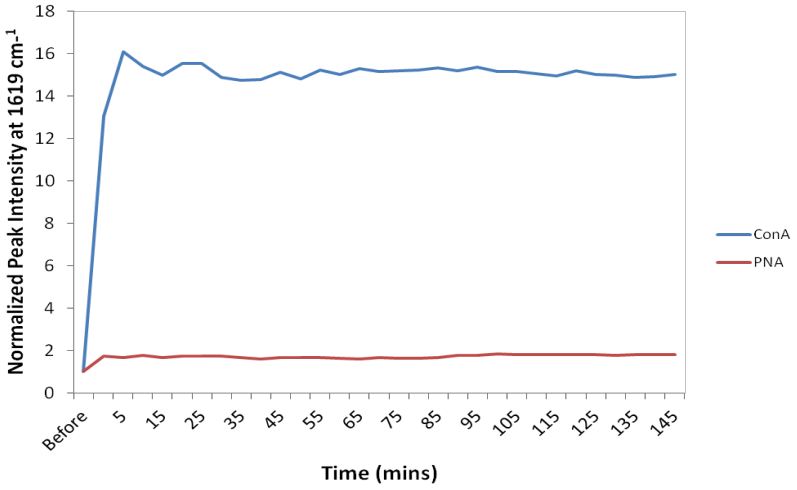

Figure 4.26 Normalised intensity of AgML3RB1 conjugates in the presence of 5 µM ConA and PNA. SERS spectra obtained at 514.4 nm using a 1 second exposure with 10 accumulations.

From figure 4.26 the initial increase in SERS intensity obtained when the AgML3 conjugates were mixed with Con A can be attributed to the formation of nanoparticle dimers and trimers from poorly enhancing monomeric particles. A plateau in signal intensity was quickly reached following the incorporation of these clusters into larger nanoparticle assemblies. The slow decrease in SERS intensity, which then occurred, was due to a decrease in cluster density present in the interrogation volume of the laser. As previously studies discovered, the formation of large nanoparticle assemblies does not correlate to an increased SERS performance.[183] A small increase in SERS intensity occurs upon the addition of PNA, which is attributed to non-specific binding having occurred producing a small number of nanoparticle clusters. However, upon comparison the increase in SERS intensity in the presence of PNA is insignificant to that obtained when ConA was present.

To clarify these results AgML3 conjugates were prepared and mixed with 5 µM ConA and PNA for 10 mins then analysed by SERS. This period was chosen as it was when the most significant increase in SERS intensity occurred. When these solutions were analysed and compared to AgML3 solutions with no ConA or PNA present it was concluded that aggregation had only occurred for the samples mixed with ConA as indicated by the observed spectra shown in figures 4.27 and 4.28.

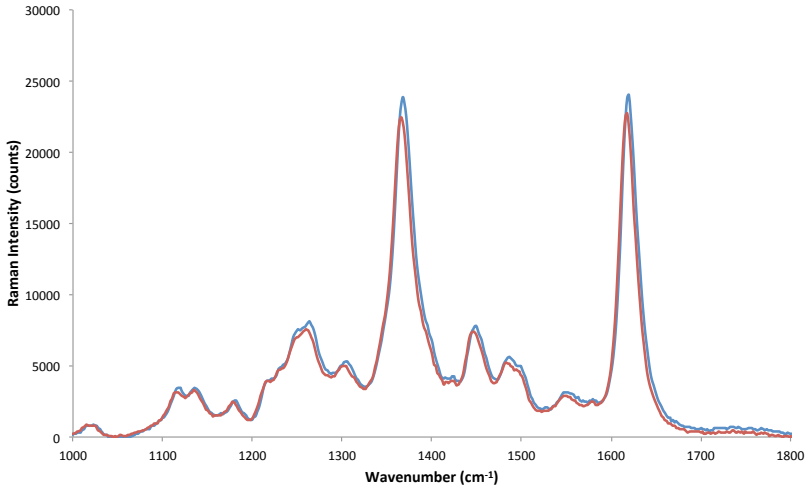

Figure 4.27 SERS spectra obtained using a 514.5 nm excitation wavelength with a 1 second exposure with 10 accumulations. AgML3 samples were analyses in the presence of no PNA (blue line) and 5 μM PNA (red line).

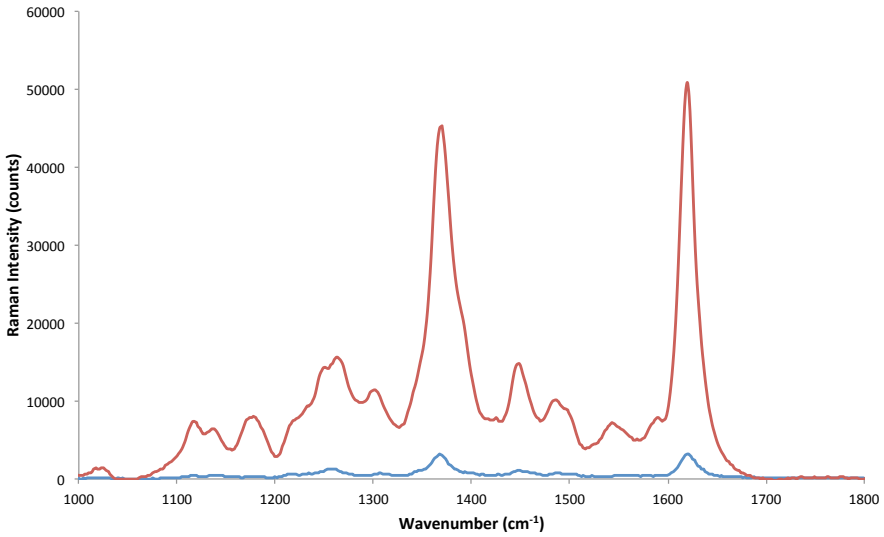

Figure 4.28 SERS spectra obtained using a 514.5 nm excitation wavelength with a 1 second exposure with 10 accumulations. AgML3 samples were analyses in the presence of no Con A (blue line) and 5 μM Con A(red line).

One of the main advantages of SERS is the extra sensitivity afforded in comparison to the other optical detection techniques. To prove this experimentally an LOD study was performed using SERS. AgML3 samples were prepared and mixed with varying concentrations of ConA then analysed by SERS.

According to the linear range of data obtained the LOD for these results, as shown in figure 4.29 and table 4.10, was 40 pM. This level of sensitivity currently remains unrivalled by other similar spectroscopic studies of such interactions.

Table 4.10 SERS intensity measurements obtained for 5 replicate AgML3RB1 samples in the presence of varied ConA concentration as shown.

ConA Concentration (nM)	Normalised 1619 cm^{-1} Peak Intensity
0	0.70 ± 0.040
5	13.29 ± 2.158
1	3.33 ± 0.504
0.5	2.12 ± 0.137
0.1	0.96 ± 0.033
0.05	0.84 ± 0.034

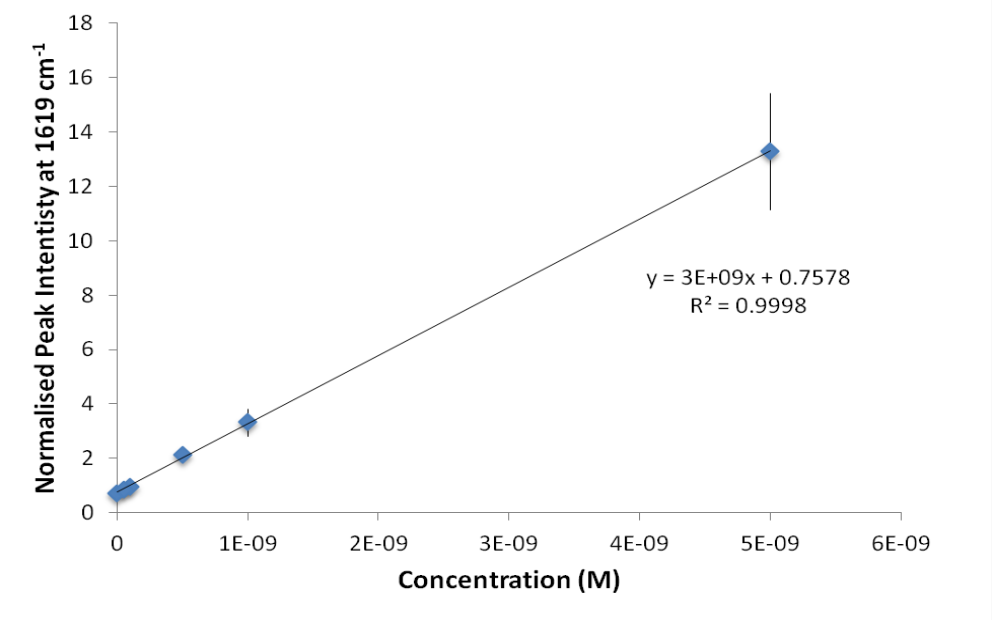

Figure 4.29 Linear range of detection obtained *via* plotting the intensity of the AgML3RB1 samples against the concentration of ConA present.

Scanning electron microscopy (SEM) images of the nanoparticles aggregated in the presence of various concentrations of ConA are shown in figure 4.30. Samples were also prepared at the LOD of 40 pM ConA to confirm the formation of aggregates occurs at this concentration.

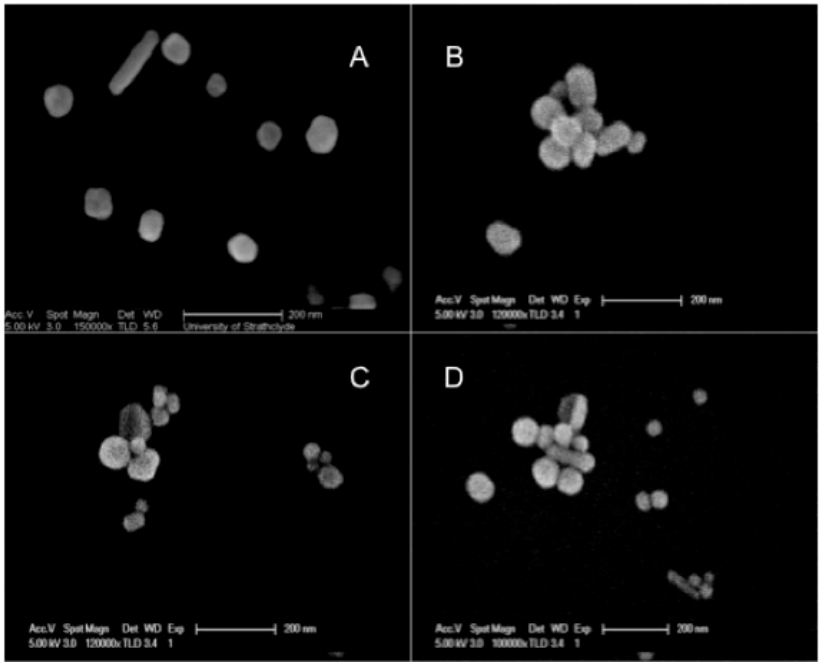

Figure 4.30 Comparison of SEM images of templated aggregate assembly with various concentrations of ConA (A) No ConA present (B) 10 μM ConA (C) 5 μM ConA and (D) 40 pM ConA

4.9 Mannose reversibility studies of ConA induced aggregation

As ConA is known to have a greater affinity towards mannose in comparison to its affinity shared with glucose then it was hypothesised that the formed nanoparticle assemblies could be reversed to monodisperse particles due to the presence of free mannose in the solution.

AgML3 conjugates were aggregated with 2 μM ConA followed by the addition of 100 μL of 0.3 mM mannose solution and the extinction properties of the conjugates monitored over time. As can be seen by figure 4.31, following the addition of free mannose to the aggregated conjugates, the significantly red shifted glyconanoparticles began to blue shift. This trend was replicated when the extinction measurements were analysed with a significant increase in the extinction of the SPR band occurring indicating the dampening effect was being reversed.

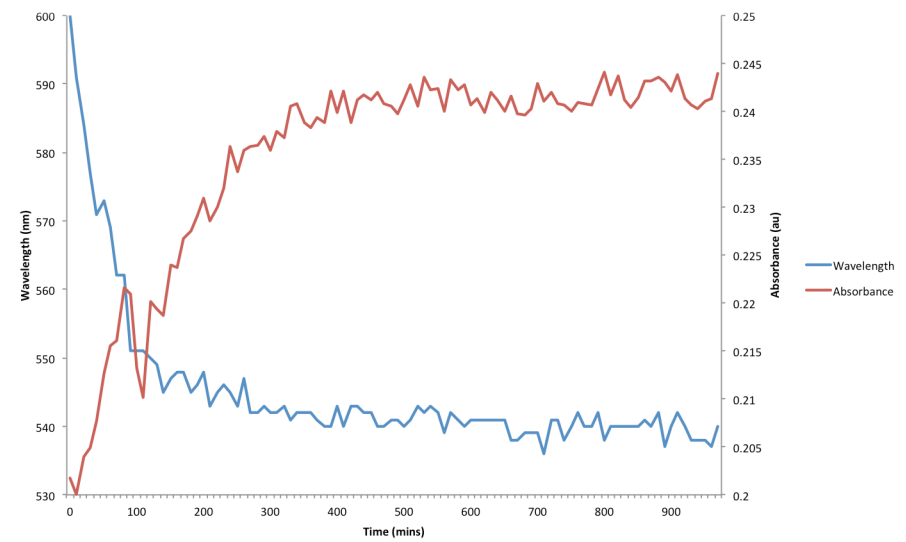

Figure 4.31 Change in extinction properties of ConA aggregated AgML3 conjugates in the presence of 0.3 mM mannose. Wavelength (blue) Extinction (red)

A similar study was also performed using SERS analysis to detect if the aggregation process was reversible. Analysis of the intensity of the RB1 peak at 1619 cm^{-1} over time, as shown in figure 4.32, showed that in the presence of free mannose the intensity of the peak decreases rapidly to a similar intensity level of the non-aggregated AgML3 conjugates. Therefore, it was possible to conclude that due to the preferential interaction of ConA with mannose in comparison to glucose, it was possible to reverse the formation of the nanoparticle aggregates. Following both the extinction spectroscopy and SERS studies the reversed aggregation solutions were purified by centrifugation and it was possible to remove the bound ConA mannose complex producing free monodisperse AgML3 glyconanoparticles which can be reused for future analyses.

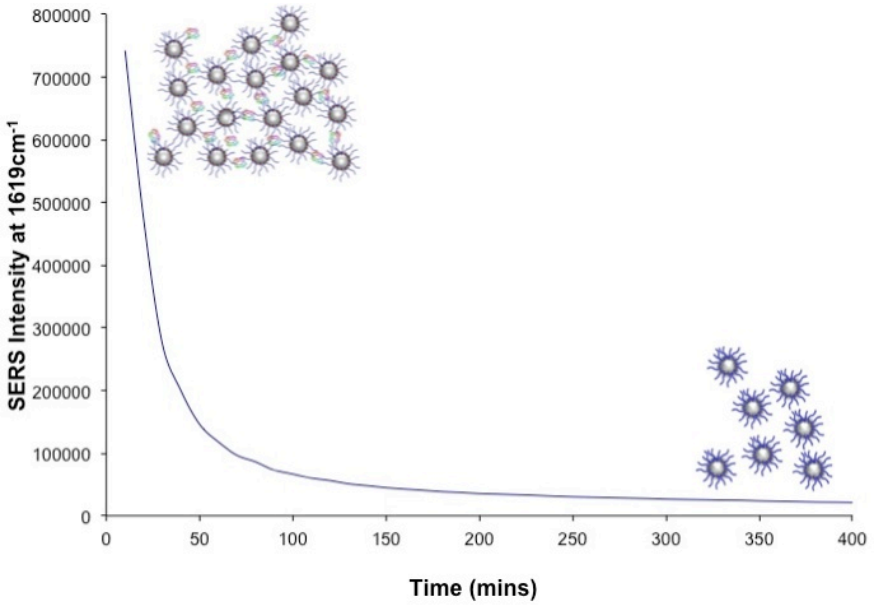

Figure 4.32 Analysis of the reversibility of ConA aggregated AgML3 conjugates in the presence of 0.3 mM mannose as monitored *via* the change in intensity of the 1619 cm^{-1} peak of RB1.

4.10 Conclusions

Using a simple but elegant approach, a novel carbohydrate linker ligand has been synthesised for the functionalisation of both gold and silver nanoparticles. Studies from the literature aided the design of this ligand and highlighted the essential requirement of a short spacer unit in order to increase nanoparticle surface density and to encourage interactions to occur close to the nanoparticle surface. An increased surface density of ligand also overcame the main requirement of the creation of a multivalent scaffold to increase the weak binding affinities of carbohydrate-protein interactions.

An assay has been developed by which the interactions of individual carbohydrates with lectins can be detected within solution. Analysis of such interactions has been undertaken by extinction spectroscopy where a detection limit of 78 nM was achieved that was in the region of the previous detection limit obtained by a fellow research group. This indicated that this approach to carbohydrate-lectin interactions was on a comparable scale to studies already published.

This assay was then extended to SERS analysis *via* the conjugation of a surface complexing benzotriazole dye to the nanoparticle surface, which provided reproducible analysis. Analysis of the carbohydrate-protein interactions using SERS has achieved a detection limit of 40 pM which is unparalled by any comparative spectroscopic technique including dynamic light scattering, extinction spectroscopy and fluorescence spectroscopy. Thus demonstrating a significant increase in sensitivity was gained when using SERS for the analysis of biological interactions.

4.11 Future Work

The future work for this research would be to extend the functionalisation of these nanoparticle species to a multiplexed detection assay utilizing various carbohydrate-lectin interactions. Research towards achieving such a multiplexed assay is detailed in chapter 5.

5. Multiplexed detection of carbohydrate protein interactions

The field of bioanalysis is focused upon the detection of biomolecules such as DNA, enzymes and proteins within complex biological matrices. Currently, the methods used to analyse these materials are reliant upon the separation and purification of individual components from both the matrix and from each other prior to analysis. Major disadvantages of such processes are the loss or dilution of the analytes to be detected and the complexity and cost of the processes by which they are isolated. To overcome these problems it is desirable to be able to successfully detect multiple analytes simultaneously and overcome the need for separation of each individual component from biological matrices. The discernable detection of multiple analytes is a key advantage of SERS in comparison to other spectroscopic techniques currently available. The most common method used for biological detection is fluorescence spectroscopy, which is disadvantageous due to the broad nature of the emission spectra of each analyte causing significant overlap when multiple analytes are being targeted. Using SERS a wealth of information is gained from the information rich vibrational spectra of each analyte resulting in the increased possibility of successful analyte detection within biological matrices.[184]

The multiplexing capabilities of SERS have been exploited primarily in the fields of DNA and protein detection. One approach adopted was the solution-based detection of DNA, which makes use of DNA functionalised nanoparticles, which have been aggregated using a sequence specific hybridization event to 'turn on' the SERRS signal *via* the controlled assembly of DNA functionalised particles into aggregates. By coding each set of DNA functionalised nanoparticles with a different sequence of DNA and a different dye label the presence of two different DNA target sequences was distinguishable by the absence or presence of the SERRS spectra of the dye present on the corresponding labeled nanoparticle set. The aggregation event caused a large increase in the electromagnetic field strength and the SERRS intensity of the corresponding dye.[185] Graham *et al*. were also the first to report the use of SERS multiplexing for DNA genotyping. Using a combination of an amplification refractory mutation system (ARMS) approach with SERS the cystic fibrosis trans membrane conductance regulator (CFTCR) gene was detected in each of the three formats it presented in. Labeled primers were incorporated into the PCR product and the mutational status of each of these particular samples was able to be determined.[186] SERS multiplexing has also been exploited for DNA detection in various DNA assay formats. One example of this being

the approach by Irudayaraj and co-workers who used non-fluorescent Raman reporter molecules to achieve a multiplex detection system for the detection of alternative splicing junctions of the breast cancer susceptibility gene 1 (BRCA1). Each nanoparticle was coded with a different reporter molecule and a specific target sequence then only in the presence of both the target and appropriate capture sequence were the nanoparticles captured onto a surface *via* a sandwich hybridization assay.[187,188]

The SERS multiplexed detection of proteins has been explored to a lesser extent than that of DNA. However, the two most common approaches to SERS protein multiplexes can be classified as either immunoassays or enzyme analysis. Recent developments have seen Porter and co-workers reporting a SERS immunoassay array format which detects pancreatic adenocarcinoma (PA) biomarkers with much greater sensitivity than the gold standard ELISA technique currently used.[189] Protein immunoassays typically use a capture substrate, which has been functionalised with different antibodies and specific reporter molecules. Specific antigens are then introduced and a response is only obtained through a bio recognition sandwich event involving the target antigen. This has been successfully utilised in a SERS format for the detection of four different antibody-antigen complexes, although, higher order multiplexing is reported to be difficult due to cross reactivity between the antibodies.[106]

To date there is currently a lack of reported research that explores the area of carbohydrate detection using a SERS based format. The work reported previously in chapter 4 showed the proof of concept of a SERS based assay, which utilised a 'turn on' SERS effect due to controlled nanoparticle formation *via* the specific interaction of carbohydrate functionalised particles and lectins. Expanding on this format the following work aimed to achieve multiplexed carbohydrate detection *via* multiple ''on'' ''off'' SERS binding events.

5.1 Synthesis of carbohydrate linker compounds

In order to attempt the multiplexing of this assay system a number of new carbohydrate functionalised linker compounds were synthesised for use as nanoparticle ligands.

5.1.1 Synthesis of MM1 and MG2 linkers

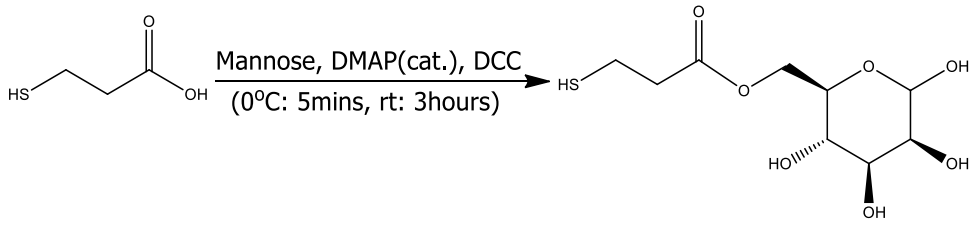

Scheme 5.1 Steiglich esterification of mannose using DMAP, DCC to obtain the mercaptopropionic functionalised mannose compound denoted as MM1.

Following the optimisation of a protocol for carbohydrate esterification as presented in section **4.3.1**, several further linkers were created. Scheme 1.5 and 1.6 present the experimental details for the synthesis of both short-chained mannose and galactose containing linkers respectively. Briefly, a Steiglich esterification of the respective sugar was performed to couple the carbohydrate to the thiol containing compound 3-MPA. This reaction proceeded *via* a carbodiimide intermediary and was catalysed via the use of DMAP to obtain the correct product. Following the synthesis of these compounds both ^{1}H NMR and MS analyses confirmed their structures.

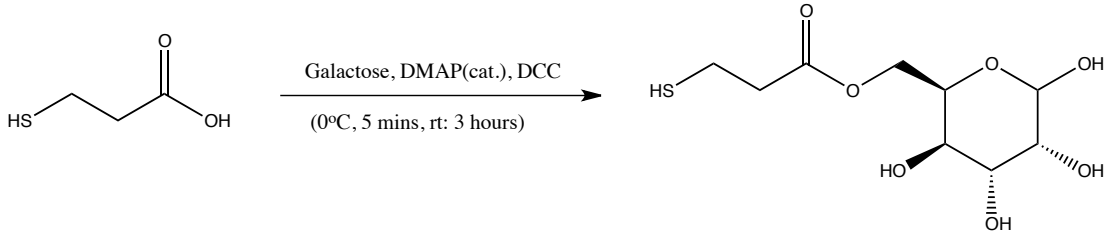

Scheme 5.2 Steiglich esterification of galactose using DMAP, DCC to obtain the mercaptopropionic functionalised galactose compound denoted as MG2.

5.1.2 Benedicts reagent testing

As in section **4.3.2**, the MM1 and MG2 linkers were both tested using Benedicts reagent to confirm the presence of the reducing sugar within the linker. Positive results were obtained for both linkers further confirming the success of the linker synthesis which is in accordance with the results obtained by both ^{1}H NMR and MS.

5.2 Nanoparticle – linker optimisation studies

As in section **4.4**, nanoparticle stability tests were performed to achieve the optimal linker concentration on the nanoparticle surface. Ideally, a final concentration of 1 μM of linker was desirable as the studies previously of ML3 used such a concentration for this linker. This

would allow comparisons to be achieved between both systems. The nanoparticle linker conjugates were prepared at this concentration and studies were performed using extinction spectroscopy, DLS and zeta potential measurements were obtained to indicate the viability of these conjugates.

Table 5.1 Extinction study measurements of Ag nanoparticles functionalised with 1 μM final concentrations of MM1 and MG2 linkers respectively.

Sample	λ_{max} (nm)	Extinction (au)
Ag Colloid	404	0.612
AgMM1	404	0.635
AgMG2	403	0.622

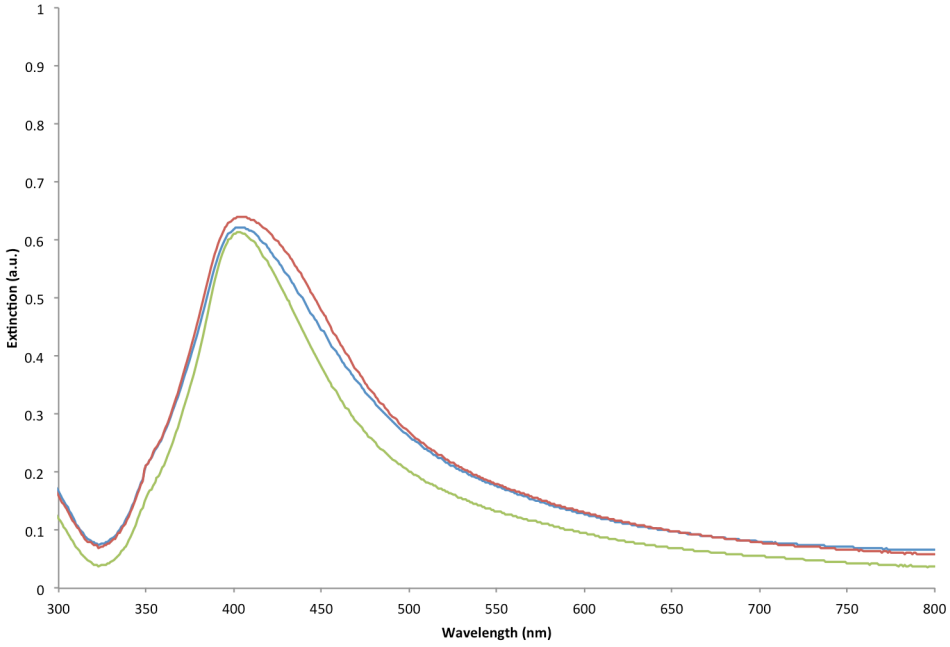

Figure 5.1 Extinction spectra of functionalised Ag nanoparticles with linkers MM1 and MG2. AgCitrate control spectra shown to indicate any changes in extinction profile of nanoparticle conjugates. Ag Citrate (green), AgMM1 (red) and AgMG2 (blue).

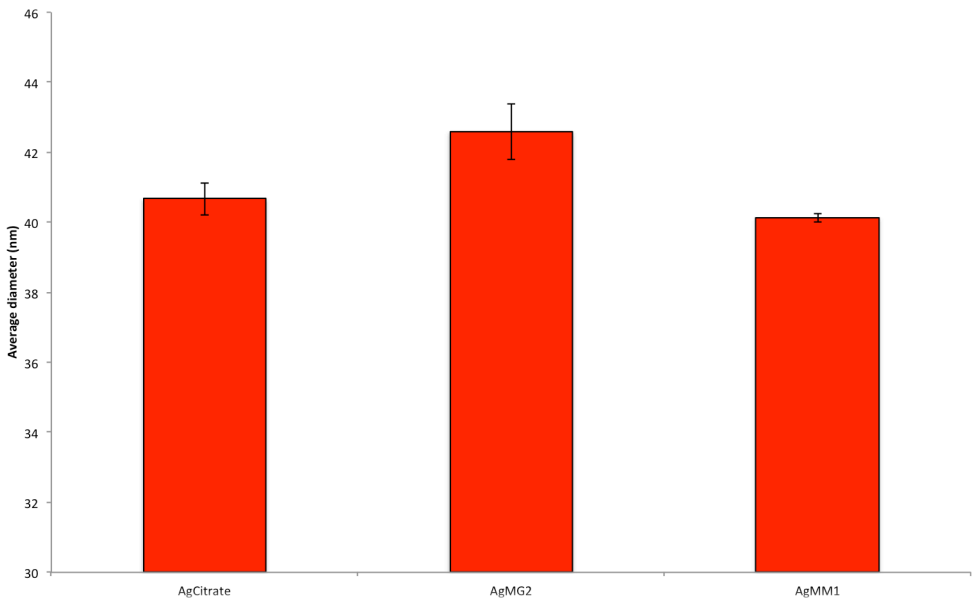

Figure 5.2 Measurement of the average diameter of the non-functionalised and functionalised Ag nanoparticles using DLS. Error bars shown are the standard deviation of triplicate measurements.

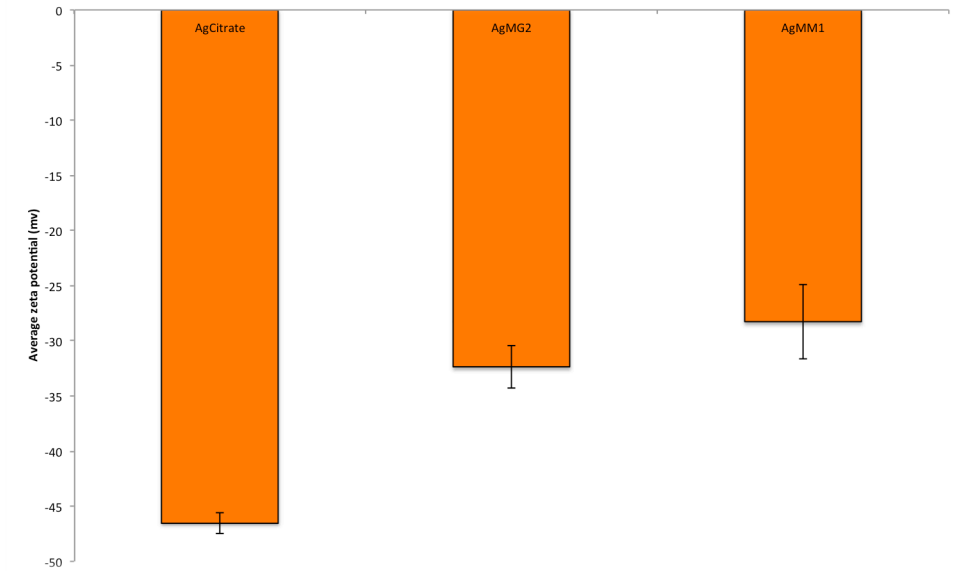

Figure 5.3 Zeta potential measurements of the non-functionalised and functionalised Ag nanoparticles using the Nanosizer. Error bars shown are the standard deviations of triplicate measurements.

The characterisation data, as shown in table 5.1 and figures 5.1-5.3, obtained for these nanoparticle conjugates indicated that in comparison to the citrate functionalised Ag nanoparticles the corresponding nanoparticle conjugates were stable. The only notable anomalous results were for the AgMM1 conjugates, which exhibited a small decrease in their average diameter and displayed a relatively low zeta potential in comparison to the

unmodified Ag citrate nanoparticles. The relatively low zeta value obtained was attributed to lower levels of surface coverage on the silver nanoparticle surface in comparison to the citrate molecules; therefore, there would be a lower net negative charge present at physiological pH in comparison. A decrease in particle motility could also be the cause for this decrease due to modified particles having an increased steric bulk in comparison to the unmodified nanoparticles. The decrease in zeta potential can also be noted for the AgMG2 particles and can be explained in the same context. The small decrease in size of the AgMM1 nanoparticles could be attributed to the electrostatic and steric repulsion potential of the modified nanoparticles being greater than that of the citrate complexed particles. Thus, the modified nanoparticles are able to maintain a distance from one another preventing aggregation and a significant increase in size being detected by DLS measurements.

Optimisation studies therefore concluded that the carbohydrate-modified nanoparticles were stable and the investigation could be progressed to determining the stability of these nanoparticle conjugates in the presence of galactose and mannose specific lectins.

5.3 Extinction spectroscopy aggregation studies of galactose and mannose functionalised particles

To expand on the studies of chapter 4 the aggregation of the AgMM1 and AgMG2 functionalised nanoparticles was initially established using extinction spectroscopy. These studies were performed prior to any multiplexing analysis to prove that it was possible to aggregate these functionalised nanoparticles individually. As previously determined the LOD of the AgML3-ConA interaction was established to be at 40 pM by SERS and 78 nM by extinction spectroscopy. It was assumed that a concentration vastly in excess of this should aggregate the particles and that detection by extinction spectroscopy would be possible. Initial studies were performed to prove the nanoparticle instability in the presence of lectins, which in nature bind specifically to galactose and mannose. To determine the time and concentration dependence of these interactions the first step of this investigation involved the attempted aggregation of the carbohydrate functionalised nanoparticles in the presence of a 100 nM concentration of each respective lectin.

5.3.1 Aggregation of MG2 functionalised nanoparticles using Jacalin

Jacalin is a lectin from the jackfruit *Artocarpus integrifolia* which has emerged as a valuable tool for interaction with *O*-glycoproteins such as mucins and IgA1.[190] Jacalin is a tetrameric lectin which consists of two polypeptide chains, a long alpha chain and a short beta chain which are produced following proteolysis.[191]

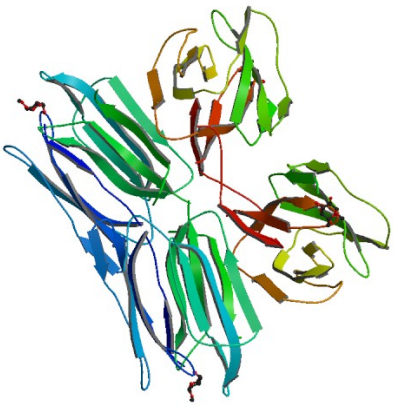

Figure 5.4 Crystal structure of jackfruit lectin Jacalin. PDB ID: 1JAC

The specificity of Jacalin towards galactose containing glycoproteins or single monosaccharides has been documented on many occasions. Therefore, the interactions of Jacalin were studied using the MG2 functionalised silver nanoparticles. Initial studies were performed to prove that the aggregation of these nanoparticles was possible using the Jacalin lectin. To do this a 100 nM concentration of Jacalin was added to the AgMG2 particle suspensions and changes in their extinction band were monitored over a period of 16 hours.

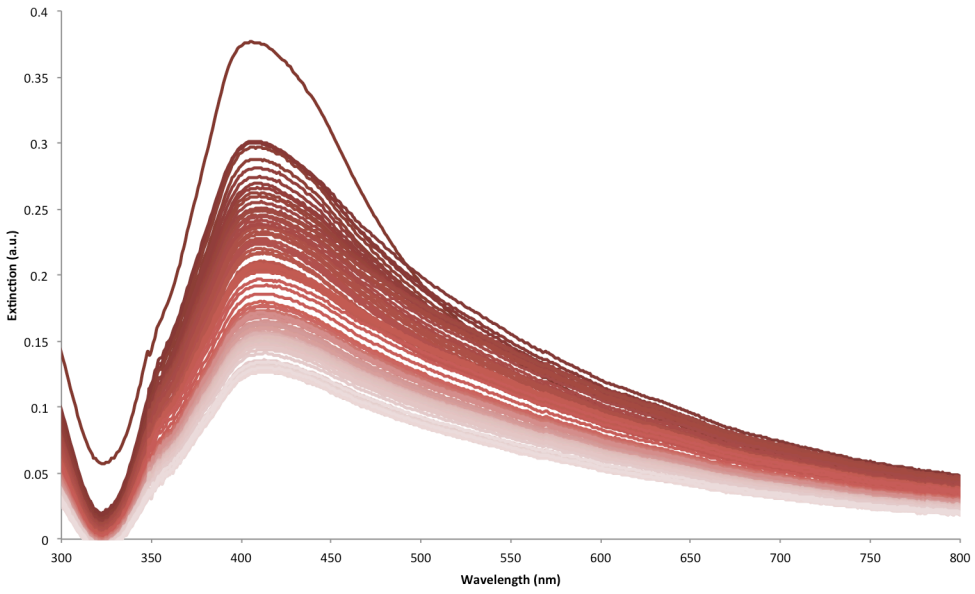

Figure 5.5 Extinction spectra of AgMG2 with a final concentration of 100 nM Jacalin added. Measurements taken every 5 minutes over a 16 hour period.

As shown by figure 5.5, over the period of 16 hours there was a significant broadening and dampening of the extinction resonance band indicating that aggregation of these nanoparticles had occurred in the presence of a 100 nM final concentration of the lectin.

These results are as expected and to provide further conformation of this aggregation process studies were performed using DLS.

As shown in figure 5.6, over the period of 1 hour it was possible to establish that at high Jacalin concentrations i.e. 50 and 100 nM, aggregation occurs and large nanoparticle clusters are formed. For lower concentrations of Jacalin aggregation was unable to be detected by DLS analysis. As the study of AgML3 conjugates with ConA also identified difficulty in establishing aggregation had occurred at lower concentrations using DLS the next stage of this investigation was to experimentally obtain a linear range of detection for the aggregation of these nanoparticle conjugates using extinction spectroscopy.

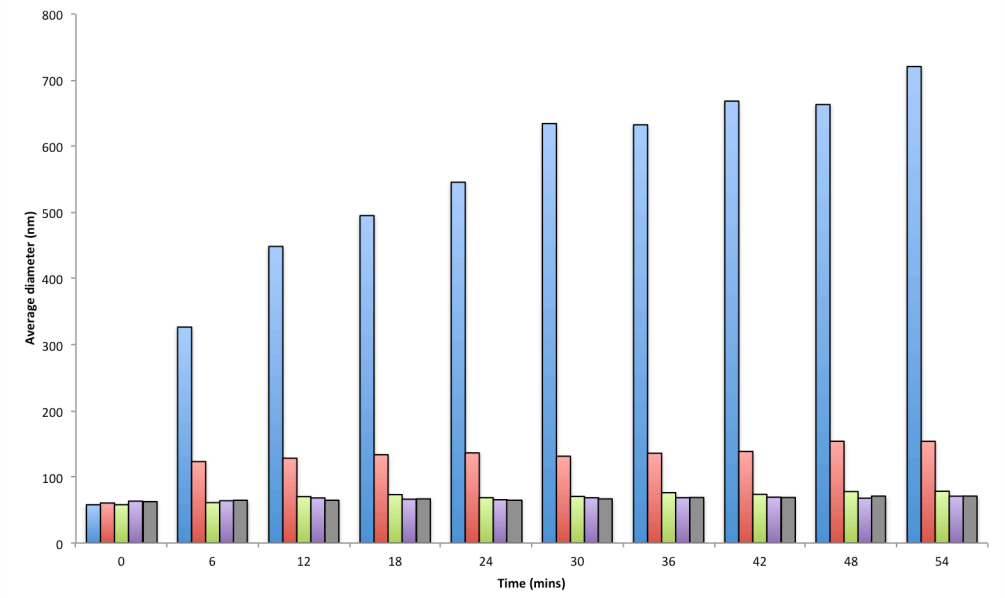

Figure 5.6 DLS study of the aggregation of AgMG2 with Jacalin at varied concentrations over the period of one hour. Graph colour coordinated in respect of concentration of Jacalin added; 100 nM (blue), 50 nM (red), 10 nM (green) 5 nM (purple) 1 nM (grey)

Figure 5.7 presents the linear range of detection, which was obtained by extinction spectroscopy for the aggregation of AgMG2 functionalised nanoparticles with varied concentrations of Jacalin.

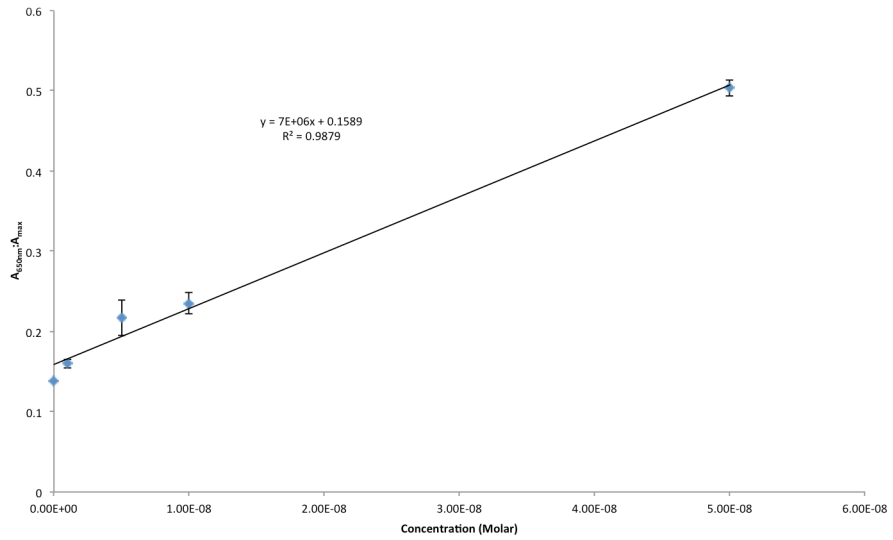

Figure 5.7 Linear range of detection obtained for the interaction of AgMG2 with lectin Jacalin. Ratios of extinction at 700 nm and the λ_{max} of the AgMG2 samples ($\boldsymbol{\lambda_{max}}$ = 413 nm) have been plotted against varied lectin concentration. Error bars shown are the standard deviations of 5 replicate measurements.

From the data obtained the experimental LOD for this system was calculated to be 2.3 nM. The LOD obtained is superior to the previous LOD of 78 nM obtained for the extinction spectroscopy analysis of AgML3 mediated aggregation by ConA.

5.3.2 Aggregation of MM1 functionalised nanoparticles using Jacalin and *Lens culinaris*

The carbohydrate specificity of Jacalin has long been considered to be towards galactose residues, however, using SPR, X-Ray crystallography and molecular modeling it has been revealed that this assumption was misconceived.[192] Jacalin in fact displays multiple specificities towards not only galactose but to its other epimeric carbohydrates mannose and glucose. These additional specificities arise from the interaction of C-2 and C-4 hydroxyl groups which have different orientations and bulky substituents with the carbohydrate binding cleft of Jacalin.[193]

The observation of Jacalin specificity towards mannose residues was experimentally tested by using Jacalin to aggregate MM1 modified Ag nanoparticles. Extinction spectroscopy was used to monitor the aggregation of these particles over 16 hours.

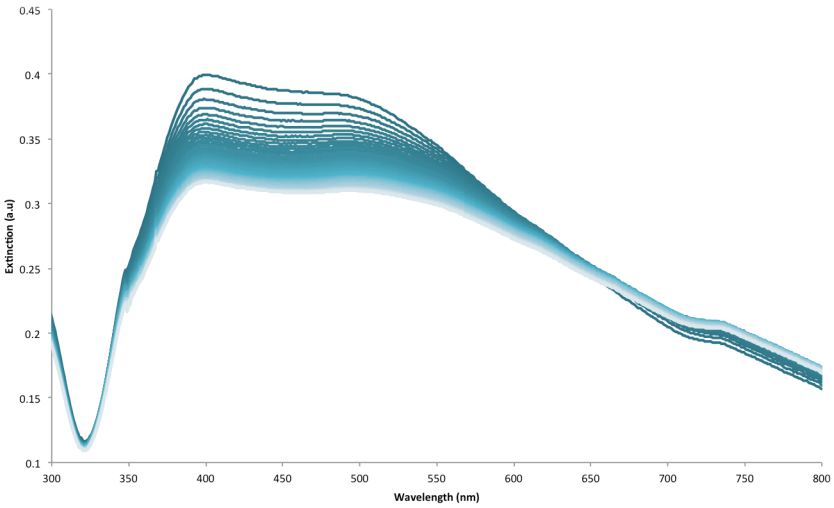

Figure 5.8 Extinction spectra obtained of AgMM1 when 100 nM of Jacalin was added. Spectra have been measured over 16 hours to show the change in extinction band as aggregation of the particles occur. Measurements taken every 5 minutes over a 16-hour period.

As shown in figure 5.8 the spectra of the AgMM1 particles show aggregation occurred in the presence of Jacalin as expected due to its multiple specificities. Over the course of 16 hours severe dampening of the extinction band occurred whilst a secondary peak began to develop between 650 – 750 nm indicative of the coupling of neighbouring plasmons produced by the formation of nanoparticle clusters. The aggregation of these particles by 100 nM Jacalin was then quantified by identifying the LOD for the MM1 particle system in the presence of varied Jacalin concentrations. Figure 5.9 presents the data obtained from the LOD study. From the linear regression fit, the LOD was calculated to be 3.7 nM.

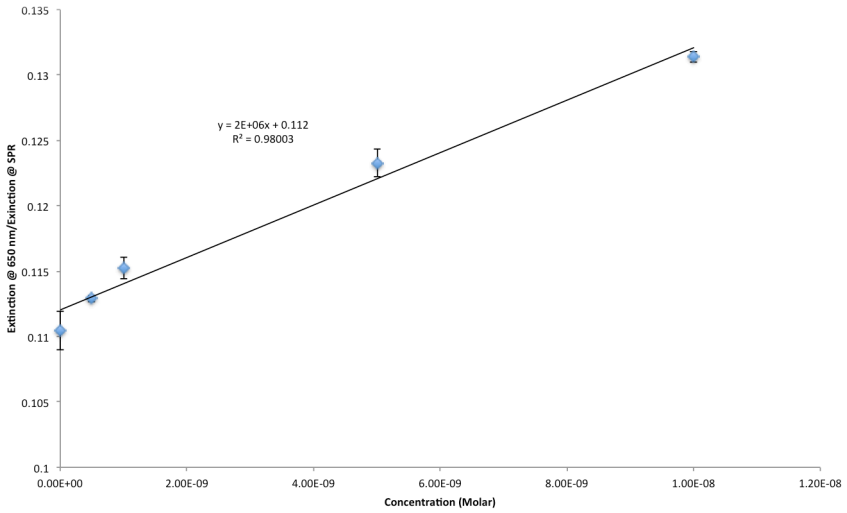

Figure 5.9 Linear range of detection obtained for the interaction of AgMM1 with lectin Jacalin. Ratios of extinction at 700 nm and the λ_{max} of the AgMM1 samples ($\boldsymbol{\lambda_{max}}$ = 410 nm) have been plotted against varied lectin concentration. Error bars shown are the standard deviations of 5 replicate measurements.

A second lectin was used to interact with the mannose functionalised particles. *Lens culinaris* is a mannose specific protein, which also shows affinity towards glucose residues. The binding site of *Lens culinaris* interacts with the mannose residue through the following interactions (a) the C-4 hydroxyl group acts as a hydrogen bond acceptor for an Asn residue in the protein backbone (b) an Asp residue acts as a hydrogen bond acceptor at the same hydroxyl group whilst (c) the hydroxyl group of C-3 acts as an acceptor of an NH of the peptide backbone. Stabilisation is further provided by the occurrence of van der Waals interactions between the sugar ring and a phenyl ring of the amino acid residue Phe123.[194]

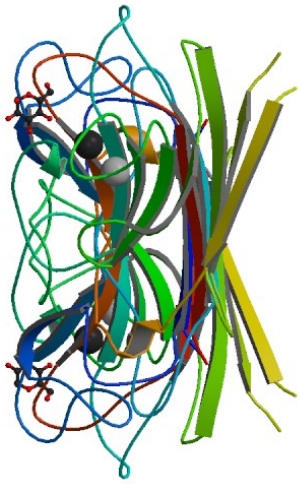

Figure 5.10 Biological assembly of lentil lectin Lens Culinaris in complex with sucrose

This dimeric lectin was investigated in the same manner as the Jacalin lectin previously. An extinction spectroscopy time study was performed to monitor changes in the plasmon resonance band for signs of nanoparticle aggregation. Figure 5.11 shows a dampening of the plasmon band as well as the formation of a secondary plasmon band due to the coupling of plasmons in nanoparticle clusters formed due to *Lens culinaris* mediated aggregation.

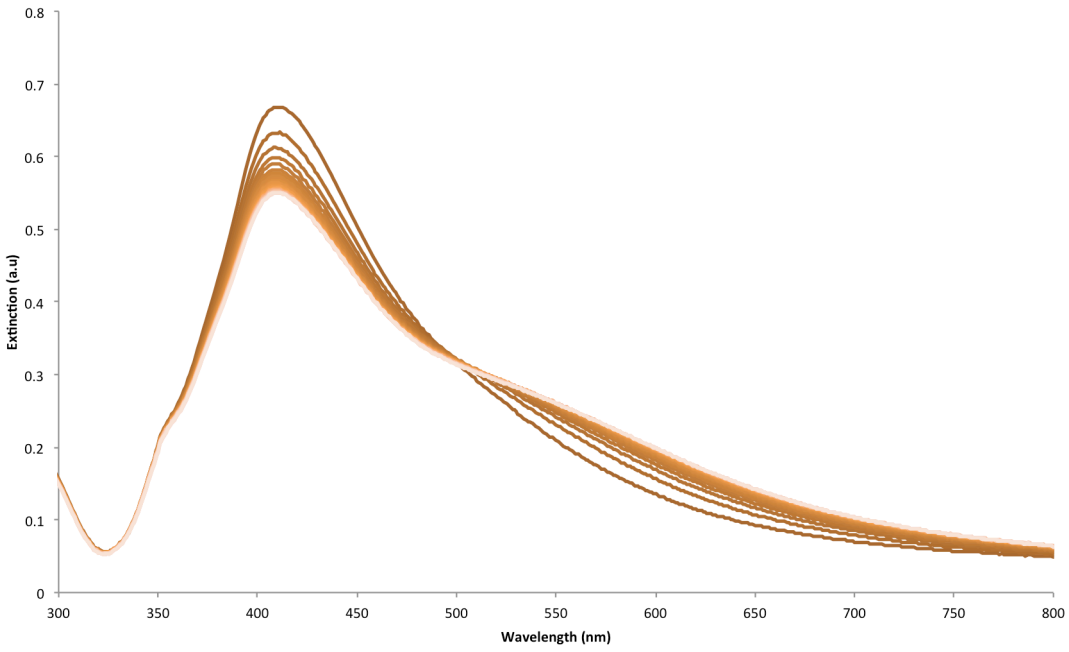

Figure 5.11 Extinction spectra time study for AgMM1 nanoparticles in the presence of 100 nM Lens Culinaris. Measurements taken every 5 minutes over a 2.5-hour period.

Following confirmation that aggregation shall occur in the presence of the *Lens culinaris* lectin an LOD study was performed using extinction spectroscopy.

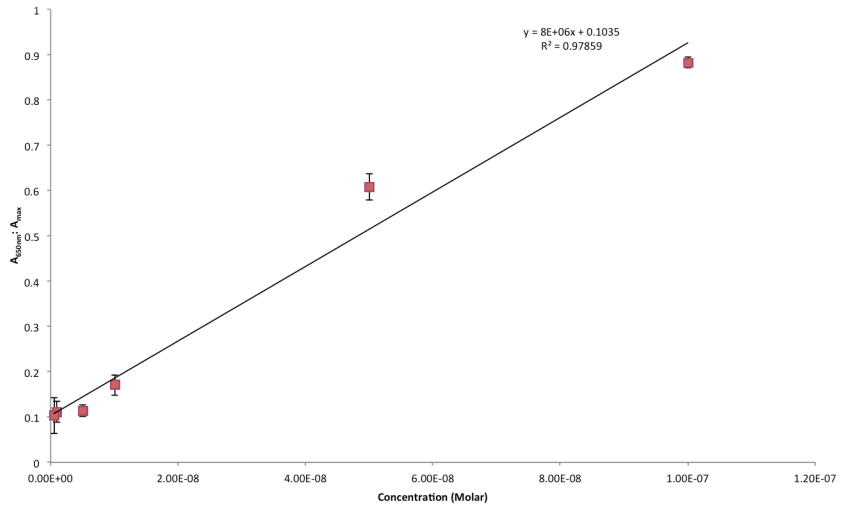

Figure 5.12 Linear range of detection obtained for the interaction of AgMM1 with lectin *Lens Culinaris*. Ratios of extinction at 700 nm and at the λ_{max} of the AgMM1 samples ($\boldsymbol{\lambda_{max}}$ = 410 nm) have been plotted against varied lectin concentration. Error bars shown are the standard deviations of 5 replicate measurements.

From the linear regression equation, it was calculated that the experimental LOD was 5 nM by extinction spectroscopy. In comparison to when Jacalin was used this shows that in comparable systems Jacalin and *Lens culinaris* have very similar binding affinities to mannose residues.

These results for MG2 and MM1 modified nanoparticles show that the system created for the aggregation of nanoparticles *via* carbohydrate-lectin interactions can be extended to a range of specific interactions that can be monitored using extinction spectroscopy. As three different carbohydrate functionalised nanoparticle sets had been created, the next stage of this investigation was to test if these particles could be aggregated specifically in a multiplexed format. Due to the limitations of extinction spectroscopy the multiplexed detection of this system was not possible using this technique. In order to facilitate multiplexed detection two further Raman reporter molecules were required to enable the AgMM1 and AgMG2 nanoparticles to be active for SERS multiplexed analysis.

5.4 Assessment of Raman reporter molecules for use in multiplex

The reporter molecule requirements were that they each could provide unique vibrational spectra when analysed separately and contained identifiable peaks, which could be used to

detect each component in a solution containing all three species. RB1 has previously been established as an adequate reporter molecule in chapter 4. As a result, further reporter molecules were considered including other benzotriazole dyes. Figure 5.13 shows the structures of the reporter molecules considered for analysis.

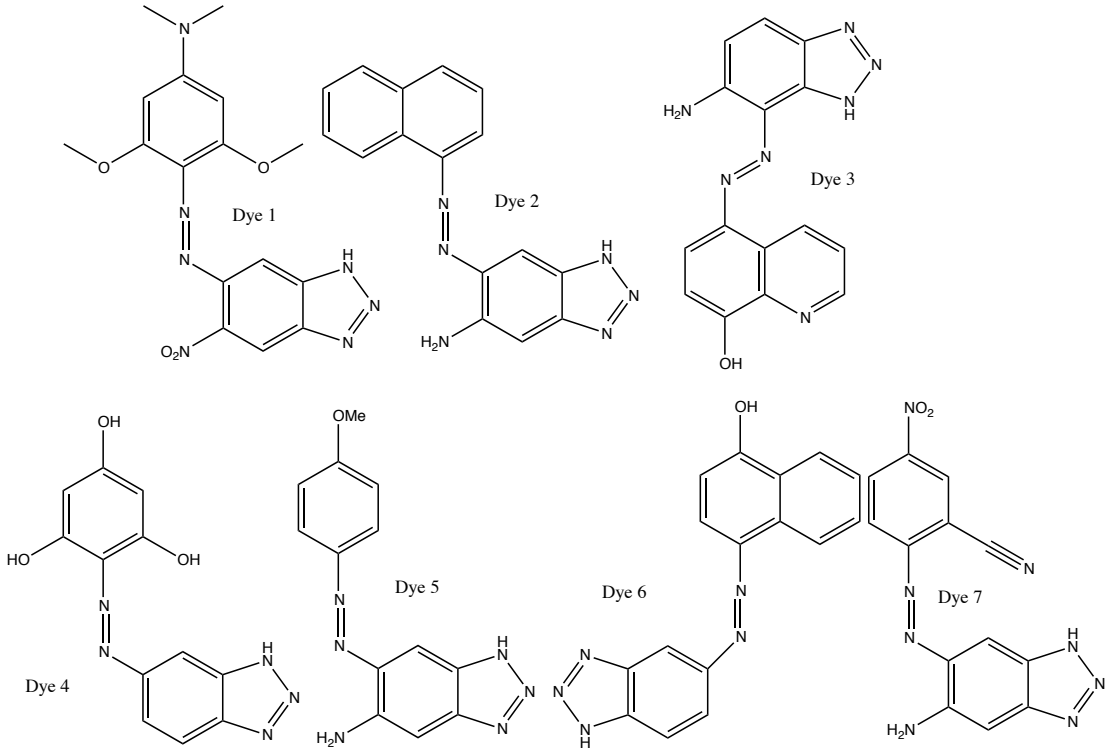

Figure 5.13 The structures of the seven Raman reporter molecules studied for use in the multiplexed detection of carbohydrate-protein interactions. These compounds had previously been synthesised in-house by Dr. Andrew Ingram.

Of the 7 molecules considered, six of those were benzotriazole dyes. Due to their irreversible binding to silver nanoparticles, their use was highly desirable to obtain the reproducible analysis required when performing multiplexed measurements.

5.4.1 Identifying components for multiplexed SERS studies

Individual SERS spectra were obtained of each dye, as were duplex and triplex spectra of all possible combinations. Studies were also performed using extinction spectroscopy to indicate the stability of the nanoparticle conjugates when the dyes were added at a final 1 μM concentration.

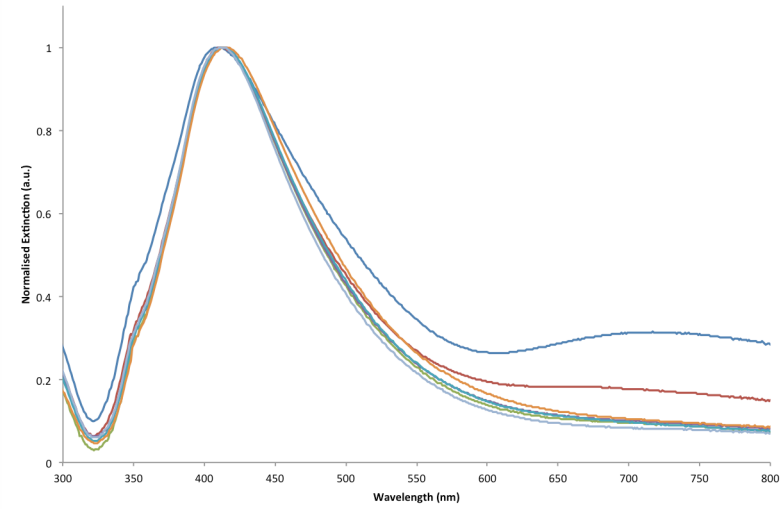

Figure 5.14 Normalized extinction spectra of each dye added at a final 1 μM concentration to the silver nanoparticle suspensions. Dye 1 (blue) and dye 2 (red) exhibit a secondary aggregation peak between 700 and 750 nm. The other Ag nanoparticles functionalised with dyes 3 to 7 show extinction properties similar to those of Ag citrate nanoparticles.

The extinction spectroscopy results, as shown in table 5.2 and figure 5.14, indicate the formation of a secondary plasmon peak, which can be, defined as an aggregation peak for dye 1 and 2 functionalised nanoparticles in the 650-750 nm region. By calculation of the ratio between the extinction measurements obtained at the nanoparticle λ_{max} and the values obtained at 700 nm it was possible to determine which dye molecules were the most stable.

Table 5.2 Extinction measurements recorded for each set of conjugates including measurements at the λ_{max} and at 700 nm which is within the area at which secondary peaks form due to nanoparticle aggregation

Sample	λ_{max} (nm)	Extinction at λ_{max} (a.u.)	Extinction at 700 nm	700:λ_{max}
Ag Citrate	415	0.66	0.05	0.07
Dye 1	410	0.42	0.13	0.30
Dye 2	412	0.45	0.08	0.18
Dye 3	413	0.33	0.03	0.09
Dye 4	412	0.60	0.06	0.10
Dye 5	413	0.59	0.06	0.01
Dye 6	415	0.59	0.06	0.10
Dye 7	413	0.51	0.04	0.08

From these results the most stable reporter molecule combinations were identified as being those of dye 3, 5 and 7 as they gave the lowest extinction ratio's indicating aggregation was not occurring when they were present on the nanoparticle surface.

Figures 5.15-5.17 shows the SERS spectra obtained from the most stable dye-nanoparticle conjugates

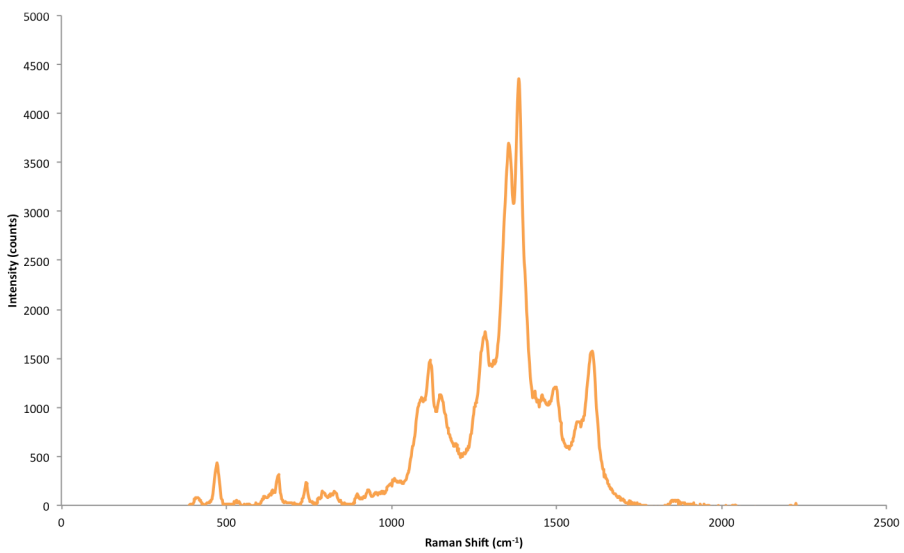

Figure 5.15 Spectrum shown was calculated from the average of 5 spectra obtained using a 1s exposure time with 10 accumulations for dye 3

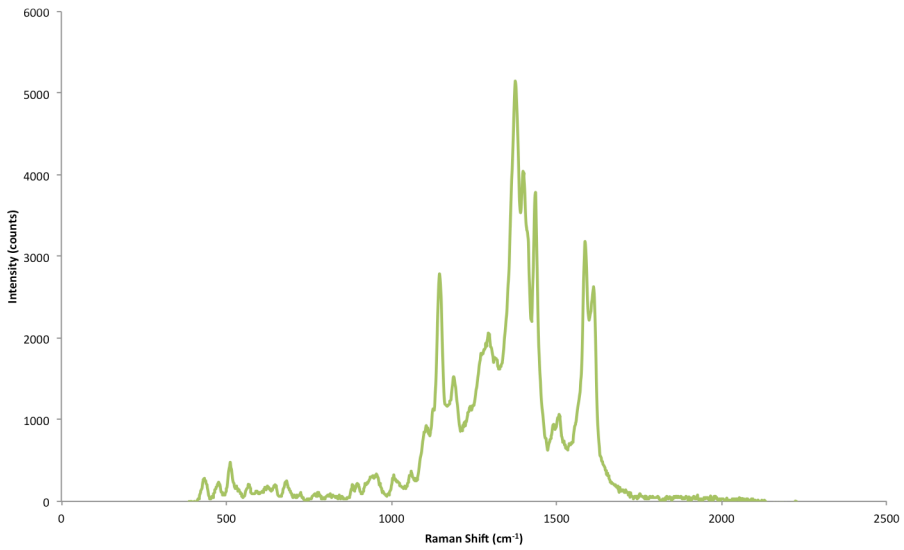

Figure 5.16 Spectrum shown was calculated from the average of 5 spectra obtained using a 1s exposure time with 10 accumulations for dye 5

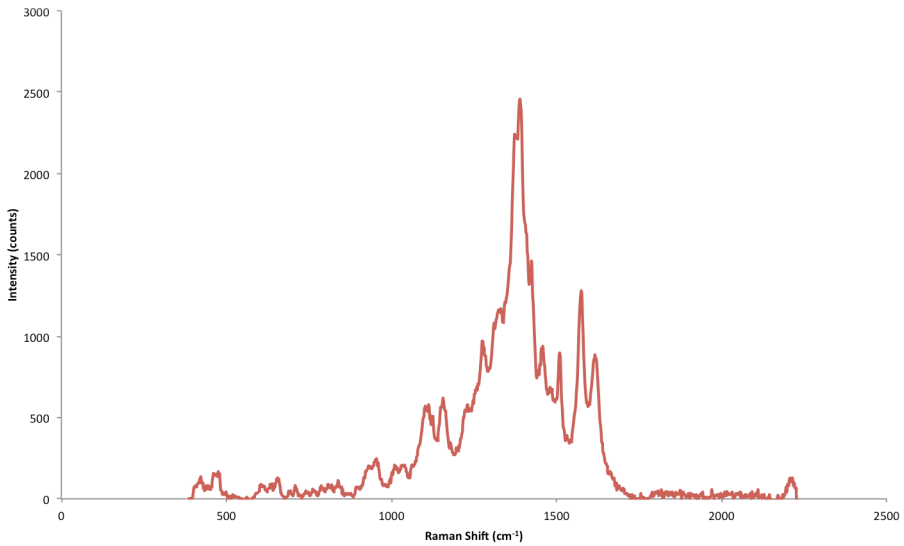

Figure 5.17 Spectrum shown was calculated from the average of 5 spectra obtained using a 1s exposure time with 10 accumulations for dye 7

The spectra obtained for dyes 3, 5 and 7 were found to be very similar and as such it was decided that the use of two of these dyes in the same multiplex would make detection of each individual component too complex and would require more extensive analysis. To circumvent the issue a new reporter molecule was sought in the form of the 8-hydroxyquinoline dye denoted as J7E. This dye has previously been made in house by Dr. Jennifer Dougan and had been shown to exhibit a unique vibrational spectrum when used for SERS analysis.

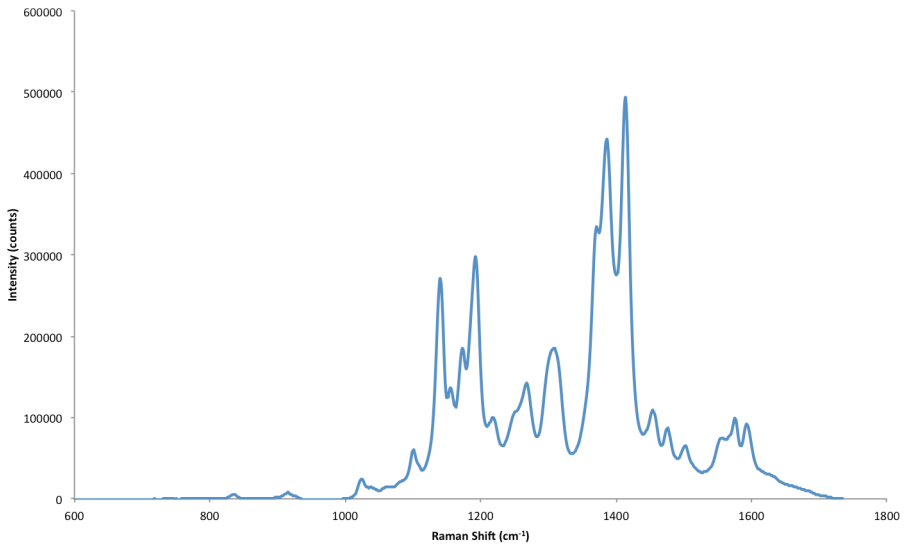

Figure 5.18 Spectrum shown was calculated from the average of 5 spectra obtained using a 1s exposure time with 10 accumulations for 1 μM concentration of J7E on silver nanoparticles.

The combination of dyes 3, 5, 7, J7E and RB1 were further investigated to obtain a suitable triplex for further analysis. Multiple combinations of each dye and at varying ratios were analysed to elicit a triplex spectrum, which contained a unique vibrational peak for each individual component that could be identified easily by eye. The final triplex combination was obtained from dye 5, J7E and RB1. The subsequent triplex and individual component spectra are shown in figure 5.19.

Each unique peak has been colour coordinated for ease of identification. All spectra were obtained using the same concentration of reporter molecule (1 μM) and the final triplex was obtained using a ratio of 7:1:7 for dye 5, J7E and RB1 respectively.

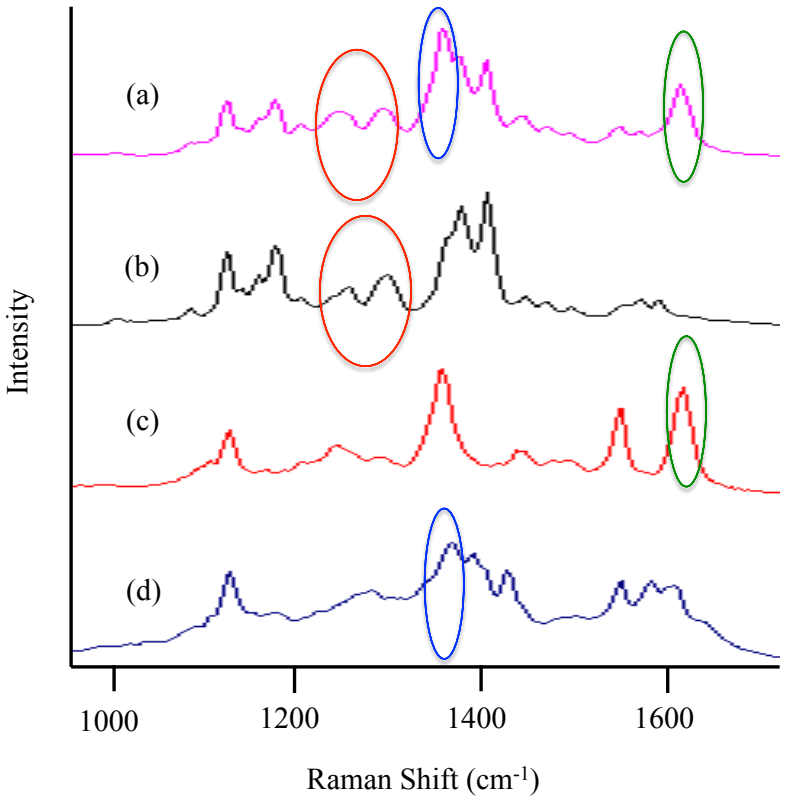

Figure 5.19 SERS measurements obtained using a 1s exposure time with 10 accumulations after centering at 1350 cm^{-1} (a) Triplex, (b) J7E (c) RB1 (d) Dye 5

As qualitative SERS spectra for each component had been obtained it was essential to prove that quantitative measurements were possible using three different carbohydrate linker and reporter molecule combinations. For the purposes of the subsequent studies ML3 and RB1, MM1 and BT5 and MG2 and J7E were the chosen combinations.

5.5 SERS detection of carbohydrate-protein interactions

As the three vibrationally distinct reporter molecules had been selected for the multiplex studies, the detection limits of the carbohydrate-protein interactions were investigated individually using SERS.

5.5.1 SERS LOD studies of AgMM1 with *Lens culinaris* and Jacalin

The aggregation of MM1 modified Ag particles was performed using a 514.5 nm excitation wavelength which was chosen as due to being close to the resonance excitation of the reporter molecule chromophores.

Using a mixed monolayer strategy, Ag nanoparticles were functionalised in a mixed monolayer format following the tandem addition of the MM1 linker and J7E at a final dye

and linker concentration of 1 μM. Solutions of the prepared nanoparticles were then analysed individually in the presence of various concentrations of the lectins *Lens culinaris* and Jacalin. From the SERS intensities obtained for each batch of nanoparticles the average peak intensity of the principal peak chosen for analysis was plotted against the concentration of lectin used to achieve a linear detection range. The LOD value was then calculated as shown in section 9.15.

Figure 5.20 presents the linear range of detection obtained from the interaction of MM1 modified nanoparticles with the lectin *Lens culinaris.* From the equation obtained the LOD was calculated to be 0.38 nM. This concentration is higher than expected considering that the LOD obtained for this study using extinction spectroscopy produced an LOD of 5 nM. Previous results have shown that SERS detection has been in the region of at least 100 times more sensitive than extinction spectroscopy for these systems yet this result only indicates a 10 times increase in sensitivity when the same system is mirrored using SERS.

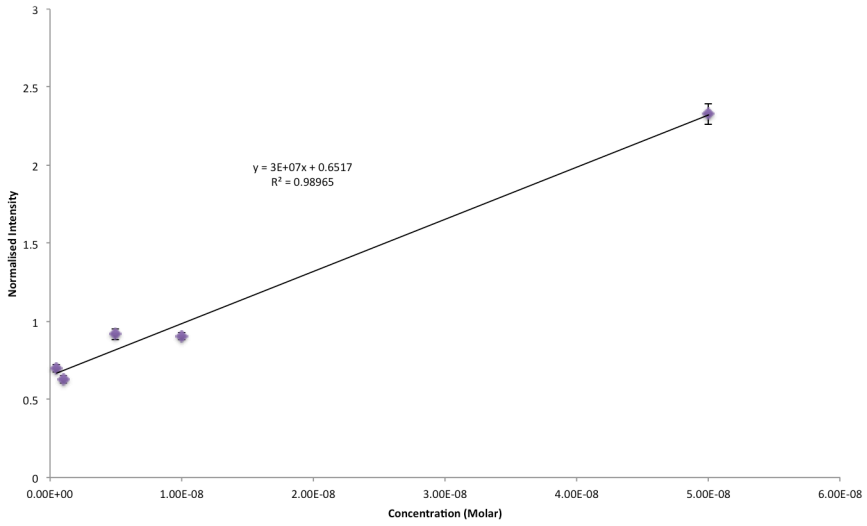

Figure 5.20 Linear range of detection obtained for the interaction of MM1 functionalised silver nanoparticles with *Lens Culinaris* at various concentrations. SERS analysis performed using a 1 second exposure with 10 accumulations.

Repeated analysis of this system using SERS has produced similar results in the sub nanomolar range. As *Lens culinaris* is a dimeric lectin and can only interact with two modified nanoparticles simultaneously then the creation of nanoparticle hot spots will be reduced due to a decreased number of nanoparticle clusters forming as less carbohydrate-protein interactions would have been occurring. Therefore, the electromagnetic enhancement gained from the substantial number of clusters formed in previous studies was not mirrored

when monitoring the interaction of *Lens culinaris* mannose-modified particles and as such, a decrease in sensitivity was observed.

Due to the multiple carbohydrate specificities of Jacalin an LOD study was performed using SERS. The LOD obtained for extinction spectroscopy was 3.7 nM. However, repeated attempts to obtain a linear range of detection using SERS proved futile. The inability to obtain an LOD for this study using SERS remains confusing and as such further work is required to resolve this issue.

5.5.2 SERS LOD studies of AgMG2 with Jacalin

Although a linear range of detection was not observed for the interaction of Jacalin with mannose-modified nanoparticles, investigations continued to elucidate an LOD for the interaction of Jacalin with galactose modified nanoparticles. An LOD for this system was obtained in the region of 13 pM which established an increase in sensitivity in comparison to the ConA ML3 studies performed in chapter 4. Figure 5.21 shows the linear range of detection as obtained from the plot of the average intensity of the principal component peak versus the concentration of Jacalin added to the nanoparticle solution.

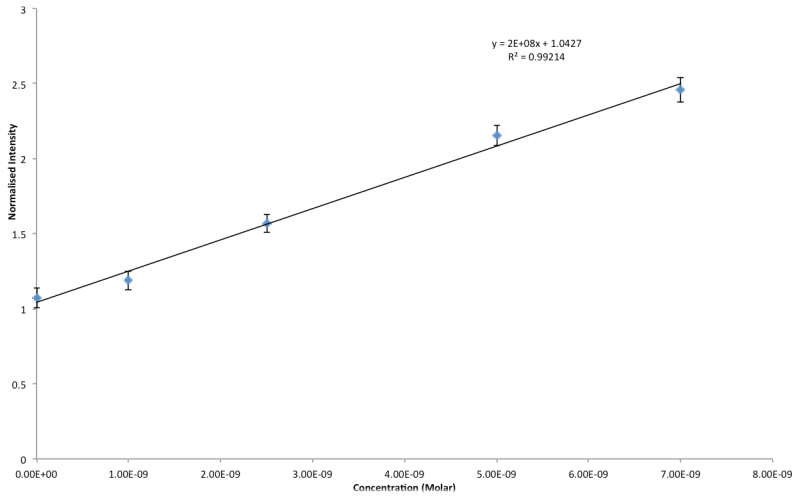

Figure 5.21 Linear range of detection obtained for the interaction of MG2 functionalised silver nanoparticles with Jacalin at various concentrations. SERS analysis performed using a 1 second exposure with 10 accumulations.

In comparison to the previous LOD obtained *via* extinction spectroscopy of 2.3 nM the SERS results indicate a 10^3 fold increase in sensitivity. This is to be expected due to the enhancement gained from the hot spots formed upon nanoparticle aggregation. From each of the individual LOD studies obtained in both chapters 4 and the initial sections of chapter 5 it

can be concluded that for monitoring individual carbohydrate-protein interactions a significant increase in sensitivity is obtained using SERS in comparison to extinction spectroscopy.

5.6 SERS multiplex studies of carbohydrate-protein interactions

Following the completion of individual component LOD studies using SERS detection the aggregation of each individual component in the triplex mixture was then studied.

5.6.1 Multiplex study of Triplex interaction with the lectin Lens Culinaris

Initial studies were performed to achieve the isolated aggregation of each individual component within the triplex. It was decided that addition of an excess of each lectin at a concentration of 100 nM initially should allow for the aggregation of individual components within the triplex to be detected.

The first study performed monitored the addition of the lectin *Lens culinaris* to the triplex mixture. Triplex samples were prepared and analysed without the lectin present followed by the subsequent addition of lectin. The lectin containing samples were then left sealed at room temperature for 1 hour for aggregation to occur and then SERS measurements were taken for comparison to the non-lectin containing solutions.

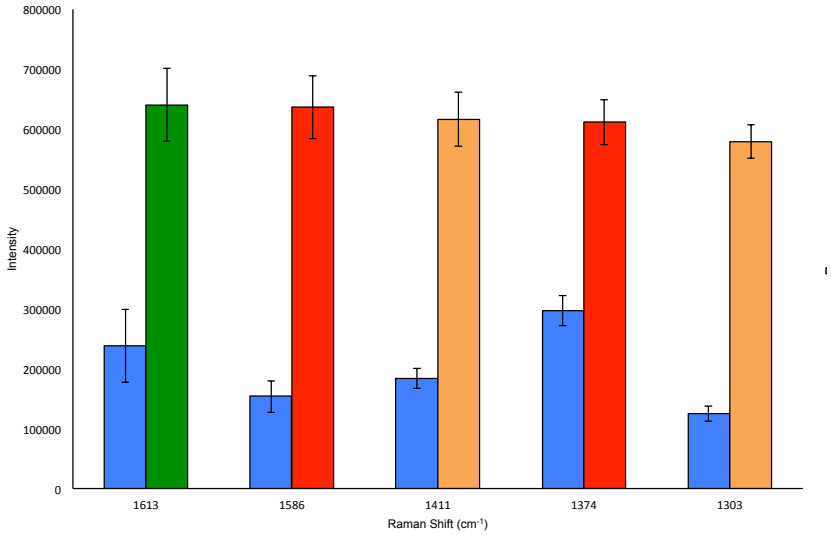

Figure 5.22 SERS intensities obtained prior and post addition of 100 nM *Lens Culinaris* to a triplex solution containing each modified nanoparticle component; AgML3-RB1 (green), AgMM1-BT5 (red) and AgMG2-J7E (orange). The blue bars represent the SERS measurements prior to lectin addition. SERS analysis performed on each solution using a 1 second exposure with 10 accumulations at 100% laser power. Error bars shown are the standard deviation of five replicate measurements.

As shown in figure 5.22 for the corresponding glyconanoparticle-dye combinations, the SERS response for the most intense reporter peaks are displayed prior to and post lectin addition. As *Lens culinaris* has displayed an affinity for mannose, it was foreseen that upon aggregation only the peaks identified, as those of the reporter molecule dye 5 should be increased. However, as shown by figure 5.22, although there was a significant increase in the SERS intensity of both of these peaks following the aggregation of the nanoparticles, a number of other peaks correlated to the reporter molecules J7E and RB1 also exhibited a significant increase in SERS intensity. Therefore, although aggregation may have occurred it is possible that aggregation of the other modified nanoparticles had also occurred concurrently. It has been established that *Lens culinaris* displays an affinity for gluscose residues as well as mannose containing carbohydrates, therefore, the increase in SERS intensity of RB1 (1613 cm^{-1} peak) was not unexpected. However, as no such binding affinity has been displayed towards galactose containing carbohydrates the aggregation of the AgMG2 nanoparticles could possibly be due to non-specific absorption of the lectin leading to the formation of small aggregate clusters, which have an increased electromagnetic enhancement due to the formation of hot spots, and as a result, a significant increase in SERS intensity occurred. Another possible reason could be that following the formation of the lectin directed nanoparticle aggregates a significant enhancement of the surrounding non-aggregated nanoparticles due to their proximity to the aggregate clusters could have occurred. To overcome any issues of non-specific protein binding the concentration of *Lens culinaris* added to the triplex solution was decreased to 10 nM, which was closer to the LOD concentration of *Lens culinaris* detected previously by extinction spectroscopy. The rationale behind this shift in experimental parameters was that it was known that aggregation could still be detected at a concentration of 10 nM *Lens culinaris* for the AgMM1 functionalised nanoparticles. Therefore, at this concentration it was believed that aggregation of the other carbohydrate species would not occur due to the low concentration of lectin present.

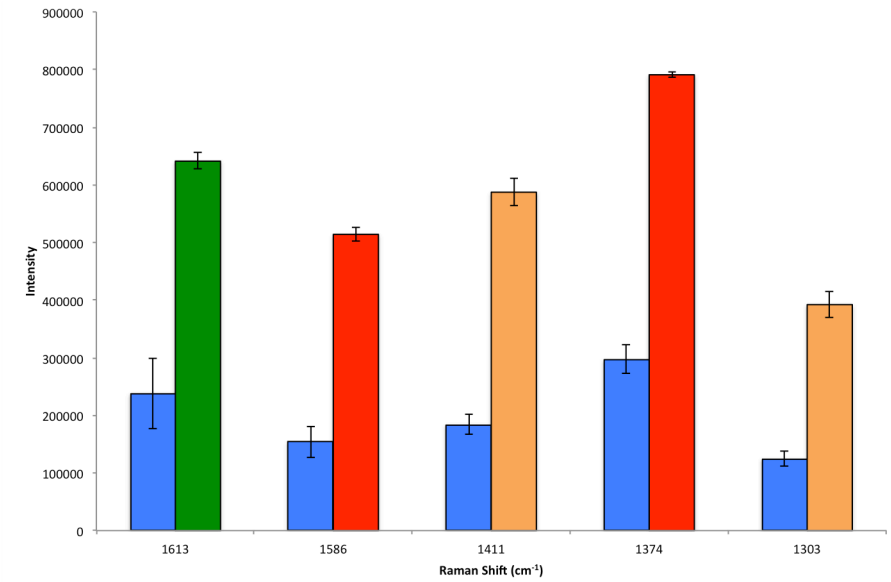

Figure 5.23 SERS intensities obtained prior and post addition of 10 nM Lens Culinaris to a triplex solution containing each modified nanoparticle component; AgML3-RB1 (green), AgMM1-BT5 (red) and AgMG2-J7E (orange). The blue bars represent the SERS measurements prior to lectin addition. SERS analysis performed on each solution using a 1 second exposure with 10 accumulations at 100% laser power. Error bars shown are the standard deviation of five replicate measurements.

However, as shown by figure 5.23, once again a significant increase in SERS intensity was detected for the major peaks correlated to each set of carbohydrate-modified nanoparticles. *Lens culinaris* is a mannose binding lectin, however, a number of mannose binding ligands also present specificity towards glucose containing carbohydrates. Therefore, it is possible that the peak at 1613 cm^{-1} increases significantly due to the aggregation of ML3 modified nanoparticles. Yet, this still does not explain the increase in SERS intensity of the peaks at 1411 and 1309 cm^{-1} respectively which are correlated to those of the AgMG2 bound reporter molecule J7E.

5.6.2 Multiplex study of Triplex interaction with the lectin Jacalin

Consequently, SERS analysis was performed of the triplex solution in the presence of 100 nM concentration of Jacalin. Figure 5.24 displays the difference in SERS intensities for the respective peaks prior and post lectin addition.

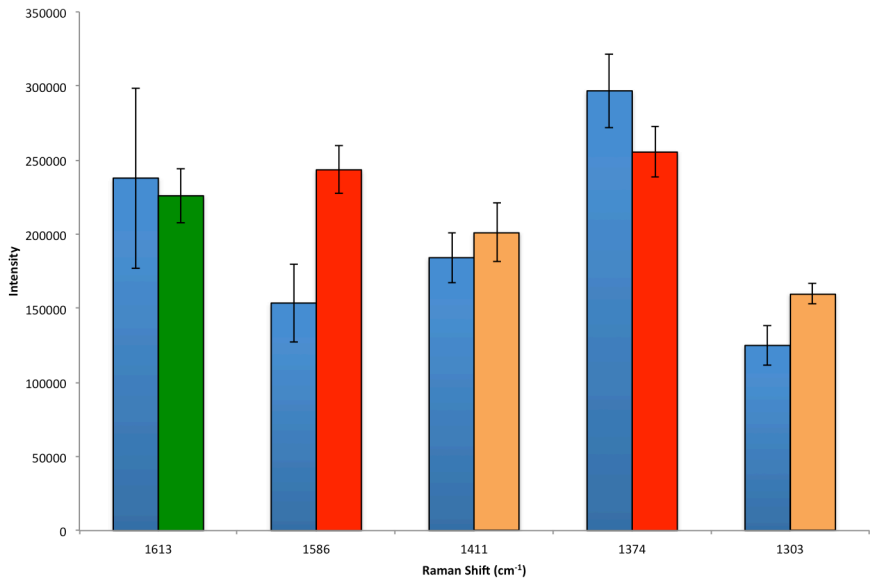

Figure 5.24 SERS intensities obtained prior and post addition of 100 nM Jacalin to a triplex solution containing each modified nanoparticle component; AgML3-RB1 (green), AgMM1-BT5 (red) and AgMG2-J7E (orange). The blue bars represent the SERS measurements prior to lectin addition. SERS analysis performed on each solution using a 1 second exposure with 10 accumulations at 100% laser power. Error bars shown are the standard deviation of five replicate measurements.

Following lectin addition an increase in intensity is achieved for only 3 peaks, 1586 cm^{-1} of dye 5 present on the MM1 modified nanoparticles and 1411 and 1303 cm^{-1} of J7E present on the MG2 modified nanoparticles. The error bars for the peaks correlated to J7E overlap indicating the SERS intensity increase seen here cannot be classified as being significant. These results are as expected due to Jacalin lectin being known to complex both galactose and mannose residues. Interestingly, when Jacalin was previously analysed using SERS with the mannose-modified particles it was not possible to obtain any correlation between signal intensity and lectin concentration. The notable increase in SERS intensity for the mannose related peak could be due to the formation of hetero aggregate clusters formed from the aggregation of MG2 and MM1 nanoparticles together. These results also shown no increase in intensity has been achieved for the ML3 modified conjugates, thus, it could be assumed that aggregation of all three nanoparticle sets previously was in fact due to the non-specific binding of *Lens culinaris*. The concentration of Jacalin was also lowered to 10 nM to detect any concentration dependence on SERS intensity increase.

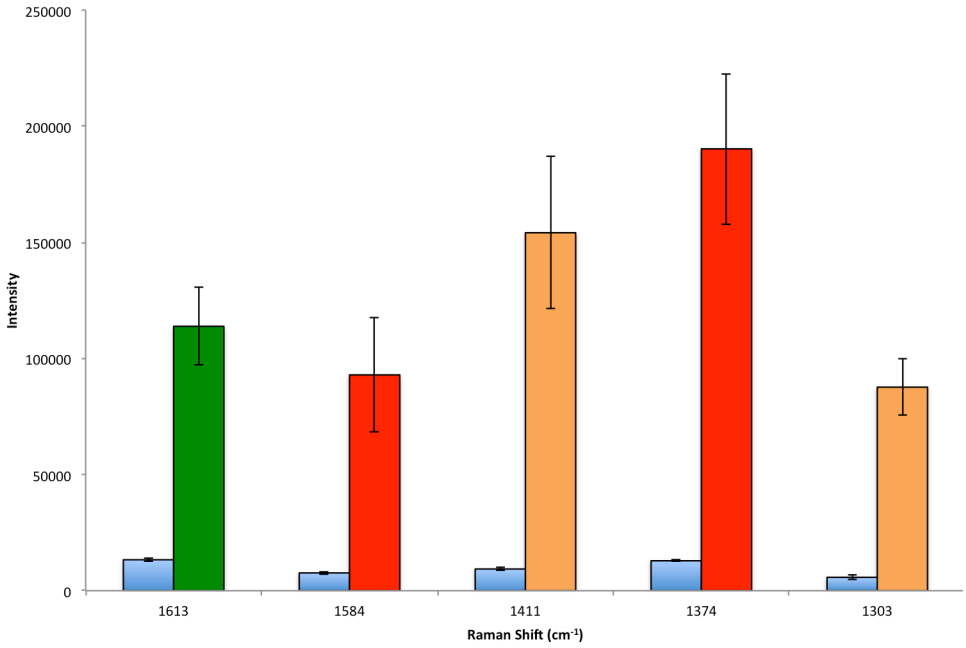

Figure 5.25 SERS intensities obtained prior and post addition of 10 nM Jacalin to a triplex solution containing each modified nanoparticle component; AgML3-RB1 (green), AgMM1-BT5 (red) and AgMG2-J7E (orange). The blue bars represent the SERS measurements prior to lectin addition. SERS analysis performed on each solution using a 1 second exposure with 10 accumulations at 100% laser power. Error bars shown are the standard deviation of five replicate measurements.

As can be seen in figure 5.25, following the decrease in lectin concentration to 10 nM Jacalin a significant increase in SERS intensity is achieved for each of the monitored peaks thus indicating aggregation has occurred for each modified nanoparticle component. Lower concentrations of lectin present should ideally decrease the SERS intensity achieved by aggregation due to less protein being present, therefore, less nanoparticles could be aggregated together which would result in the formation of less electromagnetic hot spots. Similar results were achieved for additions of 100 nM and 10 nM concentrations of Con A as shown in figures 5.26 and 5.27.

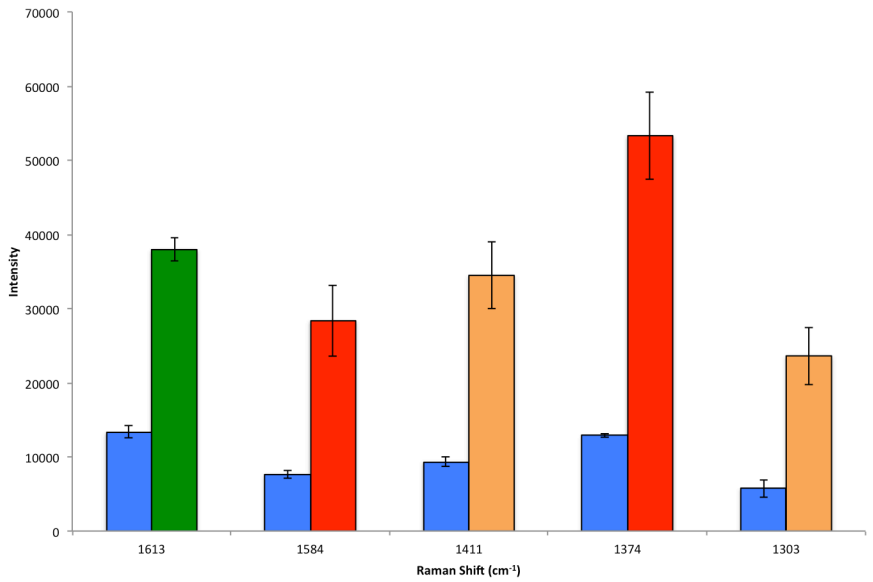

Figure 5.26 SERS intensities obtained prior and post addition of 100 nM ConA to a triplex solution containing each modified nanoparticle component; AgML3-RB1 (green), AgMM1-BT5 (red) and AgMG2-J7E (orange). The blue bars represent the SERS measurements prior to lectin addition. SERS analysis performed on each solution using a 1 second exposure with 10 accumulations at 100% laser power. Error bars shown are the standard deviation of five replicate measurements.

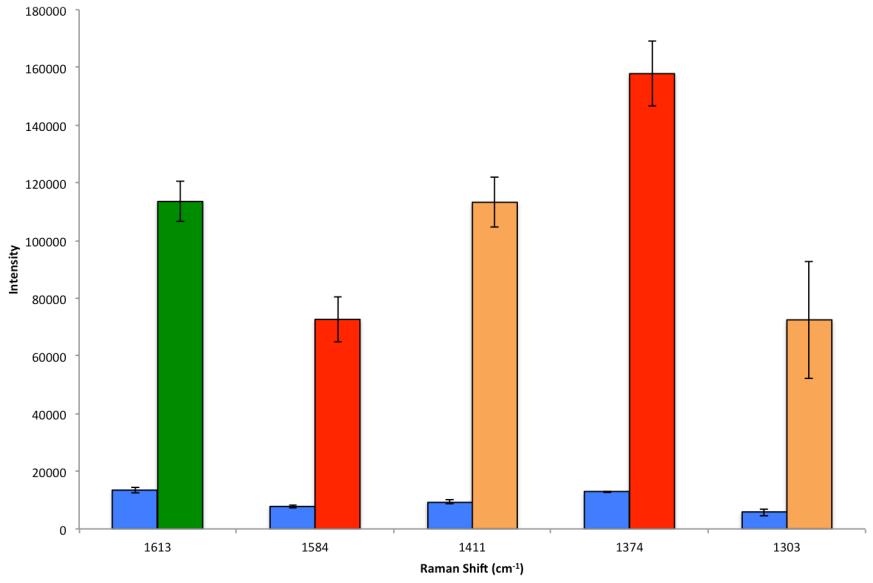

Figure 5.27 SERS intensities obtained prior and post addition of 10 nM ConA to a triplex solution containing each modified nanoparticle component; AgML3-RB1 (green), AgMM1-BT5 (red) and AgMG2-J7E (orange). The blue bars represent the SERS measurements prior to lectin addition. SERS analysis performed on each solution using a 1 second exposure with 10 accumulations at 100% laser power. Error bars shown are the standard deviation of five replicate measurements.

These results indicate that there must be more than one interaction-taking place within solution. Explanations for this could be the formation of dimeric or higher order complexes between individual lectin species following their addition to the nanoparticle solution. Studies have shown that due to dynamic fluctuations between protein-carbohydrate interactions protein aggregation can occur.[195,196] These studies indicate that intramolecular dissociation of carbohydrates may occur from protein surfaces and as a result intermolecular protein-protein and carbohydrate-carbohydrate interactions are promoted as a result. It is the stress of these fluctuations, which cause protein aggregation. Therefore, in the presence of multiple carbohydrate species which may interact with each lectin in a specific or non-specific manner there shall be a number of association, dissociation process ongoing between the lectin introduced to the system and the carbohydrates present. As a result, aggregation of the lectin may result in the formation of homomeric lectin complexes which give rise to different binding affinities resulting in the aggregation of each carbohydrate-nanoparticle species present. It could also be suggested that as these multiple carbohydrate-nanoparticle species are brought together in close proximity a number of carbohydrate-carbohydrate interactions could occur between adjacent carbohydrate residues. These multiple interactions would result in the formation of dense areas of plasmon due to the close proximity of adjacent nanoparticles and as a result, the increase in SERS intensity as detected shall occur.

The differences in SERS intensity obtained in comparison to a higher lectin concentration to a lower lectin concentration being present are more difficult to explain. It would be expected that in an excess of lectin environment larger protein complexes shall be forming due to the multiple carbohydrate-protein interactions occurring, therefore, a greater SERS intensity would be detected due to the enhancement gained by the formation of nanoparticle clusters. However, the converse was obtained with lower protein concentrations resulting in the most intense SERS signals. It could be suggested that if higher protein concentrations are present and large protein complexes are forming then the nanoparticles shall be kept further apart and as a result the clusters formed shall remain to have areas of dense plasmon but these shall be decreased in comparison to the small protein complexes formed in a low protein concentration environment.

5.7 Conclusions

Further progress has been made in the studying of carbohydrate-lectin interactions *via* the design and functionalisation of silver citrate nanoparticles with novel short-chained carbohydrate linkers containing both mannose and galactose. The interactions of the lectins Jacalin and *Lens culinaris* have been explored with different carbohydrate species and concentration dependence has been exhibited. Linear ranges of detection for each carbohydrate-lectin interaction have been obtained by both extinction spectroscopy and SERS with an LOD in the picomolar region being achieved for the interaction of the lectin Jacalin with galactose functionalised nanomaterials. These results supercede the LOD previously obtained for lactose functionalised nanoparticles and the lectin ConA.

The specific interactions of Jacalin with galactose, *Lens Culinaris* with mannose and ConA with lactose have also been tested in a multiplexed format. By forming a triplex solution of each modified nanoparticle component, with each being functionalised previously with a specific Raman reporter molecule, it has been possible to attempt to aggregate each individual component via addition of the lectin to which they have each displayed a specific affinity for. However, problems were encountered when performing this analysis using SERS as aggregation of all three components was detected when only one lectin was present. This initially was believed to be due to cross reactivity between the lectin species and multiple carbohydrate residues. However, following the reduction of lectin concentration this total aggregation effect has not diminished and as a result it has been hypothesised that there may be ongoing interactions in solution between not only the lectin and the carbohydrate species but also lectin-lectin and carbohydrate-carbohydrate interactions could be occurring. Therefore, although a multiplexed assay has not been reached a more interesting and complex phenomena has been explored.

5.8 Future Work

Ultimately the main objective of this chapter has not been achieved i.e. the multiplexing of carbohydrate-lectin interactions using SERS. However, significant advances have been made towards this end goal with the design of new carbohydrate species and the attainment of a triplex formation for SERS detection.

At this point before multiplexed detection can be performed successfully analysis must be carried out to obtain information in regards to the various interactions which may be ongoing within solution which have resulted in this total aggregation effect of all three modified nanoparticle species in the present of non-specific lectins. Modeling of these interactions using SERS could lead to a greater understanding of the fluctuating dynamics of protein-carbohydrate interactions which are ongoing not only within solution but at the cell surface. Exploration of these interactions could provide a new pathway by which the interactions of these species could not only be detected but also exploited for new therapeutic targets.

6. Design of nanoparticle-lectin conjugates for use as cellular imaging agents

Glycans can be found covering the cell walls of all living organisms and are the first point of contact with other approaching cells or pathogens.[197] Cell surface glycans have been exploited by nature to mediate a variety of biological processes such as cell signaling, molecular recognition and immunity through weak carbohydrate-protein interactions.[198-200] As the field of glycomics has received markedly less funding than genomics or proteomics, there currently exists a deficiency in specific tools for the elucidation of both glycan function and structure. By merging this field with nanotechnology, novel multivalent scaffolds have been created which increase the avidity of these materials by several orders of magnitude.

The field of molecular imaging has been reinvigorated by the use of nanomaterials due to their high surface to volume ratio and tunable physical properties positioning them as the key scaffolding materials for new *in vivo* and *in vitro* imaging agents.[201] Examples of such are carbohydrate functionalised quantum dots which have been used for specific cell targeting and *in vivo* optical imaging, glycan terminating carbon nanotubes used for radiation therapy of thyroid tumours and carbohydrate functionalised iron oxide magnetic nanoparticles as contrast agents for magnetic resonance imaging (MRI).[202-204] Pioneering work by Huang and co workers exploited the altered expression of glycan receptors in cancerous cells using a range of carbohydrate functionalised magnetic nanoparticles. MRI was used to explore the cell surface receptors of different tumour cell lines.[11] Significant differences were established between the MRI signature achieved for normal and that of cancerous tissue. Using MRI the simultaneous detection of cancer cells as well as the differentiation of related cancer cell subtypes was possible without the requirement of previous knowledge of endogenous carbohydrate receptors. Following this study, Lee and co-workers performed similar work using iron oxide nanoparticles coated with heparin to detect human mesenchymal stem cells *in vivo*. Improved endocytosis mediated uptake was achieved using the heparin coated nanoparticles in comparison to dextran coated analogues. The other key findings of this study were that neither cell viability, proliferation or differentiation potential were affected by the heparin nanoparticles thus indicating these particles could be used for stem cell tracking in a variety of disease models.[205]

6.1 Design of nanoparticle-lectin conjugates

Following the success of the carbohydrate functionalised nanoparticle aggregation assay described in chapter 4 the applications of lectin protein interactions were investigated further. Previous work by other groups had established the use of carbohydrate functionalised nanoparticles for cellular imaging and with the knowledge that mammalian cells are covered in nine common monosaccharides it was suggested that carbohydrate recognition upon lectin attachment could be monitored. To facilitate this recognition the previous nanoparticle conjugate design was altered to functionalise the silver nanoparticles with lectins instead of carbohydrates.

The PEGlayted linker compounds, which were successfully used in a bioassay format in chapter 2, were introduced in this concept to be used to link the lectins to the nanoparticle surface. Figure 6.1 represents a conceptual diagram of the functionalisation of the nanoparticles for this investigation.

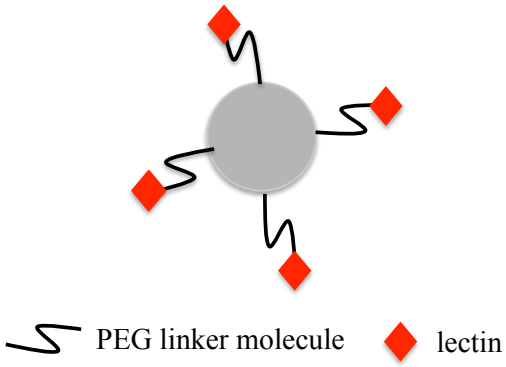

Figure 6.1 Diagram of lectin functionalised silver nanoparticles

The intrinsic benzotriazole dye molecule contained within the PEG linker molecules circumvented the requirement of a mixed monolayer functionalisation method, normally a separate Raman reporter molecule would be used, which simplified the conjugation process. The attachment of a lectin molecule to the linker modified nanoparticles was attempted for a number of specific lectins including Concanavalin A (Con A), Jacalin, *Lens culinaris* (LC) and Wheat Germ Agglutinin (WGA). The structures of each of these lectins are shown in figures 1.11, 5.9, 5.10 and 6.2 respectively. Each of these lectins displays different carbohydrate specificities as summarised in table 6.1.

Table 6.1 Summary of lectin types for attachment to nanoparticles and their carbohydrate specificities

Lectin Type	Carbohydrate Specificity
Con A	α-*D*-mannosyl and α-*D*-glucosyl groups
Jacalin	α-Gal-OMe
Lens culinaris	α-Mannose
Wheat Germ Agglutinin (WGA)	(GlcNAc)2, NeuNAc

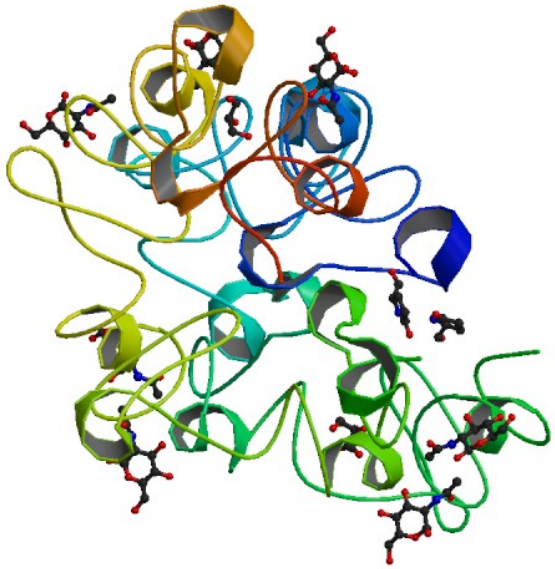

Figure 6.2 Crystal structure of wheat germ agglutinin (WGA lectin) in complex with N-acetyl-D-glucosamine PDB ID: 2UVO

6.2 Functionalisation of Ag nanoparticles with lectin

Initial attempts were made to functionalise the Ag particles with the various lectins, which had been prepared in stock concentrations of 1 mg/mL in 10 mM pH 7.4 phosphate buffer. Utilising EDC.HCl and sulfo NHS coupling chemistry the free carboxylic acid at the terminus of the PEG linker molecules was activated followed by addition of the free lectin to the nanoparticle solution. Following incubation at 4°C overnight the nanoparticles were then purified by centrifugation and redispersed in 10 mM Tris buffer (pH 7.4), however, following centrifugation sedimentation of the nanoparticles repeatedly occurred. To prevent this aggregation occurring the coupling of the lectin to the nanoparticle surface was performed under various conditions including limiting the conjugation time from 16 hours at 4°C to 1 hour at room temperature. Other parameters altered to achieve successful

functionalisation of the particles with ConA included lowering the concentration of lectin added to the nanoparticle solution. Unfortunately, none of the attempted changes to the protocol were successful.

An alternative method of nanoparticle functionalisation was attempted which included the pre-functionalisation of the PEG linker molecules with lectin prior to conjugation to the nanoparticle surface. The chosen PEG linker was incubated in 10 mM phosphate buffer containing EDC.NHS, sulfo-NHS and each respective lectin at room temperature for three hours. Following the conclusion of this period the functionalised linker molecules were attached to 500 µL of Ag citrate nanoparticles by shaking overnight for 16 hours. Following duplicate cycles of centrifugation and washing with Tris Buffer these nanoparticle conjugates appeared stable when analysed by extinction spectroscopy, as shown in figure 6.3.

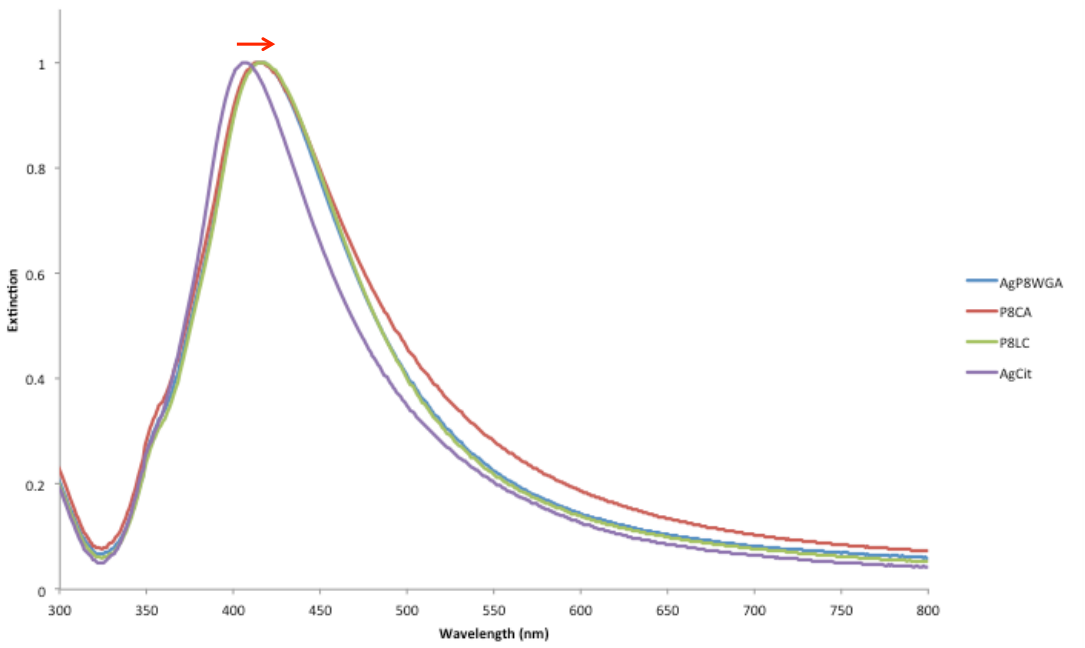

Figure 6.3 Extinction spectra of lectin functionalised Ag nanoparticles showing red shifting of the SPR band following attachment of Con A (CA), Lens Culinaris (LC) and Wheat Germ Agglutinin (WGA) respectively

Figure 6.3 indicates successful functionalisation of the Ag citrate nanoparticles with small red shifting of the plasmon band indicative of changes in the surface dielectric, which has occurred due to functionalisation of the nanoparticle surface with the respective lectin species. Further conformation of the nanoparticle functionalisation was achieved using gel electrophoresis. Gel electrophoresis is one of the most common techniques used in order to separate proteins based upon their size and charge. Separation of metallic nanoparticles

through agarose gels have previously been reported and their use to detect protein nanoparticle binding and for the purification of DNA-nanoparticle conjugates are two of the key uses of this separation technique.[206-208] The functionalised nanomaterials should exhibit a difference in electrophoretic mobility in comparison to the lectin functionalised and unmodified nanoparticles hence this technique was used as a means by which to confirm the success of lectin functionalisation. Figure 6.4 shows the image of the gel obtained when the lectin functionalised nanoparticles were analysed concurrently with both unmodified and linker only functionalised nanoparticles in a 1% agarose gel. The dashed line of figure 6.4 indicates the distance moved by the loading buffer, which had been added to each nanoparticle solution to improve the density of the solution within each well. The nanoparticle solutions analysed were prepared by centrifugation at 6000 rpm for 20 minutes followed by resuspension in 10 µL of 10 mM Tris buffer pH 7.4. To these resuspended solutions 1 µL of loading buffer (6x) was added and the resulting solution added to each well. Comparison of the distances moved has shown that the lectin functionalised nanoparticles have moved a greater distance than those of the non-lectin modified nanoparticles, therefore, in conjunction with the other characterisation data it can be concluded that lectin functionalisation has successfully been achieved.

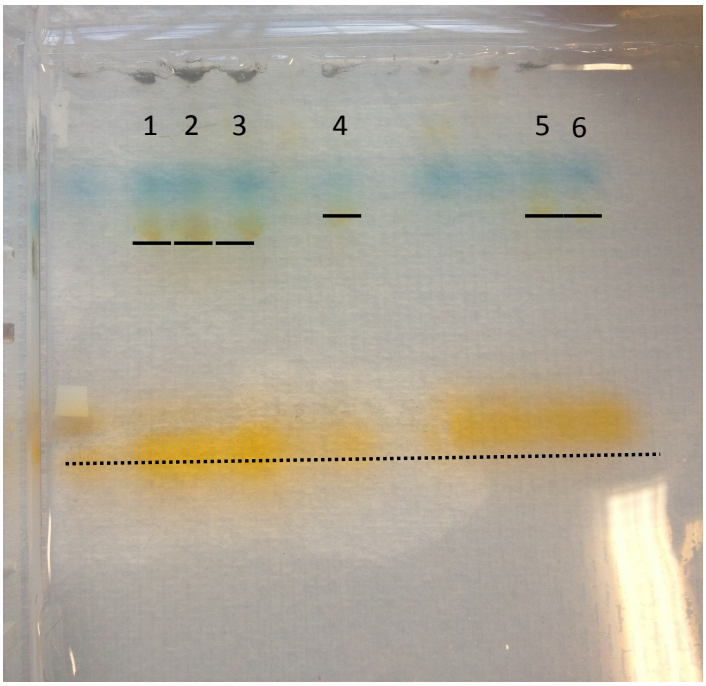

Figure 6.4 Gel electrophoresis: 1% Agarose gel ran in 1 x TBE buffer for 90 minutes at 160 volts: (1) AgP8ConA (2) AgP8LC (3) AgP8WGA (4) AgP8 only (5) and (6) AgCitrate nanoparticles

Toxicity concerns still plague the widespread use of silver nanoparticles for *in vivo* applications. However, these materials remain active in catheters and wound dressings for therapeutic applications despite these concerns.[209] Studies of the toxicity of silver nanoparticles in human cell lines indicate the toxicity of these materials can initially be detected through morphological changes of the cell.[210] Following comparison of the cells used in these experiments during culture and post-nanoparticle incubation no such significant changes were detected which indicated cell viability had not been compromised. Cell viability experiments were also conducted by staining cell culture samples with 0.1% Trypan Blue and performing a cell count of non-stained cells. Cells, which have been stained, had interacted with the dye, due to membrane damage of the cells, and were therefore dead. The cell counts obtained prior and post nanoparticle incubation were again almost identical which indicated the cell viability was uncompromised. The lack of cell necrosis may also be a result of the capping of the silver nanoparticles with the polymeric ligands preventing interaction of the silver ions with cellular organelles. As the following studies are concerned with *in vitro* profiling of cells no other cell viability studies were performed. However, it is acknowledged that prior to any future studies in an *in vivo* environment stringent toxicological studies should be performed.

6.3 SERS analysis of CHO and HeLa cells

Following the successful conjugation of each lectin to the nanoparticle surface, it was then possible to incubate these particles with the chosen cell lines. Chinese hamster ovarian cells (CHO) were chosen due to their robust nature and widespread use for repeated cell culture. CHO cells have been widely used in proteomic research as host cells for the expression of recombinant proteins whilst also being a vital cell line for both genetic and toxicity studies.[211,212] The HeLa cell line is an immortal cell line derived from ovarian cancer cells of Henrietta Lacks and these cells have been used routinely in research for applications ranging from the testing of polo vaccines to new medicinal treatments for ovarian cancer.[213] As this is such a prolific cell line that can be cultured routinely, these cells were chosen for analysis in this study.

Initial studies performed focused on the addition of lectin functionalised nanoparticles to the two chosen cell lines. The protocols by which these cells were cultured and nanoparticle addition was performed are described in experimental section 9.10.5. Ideally for biological analysis, detection would move what is referred to as the ‘’biological imaging window’’ by using a near-IR 785 nm laser excitation wavelength to overcome any fluorescent background signals. For these studies, analyses of each cell line were performed at 633 nm and 532 nm

due to the availability of confocal mapping capabilities. The use of confocal mapping further enhances the signal obtained from the cellular samples due to the arrangement of the optics in such systems ensuring only a small-defined volume is being sampled which increases spatial resolution and rejects background light.[214] As individual cells are being analysed relatively weak background fluorescence signals are achieved in comparison to the analysis of intact tissue, therefore, 633 and 532 nm excitation wavelengths could be used without significant levels of detrimental background fluorescence.[215]

6.3.1 Analysis of CHO cells at 633 nm excitation.

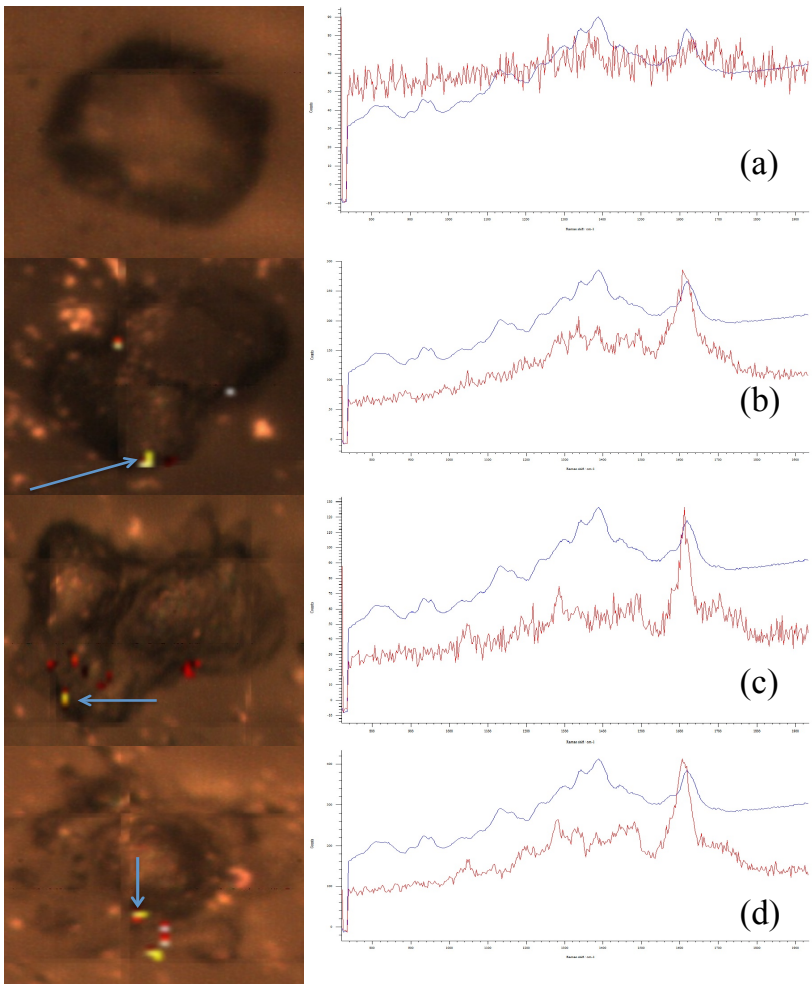

Figure 6.5 CHO Cells analysed using a 633 nm excitation wavelength. Analysis performed using Streamline™ using a 0.5 µm step size and a 5 second exposure time with 10% laser power. White light images of each analysed cell are shown with the DCLS data overlayed to show areas of localised intensity due to the presence of the functionalised nanoparticles. (a) Analysis performed after incubation of AgP8ConA nanoparticles for 1 hour. (b)-(d) analysis performed after incubation of AgP8ConA nanoparticles for 3 hours.

To obtain data of the highest resolution possible mapping analysis was performed using a 0.5 μm step size with a 5 second accumulation period. Prior to cell incubation nanoparticles were functionalised with the lectin ConA. ConA should become attached to monosaccharides or complex carbohydrates containing mannose or glucose residues. Following the analysis of these cells, the mapping data obtained was analysed using a direct classical least squares (DCLS) algorithm, which compared the spectra obtained with a reference spectra taken previously. The algorithm calculates regions of the map with spectra similar to that of the reference spectrum. These areas, with the most intense colour, are those where the greatest match to the reference spectra occurs. The advantages of using such data analysis methods are that the reference spectra can be fitted to the complete component spectra obtained, therefore, the signals obtained are not only a result of analyzing the signal intensity achieved at just one point.

The functionalised nanoparticles were added to the CHO cells and incubated for different periods to identify the optimised conditions to achieve the best signal from the nanoparticle conjugates. Unfortunately the signals achieved from these cells were not as envisaged. Figure 6.5 presents the spectra of individual cells following incubation for different periods. After 1 hour no signal was achieved from the CHO cells (image (a)), however, the signal obtained was significantly increased following incubation for a period of 3 hours (images (b)-(d)). This indicated greater binding had occurred following the increase in incubation time.

From figure 6.5 image (a) shows that no nanoparticles were present within or surrounding this CHO cell. Whereas image (b)-(d) show a small number of low intensity signals located on the periphery of each cell. These low intensity signals are due to the presence of a peak in the region of 1613 cm^{-1}, which can be correlated to the quadrant ring stretch of the reporter molecule. Further peaks were identified in the spectra obtained from the cell analysis, which have a similar spectral fit to those of the reference spectra but have a very low intensity. This spectral fit indicates the signals being elucidated from the cellular analysis were those of the functionalised nanomaterials incubated with the cells and were not because of background signals generated from components of the cell or the cellular media. The low signal intensity measured could be a result of the 633nm laser excitation which is significantly shifted from the resonance of both the silver nanoparticles and the benzotriazole dye being used or it could be due to poor binding of the nanoparticles with the CHO cell type.

6.3.2 Analysis of HeLa cells at 633 nm excitation.

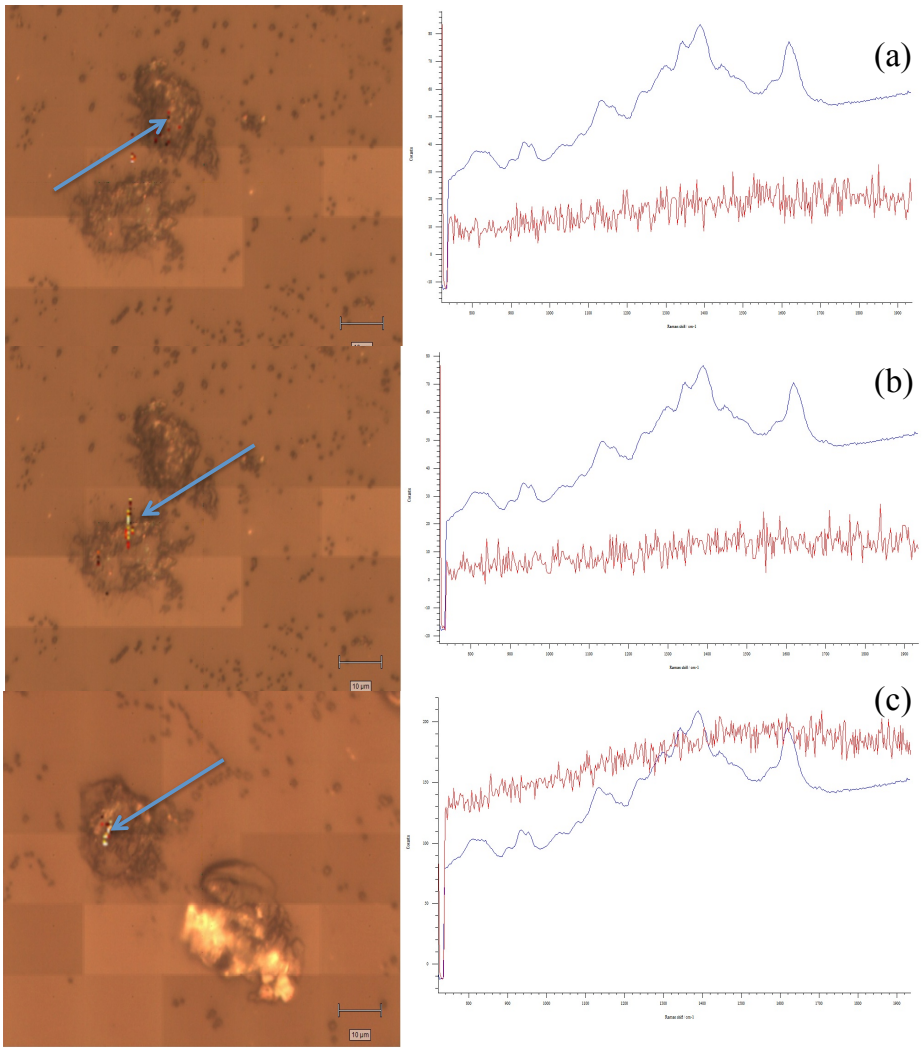

Figure 6.6 Results from HeLa cell line following the incubation of (a) and (b) ConA functionalised AgP8 nanoparticles and (c) Jacalin functionalised AgP8 nanoparticles for a 3 hour period prior to analysis. For each sample 10 cells were analysed and the spectra shown are those which provided the highest intensity signals when analysed using a 0.5 µm step size with 5 seconds exposure at 10% laser power.

To further investigate the lack of signal obtained from the CHO cells when using the 633 nm excitation a second cell line was used. Previous studies established that incubation of the nanomaterials for a 3-hour period afforded the best signals; therefore, this incubation period was adopted for further studies. However, once again when using a 633 nm excitation to analyse lectin functionalised nanoparticles within HeLa cells the results obtained were underwhelming. No distinct signal could be detected in any of the cells tested when this cell line was used in combination with a 633 nm excitation wavelength. Figure 6.6 provides

representative spectra of the HeLa cells analysed and the spectra obtained from the brightest areas following analysis using DCLS. Images (a) and (b) of figure 6.6 represent HeLa cells following the addition of ConA functionalised nanoparticles. DCLS analysis of these cells indicated low areas of intensity across each cell, however, the spectra in relation to each of these areas did not fit the data as expected and was in fact a false positive provided due to an increased background contribution. This increase in background signal was attributed to autofluorescence from the HeLa cells. As no signal had been achieved when ConA functionalised particles were used in either cell line, a second lectin was tested to discover the route of the issue.

Jacalin functionalised nanoparticles were added to the HeLa cells and complexing of either galactose or mannose containing carbohydrates was expected. However, once again no significant signal intensities were found following mapping analysis of these cells. Image (c) displays a representative image, which contains a small number of co-localised high intensity areas, however, these areas of localized intensity were in fact once again found to be due to an increased background signal due to auto-fluorescent contributions from the cell.

Analysis of both cell types with different types of lectin functionalised nanoparticles have shown that very low signal intensities were achieved using a 633 nm excitation. As a result, it was concluded that for future analysis it was more important to move closer to the resonance of both the nanoparticles and the benzotriazole reporter molecule attached. Ideally for biological analysis detection would move to the near infrared region using a 785 nm laser excitation wavelength to overcome any fluorescent background signals. However, as the most intense signals for these conjugates shall be achieved when using an excitation wavelength closer to the resonance of both the nanoparticles and the reporter molecule a change in excitation wavelength to 532 nm was opted for.

6.3.3 Analysis of CHO and HeLa cell lines at 532 nm excitation wavelength.

Using the WITec Alpha 3000 R confocal Raman microscope non-destructive cellular analysis was possible. This system permitted the ability to acquire individual Raman spectrum at each pixel of the imaging area selected for each cell. This gives rise to thousands of individual Raman spectra, which can be used to construct an intensity map profile of each cell to determine the localization of a particular chemical substance. Following the unsuccessful studies at 633 nm a fresh approach was taken when conducting the experiments at 532 nm.

Both cell types chosen previously, CHO and HeLa, were incubated with silver nanoparticles, which had been functionalised with the novel P8 linker and the lectin *Lens culinaris* (LC) was attached. As stated previously, *Lens culinaris* exhibits carbohydrate specificity towards mannose residues.

Figure 6.7 shows that by using the 532 nm excitation wavelength definitive signals could be achieved. These images are the result of the modified nanoparticles becoming localised in areas which are rich in mannose or glucose containing residues. As can be seen from these images the binding is highly specific with localization of the nanotags restricted to specific areas indicating non-specific binding has been circumvented due to the use of the PEG spacer ligand. Figure 6.8 presents representative spectra obtained using a 532 nm excitation wavelength of functionalised AgP8 nanoparticle samples. Image (a) shows the reference spectrum obtained for AgP8 samples prior to cellular analysis with image (b) displaying a representative average spectrum, which has been obtained when cell analysis was performed using AgP8LC probes.

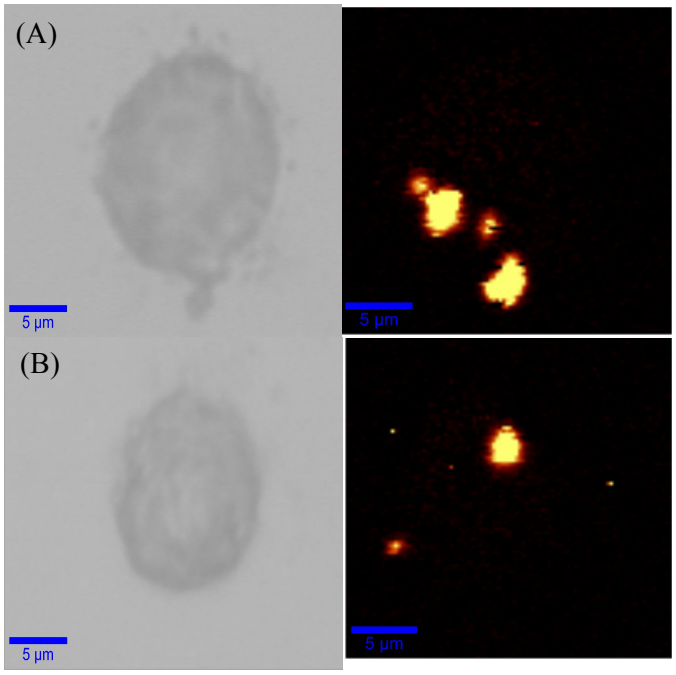

Figure 6.7 HeLa cell images obtained using a 532 nm excitation wavelength and mapping a 25 x 25 µm area with 100 points per 100 lines for each measurement taken. (A) and (B) both are the resulting white light and false colour images generated from the addition of the *Lens culinaris* modified nanoparticles. False colour images intensity thresholds set to a maximum limit of 5000 counts and low limit intensity of 0.

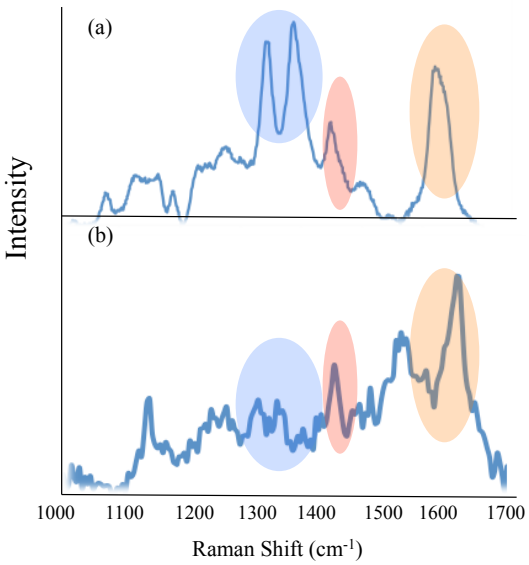

Figure 6.8 Representative spectra obtained for (a) AgP8 analysed at 532 nm using a 1 second exposure with 10 accumulations (b) baselined and average spectrum of AgP8LC and AgP8ConA samples in HeLa cells

From these cellular analyses, it can be concluded that specific interactions between HeLa cellular components and lectin functionalised nanomaterials can be detected efficiently using a 532 nm excitation wavelength. To expand on this investigation lectin functionalised nanomaterials were incubated with CHO cells and analysed using a 532 nm excitation wavelength. Figure 6.9 displays white light images of the CHO cells and the corresponding false colour images of these cells obtained.

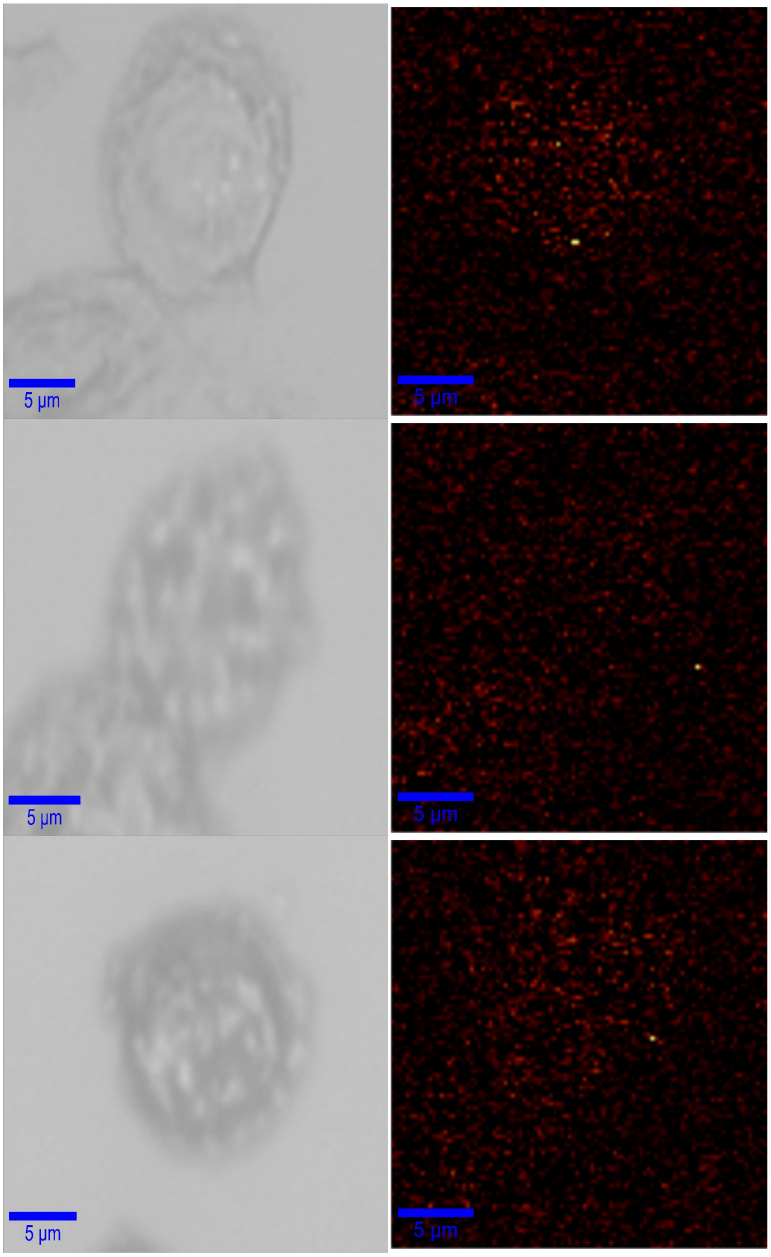

Figure 6.9 532 nm excitation analysis of CHO cells after the addition of *Lens culinaris* modified nanoparticles. Threshold of images is 1000 to 0.

Analysis of CHO cells following the incubation of AgP8LC probes for 3 hours provided no areas of defined high intensity when analysed using a 532 nm excitation wavelength. Small intensity correlations are seen in the false colour images which are due to autofluorescence from background cellular materials. As a result of these analyses the CHO cell line was abandoned as no discernable signals could be achieved using either 532 nm or 633 nm excitation wavelengths. This could be attributed to poor binding of the lectin functionalised

nanomaterials to the CHO cell lines, a lack of signal enhancement gained from the use of the silver nanoparticles or reporter molecule due to the use of a 633 nm excitation wavelength or most probably a combination of both. However, as successful signals were achieved using the HeLa cell line it has been established that these lectin functionalised nanomaterials could be used for carbohydrate imaging of mammalian cells.

6.4 HeLa cell analysis using differing linker lengths

Following the success of employing lectin functionalised nanoparticles as cellular imaging agents of the HeLa cell line using 532 nm excitation wavelength further studies were completed to investigate the dependence of the intensity of the signal obtained to the length of spacer molecule attaching the lectin to the nanoparticle surface. As discussed in chapter 3, two PEG linkers were devised which differed in the length of the polymeric spacer group. Previous studies have shown that the use of short spacer groups has provided an increased SERS intensity when employed in a carbohydrate-lectin assay (chapter 4). Therefore, an investigation was carried out to ascertain if dependence existed on the signal intensity gained due to the proximity the lectin molecule was held to the nanoparticle surface when being used as a cellular imaging agent.

This study was carried out by pre-functionalising solutions of both the individual P8 and P41 linkers as well as a mixed solution of both linkers with the lectins *Lens culinaris* (LC) and wheat germ agglutinin (WGA). Following attachment of the lectin functionalised ligands to silver nanoparticles and the incubation of these materials with HeLa cells, SERS analysis was performed at 532 nm excitation to identify any differences in signal intensity obtained. Figure 6.10 shows the white light and false colour images obtained for HeLa cells incubated with these functionalised materials and plots of SERS intensity for the 1613 cm^{-1} peak for each ligand used. As is clear from the data obtained there is a significant increase in intensity when the lectin is attached to the P8 functionalised nanoparticles. This is as expected as more nanoparticles are able to come within close proximity of the surface bound carbohydrate receptors due to the small spacer ligand. Therefore giving rise to areas of dense plasmon, which shall result in increased SERS intensity.

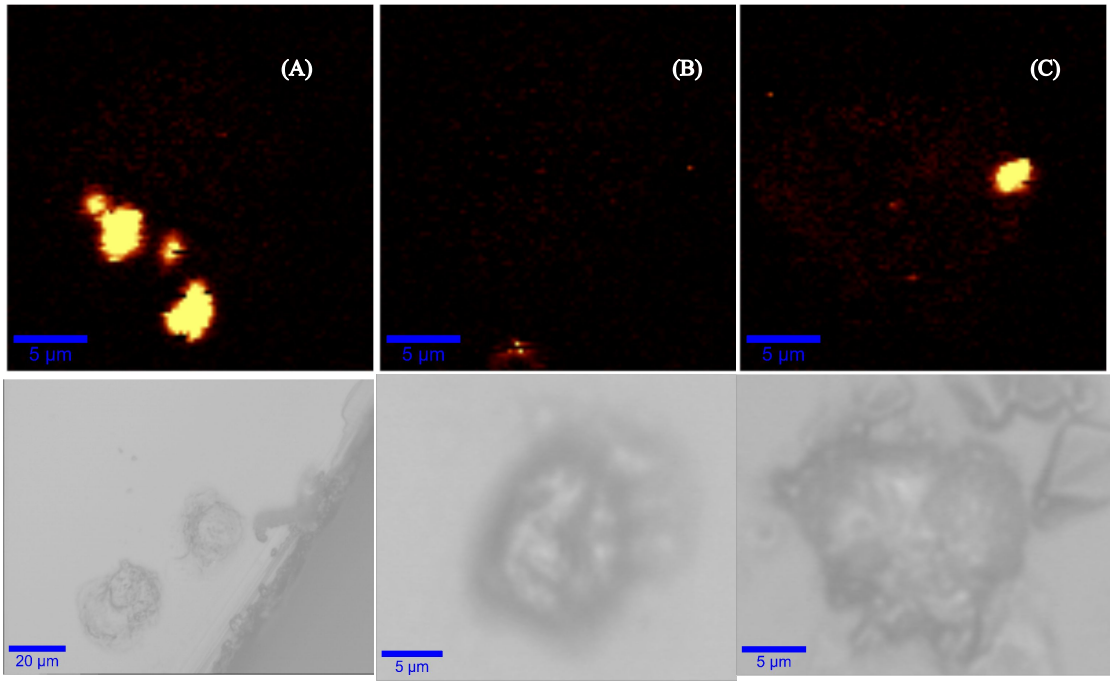

Figure 6.10 False colour images and the corresponding white light images of HeLa cells incubated with (a) AgP8LC conjugates (b) AgP41LC conjugates and (c) AgP8P41LC conjugates. False colour images set at a threshold of 5000 to 0 counts.

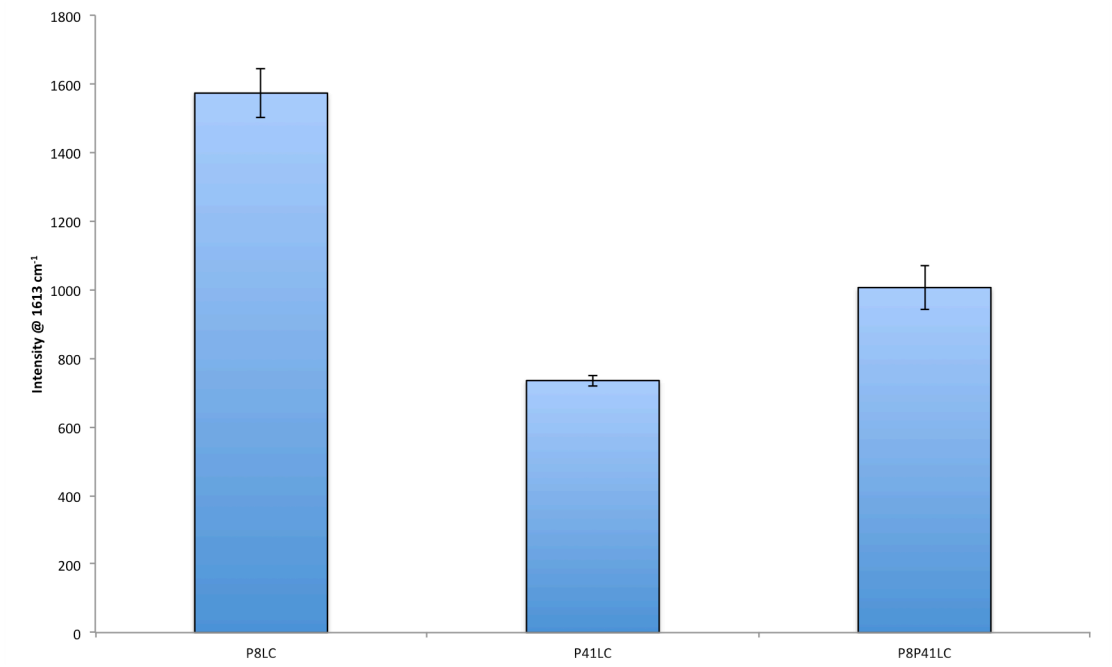

Figure 6.11 SERS intensity measured at 1613 cm^{-1} using a 532 nm excitation wavelength measured for each set of incubated conjugates in HeLa cells. Average of 15 spectra from each false colour image set at the threshold of 5000 to 0 counts. Error bars are the result of the standard deviation of these measurements.

From the images shown in figure 6.10 and the intensity measurements collated in figure 6.11 it is clear that the most intense signals are obtained when the nanoparticles are functionalised with the P8 linker. As discussed previously this is to be expected due to the close proximity in which the nanoparticles will be bound creating dense areas of plasmon. A decrease in intensity is apparent for P41 functionalised nanoparticles, which shall be due to the increased distance between lectin functionalised nanoparticles bound to the carbohydrate species due to the increase in spacer length preventing the nanoparticles from being bound in close proximity. An increase in intensity is detected for the P841 conjugates in comparison to the signals achieved for the P41 functionalised nanomaterials. This is most likely to be due to the lectin being attached to the P8 linker moiety resulting in a number of nanoparticles being brought together in close proximity.

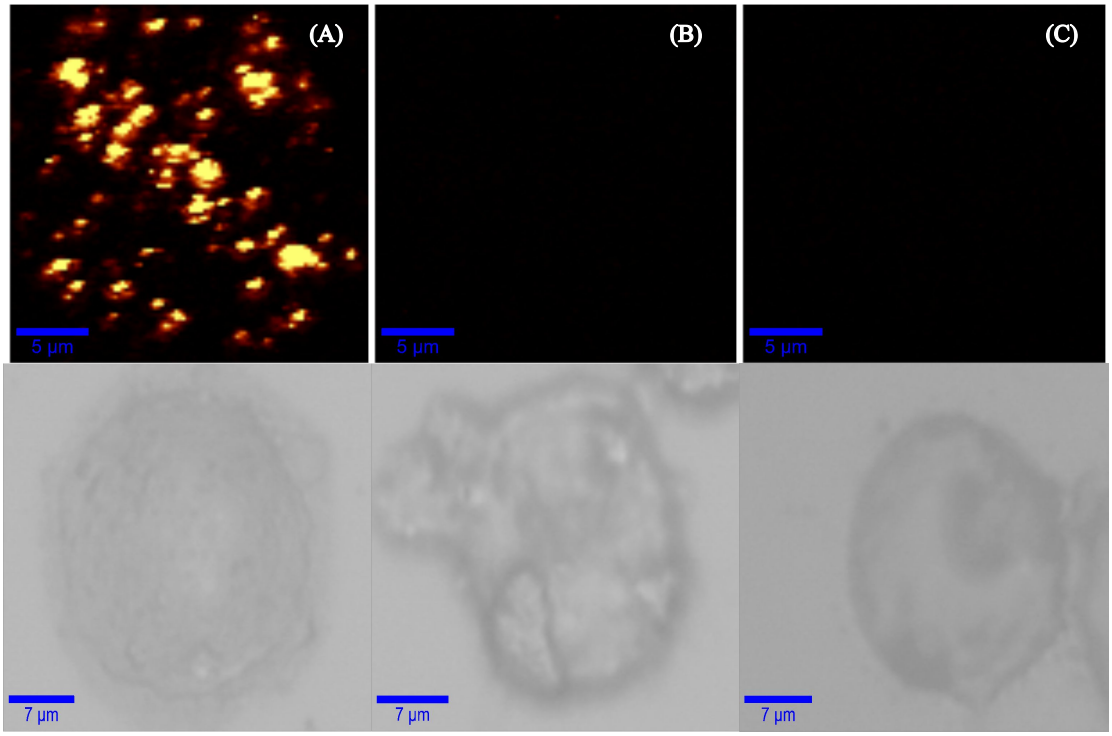

Figure 6.12 False colour images and corresponding white light images of PC3 cells incubated with (a) AgP8WGA conjugates (b) AgP41WGA conjugates (c) AgP8P41 conjugates. False colour images set at a threshold of 15000 to 0 counts.

Figure 6.12 shows that following incubation with all three sets of conjugates high intensity signals are only obtained for AgP8WGA conjugates which once again can be correlated to a shorter spacer molecule allowing for multiple interactions of the bound lectin residues with cell surface carbohydrates. As a result, more nanoparticles are brought in to a closer proximity and an increase SERS intensity is obtained. However, little to no signal is

achieved for the P41 and P8P41 conjugates. This is believed to be due to steric hindrance due to the presence of the significantly longer spacer ligand preventing a similar number of carbohydrate-lectin interactions to occur in comparison to the P8 functionalised nanomaterials. The intensity obtained for each set of conjugates are shown in figure 6.13 and are directly correlated to the false colour images shown in figure 6.12. Therefore, it can be concluded that using a shorter ligand molecule results in a higher number of carbohydrate-lectin interactions being possible due to an increased surface density of lectin residues and the ability to bring more nanoparticles into closer proximity due to the short-range interactions occurring.

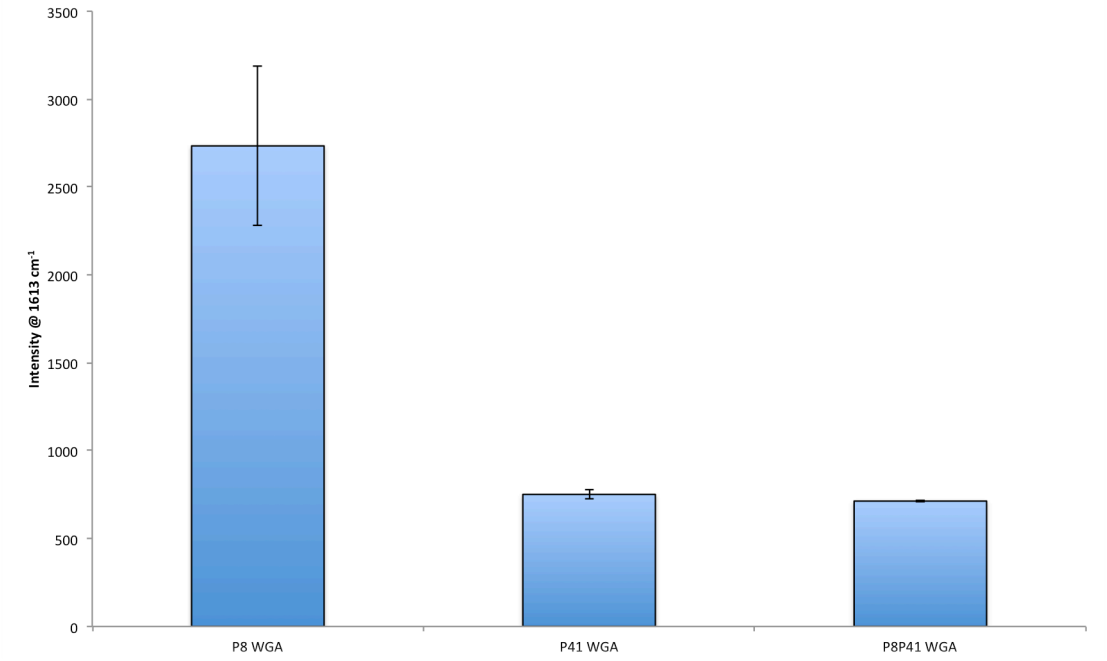

Figure 6.13 SERS intensity measured at 1613 cm^{-1} using a 532 nm excitation wavelength measured for each set of incubated conjugates in HeLa cells. Average of 15 spectra from each false colour image set at the threshold of 15000 to 0 counts. Error bars are the result of the standard deviation of these measurements.

6.5 Cancerous cell detection using nanoparticle-lectin imaging agents

Histological features such as irregular stratification, loss of intercellular adherence and polarity alongside changes in nuclear size and changes in miotic activity are currently used to evaluate cancer cell development.[216] The combined evaluation of these factors forms the basis of histological classification, which is responsible for the grading of cancerous tumours. These evaluations are typically made of *ex-vivo* tissue samples, which are obtained from biopsies that are typically randomly retrieved from a patient. This results in a large number

of unnecessary surgical procedures and a high level of stress for the patient.[217] To reduce the number of irrelevant biopsies being performed a new methodology of tissue identification is required which can be used for either real time diagnoses or as an aid to guide the biopsy process to areas of relevant tissue.[218,219] As such at the forefront of this research are an array of spectroscopic techniques which are being studied to fulfill this purpose.[220] Raman spectroscopy has been successfully applied in this respect to discriminate between normal and pre-malignant tissue using multivariate classification techniques during *in vitro* studies.[215,221] To date there remains an opportunity for Raman spectroscopy to be utilised as the leading technique for *in vivo* spectroscopic analysis, however, to ensure this occurs advancements must be made in the development of sensitive equipment and powerful spectral analysis to obtain the real-time extraction of clinically relevant parameters which shall enable tissue malignancy to be detected without the need for a surgical biopsy.

Following the successful detection of carbohydrate residues using the nanoparticle-lectin imaging agents, applications were sought for the use of these agents within a clinical environment. It was desired to use these nanoparticle-lectin agents to monitor changes in the carbohydrate composition of cells by modifications such as glycosylation, acetylation etc. In researching this area literature was found which detailed the over expression of sialic acid residues on colorectal cancerous cells.

Sialic acids are the outermost monosaccharide units found on glycolipids and glycoproteins, which play a key role in the recognition of pathogen attachment to cells. These sialic acids are a diverse range of sugars, which share the same nine-carbon backbone. These sialic acid residues are amongst the most diverse sugars found on glycan chains of mammalian cell surfaces. This diversity is generated from the various substitutions possible of the nine-carbon backbone and the extensive linkages able to occur at the two position.[222,223]

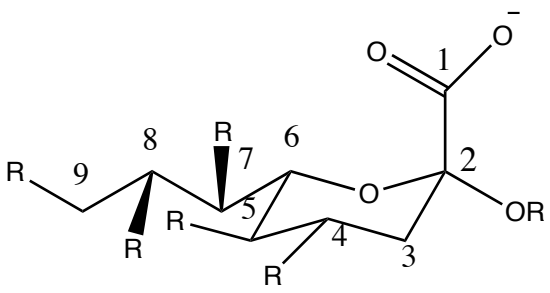

R2= H in free Sia:alpha linkage to Gal, GalNAc, GlcNAc or Sia
R4= H or O-Acetyl
R5= Amino, N-Acetyl, N-glycoyl or Hydroxyl
R7= H, O-Acetyl
R8= H, O-Acetyl, O-methyl, O-sulfate or Sia
R9= OH, O-acetyl, O-lactyl, O-phosphate, O-sulfate or Sia

Figure 6.14 Backbone structure of Sialic acid and the many possible substitutions, which may take place on the nine-carbon backbone

Sialic acids play key roles in immunity, homeostasis and injury due to being key intrinsic ligands expressed on leukocytes, platelets and endothelium.[224,225] However, the most important observation for this research is the elevated increase in sialic acid expression on cancerous cells.[226,227] The WGA lectin used in previous studies has the ability to detect sialic acids. Therefore, clinical cell samples were obtained of both cancerous and non-cancerous prostate cells from the same patient. After incubation with the AgP8WGA probes analysis was conducted using a 532 nm excitation wavelength to enable the detection of significant differences in sialic acid expression between both cell lines.

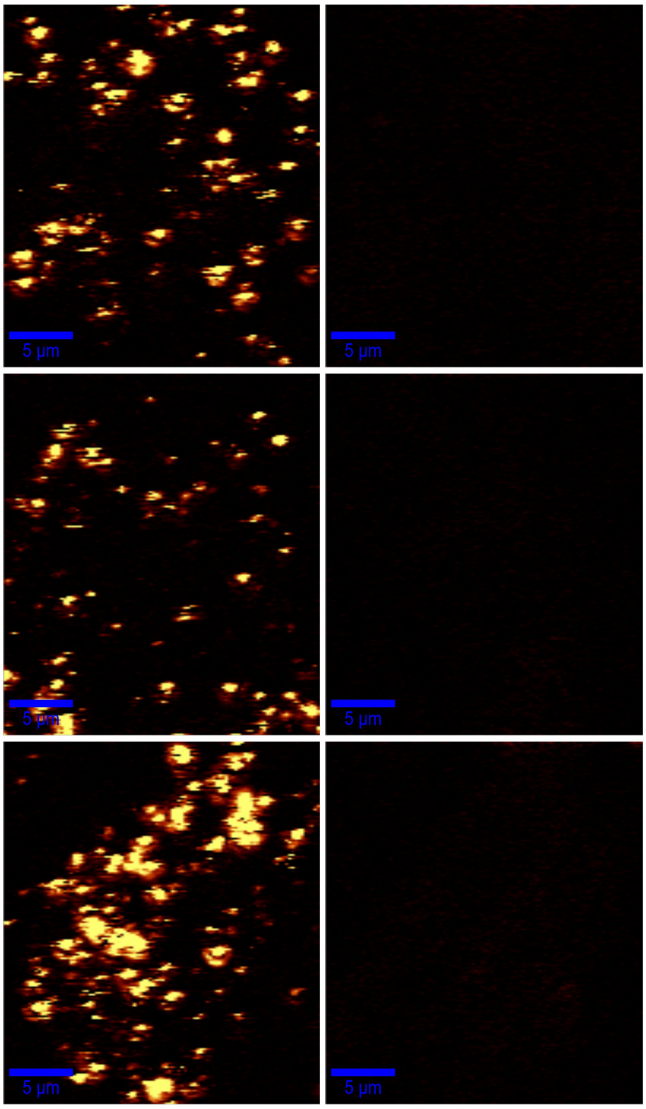

Figure 6.15 False colour images of PC3 cells (left hand side) and PNT2A cells (right hand side), which have been incubated with AgP8WGA functionalised nanoparticles. False colour images were generated *by* plotting the intensity of the 1613 cm^{-1}peak across the spectral map. Each false colour image was set to a threshold limit of 5000 maximum and 0 minimum intensity.

Figure 6.15 depicts the false colour images obtained from the analysis of multiple cells of both cell lines following the incubation of AgP8WGA probes. The false colour intensity profiles of the cancerous cells indicate highly dense intensity areas correlated to the attachment of WGA lectin to elevated levels of sialic acid residues. Analysis of PNT2A (non-cancerous) cells show a significant decrease in the intensity profile in comparison to the PC3 cells analysed. This can be correlated to the elevated expression of sialic acid residues upon rectal cancerous cells. Spectral analysis based on the peak height at 1613 cm^{-1} of the benzotriazole dye reporter molecule shows reproducible analysis is obtained for the

PC3 cells whilst significantly lower intensities are achieved for the PNT2A cell line when incubated with these probes. These results are shown in figure 6.16.

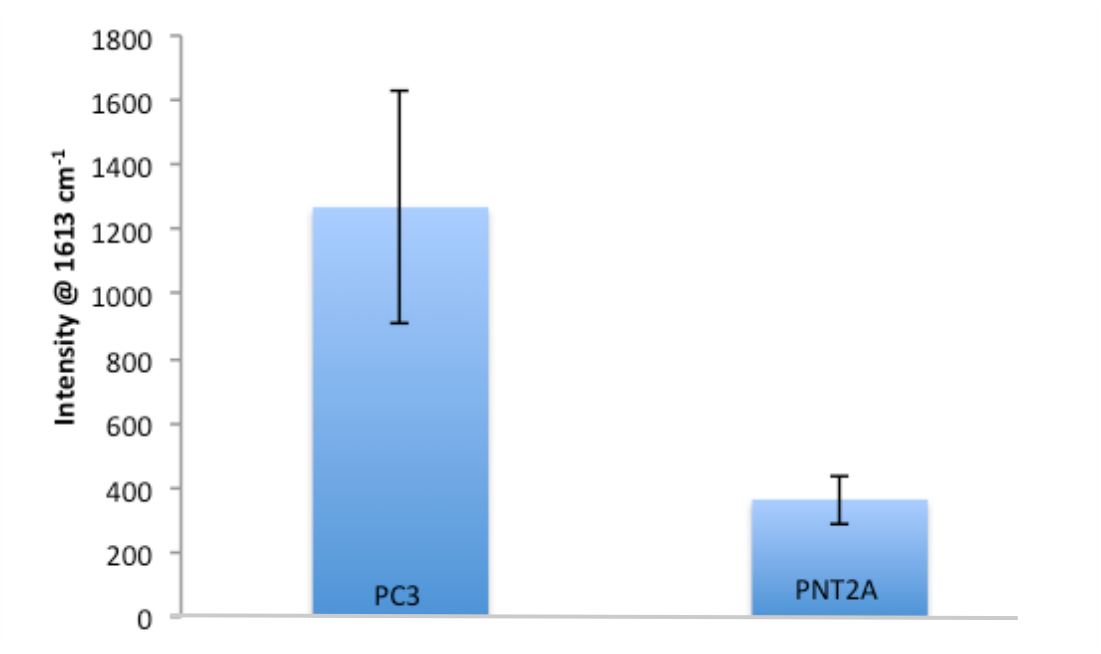

Figure 6.16 SERS intensity obtained for 15 spectra obtained from mapping AgP8WGA probes incubated with PC3 and PNT2A cells

Therefore, it can be concluded that a novel means by which prostate cancerous cell detection can be achieved in the presence of non cancerous cells has been created by comparison of the expression of sialic acid residues. These analyses were repeated over 50 cells of each type and only a small number of those are shown in this thesis. As of yet no false positives have been achieved from the PNT2A non-cancerous cell line which would provide doubt as to if this methodology was successful or not.

Further studies were performed to prove that these nanoparticle-lectin imaging agents were restricted to the surface of the cell rather than being internalised by mediated uptake by endocytosis. To facilitate this analysis depth profiling was performed using confocal Raman microscopy at a 532 nm excitation. A range of depth parameters were studied with each set of results indicating as expected that the localization of these imaging probes was restricted to the cellular surface as shown by figure 6.17. Reconstruction of the various cell slices obtained using confocal imaging permitted the construction of a 3D cellular map. The areas of high intensity correlate to the mapping of the 1613 cm^{-1} peak of the reporter molecule. This peak was used in these studies to clarify the location of the probes around the cell. Further conformation of these results is necessary and could be obtained using transmission

electron microscopy (TEM). However, facilities to conduct such analysis were unavailable at the time of reporting these results and will be completed at a later date.

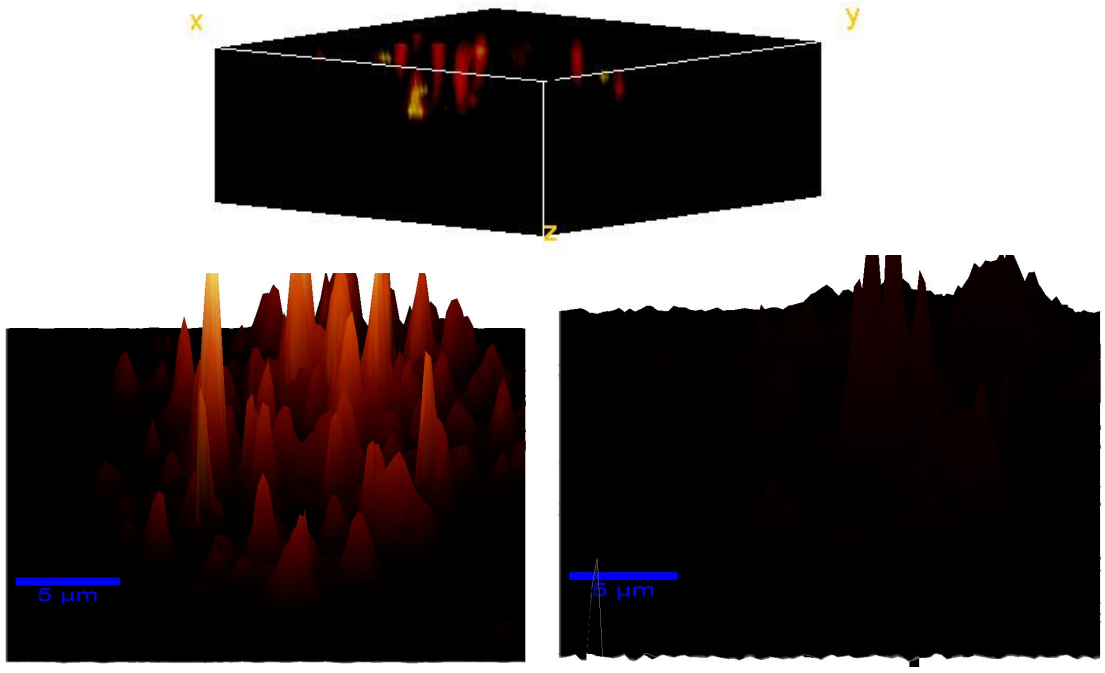

Figure 6.17 Depth profiling image of a PC3 cell-using stack profiling set at a 10 µm depth with 10 layers imaged at 1 µm depth for each slice. The resulting image shows the 3D intensity maps for the 1613 cm^{-1} peak obtained for the AgP8WGA probes. The top image is the completed stack profile whilst the image on the right is slice 1 whilst the image on the left is slice 10. The areas of highest intensity correlate to the greater concentration of probes present.

To further confirm the reproducibility of these studies as a methodology for cancerous cell detection analysis must be performed on a larger scale of samples using a high through put technique such as microfluidics. Although in its infancy, this methodology highlights the sensitivity SERS can provide in detecting biomarkers of malignant cells. Comparisons should be drawn between the histological evaluation of these cells and the detection achieved using SERS when the histological data is made available. Research by other groups has indicated that sialic acid expression becomes altered depending on the grading of tumour present.[228,229] As a result if comparisons can be drawn between the histological evaluation of these cells and the SERS intensity achieved using these imaging agents then a new comparative methodology could be pioneered to aid histological classification of cancerous cells. Identification of further carbohydrate biomarkers for disease states could also facilitate the simultaneous detection of multiple diseases due to the ease by which these imaging agents could be multiplexed with high sensitivity by using SERS.

6.6 Conclusion

The preparation and functionalisation of silver nanoparticles with three different lectin species has been successfully achieved and characterised using both extinction spectroscopy and gel electrophoresis.

The incubation of these nanomaterials with 3 distinct cell lines has also been explored and optimised prior to analysis at two distinct excitation wavelengths. The failure to achieve signal when a 633 nm excitation wavelength was used was not unexpected due to the significant move away from the resonance profile of both the silver nanoparticles and intrinsic benzotriazole reporter molecule being used. However, by moving to a shorter wavelength of 532 nm it was possible to achieve characteristic SERS spectra of the benzotriazole reporter molecule when conjugates were applied to both HeLa and prostate cancer cells.

The carbohydrate specificity of each lectin species has been exploited in an attempt to elucidate the carbohydrate composition of each of these cell lines. As a result of this success the specificity of the lectin WGA towards sialic acid residues has further been exploited for the detection of cancerous cells upon which an elevated expression of sialic acids exist. By comparison of clinical samples from the same human patient of both cancerous and healthy prostate cells it has been possible to elicit an off/on response to differentiate between cell species. This is a fundamental investigation towards devising a new histochemical approach to cancer cell detection without the need for the laborious cell staining and analyzing processes currently used. Although, it must be stated this work is in its infancy and further extensive experiments are required to support this initial data set.

6.7 Future Work

To further support the results reported TEM images must be obtained of the corresponding cells to understand fully where these nanoprobes have been located in order to support the conclusion of their localisation on the surface glycolax of mammalian cells. Further to this, it would be beneficial to next move to a higher throughput testing of the prostate cancer cell type. One means by which this could be achieved would be the incorporation of these cells and nanoprobes in a microfluidic device, which would reduce the time scales for each reagent to be delivered to the cell mainframe. This form of analysis should also allow a more accurate profile of the cell proteomic and glycomic state to be preserved and analysed in real time *via* live cell analysis.

Other approaches which could be utilised for the detection of prostate cancer by these means could be the printing of either carbohydrate or lectin arrays on a substrate for use in a microfluidic device to further investigate the composition of carbohydrates present on certain cell lines by flowing the cells into a chamber containing either a carbohydrate or protein array and identifying which cells become fixed due to the carbohydrate-lectin interactions.

7. Conclusions

As new diseases emerge and current treatments become less effective the need for early stage disease detection and the development of new therapeutics are of increasing importance. The importance of bio-nanotechnology to this field cannot be underestimated.

This research reports the first synthesis of novel ligand linker chemistries, which have established improved nanoparticle stabilisation as well as qualitative and quantitative SERS responses. The incorporation of a PEG spacer ligand has improved nanoparticle solubility, increased stability and provided a platform by which biomolecules can be attached. This has permitted the use of these nanomaterials in various biological assays with qualitative detection being achieved indicating that the biological integrity of the biomolecules attached is preserved. Thus, novel nanomaterials have been created which could be used in a range of future diagnostic assays.

One of the least understood fields in biological detection are the interactions, which exist between both the glycome and proteome. Lectins are ubiquitous carbohydrate specific proteins throughout nature and a growing concern surrounds their over consumption with links to various disease states. To further understand the basis of these interactions a sensitive platform is required to provide a means of rapid detection of such interactions. The use of SERS detection in such an assay format has been devised *via* the design of novel linker chemistries to tether carbohydrate residues to nanoparticle surfaces. From the creation of these materials, multivalent interactions were made possible with specific lectins in solution. Using SERS detection unrivalled quantitative detection limits have been achieved in comparison with extinction, dynamic light scattering and fluorescence spectroscopy limits previously published. This research has been expanded in attempts to create a multiplexed assay format, which permitted the detection of multiple carbohydrate-protein interactions simultaneously. However, although significantly lower detection limits have been achieved for multiple individual protein-carbohydrate studies it has not yet been possible to achieve multiplexed detection. The difficulties in achieving this multiplexed assay need further exploration however, due to the studies performed, it can be assumed that multiple biological interactions are ongoing which are not restricted to only carbohydrate-protein interactions but could also involve protein-protein and carbohydrate-carbohydrate interactions.

The establishment of an assay to quantify protein-carbohydrate interactions directed this research towards analyzing such interactions at the cellular interface. The identification of new cellular imaging agents are key to the detection of new disease states being established

in a high throughput manner whilst also establishing the route by which these diseases progress. New imaging agents have been created by functionalising the novel linker chemistries designed in the initial nanoparticle functionalisation studies with the lectins used previously. As the glycolax of mammalian cells is constructed from nine common monosaccharides it was hypothesised that the cell surface carbohydrate composition could be elucidated *via* the interaction of specific lectins with specific carbohydrate residues present on the surface of these cells. Using a 532 nm excitation wavelength it was possible to detect a range of lectin-carbohydrate interactions whilst also establishing the optimised conditions for achieving the maximum SERS signal intensities. It has been established that short chain linker molecules result in the most intense SERS signals being achieved *via* the formation of multiple carbohydrate-protein interactions due to a higher surface density of these linker ligands on the nanoparticle surface thus bringing the nanoparticles into closer proximity resulting in an increase in signal intensity. The success of these nanomaterials as cellular imaging agents has since been extended to the detection of cancerous cells *via* binding to surface bound sialic acid residues which are overexpressed in colorectal cancerous cells. An 'on'/'off' nanoparticle assembly assay has been designed for the discrimination between non-and cancerous cells of the same patient. Although, in its infancy with further research it is hoped this assay shall be able to rival the current standard histopathology detection techniques used to detect cancerous cells.

8. Future Work

This work has established new ligands for nanoparticle functionalisation which could be used as key SERS active materials for the conjugation of a range of biomolecules. It is necessary to now explore the many biological diagnostics formats available which could use these nanomaterials and compare both the qualitative and quantitative responses achieved to the current gold standards in the respective fields. Using the novel solid phase synthesis approach should be expanded to the generation of new nanomaterial ligands due to the improved yields and ease by which these various materials could be manipulated.

The creation of a SERS detection assay for carbohydrate-protein interactions has already superseded previous detection limits of other comparative spectroscopic techniques. The next step for this assay would be to operate in a multiplexed format. As problems have already been identified due to unknown biological interactions concurrently occurring when in solution, it remains vital to explore these interactions further and to devise an assay which can circumvent such issues. Previous pitfalls of using gold nanoparticles in such an assay format should also be overcome by devising means by which a positive aggregation assay can be performed for protein-carbohydrate detection. If such an assay can be created, then this would prove to be very important to using gold functionalised nanomaterials as cellular imaging agents to identify carbohydrate-protein interactions. By creating such materials it would be possible to move these materials to 785 nm analysis which is within the window for *in vivo* model analysis. If *in vivo* analysis was possible a new route of detection assays could be designed within animal models for various cancer biomarkers.

Secondary biomarkers should also be identified to be used simultaneously with the over expression of sialic acids to identify colorectal cancerous cells. By forming a multiplexed detection assay of biomarkers for such cancerous species a more robust technique can be fabricated as a route for cancer detection. Using a microfluidic device to detect between non-cancerous and cancerous cells shall also give rise to a new high throughput detection format which is much more robust than the single cell detection reported in this thesis. The use of high throughput detection would ensure a more robust method has been created.

9. Experimental

9.1 Chemicals and Physical Characterisation

9.1.1 Solvents and Reagents

All solvents were of laboratory grade. Chemicals were obtained from commercial sources. Water used in the preparation of colloid and all solutions was obtained from a triply distilled deionised water system.

9.1.2 Chemical analysis and spectroscopy

^{1}H NMR were recorded on a Bruker DPX 400 MHZ spectrometer (unless stated otherwise) with the appropriate solvent peak as a reference. J coupling values are quoted in Hertz. Elemental analyses were performed by an internal University analyst of a Perkin-Elmer 240 elemental analyser. High resolution FAB MS was recorded on JEOL AX505 spectrometer in methanol and nitrobenzyl alcohol/glycerol matrices.

9.1.3 Raman Instrumentation

All Raman and SERRS analyses were performed at either of the following excitation wavelengths:

514.5 nm excitation

The samples were analysed using a Renishaw InVia Raman Microscope with an argon ion laser with an excitation frequency of 514.5 nm as the source of radiation. The laser was focused onto the sample using 20x long working distance (LWD) objective lens. Detection was achieved using a charge coupled device (CCD) detector and spectra were recorded following static collection at 1350 cm^{-1}All samples were analysed using 1 second exposure and an accumulation time of 10 seconds. After analysis all spectra were baseline corrected using GRAMS/AI software.

633 nm excitation

The samples were anaylsed using a Renishaw Ramascope microscope with an He-Ne laser with an excitation frequency of 632.8 nm as the source of radiation. The laser was focused onto the sample using 20x long working distance (LWD) objective lens. Detection was achieved using a charge coupled device (CCD) detector and spectra were recorded following

static collection at 1350 cm^{-1}. All samples were analysed using an accumulation time of 10 second. After analysis all spectra were baseline corrected using GRAMS/AI software.

532 nm excitation

WITec Alpha 300 R confocal microscope (WITech, Ulm, Germany) with a 532 nm excitation wavelength. Mapping of samples was performed using 100 lines and 100 points per line for each 25 μm x 25 μm sample area using an integration time of 0.1 seconds at 5% laser power.

9.1.4 Extinction spectroscopy

Extinction readings were taken within the range of 300 – 800 nm using a Cary Eclipse extinction spectrophotometer. Spectra were baseline corrected using distilled water blank. Colloidal solutions were prepared for analysis by dilution in a 1:10 ratio.

9.1.5 DLS and Zeta Potential

Nanoparticle diameter and particle size distribution and zeta potential data were determined using a Malvern Zetasizer Nano ZS. 1 mL samples were analysed using standard disposable cuvettes.

9.2 Nanoparticle Synthesis

9.2.1 Gold Nanoparticle Synthesis

All glassware was cleaned with aqua regia before use and rinsed thoroughly with distilled water. An aqueous solution of $NaAuCl_4$ (12.5 mM 10 mL) was added to distilled water (500 mL) and heated. Upon boiling, sodium citrate (25 mM, 10 mL) was added and the solution was left to stir for 15 mins at boiling temperature. Gold nanoparticle concentrations were determined by UV-visible spectroscopy using an extinction coefficient of $2.7x10^8$ M^{-1} cm^{-1} at 520 nm.[230]

9.2.2 Silver Nanoparticle synthesis

9.2.2.1 Silver Citrate

All glassware was cleaned with aqua regia before use and rinsed thoroughly with distilled water. An aqueous solution of $AgNO_3$ (53 mM, 10 mL) was added to distilled water (500 mL) that had been heated to 40°C. Following further heating to 97°C, sodium citrate (43 mM, 10 mL) was added. The temperature of the reaction mixture was maintained at 97°C for 90

minutes. UV-Visible spectroscopy was used to determine the silver nanoparticles concentration using the extinction coefficient of $2.87x10^{10}$ $M^{-1}cm^{-1}$ at 400 nm.[231]

9.2.2.2 Silver EDTA

All glassware was cleaned with aqua regia before use and rinsed thoroughly with distilled water. To an aqueous solution of 2 litres of distilled water EDTA (16.2 mM, 10 mL) was added. Heating continued and before boiling 0.32 g of NaOH was added. After boiling silver nitrate (25 mM, 20 mL) was added in 5 mL aliquots. The water was then boiled with stirring for a further 15 minutes. UV-Visible spectroscopy was used to determine the silver nanoparticles concentration using the extinction coefficient of $2.87x10^{10}$ $M^{-1}cm^{-1}$ at 400 nm.

9.3 Synthesis of D1

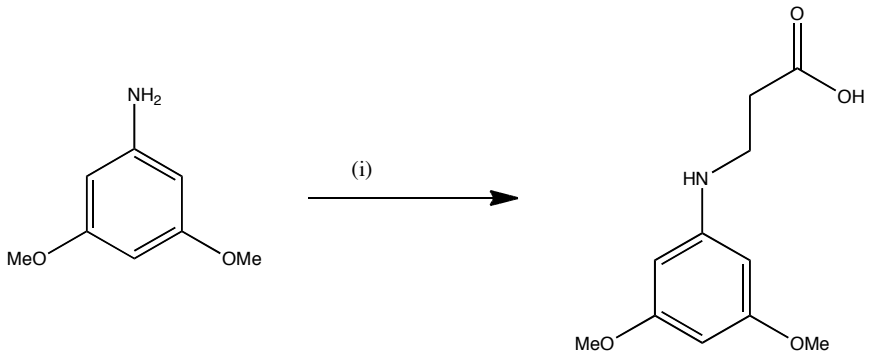

Scheme 9.1 (i) Acrylic Acid, Toluene, 110°C, 48 hours

3,5-Dimethoxyanaline (0.599 g, 1 eq, 3.9 mM) and acrylic acid (0.282 g, 1 eq, 3.9 mM) were refluxed at 110°C for 48 hours in DCM in an inert atmosphere. This gave rise to a dark coloured solution. The toluene was removed from the product under reduced pressure. The residue was then analysed by TLC. Samples of the starting material were dissolved in ethyl acetate and the eluent system was 5% methanol in ethyl acetate. Adequate separation of the spots was achieved using the eluent system. The residue was then purified by flash column chromatography using the eluent system described previously for TLC analysis. TLC analysis of the fractions obtained from the purification was conducted and it was shown an impure sample was obtained. The sample was then purified once more by flash chromatography using an eluent system of 50:50 petroleum ether: ethyl acetate. Only small impurity remained by TLC analysis. The solvent was removed from the sample and the sample was dried for 48 hours on the high vacuum drying line. Further TLC analysis showed no impurities present and only the desired product remained. This was confirmed by ^{1}H NMR analysis and CHN analysis. Yield of 44%.

^{1}H: ∂_H (400 MHz $CDCl_3$): 2.66 (2H,t, J 4.0, CH_2), 3.43 (2H, t, J 4.0, CH_2), 3.73 (6H, s, CH_3), 5.81 (2H, d, J 8.0, ArH), 5.93 (1H, t, J 4.0 ArH)

CHN: $C_{11}H_{15}NO_4$, C 58.66, H 6.71, N 6.22 % (Found: C 58.28, H 6.41, N 5.90 %)

MS: $C_{11}H_{15}NO_4$ MW: 225.10, ESI +ve: 226.24 (100 %)

TLC Rf: Product: 0.3 (Gradient 5% methanol in DCM)

9.4 Synthesis of D2

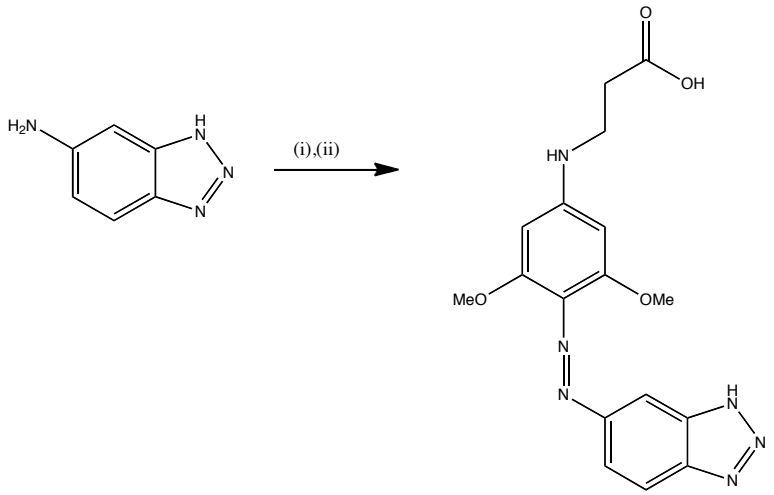

Scheme 9.2 (i)$NaNO_2$, HCl, O°C, 30 mins (ii) NaOAc (pH6), r.t., 14 hours

5-Aminobenzotriazole (0.257 g, 1 eq, 1.92 mM) was dissolved in 5 mL of HCl 50% v/v at 0°C. This solution was diazotized by the dropwise addition of sodium nitrite solution (0.141 g, 2 mM, 1 mL of water). The solution remained in the ice bath for a further 30 mins.

During this time a solution was prepared by dissolving the product D1 in a sodium acetate buffer (1 M, 10 mL, pH 6). Methanol was added dropwise to this solution until D1 had fully dissolved.

The diazotized solution of 5-aminobenzotriazole was then added to this solution dropwise and the solution was stirred overnight at room temperature, after which, the afforded dark red solid was filtered and washed several times with water. (0.46 g, 62.7 %)

^1H: ∂_H (400 MHz D_2O): 2.61 (2H, t, CH_2), 3.36 (2H, t, J 11.6, CH_2), 4.62 (6H, s, OMe), 5.30 (2H, d, ArH), 7.15 (1H, d, J 8.8, ArH), 7.2 (1H, s, ArH), 7.37 (1H, d, J 8.8, ArH)

CHN: $C_{17}H_{15}N_6O_4$: C 55.13 H 4.90 N 22.69 % (Found: C 55.46 H 5.23 N 23.01 %)

MS: $C_{17}H_{15}N_6O_4$ MW: 370.26, ESI +ve: 371.47 (100%)

9.5 Synthesis of D3.

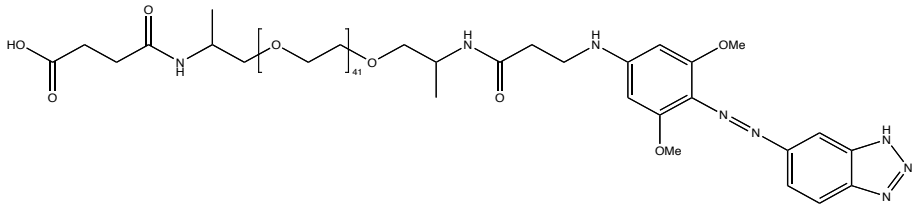

Figure 9.1 Structure of compound D3 (P_{41} linker)

Wang resin (1g), succinic anhydride (0.336 g, 3 eq) and 4-dimethylaminopyridine (DMAP) (0.397 g, 3 eq) were refluxed for 6 hours in DCM at 90°C. The resin was allowed to cool overnight before being filtered and washed five times in the following sequence: 1. DCM, 2.MeOH, 3.DCM, 4.MeOH, 5.DCM. The resin was then mixed overnight with Jeffamine ED-2001 (PEG-41) (6 g, 3 eq) and DIC (0.378 g, 3 eq) on a rotary evaporator overnight at room temperature. The resin was then filtered and washed in sequence as before. The resin was then mixed overnight with CDI (0.454 g, 2 eq) and product **D2** (0.417 g) at room temperature in DMF. The resin was then filtered and washed in sequence as previous. A light red coloured product was afforded. The target compound was then cleaved from the resin. The resin was placed in a 10% TFA in DCM solution and stirred for 3 hours. This resulted in a dark red/brown coloured solution and a red solid residue around the inside of the flask. The mixture was then filtered and washed as previous. The resin solid was removed and to the filtrate a spatula full of morphino-methyl polystyrene was added to remove any excess TFA and the resin was then filtered. The solvent was removed under reduced pressure and a red solid was obtained.

^{1}H: ∂_H (400 MHz $CDCl_3$): 1.06 (2H, t, J 4.0, CH_2) 1.12 (2H, d, J 4.0, CH_2) 2.13 (6H, d, J 7.3, CH_3), 2.65 (2H, t, J 8.1, CH_2), 3.43 (2H, t, J 8.0, CH_2), 3.62 (m, CH_2), 5.4 (1H, s, NH), 7.20 (1H, d, J 12.0, ArH), 7.28 (1H, s, ArH), 7.60 (1H, d, J 8.0, ArH), 10.51 (1H, s, OH), 12.04 (1H, s, BT NH)

MS: $C_{112}H_{206}N_8O_{47}$ MW: 2416, MALDI m/z: 2417

9.6 Synthesis of 3-mercaptopropyl β-D-lactoside (ML3)

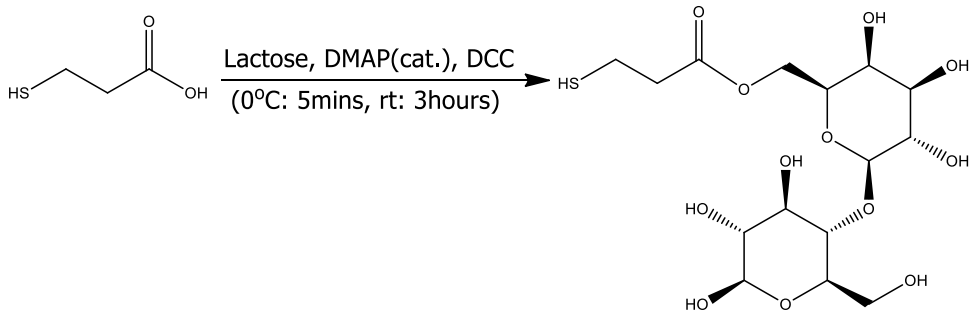

Scheme 9.3 Synthesis and final structure of ML3

Lactose (337 mg, 0.98 mmol) was dissolved in 50 mL of DMF with heating, sonication and stirring for 1 hour. 3-Mercaptopropionic acid (44 μL, ρ = 1.22 g mL^{-1}, 0.51 mmol) and DMAP (89 mg, 0.73 mmol) were added to this and cooled to 0°C. Once cooled, DCC (154.5 mg, 0.75 mmol) was added. The reaction mixture was stirred for 5 minutes at 0°C and then for 3 hours at room temperature. The solvent was removed under reduced pressure and moderate temperature (40°C) and the resulting solid frozen overnight. 30 mL of triply distilled water was added to the solid and filtered. The filtrate was collected and the water removed under reduced pressure and with moderate temperature (70°C). Toluene was added to form an azeotrope with residual water and removed by rotary evaporation to obtain a yellow solid *(110 mg, 51%).*

^1H δ_H (400 MHz DMSO): 8.11 (1H, dd, *J* 5.0), 6.60 (1H, dd, *J* 5.0), 4.90 (1H, d, *J* 3.6) , 4.33 (1H, d, *J* 7.8), 4.20 (1H, t , *J* 7.8), 3.71 (1H, dt, *J* 11.2), 3.66 – 3.22 (m, 13H), 3.18 (1H, dd, *J* 8.6), 2.94 (s, 2H), 2.51 (3H, dd, *J* 3.4), 2.31 (s, 1H).

MS: $C_{15}H_{26}O_{12}S$ 430, MALDI m/z: 431.3

9.7 Synthesis of 3-mercaptopropyl α-D-mannopyranoside (MM1)

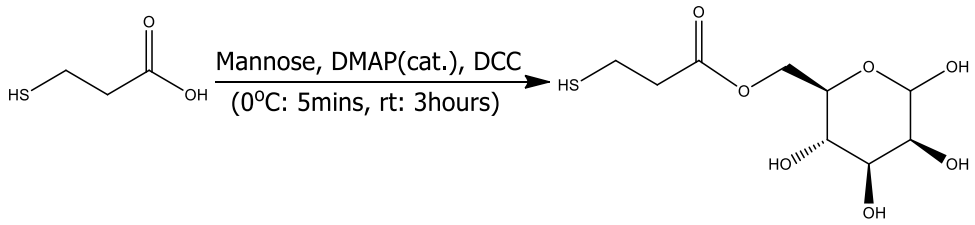

Scheme 9.4 Synthesis and structure of MM1 ligand

Mannose (90.6 mg, 0.50 mmol) was dissolved in 50 mL of DMF with stirring for 30 minutes. 3-Mercaptopropionic acid (22 μL, ρ = 1.22 g mL^{-1}, 0.26 mmol) and DMAP (43 mg, 0.35 mmol) were added to this and cooled to 0°C. Once cooled, DCC (76.8 mg, 0.37 mmol) was added. The reaction mixture was stirred for 5 minutes at 0°C and then for 3 hours at room temperature. The solvent was removed under reduced pressure and moderate temperature (40°C) and the resulting solid frozen overnight. 30 mL of triply distilled water was added to the solid and filtered. The filtrate was collected and the water removed under reduced pressure and with moderate temperature (70°C). Toluene was added to form an azeotrope with residual water and removed by rotary evaporation to obtain a white solid *(34 mg, 40%)*.

^1H: δ_H (400 MHz, DMSO): 8.18 (1H, dd, J 6.0, 1.3), 6.86 (1H, dd, J 5.9, 1.4), 4.88 (s, 1H), 3.66 (1H, ddd, J 18.4, 11.3, 2.0), 3.56 – 3.49 (m, 3H), 3.48 – 3.23 (m, 7H), 3.12 (s, 3H), 2.92 – 2.87 (m, 1H), 2.75 – 2.72 (m, 1H), 2.51 (2H, dd, J 3.6, 1.8), 2.09 (s, 1H).

MS: $C_9H_{16}O_7S$: 268, MALDI m/z: 276.20, M+2H+Na (8.3)

9.8 Synthesis of 3-mercaptopropyl α-D-galactoside (MG2)

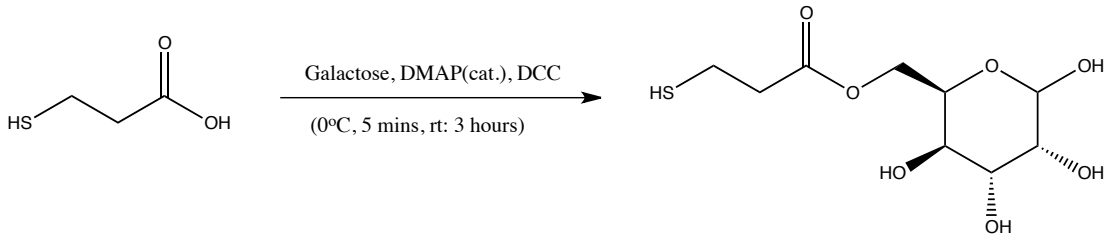

Scheme 9.5 Synthesis of MG2 ligand

Galactose (180.3 mg, 1 mmol) was dissolved in 50 mL of DMF with stirring for 30 minutes. 3-Mercaptopropionic acid (22 μL, ρ = 1.22 g mL^{-1}, 0.26 mmol) and DMAP (43 mg, 0.35 mmol) were added to this and cooled to 0°C. Once cooled, DCC (76.8 mg, 0.37 mmol) was added. The reaction mixture was stirred for 5 minutes at 0°C and then for 3 hours at room temperature. The solvent was removed under reduced pressure and moderate temperature (40°C) and the resulting solid frozen overnight. 30 mL of triply distilled water was added to the solid and filtered. The filtrate was collected and the water removed under reduced pressure and with moderate temperature (70°C). Toluene was added to form an azeotrope with residual water and removed by rotary evaporation to obtain a pale orange oil *(44.3%)*

^{1}H: δ_H (400 MHz, DMSO) 8.14 (1H, dd, *J* 6.6, 1.5), 6.64 (1H, dd, *J* 6.8, 1.7), 4.95(1H, d, *J* 3.4), 3.88-3.17(m, 6H), 2.91(2H, t, *J* 6.5), 2.61(2H, t, *J* 6.8)

MS: $C_9H_{16}O_7S$ 268, MALDI m/z: 276.80, M+2H+Na (8.3)

9.9 Nanoparticle functionalisation method

All of the nanoparticle conjugates in this thesis were produced using this method unless stated otherwise.

The various linker molecules used in each chapter were prepared in stock solutions by dissolving the appropriate mass in distilled water to obtain a stock concentration of 1 x 10^{-3} M. Subsequent dilutions were made in water to achieve desired concentrations.

The linker was attached to the nanoparticle surface at the appropriate final concentration stated *via* mixing of the appropriate volume of linker stock solution and nanoparticle solution with stirring for 20 minutes prior to purification by centrifugation at 6000 rpm for 20 minutes.

The volume of linker and nanoparticles was adjusted to include the appropriate volume of reporter molecule when it was required to be attached.

9.10 TMB ELISA Protocol

HRP functionalised goat anti-mouse IgG antibody was attached to P8P41 functionalised nanoparticles *via* EDC.HCl and sulfo NHS coupling chemistry. Briefly, to 980 μL of PEG functionalised nanoparticles dispersed in phosphate buffer (10 mM, pH 7.4), 1-ethyl-3-(3-dimethylaminopropyl) carbodiimide hydrochloride (EDC) solution (10 μL, 2 mg/mL) and N-hydroxysuccinimide (NHS) solution (10 μL, 2 mg/mL) and antibody (10 μL, 1 mg/mL) were added. The solution was mixed for 1 hour at room temperature prior to incubation at 4°C overnight. Following this incubation period, the solutions were purified to remove any free antibody *via* centrifugation at 6000 rpm for 20 minutes. Following a second purification cycle the antibody conjugated particles were redispersed in phosphate buffer (1 mL, 10 mM, pH 7.4). 100 μL of this solution was added to each maleic anhydride activated polystyrene well. The polystyrene plate was agitated for 1 hour at room temperature. Following the agitation period the nanoparticle solutions were removed and 200 μL of Tris-Tween (0.05%) was added to each well to block any free reactive sites. The Tris-Tween (0.05%) solution was then discarded and each well was washed 3 times with 1xPBS (200 μL). 100 μL of TMB was then added to each well to react with any conjugated nanoparticles. The HRP conjugated antibodies then caused the oxidation of the TMB solution resulting in the blue oxidized TMB product being produced. Removal of the TMB solution was followed by a further washing step of 3 x 200 μL of 1xPBS solution.

9.11 Bulk Protein A – IgG assay protocol

Initially an epoxy coated glass slide was marked into 16 distinct regions for bulk spotting. The antibody solution for spotting was prepared by mixing 5 μL of goat anti-mouse IgG (2 mg/mL, 13 μM, 10 mM phostphate buffer pH 7.4) with 3 μL of protein carrier buffer. To each marked region 0.3 μL of this solution was added and incubated with the slide overnight at 4°C. Following this the slide was moved to room temperature to equilibrate for 1 hour prior to washing in triplicate with 1 x PBS followed by aspiration each time. To block any reactive sites free on the glass 100 μL of 1% BSA in PBS blocking buffer was added and the slide was agitated for 1 hour. Once again each well was washed in triplicate with 1 x PBS. 100 μL of these nanoparticle conjugates were then added to each region for 5 mins prior to removal and washing once again in triplicate. Following aspiration the glass slide was then shaken in a falcon tube for 10 seconds in 50 mL of distilled water before drying with nitrogen.

9.12 Cell culture and incubation protocol

9.12.1 CHO Cell culture

CHO cells were stored in an incubator at 37°C with 5% CO_2. CHO cells were cultured in HAM F12 media supplemented with 10% foetal calf serum and streptomycin. Cells were grown to confluence prior to harvesting using trypsin/EDTA.

9.12.2 HeLa Cell Culture

HeLa cells were stored in an incubator at 37°C with 5% CO_2. HeLa cells were cultured in minimum essential medium eagle (MEME) media supplemented with 10% foetal calf serum and streptomycin and L-glutamine. Cells were grown to confluence prior to harvesting using trypsin/EDTA.

9.12.3 Cell Culture protocol

Once harvested 300 μL of the cells were seeded on glass cover slips and incubated for 24 hours at 37°C with 5% CO_2. Following this period of incubation 30 μL of the functionalised nanomaterials were added to each coverslip and again incubated for 1 hour at 37°C with 5% CO_2. The coverslips were then washed in triplicate with 1 x PBS prepared in sterile distilled water prior to fixing the cells to the coverslips using 4%-paraformaldehyde for 15 mins. Following this period the coverslips were again washed with 1 x PBS followed by washing with sterile water before allowing to air dry for 2 hours. The coverslips were then mounted to glass slides using DPX mountant prior to analysis.

9.13 Buffer preparation

9.13.1 Phosphate Buffer

100 mL of 1 M K_2HPO_4 was prepared by dissolving 17.4 g in 100 mL of triply distilled water. 50 mL of 1 M KH_2PO_4 was prepared by dissolving 6.8 g in 50 mL of triply distilled water. To obtain 1 M phosphate buffer with pH 7.4, 80 mL of 1 M K_2HPO4 was mixed with 20 mL of KH_2PO_4. A 10 mM phosphate buffer solution was required and so 1 mL of buffer was added to 99 mL of triply distilled water. The pH was measured at 7.43 and adjusted to 7.6 with 1 mM NaOH.

9.13.2 Borate Buffer

A 0.1 M borax (sodium tetraborate) solution was prepared by dissolving 3.82 g of borax in 10 mL of triply distilled water. A 0.1 M boric acid solution was prepared by dissolving 0.619 g of boric acid in 100 mL of triply distilled water. Boric acid was added to borax solution until pH 7.5 was reached.

9.13.3 Tris Buffer

A 2 M stock solution of Tris buffer was prepared by dissolving 24.2 g of Tris(hydroxymethyl)aminomethane in 100 mL of triply distilled water. 1 M Tris was prepared by taking 50 mL of the 2 M stock Tris buffer, adjusting to pH 7.5 with 1 M NaOH and adding 50 mL of triply distilled water to bring the volume of the solution to 100 mL. The working buffer (10 mM) was obtained by diluting 1 mL of 1 M Tris in 99 mL of triply distilled water.

Each sample was analysed by UV-vis. extinction spectroscopy at a 1 in 10 dilution in the corresponding buffer. 10 mM Tris buffer was used for subsequent conjugate preparation. Prepared samples were stored at 4°C until required and kept for a maximum time of 1 week.

9.14 SEM sample preparation

Silicon wafers were washed with methanol, dried and cleaned in an oxygen plasma cleaner. A solution containing 1 mL of 10 mM NaCl aqueous solution and 10 µL of ready-made polydimethyl-diallyl ammonium chloride (PDDA) solution was prepared. This liquid was coated onto the surface of the silicon wafers to give the surface a net positive charge. The wafers were left coated for 20 minutes after which time the liquid was removed by pipette and the wafers rinsed with triply distilled water and dried under a gentle stream of nitrogen. The aggregated/unaggregated silver-ML3 conjugates were coated onto the surface of the

wafers and left to equilibrate for 10 minutes. After this time the liquid was removed, the wafers rinsed with triply distilled water and dried under a gentle stream of nitrogen. The samples were then analysed using the SEM.

9.15 LOD calculation

After obtaining a linear range of detection by either extinction spectroscopy or SERS analysis the LOD can be calculated by multiplying the extinction or intensity measured of the principle peak for the control sample by 3. This value is then divided by the gradient of the linear regression line obtained to obtain the resulting linear range of detection. An example of such is provided below:

Using the intensity value obtained from this calculation and the equation of the linear range of detection it was possible to calculate the LOD. The gradient of the line from the graph is $3x10^9$:

$$\frac{0.1207}{3\times10^{-9}} = 4.022\times10^{-11}\ M$$

10. References

(1) Tyers, M., Mann, M., *Nature* **2003**, *422*, 193.

(2) Chambers, G. L., Cash, P., Murray, G., *J. Pathol.,* **2000**, *192*, 280.

(3) Anderson, L., Seilhammer, J., *Electrophoresis,* **1997**, *18*, 533.

(4) Humphrey-Smith, I., Cordwell, S.J., Blackstock, W.P., *Electrophoresis* **1997**, *18*, 1217.

(5) Wang, J., Hewick, R., *DDT,* **1999**, *4*, 129.

(6) Peng, J., Elias, J.E., Thoreen, C.C., Licklider, L.J., Gygi, S.P., *J. Proteome Res.,* **2003**, *2*, 43.

(7) Washburn, M. P., Wolters, D., Yates, J.R., *Nat. Biotechnol.,* **2001**, *19*, 242.

(8) Varki, A., Cummings, R., Esko, J., Freeze, H., Hart, G., Marth, J., *Essentials of glycobiology*; 1st ed.; Cold Spring Harbor Laboratory Press: Cold Sping Harbor, New York, 1999.

(9) Marth, J. D., *Nat. Cell Biol.,* **2008**, *10*.

(10) Varki, A., Gagneux, P., *Glycobiology,* **1999**, *9*, 747.

(11) El-Boubbou, K., Zhu, D.C., Vasileiou, C., Borhan, B., Prosperi, D., Li, Wei., Huang, X., *J. Am. Chem. Soc.,* **2010**, *132*, 4490.

(12) Garrod, A. E., *Lancet,* **1902**, *2*, 1616.

(13) Hammerling, J., *Ann. Rev. Plant Physio.,* **1963**, *14*, 65.

(14) Brachet, J., *Arch. Biologie,* **1942**, *53*, 207.

(15) Berg, J. M., Tymoczko, J.L., Stryer, L., *Biochemistry*; W.H. Freeman and Company: New York, 2006.

(16) Campbell, N. A., Reece, J.B., *Biology 6th Edition*; B. Cummings, 2001.

(17) Black, D. L., *Annu. Rev. Biochem.,* **2003**, *72*, 291.

(18) Maniatis, T., Tasic, B., *Nature,* **2002**, *418*, 236.

(19) Walsh, C. T., Garneau-Tsodikova, S., Gatto, G.J., *Angew. Chem. Int. Ed.,* **2005**, *44*, 7342..

(20) Buxbaum, E., *Fundamentals of Protein Structure and Function*; Springer US, 2007.

(21) Ozbabacan, S. E. A., Engin, H.B., Gursoy, A., Keskin, O., *Protein Eng. Des. Sel.,* **2011**, 1.

(22) Nooren, I. M., Thornton, J.M., *EMBO J.,* **2003**, *22*, 3486.

(23) Park, S. H., Reyes, J.A., Gilbert, D.R., Kim, J.W., Kim. S., *BMC Bioinform.,* **2009**, *10*, 36.

(24) Krishna, S. S., Aravind, L., *J. Struct. Biol.,* **2010**, *172*, 294.

(25) Vetter, I. R., Wittinghofer, A., *Science,* **2001**, *294*, 1299.

(26) Hou, T., Xu, Z., Wei, Z., McLaughlin, W.A., Case, D.A., Xu, Y., Wang, W., *Mol. Cell Proteomics,* **2008**, *8.4*, 639.

(27) Hudlicky, T., Entwistle, D.A., Pitzer, K.K., Thorpe, A.J., *Chem. Rev.,* **1996**, *96*, 1195.

(28) Alberts, D. B. B., Lewis, J., Raff, M., Roberts, K., Watson, J.D., *Molecular Biology of the Cell*; 3rd Edition ed.; Garland Publishing: New York, 1994.

(29) Alem, A., Addis Ababa University, Ethiopia, 2010.

(30) Brandley, B. K., Schnaar, R. L., *J. Leukocyte Biol.,* **1986**, *40*, 97.

(31) B. Alberts, D. B., J. Lewis, M. Raff, K. Roberts, J. D. Watson *Molecular Biology of the Cell*; 3rd edn. ed.; Garland Publishing, Taylor and Francis Group: New York, NY, 1994.

(32) Bucior, I., Burger, M. M., *Curr. Opin. Struc. Biol.,* **2004**, *14*, 631

(33) Muthana, S. M., Campbell, C.T., Gildersleeve, J.C., *ACS Chem. Biol.,* **2012**, *7*, 31.

(34) Drickamer, K., Taylor, M., *Introduction to Glycobiology*; 2nd ed.; Oxford University Press: Oxford, 2006.

(35) Jackson, R. L., Busch, S.J., Cardin, A.D., *Physiol. Rev.,* **1991**, *71*, 481.

(36) Kahari, V.M., Larjava, H., Uitto, J., *J. Biol. Chem.,* **1991**, *266*, 10608.

(37) Franz, H., *Adv. Lectin Res.,* **1988**, *1*, 10.

(38) Sharon, N., Lis, H., *Glycobiology,* **2004**, *14*, 53R.

(39) Summer, J. B., Howell, S.F., *J. Bacteriol.,* **1936**, *32*, 227.

(40) Boyd, W. C., Shapleigh, E., *Science,* **1954**, *119*, 419.

(41) Watkins, W. M., Morgan, W.T.J., *Nature,* **1952**, *169*, 825.

(42) Pusztai, A., Grant, G., Oliveria, J.T.A., *IRSC Medical Science,* **1986**, *14*, 205.

(43) Hemmings, W. A., *Protein transmission through living membranes*; Elsevier North-Holland, 1979.

(44) Liener, I. E., Sharon, N., Goldstein, I.J., *The Lectins: Properties, functions, and applications in biology and medicine*; Academic Press (Orlando), 1986.

(45) Lakowicz, J. R., *Principles of Fluorescence Spectroscopy*; Springer US, 2006.

(46) Gillenwater A, J., R., Ganeshappa, R., Kemp, B., El-Naggar, AK., Palmer, JL., Clayman, G., Mitchell, MF., Richards-Kortum, R., *Arch. Otolaryngol,* **1998**, *124*, 1251.

(47) Chaturvedi, P., Majumder, SK., Krishna, H., Muttagi, S., Gupta, PK., *J. Cancer Res. Ther.,* **2010**, *6*, 497.

(48) Lilley, D. M., Wilson, T.J., *Curr. Opin. Chem. Biol.,* **2000**, *4*, 507.

(49) Forster, T., *Ann. Phys.,* **1948**, *2*, 55.

(50) Clegg, R., Murchie, A.H., Zechel, A., Lilley, D.M.J., *Proc. Nat. Acad. Sci. USA,* **1993**, *90*, 2994.

(51) Tuschi, T., Gohlke, C., Jovin, T.M., Westhof, E., Eckstein, F., *Science,* **1994**, *266*, 785.

(52) Bjornson, K. P., Hsieh, J., Amaratunga, M., Lohman, T.M., *Biochemistry-US,* **1994**, *33*, 14306.

(53) Green, R., Frazier, RA., Shakesheff, KM., Davies, MC., Roberts, CJ., Tendler, SJ., *Biomaterials,* **2000**, *21*, 1823.

(54) Larmour, I. A., Graham, D., *Analyst,* **2011**, *136*, 3831.

(55) Wegner, G. J., Lee, H.J., Marriott, G., Corn, R.M., *Anal. Chem.,* **2003**, *75*, 4740.

(56) Safina, G., *Anal. Chim. Acta,* **2012**, *712*, 9.

(57) Safina, G., Duran, I. B., Alasel, M., Danielsson, B., *Talanta,* **2011**, *84*, 1284.

(58) Elghanian, R., Storhoff, J.J., Mucic, R.C., Letsinger, R.L., Mirkin, C.A., *Science,* **1997**, *277*, 1078.

(59) Mirkin, C. A., Letsinger, R.L., Mucic, R.C., Storhoff, J.J., *Nature,* **1996**, *382*, 607.

(60) Alivisastos, A. P., Johnsson, K.P., Peng, X., Wilson, T.E., Joweth, C.J., Bruchez, M.R., Schultz, P.G., *Nature,* **1996**, *382*, 609.

(61) Williams, D., *Biomaterials,* **2008**, *29*, 1737.

(62) Rosi, N., *Chem. Rev.,* **2005**, *105*, 1547.

(63) Kelly, K. L. C., Zhao, L.L., Schatz, G.C., *J. Phys. Chem. B,* **2003**, *107*, 668.

(64) Tokonami, S., Morita, N., Takasaki, K., Toshima, N., *J. Phys. Chem. C,* **2010**, *114*, 10336.

(65) Yguerabide, J. Y., *Anal. Biochem.,* **1998**, *262*, 137.

(66) Mie, G. *Annalen Der Physik* **1908**, *26*, 377.

(67) Pavlov, V., Xiao, Y., Shlyahovsky, B., Willner, I., *J. Am. Chem. Soc.,* **2004**, *126*, 11768.

(68) Maya, L., Muralidharan, G., Thundat, T. G., Kenik, E. A., *Langmuir,* **2000**, *16*, 9151.

(69) Berchmans, S., Thomas, P. J., Rao, C. N. R., *J. Phys. Chem. B,* **2002**, *106*, 4647.

(70) Smekal, A., *Naturwissenschaften,* **1923**, *11*, 873.

(71) Raman, C. V., Krishnan, K. S., *Nature,* **1928**, *121*.

(72) Pelletier, M. J., *Analytical Applications of Raman Spectroscopy 2nd Edition*; Blackwell Science Ltd.: Oxford, 1999.

(73) Smith, W.E., Dent, G., *Modern Raman Spectroscopy: A Practical approach*; 1st edition ed.; John Wiley & Sons Ltd: Chichester, West Sussex, 2005.

(74) Parker, F. S., *Applications of Infrared, Raman and Resonance Raman Spectroscopy in Biochemistry*; Plenum Press: New York N.Y., 1983.

(75) Fleischman, M., Hendra, P. J., McQuillan, A., J. *Chem. Phys. Lett.,* **1974**, *26*, 163.

(76) Jeanmaire, D. L., Van Duyne, R.P., *J. Electronanal. Chem.,* **1977**, *84*, 1.

(77) Creighton, J. A., Blatchford, C. G.; Albrecht, M. G., *J. Chem. Soc., Faraday Trans. 2* **1979**, *75*.

(78) Nie, S., Emory, S.R., *Science,* **1997**, *275*, 1102.

(79) Moskovits, M., *Rev. Mod. Phys.,* **1985**, *57*, Part I.

(80) Faulds, K., Hernandez-Santana, A., Smith, W.E., *Spectrosc. Prop. Inorg. Organomet. Compd.,* **2010**, *41*, 1.

(81) Smith, W. E., *Chem. Soc. Rev.,* **2008**, *37*, 955.

(82) Guerrini, L., Graham, D., *Chem. Soc. Rev.,* **2012**, *41*, 7085.

(83) Kneipp, K., Wang, Y., Kneipp, H., Perelman, L. T., Itzkan, I., Dasari, R., Feld, M. S., *Phys. Rev. Lett.,* **1997**, *78*, 1667.

(84) Stacy, A. M., Van Duyne, R. P., *Chem. Phys. Lett.,* **1983**, *102*.

(85) Geddes, C. D., Parfenov, A., Roll, D., Uddin, J., Lakowicz, J.R., *J. Fluoresc.,* **2003**, *13*, 453.

(86) Graham, D., Goodacre, R., *Chem. Soc. Rev.,* **2008**, *37*, 883.

(87) Howell, N. K., Arteaga, G., Nakai, S., Li-Chan, E.C.Y., *J. Agr. Food Chem.,* **1999**, *47*, 924.

(88) Xu, H. X., Bjerneld, E.J., Kall, M., Borjesson, L., *Phys. Rev. Lett.,* **1999**, *83*, 4357.

(89) Habuchi, S., Cotlet, M., Gronheid, R., Dirix, G., Michiels, J., Vanderleyden, J., De Schryver, F.C., Hofkens, J., *J. Am. Chem. Soc.,* **2003**, *125*, 8446.

(90) Feng, M., Tachikawa, H., *J. Am. Chem. Soc.,* **2008**, *130*, 7443.

(91) Keating, C. D., Kovaleski, K.M., Natan, M.J., *J. Phys. Chem. B,* **1998**, *102*, 9404.

(92) Broderick, J. B., Natan, M.J., Ohalloran, T.V., Van Duyne, R.P., *Biochemistry-US,* **1993**, *32*, 13771.

(93) Rospendowski, B. N., Kelly, K., Wold, C.R., Smith, W.E., *J. Am. Chem. Soc.,* **1991**, *113*, 1217.

(94) Sivanesan, A., Ly, H.K., Kozuch, J., Sezer, M., Kuhlmann, U., Fischer, A., Weidinger, I.M., *Chem. Commun.,* **2011**, *47*, 3553.

(95) Voller, A., Bartlett, A., Bidwell, D.E., *J. Clin. Pathol.,* **1978**, *31*, 507.

(96) Hicks, J., *Hum. Pathol.,* **1984**, *15*, 112.

(97) Shan, G., Huang, W., Gee, S.J., Buchholz, B.A., Vogel, J.S., Hammock, B.D., *P. Natl. Acad. Sci. USA,* **2000**, *97*, 2445.

(98) Alvarez-Puebla, R. A., Liz-Marzan, L.M., *Small,* **2010**, *6*, 604.

(99) Rohr, T. E., Cotton, T.M., Ni, F., Tracha, P.J., *Anal. Biochem.,* **1989**, *182*, 388.

(100) Chen, J. W., Luo, Y., Liang, Y., Jiang, J.H., Shen, G.L., Yu, R.Q., *Anal. Sci.,* **2009**, *25*, 347.

(101) Ni, J., Lipert, R. J., Dawson, G. B., Porter, M. D., *Anal. Chem.,* **1999**, *71*, 4903.

(102) Driskell, J. D., Kwarta, K.M., Lipert, R.J., Porter, M.D., *Anal. Chem.,* **2007**, *79*, 4141.

(103) Grubisha, D. S., Lipert, R. J., Park, H. Y., Driskell, J., Porter, M. D., *Anal. Chem.,* **2003**, *75*, 5936.

(104) Park, H.-Y., Lipert, R.J., Porter, M.D., *Proc. SPIE,* **2004**, 464.

(105) Park, H. Y., Driskell, J.D., Kwarta, K.M., Lipert, R.J., Porter, M.D., Schoen, C., Neill, J.D., Ridpath, J.F., *Top. Appl. Phys.,* **2006**, *103*, 427.

(106) Wang, G., Park, H.-Y, Lipert, R.J., Porter, M.D., *Anal. Chem.,* **2009**, *81*, 9643.

(107) Ingram, A., Stokes, R.J., Redden, J., Gibson, K., Moore, B., Faulds, K., Graham, D., *Anal. Chem.,* **2007**, *79*, 8578.

(108) Ingram, A., Byers, L., Faulds, K., Moore, B.D., Graham, D., *J. Am. Chem. Soc.,* **2008**, *130*, 11846.

(109) Ingram, A., Moore, B.D., Graham, D., *Bioorg. Med. Chem. Lett.,* **2009**, *19*, 1569.

(110) Moore, B. D., Stevenson, L., Watt, A., Flitsch, S., Turner, N.J., Cassidy, C., Graham, D., *Nat. Biotechnol.,* **2004**, *22*, 1133.

(111) Marrache, S., Dhar, S., *P. Natl. Acad. Sci. USA,* **2012**, *109*, 16288.

(112) Murphy, C. J., Gole, A.M., Stone, J.W., Sisco, P.N., Alkilany, A.M., Goldsmith, E.C., Baxter, S.C., *Acc. Chem. Res.,* **2008**, *41*, 1721.

(113) Connor, E. E., Mwamuka, J., Gole, A., Murphy, C.J., Wyatt, M.D., *Small,* **2005**, *1*, 325.

(114) Mahmoudi, M., Azadmanesh, K., Shokrgozar, M.A., Journeay, W.S., Laurent, S., *Chem. Rev.,* **2011**, *111*, 3407.

(115) Kneipp, K., Haka, A.S., Kneipp, H., Badizadegan, K., Yoshizawa, N., Boone, C., Shafer-Peltier, K.E., Motz, J.T., Dasari, R.R., Feld, M.S., *Appl. Spectrosc.,* **2002**, *56*, 150.

(116) Kneipp, J., Kneipp, H., Wittig, B., Kneipp, K., *Nano Lett.,* **2007**, *7*, 2819.

(117) Pallaoro, A., Bruan, G.B., Reich, N.O., Moskovits, M., *Small,* **2010**, *6*, 618.

(118) Scaffidi, J. P., Gregas, M.K., Seewaldt, V., Vo-Dinh, T., *Anal. Bioanal. Chem.,* **2009**, *393*, 1135.

(119) Yu, K. N., Lee, S-M., Han, Ji-Y., Park, H., Woo, Min-Ah., Noh, Mi-Suk, Hwang, S-K., Kwon, J-T., Jin, H., Kim, Y-K., Hergenrother, P.J., Jeong, D.H., Lee, Y-S., Cho, M-H., *Bioconjugate Chem.,* **2007**, *18*, 1155.

(120) Qian, X. M., Peng, X. H., Ansari, D. O., Yin-Goen, Q., Chen, G. Z., Shin, D. M., Yang, L., Young, A. N., Wang, M. D., Nie, S. M., *Nat. Biotechnol.,* **2008**, *26*, 83.

(121) Graham, D., Mallinder, B.J., Whitcombe, D., Watson, N.D., Smith, W.E., *Anal. Chem.,* **2002**, 1069.

(122) Tsoi, K. M., Dai, Q., Alman, B.A., Chan, W.C.W., *Acc. Chem. Res.,* **2013**, *46*, 662.

(123) Le Ru, E. C., Meyer, M., Etchegoin, P.G., *J. Phys. Chem. B,* **2006**, *110*, 1944.

(124) Ingram, A., University of Strathclyde, 2007.

(125) Mulvaney, S. P., Musick, M.D., Keating, C.D., Natan, M.J., *Langmuir,* **2003**, *19*, 4784.

(126) Doering, W. E., Nie, S., *Anal. Chem.,* **2003**, *75*, 6171.

(127) Otsuka, H., Nagasaki, Y., Kataoka, K., *Adv. Drug Deliver. Rev.,* **2003**, *55*, 403.

(128) Bergstrom, K., Osterberg, E., Holmberg, K., Hoffman, A. S., Schuman, T. P., Kozlowski, A., Harris, J. H., *J. Biomater. Sci. Polym. Edn.,* **1994**, *6*, 123.

(129) Yokoyama, M., Mitauchi, M., Yamada, N., Okano, T., Sakurai, Y., Lnoue, S., *J. Control. Release,* **1990**, *11*, 269.

(130) Gref, R., Minamitake, Y., Peracchia, M. T., Trubetskoy, V., Torchilin, V., Langer, R., *Science,* **1994**, *263*, 1600.

(131) Peracchia, M. T., Vauthier, C., Desmaele, D., Gulik, A., Dedieu, J. C., Demoy, M., d'Angelo, J., Couvreur, P., *Pharm. Res.,* **1998**, *15*, 550.

(132) Peracchia, M. T., Vauthier, C., Puisieux, F., Couvreur, P., *J. Biomed. Mater. Res.,* **1997**, *34*, 317.

(133) Douglas, P., McCarney, K. M., Graham, D., Smith, W. E., *Analyst,* **2007**, *132*, 865.

(134) Guven, B., Basaran-Akgul, N., Temur, E., Tamer, U., Boyaci, I.H., *Analyst,* **2010**, *136*, 740.

(135) Michota, A., Bukowska, J., *J. Raman Spectros.,* **2003**, *34*, 21.

(136) McAnally, G., McLaughlin, C., Brown, R., Robson, D. C., Faulds, K., Tackley, D. R., Smith, W. E., Graham, D., *Analyst,* **2002**, *127*, 838.

(137) Wilson, H., Smith, W.E., *J. Raman. Spectrosc.,* **1994**, *25*, 899.

(138) Ling, Y., Guan, Y., Han, K.N., *Corros. Sci.,* **1995**, *51*, 367.

(139) Graham, D., McLaughlin, C., McAnally, G., Jones, J. C., White, P. C., Smith, W. E., *Chem. Commun.,* **1998**, 1187.

(140) Lee, P. C., Meisel, D., *J. Phys. Chem-US,* **1982**, *86*, 3391.

(141) Stewart, A., Zheng, S., McCourt, MR., Bell, S.E.J., *ACS Nano* **2012**, *6*, 3718.

(142) Guarrotxena, N., Liu, B., Fabris, L., Bazan, G.C., *Adv. Mater.,* **2010**, *22*, 4954.

(143) McKenzie, F., Steven, V., Ingram, A., Graham, D., *Chem. Commun.,* **2009**, 2872.

(144) Palmqvist, N., Foster, T., Tarkowski, A., Josefsson, E., *Microb. Pathogenesis,* **2002**, *33*, 239.

(145) Uhlen, M., Guss, B., Nilsson, B., Gatenbeck, S., Philipson, L., Lindberg, M., *J. Biol. Chem.,* **1984**, *259*, 1695.

(146) Chalon, M. P., Milne, R.W., Vaerman, J.P., *Scand. J. Immunol.,* **1979**, *9*, 359.

(147) Abrahmsen, L., Moks, T., Nilsson, B., Hellmann, U., Uhlen, M., *EMBO J.,* **1985**, *138*, 3901.

(148) Hober, S., Nord, K., Linhult, M., *J. Chromatogr. B,* **2007**, *848*, 40. (149) Sumner, J. B., Howell, S.F., *J. Bacteriol.,* **1936**, *32*, 227.

(150) Goldstein, I. J., Academic Press: New York and London, 1972, Vol. 6.

(151) Cifonelli, J. A., Montgomery, R., Smith, F., *J. Am. Chem. Soc.,* **1956**, *79*, 5055.

(152) Agrawal, B. B. L., Goldstein, I.J., *Arch. Biochem. Biophys.,* **1968**, *124*, 218.

(153) Kalb, A. J., Lustig, A., *Biochim. Biophys. Acta,* **1968**, *168*, 366.

(154) Yariv, J., Kalb, A.J., Levitz, K.A., *Biochim. Biophys. Acta,* **1968**, *165*, 303.

(155) Kalb, A. J., Levitzki, A., *Biochem. J.,* **1968**, *109*, 669.

(156) Edelman G.M., C., B.A., Reeke, G.N., Becker, J.W., Waxdal, M.J., Wang, J.L., *P. Natl. Acad. Sci. USA,* **1972**, *69*, 2580.

(157) Reeke, G. N., Becker, J.W., Cunningham, B.A., Gunther, G.R., Wang, J.L., Edelman, G., *Ann. N.Y. Acad. Sci.,* **1974**, *234*, 369.

(158) Shoham, M., Kalb, A.J., Pecht, I., *Biochemistry-US,* **1973**, *12*.

(159) Barber, B. H., Carver, J.P., *J. Biol. Chem.,* **1973**, *248*, 3353.

(160) Derewenda, Z., Yariv, Y., Helliwell, J.R., Kalb, A.J., Dodson, E.J., Papiz, M.Z., Wan, T., Campbell, J., *EMBO,* **1989**, *8*, 2189.

(161) Tang, B., Cao, L., Xe K., Zhuo, Z., Ge J., Li, Q., Yu, L., *Chem. Eur. J.,* **2008**, *14*, 3637.

(162) Hone, D. C., Haines, A. H., Russell, D. A., *Langmuir,* **2003**, *19*, 7141.

(163) Lin, C. C., Yeh, Y. C., Yang, C. Y., Chen, C. L., Chen, G. F., Chen, C. C., Wu, Y. C., *J. Am. Chem. Soc.,* **2002**, *124*, 3508.

(164) Wang, X., Ramstrom, O., Yan, M. D., *Anal. Chem.,* **2010**, *82*, 9082.

(165) Wang, X., Ramstrom, O., Yan, M. D., *Adv. Mater.,* **2010**, *22*, 1946.

(166) Mahon, E., Aastrup, T., Barboiu, M., *Chem. Commun.,* **2010**, *46*, 5491.

(167) Benaissa-Trouw, B., Lefeber, D.J., Kamerling, J.P., Vliegenthart, J.F., Kraaijeveld, K., Snippe H., *Infect. Immun.,* **2001**, *69*, 4698.

(168) Cloninger, M. J., *Curr. Opin. Chem. Biol.,* **2002**, *6*, 742.

(169) You, L. C., Lu, F.Z., Li, Z.C., Zhang, W., Li, F.M., *Macromolecules,* **2003**, *36*, 1.

(170) Schofield, C. L., Field, R. A., Russell, D. A., *Anal. Chem.,* **2007**, *79*, 1356.

(171) Chen, T., Wang, H., Chen, G., Wang, Y., Feng, Y., Teo, W. S., Wu, T., Chen, H., *ACS Nano,* **2010**, *4*, 3087.

(172) Graham, D., Stevenson, R., Thompson, D. G., Barrett, L., Dalton, C., Faulds, K., *Faraday Discuss.,* **2011**, *149*, 291.

(173) Faulds, K., McKenzie, F., Smith, W. E., Graham, D., *Angew. Chem. Int. Edit.,* **2007**, *119*, 1861.

(174) Chortyk, O. T., Pomonis, J. G., Johnson, A. W., *J. Agr. Food Chem.,* **1996**, *44*, 1551.

(175) Choi, R., Yang, J., Choi, J., Lim, E.-K., Kim, E., Suh, J.-S., Huh, Y.-M., Haam, S., *Langmuir,* **2010**, *26*, 17520.

(176) Neises, B., Steglich, W., *Angew. Chem. Int. Edit.,* **1978**, *17*, 522.

(177) Thelwall, L. A. W., *J. Dairy Res.,* **1982**, *49*, 713.

(178) Labat, Y., Muller, J. P., Litvine, D., SNEA , Fr. 1991, p 8 pp.

(179) Simoni, R. D., Hill, R.L., Vaughan, M., *J. Biol. Chem.,* **2002**, *e5*, 277.

(180) Barrett, L., Dougan, J.A., Faulds, K., Graham, D., *Nanoscale,* **2011**, *3*, 3211.

(181) Schofield, C. L., Haines, A. H., Field, R. A., Russell, D. A., *Langmuir* **2006**, *22*, 6707.

(182) Taylor, R. W., Lee, T-C., Scherman, O.A., Esteban, R., Aizpurua, J., Huang, F.M., Baumberg, J.J., Mahajan, S., *ACS Nano,* **2011**, *5*, 3878.

(183) Wustholz, K. L., Henry, A.I., McMahon, J.M., Freeman, R.G., Valley, N., Piotti, M.E., Natan, M.J., Schatz, G.C., Van Duyne, R.P., *J. Am. Chem. Soc.,* **2010**, *132*, 10903.

(184) Dougan, J. A., Faulds, K., *Analyst,* **2012**, *137*, 545.

(185) Graham, D., Thompson, D.G., Smith, W.E. and Faulds, K., *Nat. Nanotechnol.,* **2008**, *3*, 548.

(186) Graham, D., Mallinder, B.J., Whitcomber, D., Watson, N.D. and Smith, W.E., *Anal. Chem.,* **2002**, *74*.

(187) Sun, L., Yu, C., Irudayaraj, J., *Anal. Chem.,* **2008**, *80*, 3342.

(188) Sun, L., Yu, C., Irudayaraj, J., *J. Phys. Chem. B,* **2009**, *113*, 14021.

(189) Granger, J. H., Granger, M.C., Firpo, M.A., Mulvihill, S.J., Porter, M.D., *Analyst,* **2013**, *138*, 410.

(190) Loomes, L. M., Stewart, W.W., Mazengera, R.I., Senior, B.W., Kerr, M.A., *J. Immunol. Methods.,* **1991**, *141*, 209.

(191) Sankaranarayanan, R., Sekar, K., Banerjee, R., Sharma, V., Surolia, A., Vijayan, M., *Nat. Struct. Mol. Biol.,* **1996**, *3*, 596.

(192) Barre, A., Bourne, Y., Van Damme, E.J.M., Peumans, W.J., Rouge, P., *Biochimie,* **2001**, *83*, 645.

(193) Bourne, Y., Astoul, C.H., Zamboni, V., Peuman, W.J., Menu-Bouauiche, L., Van Damme, E.J.M., Barre, A., Rouge, P., *Biochem. J.,* **2002**, *364*, 173.

(194) Loris, R., Casset, F., Bouckaert, J., Pletinckx, J., Dao-Thi, M-H., Poortmans, F., Imberty, A., Perez, S., Wyns, L., *Glycoconjugate J.,* **1994**, *11*, 507.

(195) Voynov, V., Chennamsetty, N., Kayser, V., Helk, B., Forrer, K., Zhang, H., Fritsch, C., Heine, H., Trout, B.L., *PLoS ONE,* **2009**, *4*, e8425.

(196) Quiocho, F. A., *Curr. Top. Microbiol. Immunol.,* **1988**, *139*, 135.

(197) Reichardt, N. C., Martin-Lomas, M., Penades, S., *Chem. Soc. Rev.,* **2013**.

(198) Ahuja, R., Singhal, N. K., Ramanujam, B., Ravikumar, M., Rao, C. P., *J. Org. Chem.,* **2007**, *72*, 3430.

(199) Jelinek, R., Kolusheva, S., *Chem. Rev.,* **2004**, *104*, 5987.

(200) Sharon, N., *Adv. Exp. Med. Biol.,* **1996**, *408*, 1.

(201) Smith, A., Duan, H., Mohs, A., Nie, S., *Adv. Drug Deliver. Rev.,* **2008**, *60*, 1226.

(202) Hong, S. Y., Tobias, G., Al-Jamal, K.T., Ballesteros, B., Ali-Boucetta, H., Lozano-Perez, S., Nellst, P.D., Sim, R.B., Finucane, C., Mather, S.J., Green, M.L.H., Kostarelos, K., Davis, B.G., *Nat. Matter.,* **2010**, *9*, 485.

(203) Strijkers, G. J., Mulder, M., Willem, J., Van Tilborg, F., Geralda, A., Nicolay, K., *Curr. Med. Chem.,* **2007**, *7*, 291.

(204) Marradi, M., Garcia, I., Penades, S., *Prog. Mol. Biol. Transl. Sci.,* **2011**, *104*, 141.

(205) Lee, J., Jung, M., Hwang, Y., Lee, Y., Lee, S., Lee, D., Shin, H., *Biomaterials,* **2012**, *32*, 4861.

(206) Zheng, M., Davidson, F., Huang, X., *J. Am. Chem. Soc.,* **2003**, *125*, 7790.

(207) Zanchet, D., Michael, C.M., Parak, W.J., Gerion, D., Alivisatos, A.P., *Nano Lett.,* **2000**, *1*, 32.

(208) Hanauer, M., Pierrat, S., Zins, I., Lotz, A., Sonnichsen, C., *Nano Lett.,* **2007**, *7*, 2881.

(209) Samuel, U., Guggenbichler, J.P. *J. Antimicrob. Agents* **2004**, *23*, 575.

(210) AshaRani, P. V., Mun, G.L.K, Hande, M.P., Valiyaveetil, S., *ACS Nano,* **2009**, *3*, 279.

(211) Chen, P., Harcum, S.W., *Appl. Biochem. Biotechnol.,* **2007**, *141*, 349.

(212) Weikert, S., Papac, D., Briggs, J., Cowfer, D., Tom, S., Gawlitzek, M., Lofgren, J., Mehta, S., Chisholm, V., Modi, N., Eppler, S., Carroll, K., Chamow, S., Peers, D., Berman, P., Krummen, L., *Nat. Biotechnol.,* **1999**, *17*, 1161.

(213) Rich, A., Darnell, J., Becker, S., Hall, C., *Science,* **1963**, *142*, 1658.

(214) Turrell, G., Corset, J. *Raman Microscopy*; Wiley: New York, 1996.

(215) Hanlon, E. B., Manoharan, R., Koo, T-W., Shafer, K.E., Motz, J.T., Fitzmaurice, M., Kramer, J.R., Itzkan, I., Dasari, R.R., Feld, M.S., *Phys. Med. Biol.,* **2000**, *45*, R1.

(216) Bakker Schut, T. C., Witjes, M.J.H, Sterenborg, H.J.C.M., Speelman, O.C., Roodenburg, J.L.N., Marple, E.T., Bruining, H.A., Puppels, G.J., *Anal. Chem.,* **2000**, *72*, 6010.

(217) Falk, G. W., Rice, T.W., Goldblum, J.R., Richter, J.E., *Gastrointest. Endosc.,* **1999**, *49*, 170.

(218) Barr, H., *Lancet,* **1998**, *352*, 1242.

(219) Van den Boogert, J., van Hillegersberg, R., de Bruin, R.F., Tilanus, H.W., Siersema, P.D., Scand, J., *Gastroenology,* **1998**, *33*, 449.

(220) Bohorfoush, A. G., *Endoscopy,* **1996**, *28*, 372.

(221) Boustany, N. N., Crawford, J.M., Manoharan, R., Dasari, R.R., Field, M.S., *Lab. Invest.,* **1999**, *79*, 1201.

(222) Schauer, R., *Glycoconjugate J.,* **2000**, *17*, 485.

(223) Angata, T., Varki, A., *Chem. Rev.,* **2002**, *102*, 439.

(224) Ley, K., *Trends Mol. Med.,* **2003**, *9*, 263.

(225) McEver, R. P., *Curr. Opin. Cell Biol.,* **2002**, *14*, 581.

(226) Qiu, Y., Patwa, T.H., Xu, L., Shedden, K., Misek, D.E., Tuck, M., Jin, G., Ruffin, M.T., Turgeon, D.K., Synal, S., Bresalier, R., Marcon, N., Brenner, D.E., Lubman, D.M., *J. Proteome Res.,* **2008**, *7*, 1693.

(227) Matsuno, Y., Saito, T., Gotoh, M., Narimatsu, H., Kameyama, A., *Anal. Chem.,* **2009**, *79*, 5698.

(228) Dube, D. H., Bertozzi, C.R. *Nat. Rev. Drug Discovery.,* **2005**, *4*, 477.

(229) Feng, L., Hong, S., Rong, J., You, Q., Dai, P., Huang, R., Tan, Y., Hong, W., Xie, C., Zhao, J., Chen, X., *J. Am. Chem. Soc.,* **2013**, *135*, 9244.

(230) Turkevitch, J., Stevenson, P. C., Hillier, J. *Discuss. Faraday Soc.,* **1951**, *11*.

(231) Lee, P., Miesel, D., *J.Phys.Chem* **1982**, *86*, 3391.